Numerical Simulation of a Mesoscale Convective Complex: Model Development and Numerical Results

by Craig J. Tremback

Colorado State University

DEPARTMENT OF ATMOSPHERIC SCIENCE

PAPER NO.
465

NUMERICAL SIMULATION OF A MESOSCALE CONVECTIVE COMPLEX: MODEL DEVELOPMENT AND NUMERICAL RESULTS

by

Craig J. Tremback

Department of Atmospheric Science

Colorado State University

Fort Collins, CO 80523

Research Supported by

The National Science Foundation

under grants ATM-8312077, ATM-8512480, and ATM-8814913

Air Force Geophysics Laboratory

under contracts AFGL-TR-87-0219 and AFGL-TR-84-0028

Electric Power Research Institute

under contract #1630-53

Army Research Office

under contract DAAL03-86-K-0175

and

Air Force Office of Scientific Research

under contract AFOSR-88-0143

Atmospheric Science Paper No. 465

ABSTRACT

NUMERICAL SIMULATION OF A MESOSCALE CONVECTIVE COMPLEX: MODEL DEVELOPMENT AND NUMERICAL RESULTS

A mesoscale numerical model has been developed and used to study the complex circulations of a baroclinic environment which supported the development of a mesoscale convective complex (MCC). The hydrostatic numerical model was first written as a separate version of the CSU cloud/mesoscale model. The non-hydrostatic cloud model and the hydrostatic meso-/synoptic-scale model were combined in 1983 to form the CSU Regional Atmospheric Modelling System (RAMS). Some of the aspects of RAMS developed during the coarse of this research were a hydrostatic "time-split" time differencing scheme, a prognostic soil temperature and moisture model, a new form of the higher ordered forward upstream advection scheme, an improved version of the Fritsch and Chappell convective parameterization scheme, a simple form of the Kuo-type convective parameterization scheme, and an isentropic data analysis package.

The goal of the numerical simulations was to employ the numerical model to study an MCC with higher space and time resolution than is available through observational means, not to reproduce the observations that were available. The model results were compared with the observations, however, to examine the credibility of the model. While there were many differences, the coarse resolution (about 110 km) control run simulated an MCC whose meso-α-scale structure and environment evolved similarly with the observed convective system to establish the credibility of the numerical model. Two additional coarse resolution simulations were used to examine the predictability of the model formulation and sensitivity to initial conditions These simulations showed more research still needs

to be done on basic modelling problems in order to apply these models to operational forecasting.

Higher resolution simulations (about 45 km) were made to increase the spatial resolution. A comparison between the coarse resolution and higher resolution runs showed only small differences in the gross behavior of the simulated MCC disturbance. The results of the higher resolution control run were examined for the important forcing mechanisms of this MCC. For the development of the MCC, an important forcing mechanism was the development and propagation of the mountain/plains solenoidal circulation which was forced by the baroclinicity created by the physiographic features of the topography slope and horizontal gradients of soil moisture. Other factors present in the simulation that were hypothesized to be important were a low-level "heat low" in the Montana-Wyoming region, the Bermuda high providing a favorable pressure gradient over the central plains for the development of a strong nocturnal low-level jet, a weak front moving southward from Canada, and an upper level jet core in a favorable position to provide upper-level divergence.

Results from a two-dimensional simulation, in which a simplified physiographic forcing was used to create a solenoid, verified many features of the solenoid's behavior. The solenoid may also be responsible for the nocturnal preference for MCCs and the frequently observed mid-level shortwave that often accompanies the convective systems.

Two higher resolution sensitivity simulations were performed. The first, in which the convective parameterization was not used, showed the expected result that no mesoscale circulations developed that exhibited the characteristics of an MCC. This dry run, as with the control run, produced a low-level solenoidal circulation which propagated across the Dakotas. At the end of the simulation, the dry solenoid looked very similar to the solenoid in the control run after the MCC disturbance outran the solenoid. The second sensitivity experiment with the resolved microphysical parameterizations activated showed that the gross behavior of the MCC was similar to the control run although there were differences in the details of the mesoscale vertical motion fields and locations of convection underneath the anvil.

Craig J. Tremback
Department of Atmospheric Science
Colorado State University
Fort Collins, Colorado 80523
Spring, 1990

ACKNOWLEDGEMENTS

I would like to express my gratitude to my adviser, Dr. William Cotton, for his excellent guidance, advice, and patience over the years of this research. His suggestions concerning the direction of this research proved invaluable. Dr. Roger Pielke, who served on my graduate committee, participated in many discussions about numerical modelling through the years and made many good suggestions on this dissertation. My other committee members, Professor L. Grant and Dr. J. Peterka, also made some useful comments on this manuscript.

Other individuals also contributed greatly to the development of the numerical model. Dr. Greg Tripoli is acknowledged for the development of the earlier versions of RAMS and literally dozens of useful discussions about modelling and meteorology during the early stages of this work. Dr. Robert Walko assisted greatly in the development of the later versions of the model. Other past and current members of Drs. Cotton's and Pielke's research groups, especially Ray McAnelly, Dr. Kevin Knupp, Dr. Chaing Chen, Jennifer Cram, Michael Moran, Jerry Schmidt, and Piotr Flatau, also helped in various ways including acquisition of data and software, scientific suggestions, and development and testing of portions of the model code.

This work could not have been completed without the unwavering support of my family and especially my wife, Lisa. Her support and patience made the pursuit of this degree possible.

I would like to thank Brenda Thompson and Shari Thorson for their excellent preparation of this manuscript. Much of the computing was done at the National Center for Atmospheric Research (NCAR) which is supported by the National Science Foundation. The observational data was accessed from datasets archived by the Data Support

Section at NCAR. This research was funded by the National Science Foundation under grants ATM-8814913, ATM-8512480, and ATM-8312077, by the Air Force Geophysics Laboratory under contracts AFGL-TR-87-0219 and AFGL-TR-84-0028, by the Air Force Office of Scientific Research under contract AFOSR-88-0143, by the Electric Power Research Institute under contract #1630-53, and by the Army Research Office under contract DAAL03-86-K-0175.

TABLE OF CONTENTS

LIST OF FIGURES

LIST OF TABLES

Chapter 1

INTRODUCTION

The nocturnal maximum in summertime convection in the central and eastern U.S. has been recognized for most of the twentieth century. Wallace (1975) provides a review of some of the earlier work dating back to 1901. Some of the reasons given by past researchers include destabilization from radiational cooling aloft (Hewson, 1937) and low-level warm advection (Means, 1944). However, there is compelling evidence (Hering and Borden, 1962; Pitchford and London, 1962; Means, 1952; Blackadar, 1957) that the nocturnal maximum is related to the low-level jet. The boundary layer mass convergence created by the jet can cause enough vertical motion to release the convective instability that occurs over much of the U.S. in summer (Wallace, 1975; Curtis and Panofsky, 1958). A climatology of the low level jet has been performed by Bonner (1968).

Most of the thunderstorms responsible for the nocturnal maximum occur in mesoscale convective systems. The two most significant of these systems are the frontal and pre-frontal squall line and the recently defined mesoscale convective complex (MCC) (Maddox, 1981). The squall line has been the most studied, with cases being reported by Newton (1950), Newton and Newton (1959), Fujita (1959), and Ogura and Liou (1980), among others. Studies of MCC-type systems included Maddox (1981), Bosart and Sanders (1981), Cotton et al. (1983), Wetzel et al. (1983), Fritsch and Maddox (1981a), and Fortune (1989).

Although these mid-latitude mesoscale convective systems have been recognized and studied for many years, only recently have the major systems been sub-divided into squall line type systems and the mesoscale convective complex (MCC) (Maddox, 1981). This subdivision was based on the areal extent and shape of the anvil shield as discerned from

IR satellite images; a system needed to have a large nearly circular anvil shield to be classified as a MCC. Maddox also noted differences in the environments that supported each type of system. A squall line system tended to form in strongly baroclinic, highly sheared environments with the active convective cells oriented perpendicular to the shear, while the MCC tended to form in weakly sheared, less baroclinic environments with the convection oriented parallel to the shear.

Unfortunately, this dynamical subdivision is not always followed by the atmosphere. A system that meets Maddox's criteria can form in a squall line type environment and some ordinary squall lines (not prefrontal) may have anvil structures which fall under Maddox's anvil shape criteria. A case in point was the MCC which formed on 3 August 1981 in eastern Montana and the western Dakotas in an environment characterized by strong shear and baroclinicity. The early stages of this MCC was analyzed by Schmidt and Cotton (1989). Although this system was able to support the large anvil circulation similar to the "classical" MCC, the strongest convection was oriented perpendicular to the shear for much of the system's lifetime, more similar to a squall line. Also the severe weather produced by this system was more indicative of a squall line (mostly high winds). Thus, this MCC appeared to be somewhat of a hybrid system.

The lack of a dynamical definition of the MCC inhibits both our understanding and forecasting ability of this type of convective system. As a start toward a dynamical definition, Cotton et al. (1989) proposed the following: "A mature MCC represents an inertially stable mesoscale convective system which is nearly geostrophically balanced and whose horizontal scale is comparable to or greater than λ_R (Rossby radius of deformation)."

Recently, the science, engineering, and technology of numerical modelling on the mesoscale has progressed to the point where it is feasible to simulate mesoscale convective systems. Modelling results reported in the literature include Fritsch and Chappell (1980b), Fritsch and Maddox (1981b), Perkey and Maddox (1985), Zhang and Fritsch (1985), and Zhang et al. (1989). These results show that it is possible through the use of a numerical model to make inferences of the dynamical structure and evolution of mid-latitude convective systems.

This dissertation will investigate the 3 August 1981 MCC in an attempt to isolate some of the important dynamical and physical characteristics responsible for the generation and maintenance of this MCC. Various aspects of the initiation and growth of the MCC, with a focus on the meso-α scale forcing mechanisms and the quasi-balanced circulation that is mostly responsible for the circular appearance of the cloud shield, will be investigated.

To study these systems, a numerical model has been developed which includes the physical processes necessary to simulate the complex circulations and interactions of a MCC and its environment. A numerical model is necessary for this study because it not only provides higher spatial and temporal resolution than the standard upper air rawinsonde network, but it also allows the opportunity to examine the important physical processes governing MCC behavior through model sensitivity experiments.

Obviously, caution must be taken in the interpretation of the model results and the generalization to even the specific case studied, let alone the extension to other convective systems. A numerical model simulation contains degrees of uncertainty and approximations in many areas including formulation of physical processes, numerical procedures, spatial resolution, and initial conditions. This thesis will, therefore, take the following approach. After a review of some of the previous work in this area, the formulation of the numerical model will be described. Then, a discussion and some model sensitivity simulations testing some of the uncertainties in the model formulation and initial conditions will be presented. The choice of a "control" simulation will be made and it will be shown that the control simulation has reproduced many of the observed characteristics of the MCC. The goal of this research is not to exactly reproduce the observations but to provide a vehicle in which to study the atmospheric circulations associated with an MCC. Still, the realism of the model results must be verified to some degree. Sensitivity simulations testing some physical processes will then be presented and a particularly important mesoscale forcing mechanism will be focused upon.

Chapter 2

PREVIOUS RESEARCH

This chapter will briefly review some of the research done on the MCC, it's environment, and attempts made to numerically model some case studies.

2.1 Observational studies

Maddox (1980, 1981) was the first to differentiate between the MCC and other types of mesoscale convective systems. According to his definition which was based on satellite imagery, a convective system can be classified as an MCC if the areal extent of the $-32°$C isotherm covers more than $100,000km^2$ and the $-52°$C isotherm is larger than $50,000km^2$ for at least 6 hours. In addition the eccentricity of the anvil shield needs to be greater than 0.7 . Maddox composited ten cases of MCC development. Cotton et al. (1989), with a much larger number of cases (over 150), was able to verify some of Maddox's conclusions and add to the knowledge of the structure and life cycle of the MCC. Some of Cotton et al.'s and Maddox's conclusions are:

- The development and propagation of the MCC is tied to the movement of a tropospheric shortwave trough.
- A large regional coverage of conditionally unstable air occurs ahead of the shortwave.
- The MCC usually develops near an east-west oriented, surface frontal zone and moves with the mid-level steering flow.
- The nocturnal development of the low-level jet resupplies the conditional instability. The MCC occurs within the convergent region at the nose of the low-level jet.

- The strongest convection often occurs in the right rear quadrant of the system, sometimes assuming a linear organization parallel to the systems direction of movement.
- The environment responds to the convective heating by developing a deep inflow into the system that extends to the mid-troposphere. At times, this may be a mid-level "jet-like" inflow having a maximum intensity at about 600 hPa and may support a mesoscale downdraft and enhance the circulation of the entire system. Much of the inflow probably contributes to a central region of mesoscale ascent.
- Early in the life cycle of the MCC, the mesoscale upward motion is centered about 700 hPa. As the MCC matures, the maximum mesoscale updraft rises to about 400 hPa while a layer of downward motion develops from 700 hPa to the surface.
- The MCC is cold core near the surface, warm core through most of the troposphere, and cold core in the upper troposphere and lower stratosphere. This thermal structure produces a surface mesohigh, a mid-tropospheric mesolow, and a mesohigh in the upper troposphere. This pressure structure, in turn, produces enhanced low to mid- level inflow and an upper level anticyclonic outflow jet along the northern edge of the system. The mid-level mesocyclone is confined from the surface to about 700 hPa.

As pointed out by Maddox (1981), Lin (1986), Wetzel et al. (1983), and others, the MCC has several characteristics in common with tropical cloud clusters such as those studied by Williams and Gray (1973), Frank (1978), McBride and Zehr (1981), and Lee (1986). Aside from the obvious similarities of a precipitating system with deep convective cells and a thick anvil shield, the systems also exhibit similarities in other aspects of their circulations. Vertical motion and divergence profiles (Wetzel, et.al., 1983) were similar between the two systems with a relatively shallow layer of strong divergence near the tropopause and a general convergence through the mid-troposphere and an upward vertical motion maximum in the upper troposphere. Maddox (1981) mentioned that both systems tend to be warm core in the middle to upper troposphere and that the environments tend to be similar with little vertical wind shear and weak mid-level vorticity advection. Maddox (1981) and Wetzel et al. (1983) stated that both systems transport little energy meridionally to reduce the existing baroclinicity. In comparing a composite MCC to the composite tropical cluster of Tollerud and Esbensen (1985), Cotton et al. (1989) showed that the MCC developed maximum values of mean upward motion, upper-tropospheric divergence, and vorticity at the mature stage of the system which then persisted until dissipation. The tropical cluster, on the other hand, exhibited maximum values of these features at the mature stage, but then weakened. The composite tropical cluster, however, probably included individual systems which were less than the Rossby radius of deformation.

Although the MCC does exhibit some aspects of a baroclinic system (Maddox, 1981), they do appear to be more similar to the tropical clusters than to the mid-latitude squall line (Cotton et al., 1989). The squall line usually forms in an environment characterized by high vertical wind shear, hence strong baroclinicity. The convective cells in a squall line are usually oriented perpendicular to the wind shear, while in an MCC, the cells can take a variety of organizations from randomly organized ("popcorn") convection to arc-shaped lines (Leary and Rappaport, 1983) to lines oriented parallel to the shear (Maddox, 1981) to a wave-cyclone organization (Fortune, 1989).

To combine these conclusions and other findings into an observational model, the synoptic scale provides several of the necessary ingredients for the development of the MCC. These include a large area of conditional instability, warm, moist inflow into the system, typically from the nocturnal central plains "low-level jet" produced by an inertial oscillation of the wind over the sloping Great Plains as the atmosphere decouples from the surface due to radiational cooling in the presence of a favorable synoptic pressure gradient which is enhanced by differential thermal forcing due to the terrain slope (McNider and Pielke, 1981), and a "trigger" mechanism which may be a surface front or previous convection generated by perhaps "orogenic" convection (George, 1979) which propagates off the mountains (Wetzel et al., 1983; Cotton et al., 1983). Mid-level moist inflow from the southwest (North American "monsoon") may also be important in some cases (Culverwell, 1982), especially in the mid-to-late summer. Convection then develops or the previous convection merges which may result in explosive development (Maddox, 1981). The convective heating results in a mesoscale modification of the pressure fields, creating a mid-level mesocyclone and an upper level mesohigh which then forces mid level inflow and creates an upper level outflow jet streak.

This observational model leaves several unanswered questions regarding the forcing components, the necessity of them, and cause/effect relationships. For instance, is the trigger mechanism necessary? Can convection develop *in situ* which will organize into an MCC? Is there a particular environment that is an exclusively MCC environment as opposed to a squall line environment? Are there other physical processes that are important in organizing the convection on the mesoscale, such as radiational processes? What are the physical processes that modulate the strength of the mesoscale circulation? How does a mid-level shortwave "happen" to appear at the time that other synoptic scale conditions are favorable to produce a nocturnal preference for the MCC? Particularly perplexing is the fact that MCCs often appear in seven to ten day episodes with shortwaves occurring with each MCC that forms.

2.2 Modelling studies

Only until very recently, within the past decade, has it been feasible to numerically simulate the MCS, although numerical models have been in use, even operationally, for much longer. Unlike the synoptic scale, where early success in modelling was attained with two dimensional barotropic vorticity models, the MCS is inherently three dimensional. This requires then that a more complicated equation set, most likely a primitive equation model, be considered. Coupled with the three dimensionality, the strong nonlinear character of the system, and the need to resolve the mesoscale spatial scales with the model resolution (hence, requiring higher time resolution also), the computational task was more than computers of the middle 1970's and before could handle. The lack of adequate computer power also affected other aspects of the simulation of MCS's; most notably it has dictated the need for the parameterization of convection, which continues to be perhaps the most difficult problem facing mesoscale numerical modellers today.

Most of the MCS related modelling work of the past decade has focused on reproducing features of the observed systems and their associated precipitation. Fritsch and Chappell (1980b) and Fritsch and Maddox (1981b), using analytic initial conditions, found that there were some of the observed features of MCS's in the model fields and stressed the importance of the convective parameterization in producing these features. Perkey and Maddox (1985) in a case study found that model-generated upscale feedbacks occurred which were similar to observed features and that the convective tendencies were required to produce the upscale response.

With a stated goal "... to establish the potential to operationally predict MCS's," Zhang (1985) very successfully reproduced the precipitation patterns associated with the Johnstown flood case study (Bosart and Sanders, 1981). In addition, with numerous sensitivity experiments, he was able to shed some light as to which of the physical processes included in the model were important in creating the pattern. He found that the moisture when included as part of the virtual temperature was necessary for the development of the MCC as was the convective heating. Parameterized convective downdrafts were also important. In his simulation, resolvable precipitation accounted for a significant fraction (30-40%) of the total rainfall which points to the necessity of including both a convective parameterization and a resolvable precipitation scheme in the model. Also, "bogus" soundings, from the analyses of Bosart and Sanders (1981), were needed in the initial conditions of the model simulation.

Koch (1985) performed a study which attempted to find how well a mesoscale model was able to predict MCS development. He ran 30 model forecasts in cases where 149 convective systems were observed. A total of 48% of the convective systems were predicted within 3 hours and 250 km of that observed and that underforecasts were more frequent than overforecasts. Reasons for the underforecasts included poorly forecast upper tropospheric shortwaves, errors in the initialization of the moisture fields, boundary condition problems, and " a host of problems related to deep convection physics." He also stated that "... proper handling of moist convective physics is ... essential to sustaining mesoscale model performance levels."

Taking a very different modelling approach compared to the other studies, Tripoli (1986) and Tripoli and Cotton (1989a,b) used a two-dimensional cloud model with enough horizontal resolution to produce realistic convective circulations without the use of a parameterization and enough grid points to cover a mesoscale domain. By forcing the circulation only through the diurnal heating cycle which created the mountain/plains solenoidal upslope flows, they were able to produce an MCS from the circulation patterns of the slope flows. The convection subsequently deepened the solenoid to the entire depth of the troposphere. The model produced many of the same features in two dimensions (mid-level cyclone, upper-level anti-cyclone, etc.) as most of the other 3-D modelling work, implying a somewhat consistent signature of mesoscale convective systems on the larger scales. They considered the system an ongoing geostrophic adjustment process that is modulated by local conditions. Other of their findings include the importance of the boundary layer on the plains in which the capping inversion at the top of the PBL helps induce a strong slope flow by confining the early morning surface heating to a shallow layer and preventing the surface moisture from mixing out and by preventing transient gravity waves which are forced by developing convection from forming new convection, hence focusing the convective heating to a rather limited region. They also stated that "...the MCS may in some ways be a deepened slope flow powered by moist rather than dry convection." The behavior of the solenoidal slope flow was very different in a sensitivity simulation without latent heat release where the upward branch of the solenoid formed in a similar location but did not propagate toward the east as the MCS in the control simulation. Transient gravity waves in the upper and middle troposphere, also, were found to be partially trapped beneath the anvil after sunset due to radiational destabilization at the cloud top. This could possibly transform the convective system circulation from a single meso-β upward motion core to several less intense cores. Within the framework of the two-dimensional simulations, however, they were not able to generate an MCC when the modelled system reached the Kansas plains because of the lack of three-dimensional effects, mostly the absence of the southerly low-level jet.

Chapter 3

MODEL DESCRIPTION

The hydrostatic mesoscale model used in this study was developed as part of the CSU cloud/mesoscale model (Tripoli and Cotton, 1982; hereafter, TC). The hydrostatic model, along with the isentropic data analysis package described in Chapter 4 and the cloud model, has been incorporated into the CSU Regional Atmospheric Modelling System (RAMS). The general equation set, parameterizations, and numerical approximations for the options of RAMS used in this study are described in the following sections.

3.1 General equations

The general equations for the RAMS configuration used in this study are described below. The equations are the standard hydrostatic averaged equations. All variables, unless otherwise denoted, are grid-volume averaged quantities where the overbar has been omitted. The horizontal and vertical grid transformations are omitted in this section for clarity.

Equations of motion:

$$\frac{\partial u}{\partial t} = -u\frac{\partial u}{\partial x} - v\frac{\partial u}{\partial y} - w\frac{\partial u}{\partial z} - \theta\frac{\partial \pi'}{\partial x} + fv + \frac{\partial}{\partial x}\left(K_m\frac{\partial u}{\partial x}\right) + \frac{\partial}{\partial y}\left(K_m\frac{\partial u}{\partial y}\right) + \frac{\partial}{\partial z}\left(K_m\frac{\partial u}{\partial z}\right)$$

$$\frac{\partial v}{\partial t} = -u\frac{\partial v}{\partial x} - v\frac{\partial v}{\partial y} - w\frac{\partial v}{\partial z} - \theta\frac{\partial \pi'}{\partial y} - fu + \frac{\partial}{\partial x}\left(K_m\frac{\partial v}{\partial x}\right) + \frac{\partial}{\partial y}\left(K_m\frac{\partial v}{\partial y}\right) + \frac{\partial}{\partial z}\left(K_m\frac{\partial v}{\partial z}\right) \quad [1]$$

Thermodynamic equation:

$$\frac{\partial \theta_{il}}{\partial t} = -u\frac{\partial \theta_{il}}{\partial x} - v\frac{\partial \theta_{il}}{\partial y} - w\frac{\partial \theta_{il}}{\partial z} + \frac{\partial}{\partial x}\left(K_h\frac{\partial \theta_{il}}{\partial x}\right) + \frac{\partial}{\partial y}\left(K_h\frac{\partial \theta_{il}}{\partial y}\right) + \frac{\partial}{\partial z}\left(K_h\frac{\partial \theta_{il}}{\partial z}\right)$$

$$+\left(\frac{\partial\theta_{il}}{\partial t}\right)_{con}+\left(\frac{\partial\theta_{il}}{\partial t}\right)_{res}+\left(\frac{\partial\theta_{il}}{\partial t}\right)_{rad} \qquad [2]$$

Moisture and condensate mixing ratio continuity equations:

$$\frac{\partial r_n}{\partial t}=-u\frac{\partial r_n}{\partial x}-v\frac{\partial r_n}{\partial y}-w\frac{\partial r_n}{\partial z}+\frac{\partial}{\partial x}\left(K_h\frac{\partial r_n}{\partial x}\right)+\frac{\partial}{\partial y}\left(K_h\frac{\partial r_n}{\partial y}\right)+\frac{\partial}{\partial z}\left(K_h\frac{\partial r_n}{\partial z}\right)$$

$$+\left(\frac{\partial r_n}{\partial t}\right)_{con}+\left(\frac{\partial r_n}{\partial t}\right)_{res} \qquad [3]$$

Mass continuity equation:

$$\frac{\partial\rho u}{\partial x}+\frac{\partial\rho v}{\partial y}+\frac{\partial\rho w}{\partial z}=0 \qquad [4]$$

Hydrostatic equation:

$$\frac{\partial\pi}{\partial z}=-\frac{g}{\theta_v}+g\left(r_T-r_v\right) \qquad [5]$$

The symbols in the above equations are defined in Table 3.1. The numerical treatment of each equation and term is described below.

3.2 Grid structure

The grid stagger is identical to TC, who used the standard C grid (Mesinger and Arakawa, 1976). All thermodynamic and moisture variables are defined at the same point with the velocity components, u, v, and w staggered $1/2\Delta x$, $1/2\Delta y$, and $1/2\Delta z$, respectively.

The horizontal grid used in this study is in a latitude-longitude configuration. The vertical structure of the grid uses the σ_z coordinate system (Gal-Chen and Somerville, 1975a,b; Clark, 1977) which was described by TC.

3.3 Advection

The advection operator is the flux form of the sixth-order forward upstream advection scheme that was derived and tested by Tremback et al. (1987). This sixth order scheme is in the same family of schemes as the classical first order forward upstream scheme and the much used Crowley (1968) second order scheme. As described in detail by Tremback

Table 3.1: Symbols used in Chapter 3

u	–	east-west wind component
v	–	north-south wind component
w	–	vertical wind component
f	–	Coriolis parameter
k_m	–	eddy viscosity coefficient for momentum
k_h	–	eddy viscosity coefficient for heat and moisture
θ_{il}	–	ice-liquid water potential temperature
r_n	–	water mixing ratio species of total water, rain, pristine crystals, aggregates, and snow
ρ	–	density
con	–	subscript denoting tendency from convective parameterization
rad	–	subscript denoting tendency from radiation parameterization
res	–	subscript denoting tendency from resolvable scale microphysical parameterization
g	–	gravity
r_t	–	total water mixing ratio
r_v	–	water vapor mixing ratio
π	–	total Exner function
π'	–	perturbation Exner function
θ_v	–	virtual potential temperature
p	–	pressure

et al. (1987), two different forms of the flux scheme can be derived. The first, following the methodology of Crowley (1968), fits a polynomial to the field being advected then integrates the function, while the second, requires that the flux form reduce to the advective form for constant grid spacing and advecting velocity. The second form is more accurate than the first but does require that the grid spacing be constant. Therefore, the first form, called the integrated flux form, is used in the vertical where the grid spacing is stretched to provide higher resolution near the ground. The second form is used in the horizontal where the grid spacing is constant in any one direction. The advective terms in (1)-(4) then can be generically written in tensor notation assuming constant grid spacing and omitting topographical and spherical transformations for clarity, as:

$$u_i\frac{\partial\phi}{\partial x_i} = \frac{1}{\rho}\frac{\partial\rho u_i\phi}{\partial x_i} - \phi_j\frac{\partial\rho u_i}{\partial x_i} = \frac{1}{\rho_j\Delta x}\left[\left((\rho F)_{j+1/2} - (\rho F)_{j-1/2}\right) - \phi\left((\rho u)_{j+1/2} - (\rho u)_{j-1/2}\right)\right]$$

where u_i is the wind component in the x_i direction, ρ is the air density, and ϕ is the variable to be advected. The subscript j references a particular grid point. The expressions for the fluxes, F, are

-Integrated flux form

$$F_{j+1/2}\frac{\Delta t}{\Delta x} = \frac{\alpha}{256}(-3\phi_{j-2} + 25\phi_{j-1} - 150\phi_j - 150\phi_{j+1} + 25\phi_{j+2} - 3\phi_{j+3})$$
$$+\frac{\alpha^2}{3840}(-9\phi_{j-2} + 125\phi_{j-1} - 2250\phi_j + 2250\phi_{j+1} - 125\phi_{j+2} + 9\phi_{j+3})$$
$$+\frac{\alpha^3}{288}(5\phi_{j-2} - 39\phi_{j-1} + 34\phi_j + 34\phi_{j+1} - 39\phi_{j+2} + 5\phi_{j+3})$$
$$+\frac{\alpha^4}{192}(\phi_{j-2} - 13\phi_{j-1} + 34\phi_j - 34\phi_{j+1} + 13\phi_{j+2} - \phi_{j+3})$$
$$+\frac{\alpha^5}{240}(-\phi_{j-2} + 3\phi_{j-1} - 2\phi_j - 2\phi_{j+1} + 3\phi_{j+2} - \phi_{j+3})$$
$$+\frac{\alpha^6}{720}(-\phi_{j-2} + 5\phi_{j-1} - 10\phi_j + 10\phi_{j+1} - 5\phi_{j+2} + \phi_{j+3})$$

-Constant grid flux form

$$F_{j+1/2}\frac{\Delta t}{\Delta x} = \frac{\alpha}{60}(-\phi_{j-2} + 8\phi_{j-1} - 37\phi_j - 37\phi_{j+1} + 8\phi_{j+2} - \phi_{j+3})$$
$$+\frac{\alpha^2}{360}(-2\phi_{j-2} + 25\phi_{j-1} - 245\phi_j + 245\phi_{j+1} - 25\phi_{j+2} + 2\phi_{j+3})$$
$$+\frac{\alpha^3}{48}(\phi_{j-2} - 7\phi_{j-1} + 6\phi_j + 6\phi_{j+1} - 7\phi_{j+2} + \phi_{j+3})$$
$$+\frac{\alpha^4}{144}(\phi_{j-2} - 11\phi_{j-1} + 28\phi_j - 28\phi_{j+1} + 11\phi_{j+2} - \phi_{j+3})$$
$$+\frac{\alpha^5}{240}(-\phi_{j-2} + 3\phi_{j-1} - 2\phi_j - 2\phi_{j+1} + 3\phi_{j+2} - \phi_{j+3})$$
$$+\frac{\alpha^6}{720}(-\phi_{j-2} + 5\phi_{j-1} - 10\phi_j + 10\phi_{j+1} - 5\phi_{j+2} + \phi_{j+3})$$

3.4 Diffusion

The diffusion operators are a first order eddy viscosity type based on a local exchange coefficient that is a function of deformation and stability. The formulation is similar to Smagorinsky (1963) with the modifications by Hill (1974) and Lilly (1962).

$$K_m = \frac{.25}{\sqrt{2}}l^2\sqrt{1 - \frac{K_h}{K_m}Ri}\sqrt{(D^2 + MAX(-N,0)^2)}$$

$$K_h = 3K_m$$

where K_m is the exchange coefficient for momentum, K_h is the coefficient for heat and moisture, D is the deformation, N is the Brunt-Väisälä frequency, and Ri is the Richardson number which is limited to values between 1/3 and -100 for this parameterization. The turbulence scale length, l, is taken as Δz. For the vertical exchange coefficients, the three-dimensional deformation is used. For the horizontal exchange coefficients, only the horizontal components of deformation are used since vertical shear may have little to do with sub-grid scale processes on the meso-α scale resolutions considered in this research. In addition, the horizontal coefficients are limited to a small value to provide a background amount of filtering for numerical dispersion, aliasing, etc. This small value will be discussed and tested in Chapter 7 in more detail.

3.5 Pressure gradient

The horizontal pressure gradient terms are computed with with the standard form of the horizontal gradient for the vertical coordinate transformation as described in TC. A comparison between this computation method and a method in which the pressure perturbation is vertically interpolated to the appropriate level showed no significant differences in the model results.

3.6 Coriolis terms

The Coriolis force terms only include the contribution from the horizontal wind components. Since the hydrostatic equation is used, angular momentum is not conserved if the vertical component of the Coriolis force is included in the horizontal equations of motion. Numerically, the terms are computed with forward time differencing. This can be shown (*i. e.*, Pielke, 1984) to be linearly unstable if f is greater than 0, and that the amplification factor, λ, is given by:

$$\lambda = \sqrt{1 + \Delta t^2 f^2}$$

For the values of f and Δt ($10^{-4}s^{-1}$ and $120s$) used in these simulations, this is a very weak instability. With these values, a perturbation would double in about 13 days.

3.7 Hydrostatic equation and boundary condition

The hydrostatic equation is written in the nonlinearized form with the Exner function.

$$\frac{\partial \pi}{\partial z} = -\frac{g}{\theta_v}$$

$$\pi \equiv C_p \left(\frac{p}{p_{00}} \right)^{R/C_p}$$

A horizontally homogeneous reference state is used to derive the perturbation π that is actually used for the horizontal pressure gradient terms. This reference state is computed with an arbitrary sounding from the domain (grid point with the lowest topography height). The potential temperature from this sounding is interpolated to the σ_z levels at every point and a hydrostatic pressure integration is done from a constant pressure at the model top.

The boundary condition for the hydrostatic equation in the model integration is the prognostic surface pressure equation that is derived from substitution of the hydrostatic equation into the fully elastic mass continuity equation.

$$\frac{\partial p}{\partial t} = -\frac{1}{g} \int_{zg}^{zT} \left(\frac{\partial \rho u}{\partial x} + \frac{\partial \rho v}{\partial y} \right) dz \qquad [6]$$

where z_g is the height of the ground and z_T is the height of the model top.

The boundary condition assumes that the divergence above the model top is small compared to the divergence in the domain. This assumption is consistent with many σ_p coordinate models in use that set the top pressure of the model at 100 mb (LFM, Anthes and Warner, 1978, etc.). The model top for the simulations in this study was set at approximately 80 mb. Also, comparisons of model runs with this boundary condition and runs with a top boundary condition that consisted of a one-layer prognostic σ_p model that extended from the σ_z model top to $p = 0$ that attempted to account for the divergence to the top of the atmosphere showed no significant differences in the results.

3.8 Time differencing

The model is formulated with a time differencing scheme (Tremback et al., 1985) that is similar to the time-split schemes of TC and Klemp and Wilhelmson (1978). It also is similar to the split explicit scheme of Gadd (1978). The basic idea behind the scheme is to "split" off in a series of smaller timesteps those terms in the equation that are responsible for the propagation of the fast wave modes. In a hydrostatic model, the fast modes are the external gravity wave and the Lamb wave. The latter occurs through the use of the compressible continuity equation in the prognostic surface pressure equation described in the previous section. The time differencing scheme can be demonstrated as follows for a simplified two- dimensional, dry, hydrostatic equation set where the vertical and horizontal coordinate transformations have been removed for clarity.

$$\frac{\partial u}{\partial t} + \theta \frac{\partial \pi}{\partial x} = F_u$$

$$F_u = -u\frac{\partial u}{\partial x} - w\frac{\partial u}{\partial z} + fv \qquad [7]$$

$$\frac{\partial \theta}{\partial t} + w\frac{\partial \theta}{\partial z} = F_\theta \qquad [8]$$

$$F_\theta = -u\frac{\partial \theta}{\partial x}$$

$$\frac{\partial \rho u}{\partial x} + \frac{\partial \rho w}{\partial z} = 0 \qquad [9]$$

$$\frac{\partial \pi}{\partial z} = -\frac{g}{\theta} \qquad [10]$$

As mentioned the object of the time-split scheme is to compute the terms that are primarily responsible for the propagation of the fast modes on a smaller timestep than the slower modes (such as horizontal advection and the Coriolis force). The computational procedure is then as follows for a forward-backward time differencing scheme.

a) The right hand side of [7] and [8], F_u and F_θ are computed.

b) θ is stepped forward to time level $t + \Delta t_L$ where Δt_L is the long timestep.

$$\theta_*^{t+\Delta t_L} = \theta^t + F_\theta \Delta t_L$$

c) θ is stepped forward to time level $t + \Delta t_s$ where Δt_s is the small timestep.

$$\theta^{t+\Delta t_s} = \theta^{t+\Delta t_s} - \Delta t_s \left[w^t \frac{\partial \theta}{\partial z} \right]$$

d) Pressure at $t + \Delta t_s$ is computed with [10].

e) The horizontal velocity is stepped to $t + \Delta t_s$.

$$u^{t+\Delta t_s} = u^t - \Delta t_s \left[\theta \frac{\partial \pi}{\partial x} - F_u \right]$$

f) The vertical velocity at $t + \Delta t_s$ is computed with [9].

g) The pressure boundary condition is updated to $t + \Delta t_s$ with [6] using the divergence at the $t + \Delta t_s$ level.

h) The small timestep, c) - g), is repeated n times until $n\Delta t_s = \Delta t_L$.

3.9 Convective parameterization

A simplified Kuo (1974)-type convective parameterization was used for all simulations. See Chapter 5 for details.

3.10 Microphysical parameterization

To handle the "resolved" condensation and precipitation processes in the simulation that utilized them, the microphysical parameterizations described by Flatau et al. (1989) were used. These are bulk parameterizations similar to Cotton et al. (1982, 1987). In these simulations, the water species of rain, pristine ice, snow, and aggregates were prognosed.

3.11 Radiation parameterization

The parameterizations described by Chen and Cotton (1983) for both the longwave and shortwave radiational tendencies were used in these simulations. These schemes include the radiative effects of condensate, water vapor, ozone, and carbon dioxide.

3.12 Surface layer and soil model

For the lower boundary condition for the atmospheric model, the surface layer and soil model parameterizations described in detail by Tremback and Kessler (1985) were used. This scheme is a modification of the schemes described by Mahrer and Pielke (1977) and McCumber and Pielke (1981) (hereafter, MMP) in which the numerous iterative processes have been removed. This involved formulating prognostic equations for the soil surface temperature and water content by assuming a finite depth soil/atmosphere interface layer. Results shown by Tremback and Kessler (1985) indicate that with a moist soil, the modified and MMP schemes produce very similar results. With a dry soil, the modified scheme produces realistic results while the original MMP scheme can fail to numerically converge.

Similar to Banta (1982), the surface layer fluxes of heat, momentum, and water vapor into the atmosphere were computed with the scheme of Louis (1979). This scheme approximates the profile functions (which need to be solved iteratively) of Businger et al. (1971) with analytic expressions.

Chapter 4

DESCRIPTION OF THE DATA ANALYSIS TECHNIQUE AND INITIAL CONDITIONS

The data used for the initial conditions and large scale lateral boundary tendencies were processed with a mesoscale isentropic data analysis package. Isentropic coordinates have many advantages over other coordinate systems when applied to data analysis. First, since the synoptic scale flow is, to a first approximation, adiabatic, an objective analysis performed on an isentropic surface will better approximate the interstation variability of the atmospheric fields. Second, isentropes tend to be "packed" in frontal areas, thus providing enhanced resolution along discontinuities. Finally, because isentropes are sloped in the vicinity of fronts, short wavelength features are transformed into longer wavelengths that can be more accurately analyzed objectively with much less smoothing than with other coordinate systems. A few disadvantages to isentropic coordinates are also present, namely that the vertical resolution decreases as the atmospheric stability decreases (i.e., in the planetary boundary layer) and that the isentropes frequently intersect the ground.

The analysis domain covered the area from 155° W to 60° W and 10° N to 70° N at a 1.25° spacing on a latitude-longitude grid. Two main datasets were used in the analysis, the NMC mandatory level 2.5° global analysis and the available rawinsondes from the NMC datasets, both of which are archived at NCAR. All significant and mandatory level wind, temperature, and moisture data were used from the rawinsonde reports. No special soundings from the CCOPE experiment or bogus soundings were used. The horizontal wind components, pressure, and relative humidity were interpolated vertically (linearly in p^{R/C_p}) to isentropic levels of 1 K resolution from the surface to 320 K, 5 K resolution from 320 K to 380 K, and 10 K resolution from 380 K to 450 K. Any data underground were assigned a missing value and not included in the analysis. The Barnes (1973) objective analysis scheme was then applied to these variables on the isentropic surfaces with the parameters in the scheme set to yield the response function shown in Figure 4.1. This response curve was chosen to reduce the effect of the $2\Delta s$ (Δs is an average station spacing) "noise" in the fields. Although this may smooth out some of the smaller meso-α scale features, they would not be adequately resolved by the rawinsondes anyway. Once the variables were objectively analyzed to the analysis grid, the Montgomery streamfunction was then obtained in a hydrostatic integration from an objectively analyzed streamfunction "boundary condition" at 360 K.

The atmospheric variables at the earth's surface were analyzed in a similar manner to the upper air variables. Wind components, potential temperature, and relative humidity were objectively analyzed. Pressure and Montgomery streamfunction were obtained hydrostatically from the first isentrope above the ground.

The topography was obtained from a USAF 30 minute average dataset. These data were interpolated to the 1.25° analysis grid with the overlapping polynomial technique of Bleck and Haagenson (1968). However, this field contained slopes in the topography that would cause large spatial truncation errors in the numerically approximated gradients computed in the numerical model. Therefore, the Barnes analysis scheme was employed as a smoother for the interpolated topography fields with the response function shown in Figure 4.2. The unsmoothed and smoothed topography fields are shown in Figure 4.3. Figure 4.3a is the interpolated field with no smoothing. Figure 4.3b is the smoothed field with the response function shown in Figure 4.2. Figure 4.3c is the smoothed field with the response function shown in Figure 4.1. Preliminary simulations (results not shown) with the topography in Figure 4.3c showed substantial differences in the location of the modelled convective systems compared with the less smooth topography in Figure 4.2b. Upon examination of Figure 4.3a-c, it is apparent that not only does the smoothing reduce the amplitude of the topography, but also that the smoothing changes the orientation of some slopes relative to the atmospheric flow, thus, for instance, creating upslope components of the low-level flow where the flow should have been parallel to the slopes.

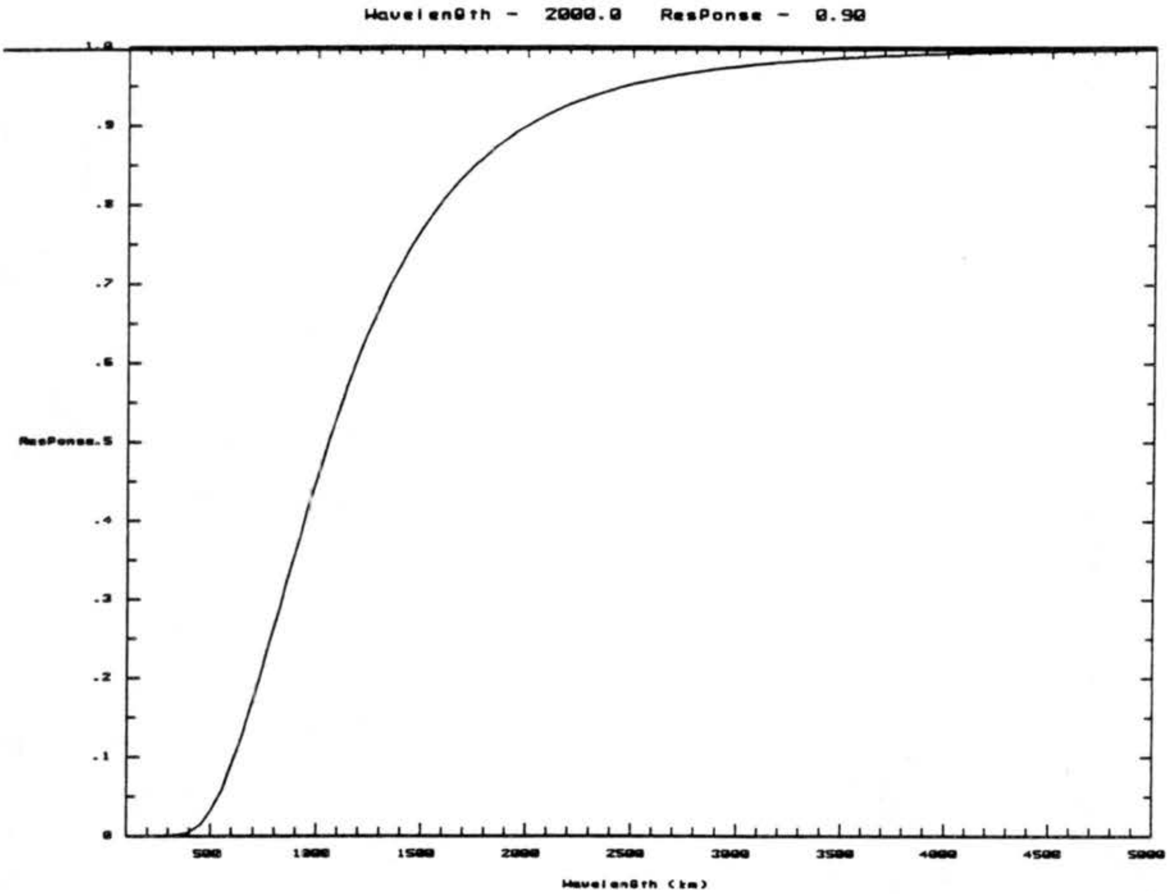

Figure 4.1: Response function for Barnes (1974) objective analysis for a 2000 km wavelength retained at 90%.

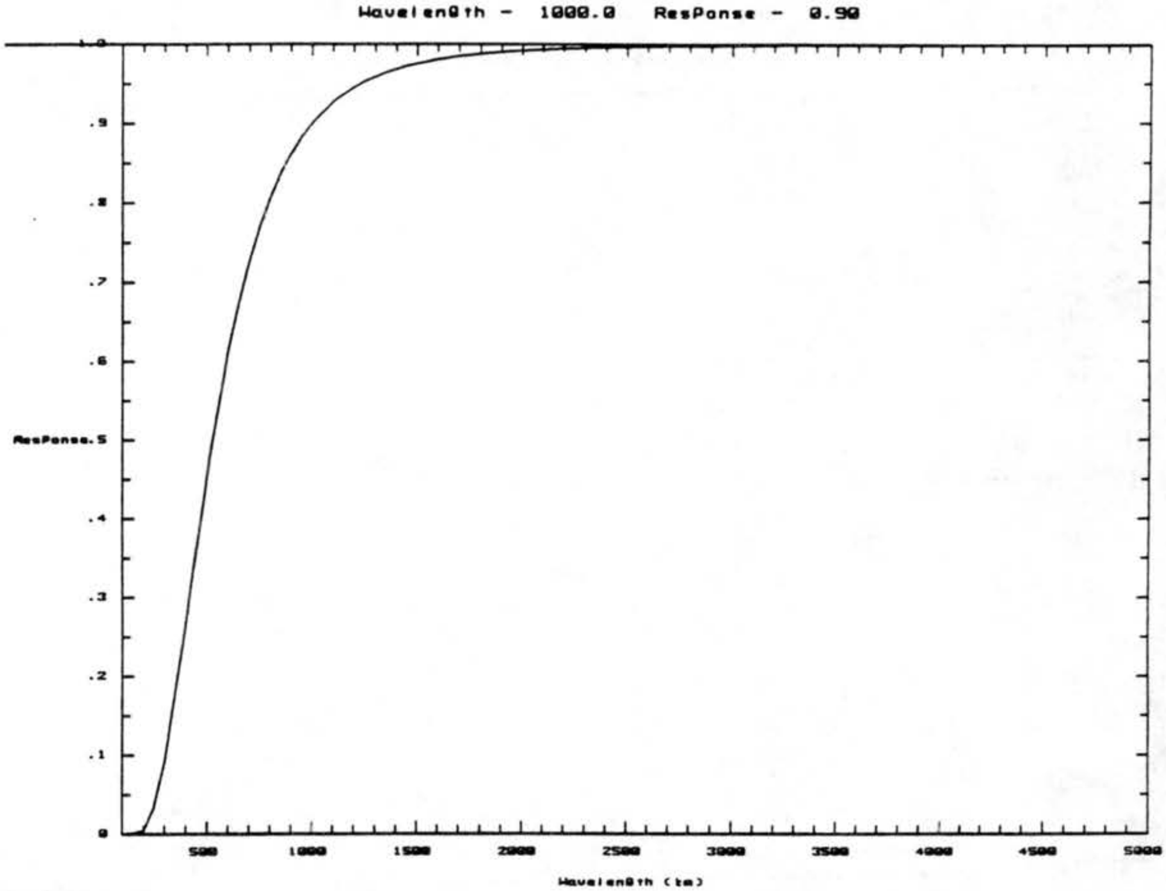

Figure 4.2: Response function for Barnes (1974) objective analysis for a 1000 km wavelength retained at 90%.

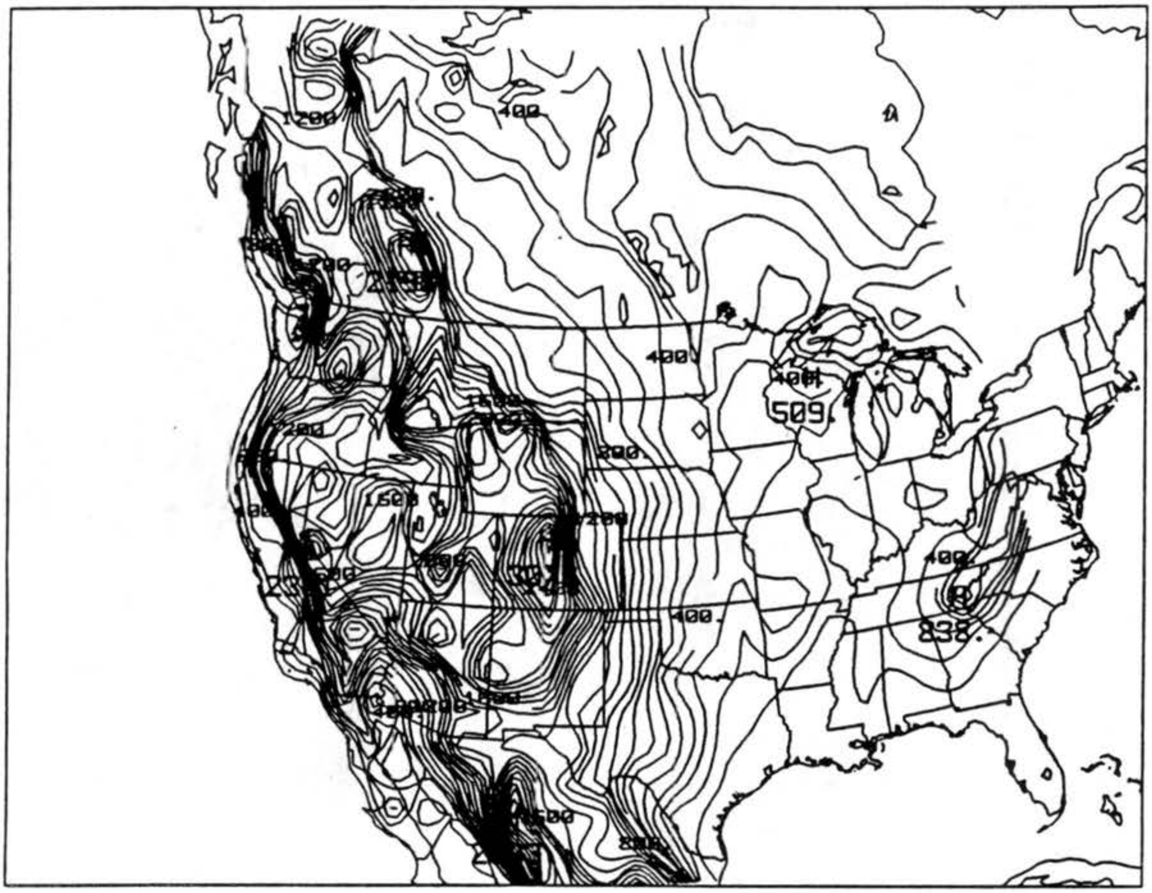

Figure 4.3: a. 1.25° topography field interpolated from 30 minute dataset with no objective analysis. Contour interval is 100 m.

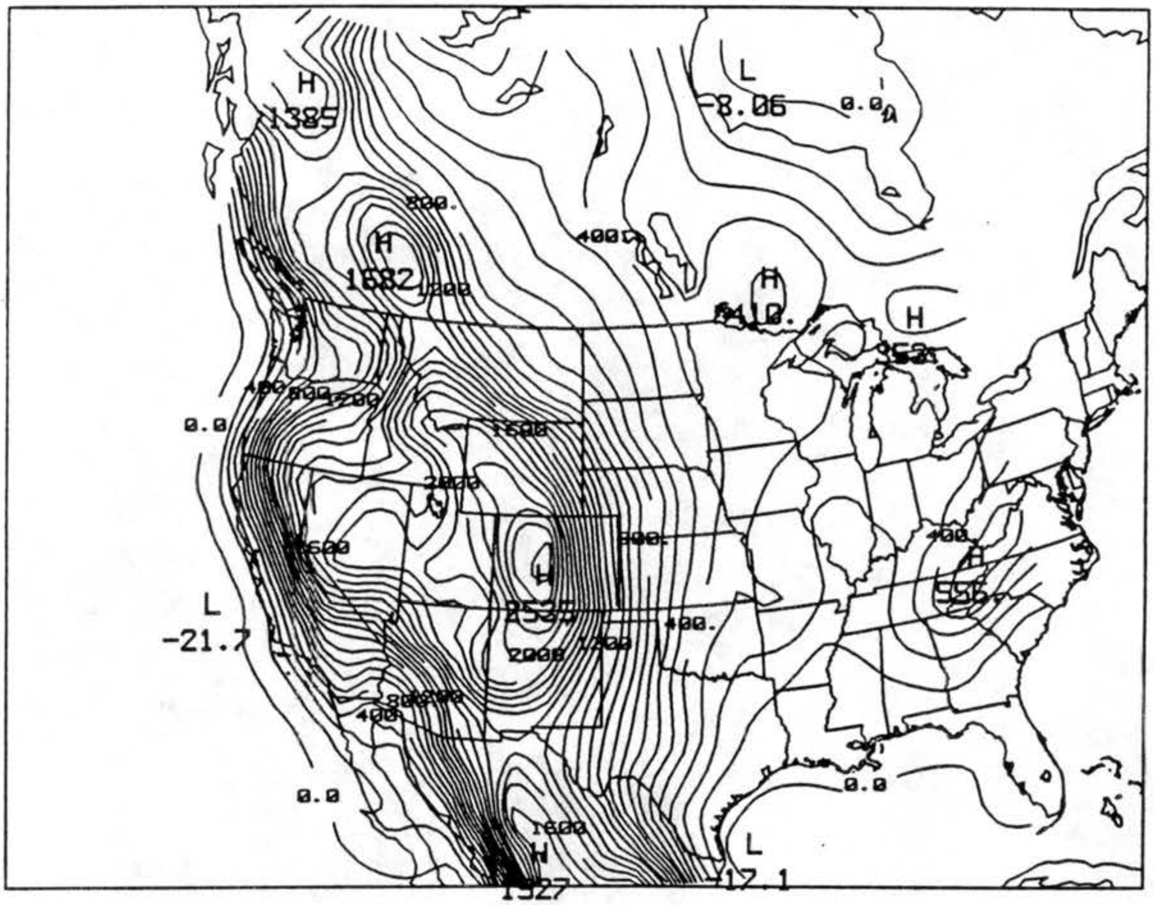

Figure 4.3: b. 1.25° topography field interpolated from 30 minute dataset with objective analysis using response function shown in Figure 4.1. Contour interval is 100 m.

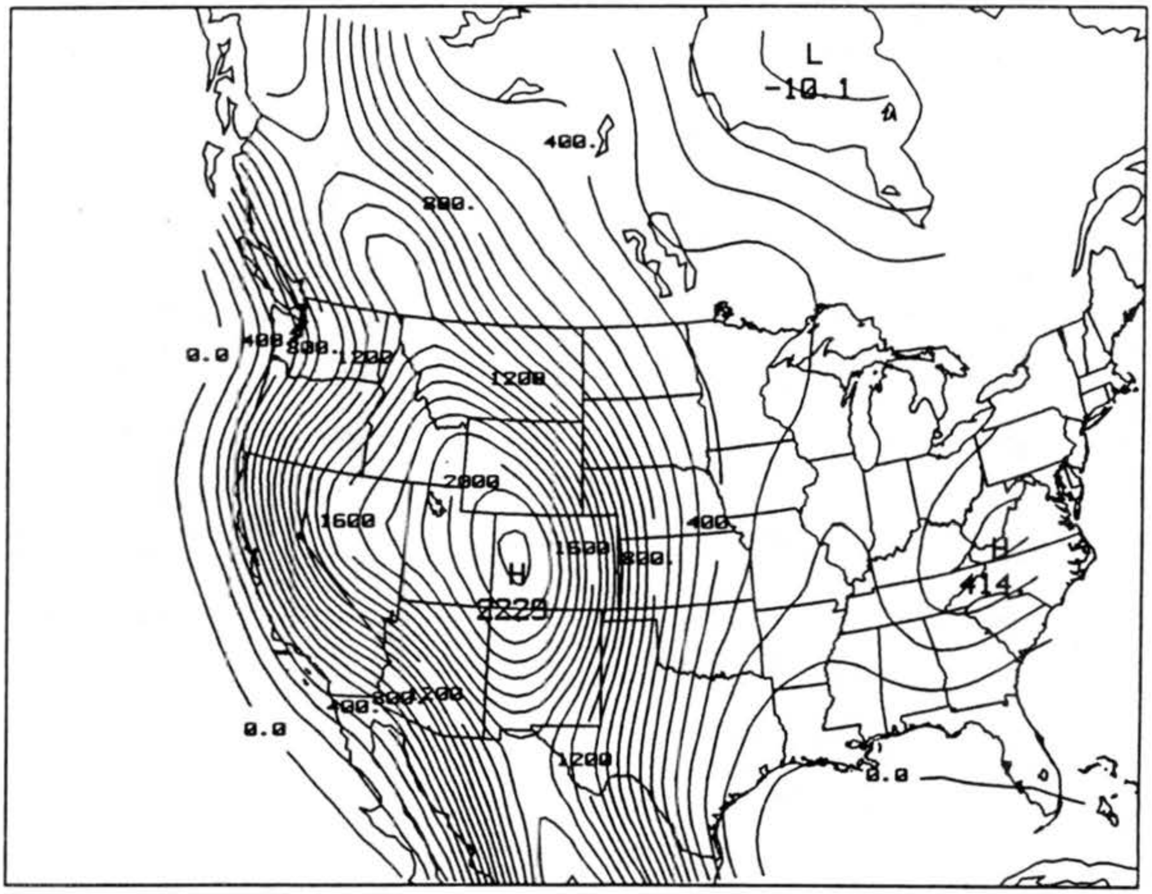

Figure 4.3: c. 1.25° topography field interpolated from 30 minute dataset with objective analysis using response function shown in Figure 4.2. Contour interval is 100 m.

Once the isentropic dataset was complete, the atmospheric variables and topography were transferred to the model grid by interpolation. First, the wind components, streamfunction, and relative humidity were interpolated on the isentropic surface to the model grid point. The height of the isentropic surface could then be found and the wind, potential temperature and relative humidity were interpolated linearly in height to the model's σ_z coordinate levels. A final hydrostatic integration was done to find the pressure on the model grid.

This procedure provided the initial conditions and lateral boundary tendencies for the atmosphere and topography for the simulations. No other initialization method (i.e., normal modes, balance equations, etc.) were used in an attempt to balance the wind and mass fields. There were two primary reasons for this. First, it is unclear from the literature whether such adjustments make an improvement in simulation skill scores and second, although the effects of the measurement errors are minimized by doing the balance, it is possible that the procedure removes actual mesoscale features from the data.

Because of the lack of routine measurements, the initialization of the soil temperature and moisture cannot be done accurately. Therefore, a simple method was used that accounted for the actual variations to a first order only. It was assumed that the surface analysis of atmospheric relative humidity at 1200 UTC also described the relative humidity in the top layer of soil. In addition, the temperature in the top layer of soil was assumed to be 4 K lower than the surface analysis since the model runs began at about local sunrise (1200 UTC). With these values, the soil moisture content in the top soil layer was solved for by using the parameterized equations from the soil model that was used as a lower boundary condition for the atmospheric model.

The profile of soil temperature was defined by assuming a linear increase of 7 K from the surface value to a depth of 20 cm, then constant to the bottom soil level at 50 cm. This profile was modified from the climatological profile given by Sellers (1965) and crudely accounts for the fact that the top soil layer is colder than the air at sunrise but the temperature increases with depth from heat storage of the previous days' radiation. The soil moisture profile was defined assuming that the top layer moisture value doubled linearly from the surface to the bottom soil level. The soil moisture values were limited to 75% of the saturation value at the surface and the saturation value under the surface. A clay loam soil textural type was assumed for all land areas.

Chapter 5

CONVECTIVE PARAMETERIZATION

Probably the most complex problem in mesoscale modelling is the parameterization of convection. Unfortunately, the convective terms are some of the most significant forcing terms in the equations that describe the atmospheric motions, even on the meso-α and synoptic scales. Also, the fact that there have not been many observational studies of the effects of convection on the mesoscale (especially in mid- latitudes) compounds the difficulty of the problem.

Various types of schemes of convective parameterizations have been devised over the years, from rather simple convective adjustment schemes (Manabe et al., 1965; Krishnamurti et al., 1980) to schemes based on equilibrium or quasi-equilibrium assumptions (Arakawa and Schubert, 1974; Kuo, 1965, 1974) to schemes derived specifically for mesoscale models (Kreitzberg and Perkey, 1976; Fritsch and Chappell, 1980a). The adjustment schemes force the grid scale thermodynamic structure toward a moist adiabat in the presence of certain conditions (conditional instability, low level convergence, etc.). The equilibrium-type schemes assume that the convection consumes the conditional instability at the rate at which the grid scale supplies the instability, while the convection consumes the instability that is present in a grid column in the mesoscale schemes.

Several general problems with the current classes of convective parameterizations can be identified:

- Our general knowledge of atmospheric moist convection, its controlling factors, and its effects on the larger scales of motion is very incomplete, at best. This makes the parameterization of convection extremely difficult since it is not clearly known what we are parameterizing. *Intuition, rather than fact, is frequently relied upon.*

- Partly because of the lack of knowledge about convection, partly because of the wide range of forms that convection can take, the current parameterization schemes lack the generality to handle the different forms of convection. Seasonal variations, environmental variations, and even diurnal variations are not well treated. There are many more subtle distinctions which current schemes also have difficulty in handling, such as convection that is not surface based, convergence that is forced by transient gravity waves which may or may not couple with the boundary layer to produce convection, and cases where conditional instability coexists with conditional symmetric instability where the schemes usually put too much energy into the convective modes rather than the slantwise modes.

- Almost all parameterization schemes currently in use treat convection as a subgrid scale process. As computer capabilities and grid resolutions have increased, this assumption is starting to be violated frequently. For example, it is frequently assumed in the parameterizations that the updrafts, downdrafts, and compensating subsidence are all contained within a single grid column. At a 15 km grid spacing, it is very unlikely that the subsidence will occur in the same column as the convection. For some types of convection, even a single updraft may not be contained in a grid column.

- The temporal resolution also needs to be addressed. The parameterizations provide more or less time-integrated convective effects over a few to several hours. With a current emphasis in the mesoscale meteorological community on nowcasting and four-dimensional data assimilation, a more accurate temporal evolution of the convection must be depicted.

Unfortunately, in spite of all these problems, convective parameterization must still be used in meso-β-scale simulations and the meso-α-scale simulations such as those presented in this dissertation. Computer technology is still at least 3 orders of magnitude away from being able to explicitly simulate the convection properly and at the same time simulate the three-dimensional mesoscale interactions of the MCC. Therefore, the remainder of this chapter will describe the development of the convective parameterization schemes studied as part of this research.

The two most used schemes today in mesoscale modelling are the Kuo (1974)-type scheme and the Fritsch and Chappell (1980a, hereafter, FC) scheme. Since Kuo's scheme is an equilibrium-type scheme, hence not accounting for convective instability existing locally, and other researchers have had apparent success in producing convective systems with FC (Fritsch and Chappell, 1980b; Fritsch and Maddox, 1981b; Zhang, 1985), that scheme was initially chosen to be implemented into RAMS.

During the initial stages of the implementation, however, several inconsistencies in the FC scheme became apparent. The two most serious problems were, first, the heating rates and the heating rate profiles produced by the scheme were inconsistent with the limited observational studies in the mid-latitudes, and second, the scheme had no requirement that water mass or total energy be conserved. Figure 11 from Fritsch and Chappell (1980b) is reproduced in Figure 5.1. The magnitude of the heating rates are 2-3 times those from the observations of Lewis (1975) whose computations where made on even a smaller scale than FC. Also, the large heating maximum in FC, directly beneath the tropopause, is inconsistent with Lewis.

Because of these unrealistic heating rates, it was decided to still use the main idea behind the FC scheme, namely the consumption of existing conditional instability within a convective time scale, but to find the source of the problems in the scheme and to fix these and other smaller problems in the original scheme. This was successfully done and the modified scheme is described below.

The difficulty with the convective parameterization problem,however, did not end there. Even though the modified scheme corrected many of the problems of the original scheme, many assumptions and arbitrariness common to both schemes still remained. Comparisons of results from the parameterization with a single parameter taking on two seemingly realistic and physical values produced vastly different simulations; sometimes it was the difference between producing a simulated convective system and not developing a system. Another case in point are the simulations of Zhang (1985). He modified several

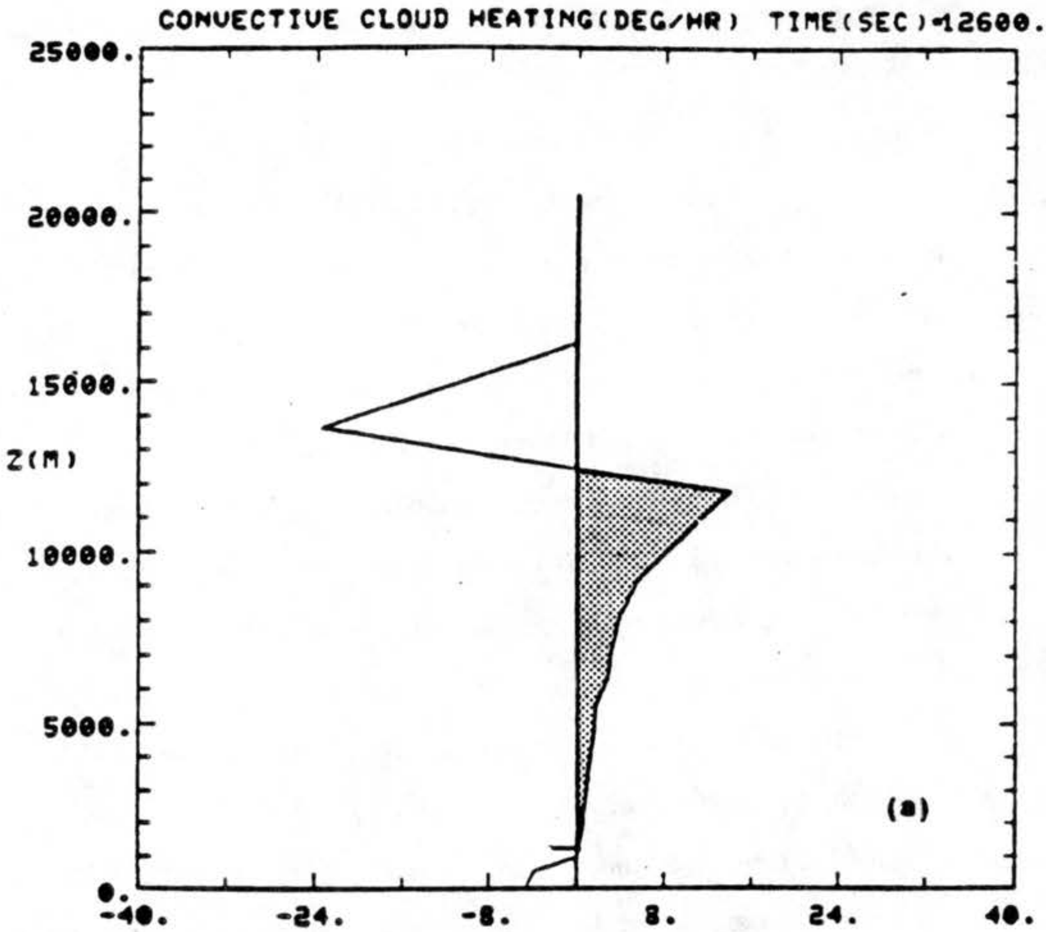

Figure 5.1: Vertical profile of convective heating from Fritsch and Chappell (1980b).

of the important parameters in his implementation of the FC scheme in order to make his model match the observations for a particular case. In simulating another case, it is likely that a different set of modifications may be necessary to again match the observations.

Therefore, a different approach was used in the simulations in the current work. Since the goal of the simulations is not to "tweak" the model to match the observations but rather to provide a test bed to examine the sensitivity of various physical processes in affecting the mesoscale circulations of the MCC, the use of a convective parameterization that is overly sensitive to small changes in the model physics is not justified. Hence, a very simple Kuo (1974) -type scheme was implemented to provide the convective heating and moistening tendencies for the mesoscale model. Although even this simple scheme is not immune to some arbitrariness, there are considerably fewer degrees of freedom than in the FC-type scheme.

The remainder of this chapter is divided into two parts. The first part will describe the Kuo-type scheme implemented in RAMS. The second part will describe the modified FC-type scheme and show some of the sensitivity to various parameters that led to the decision to abandon it in the current study.

5.1 A simplified Kuo convective parameterization

This convective parameterization is a modification of the generalized form of the Kuo (1974) parameterization described by Molinari (1985). The Kuo-type scheme is an equilibrium scheme: convection acts to consume the convective instability that is supplied by the larger scales. The terms in the thermodynamic and moisture equations due to moist convection are written as:

$$\left(\frac{\partial \theta}{\partial t}\right)_{con} = L(1-b)\pi^{-1} I \frac{Q_1}{\int_{z_g}^{z_{ct}} Q_1 dz}$$

$$\left(\frac{\partial r_T}{\partial t}\right)_{con} = bI \frac{Q_2}{\int_{z_g}^{z_{ct}} Q_2 dz}$$

The computation of each quantity in the right hand side is described below.

I is the rate at which the resolvable scale is supplying moisture to a particular grid column. This is parameterized as suggested by Molinari and Corsetti (1985) as the resolved vertical flux of water vapor through the LCL. The quantity b was defined by Kuo (1974) as a moisture partitioning parameter which determines what fraction of I is used to increase the moisture of the column. The remainder of the moisture, $1-b$, is precipitated and its latent heat warms the grid column. In this scheme, the quantity $1-b$ which also can be interpreted as the precipitation efficiency, is computed according to the empirical function given by Fritsch and Chappell (1980a).

Q_1 and Q_2 are vertical profiles of the convective heating and moistening, respectively. For Q_1, the difference between the environmental potential temperature and a convective potential temperature profile is used. To compute this convective temperature profile, a weighted average between the updraft and downdraft profiles is performed. For the updraft, the potential temperature of the moist adiabat of the source level air lifted to its lifting condensation level (LCL) is used. Downdrafts are handled in an even more approximate way. Downdrafts are defined to begin at the level of the θ_E minimum of the sounding at the same temperature as the environment. At cloud base, they are 2 K colder than the environment and at the surface the temperature deficit is 5 K. Other levels are interpolated linearly in height. The weighting function for the downdraft relative to the updraft is also somewhat arbitrarily defined to be 1% of the updraft at their beginning level, 10% at the LCL, 20% at the level of maximum downdraft mass flux (about 800 m as described by Knupp, 1985) and 100% at the surface. This weighting function is then used to define the convective temperature profile. Below cloud base, the environmental temperature is used instead of the updraft.

For Q_2, two actual regions of moisture tendency are defined. The region below cloud base is dried at the rate I. The profile of this drying is the total water mixing ratio which forces the vertical profile of the mixing ratio toward a constant value below cloud base. The anvil region is moistened by the rate bI with the moistening profile constant from 2/3 of the height between the convective source level and the cloud top (consistent with the profile of English, 1973. See section 5.3.2 for details).

As pointed out by Molinari (1985), there is no requirement built into the scheme to reach the moist adiabat in the limit. Therefore, a check is made on the potential temperature profile with the convective tendencies added to see if any level will exceed the moist adiabatic value after the total convective tendencies are applied. The moisture supply rate, I, is reduced if this is the case and all convective tendencies are recomputed with this new value to ensure mass and energy conservation.

The steps in the computation of the convective tendencies are then:

- Convection is activated if the grid column is convectively unstable and there is resolved upward vertical motion at the LCL.
- The source level air for the convection is defined as the highest θ_E air that is less than $3km$ above the ground. The LCL of the source level air is found.
- Cloud top is defined as the level above which the potential temperature of the moist adiabat becomes less than the grid temperature.
- The vertical profiles of heating and moistening are computed.
- The convective tendency terms for potential and total water are determined.

The scheme was intended to be as simple as possible. The convective tendencies produced by this scheme will be compared with the much more elaborate scheme presented in the next section.

5.2 A modified Fritsch/Chappell convective parameterization

The modified FC scheme is described in detail below, with comparisons to the computations of the original scheme wherever applicable. The convective parameterization can be subdivided into four parts for convenience: 1) the convective decision, 2) the updraft model, 3) the downdraft model, and 4) the convective closure.

5.2.1 The convective decision

As the model integration is proceeding, a decision must be made as to whether convection will occur in a given grid column. The most obvious requirement is that the column must be conditionally unstable, that is, either equivalent potential temperature or moist static energy must decrease with height in a portion of the column. This is the first requirement that must be satisfied to proceed with the convective parameterization.

FC then tested every 100 mb thick layer from the ground to 600-700 mb to see if the parcel would reach its level of free convection (LFC). The parcel was given a positive temperature perturbation at its lifting condensation level (LCL) that was proportional to the cube root of the resolved vertical velocity at the LCL. If the parcel reached its LFC, then the convection would proceed.

The new scheme does not rely on this arbitrary temperature perturbation to determine where convection occurs. To achieve a more accurate definition of the LCL, LFC and other levels that are necessary for the computations, the model sounding is interpolated to a higher resolution vertical grid of 200 m under 5 km and 500 m above 5 km. The source level of the updraft is defined to be either the air immediately above a low-level inversion (under about 1.2 km) or the highest θ_E air if an inversion is not found. Cloud base is defined to be the LCL of the source level air. If there is resolved upward vertical motion at this level, then the convective parameterization will continue.

5.2.2 The updraft model

The modified convective parameterization is similar to the original scheme in the updraft model. First, the mass flux profile is defined by a first guess that 1% of the grid area will be covered with updraft and that the mass flux of the updraft will double from the LCL to the equilibrium temperature level (ETL) of an unentrained parcel. This replaces an iterative process for the entire updraft calculation in FC where they assumed the doubling to occur from the LCL to the cloud top. Since the entrainment rate is derived from this mass flux increase, the cloud top calculation was involved in an iteration.

With the entrainment rate computed from the mass flux profile, the thermodynamic structure of the updraft can be computed. Defining an entrainment operator, E,

$$E_u(A) = \frac{\left(A_{u_{k-1}} M_{u_{k-1}} + \Delta M_u \overline{A_e}\right)}{M_{u_k}}$$

where A is a quantity to be entrained, M_u is a vertical mass flux of the updraft, $\overline{A_e}$ is the average environmental quantity between levels k and $k-1$, and ΔM_u is the change in mass flux between vertical level k and level $k-1$.

Assuming that the updraft is saturated with respect to water,

$$\theta_{E_k} = E_u(\theta_{E_{k-1}})$$

$$r_{v_k} = E_u(r_{v_{k-1}})$$

If ice is produced, θ_E is then increased to account for the latent heat of freezing. Since detailed microphysics are not included in the updraft model to account for condensate phase changes, the ice processes are handled in an approximate way. An ice level (IL), where all condensate immediately freezes ($-20°C$), and a freezing level (FL), where freezing starts to occur ($-5°C$), are defined. A percentage of the condensate produced between these levels is assumed to freeze at these levels. This percentage varies linearly with height from 0% at the FL to 100% at the IL. Additionally, a fraction of the condensate produced below the FL is carried above the FL and is frozen between the FL and IL. The fraction is dependent on the cloud base temperature and varies linearly from 0.1 at a cloud base temperature of $25°C$ and above to 1.0 at a temperature of $5°C$ and below. This crudely accounts for condensate depletion due to warm rain processes since the warmer that the cloud base is, the more vertical depth will be above freezing so that there will be more chance for warm rain to occur. In contrast, FC assumed that all condensate produced from the LCL to $-25°C$was carried to $-25°C$ and froze at that level, creating a large positive temperature perturbation in the updraft.

Once the updraft thermodynamic structure is determined, the vertical velocity profile can be computed with the steady state plume model.

$$\frac{\partial w^2}{\partial z} = \frac{2g}{\gamma}\frac{\theta_{v_u} - \theta_{v_e}}{\theta_{v_e}}$$

$$-E_u(w_{k-1})$$

where γ is the so-called "virtual mass coefficient" which attempts to compensate for non-hydrostatic effects and θ_{v_u} and θ_{v_e} are the virtual potential temperature of the updraft and environment, respectively. Water loading is not included since there is no microphysical information.

In the modified convective parameterization (since an artificial temperature perturbation is not added to the updraft at the LCL), if the vertical velocity of the parcel becomes less than 1 m/s before the parcel reaches the LFC, the vertical motion is set back to 1 m/s. The updraft top is defined where the vertical motion becomes less than 1 m/s after the parcel reaches the LFC.

5.2.3 Downdraft model

The downdraft model has been completely rewritten from the original scheme. The new model relies heavily on the observational and modelling study of Knupp (1985, 1987).

The level of free sink (LFS), the origination level of the downdraft air, is defined to be the θ_E minimum of the environmental sounding. A parcel is brought to saturation at this level by precipitation evaporation. If the parcel does not continue downward into the sub-cloud layer, then a parcel at the next lower level is tested. This procedure is continued until a parcel is found that does remain negatively buoyant into the sub- cloud layer. If no LFS is found above cloud base, then no downdrafts are assumed to be present at this time.

Similar to the updraft model, the downdraft mass flux profile is defined. According to Knupp (1985), there is a level that is approximately 800 m above the ground where the downdraft vertical velocity attains a maximum value (LMW). Vertical pressure forces will start to decelerate the downdraft below this level. From the observations of Knupp, the downdraft mass flux approximately triples from the LFS to the surface and that the mass flux at the LMW is approximately equal to the updraft mass flux at cloud base. This is the profile that is used in the downdraft model.

With the downdraft mass flux profile defined, the thermodynamic structure and vertical velocity can be determined. Defining the entrainment operator for the downdraft,

$$E_d(A) = \frac{\left(A_{d_{k+1}} M_{d_{k+1}} + \Delta M_d \overline{A}_e\right)}{M_{d_k}}$$

where A is a quantity to be entrained, M_d is a vertical mass flux of the downdraft, $\overline{A_e}$ is the average environmental quantity between levels k and $k+1$, and ΔM_d is the change in mass flux between vertical level k and level $k+1$.

The changes to the parcel due to entrainment are,

$$\theta_{E_k} = E_d(\theta_{E_{k+1}})$$

$$r_{v_k} = E_d(r_{v_{k+1}})$$

However, unlike the updraft, the downdraft is not saturated with respect to water. Either the relative humidity of the downdraft parcel needs to be specified or the evaporation rate of the precipitation falling through the downdraft needs to be computed. The latter method is used in this parameterization according to the bulk formula given by Betts and Silva Dias (1977).

$$\frac{\partial r_v}{\partial p} = \frac{r_w - r_v}{\Pi_E}$$

In this equation, r_w is the saturation mixing ratio at the wet bulb temperature and Π_E is what Betts and Silva Dias called a pressure scale for evaporation which in this work was taken to be a constant of $60mb$. With the evaporation rate known, a new potential temperature and θ_E (since the parcel did not descend saturated) can be computed.

If melting or sublimation occurs, the θ_E of the downdraft is changed further. Evaporated condensate at levels colder than $0°C$ is assumed to be sublimed. From the $0°C$ level to 2 km below, the ice fraction of the convective precipitation is melted. The ice fraction is the remainder of the precipitation that was not involved in the warm rain process that was handled in the updraft.

As with the updraft model, once the thermodynamic values are known, the downdraft vertical velocity can be determined with a similar steady state plume model. However, if a parcel is negatively buoyant throughout its descent in the downdraft, this model says that it will still be accelerating when it hits the ground. In reality, though, a downdraft parcel will encounter several effects other than those included in the plume model including pressure forces. In addition, since the downdraft model is attempting to describe the average properties of the air over the lifetime of the downdraft, the computation of the downdraft buoyancy relative to the environment air will usually be an overestimation since some of the downdraft parcels will fall through previous downdraft air or a mixture of the ambient and downdraft air. This effect is crudely taken into account by assuming that the downdraft parcel is falling through 100% environment air above $3km$, 50% environment and 50% downdraft air from $2-3km$, and 10% environment and 90% downdraft air under $2km$.

$$\frac{\partial w^2}{\partial z} = \frac{2g}{\gamma}\frac{\theta_{v_d} - \theta_{v_m}}{\theta_{v_m}} + E_d(w_{k+1})$$

where θ_{v_m} is the virtual potential temperature of the mixture of downdraft and environment air.

5.2.4 The convective closure

The closure of the convective parameterization can be defined as the determination of the actual convective heating and moistening rates that will be applied to the mesoscale model using the information supplied by the grid variables, the updraft model, and the downdraft model. This often involves the computation of convective areas, timescales, etc. The closure assumptions in the modified convective parameterization are, in general, philosophically similar to FC. The main physical concept in the closure is that a line of convection develops in response to low level convergence. This line moves across the grid volume at a given speed, stabilizing the atmosphere that it contacts. Many changes in the details of the closure, however, have been made to remedy some of the problems of the original scheme.

Before the actual closure is computed, some adjustments are made to the updraft in the new scheme. Recognizing that the 1-D Lagrangian parcel model, mostly due to the neglect of pressure forces, is not applicable to the average conditions over the lifetime of a convective cell, the cloud top and vertical velocity profile are adjusted (the reasons for these adjustments and how they affect the heating rates are given below). The cloud top is taken to be the level where the potential temperature is equal to the average of the θ_e and θ_u at the level where the updraft model stopped the updraft. This crudely accounts for the fact that much of the mass in the overshooting tops of cells descends quickly back to some equilibrium level and mixes with the environment. The average θ is assumed to be that of this level, also approximating an entrainment process on the descent.

The vertical velocity profile is then modified by the empirical function given by English (1973) which was derived from observations in Alberta, Canada. It is also consistent with the observations of Knupp (1985) and is used to first approximation here.

$$w_{u_k} = 0.91 w_{max}\left[sin\left(\frac{\pi z_k - z_{src}}{z_{ct} - z_{src}}\right) - 0.25 sin\left(2\pi\frac{z_k - z_{src}}{z_{ct} - z_{src}}\right)\right]$$

The mass flux profile of the updraft is then adjusted by a detrainment process from the vertical velocity maximum up to cloud top. The mass is detrained laterally into the anvil proportional to the vertical mass convergence profile of the modified updraft velocity.

The actual closure calculations can now be done. A convective timescale is defined as follows:

$$\tau_c = \frac{\Delta x_c}{U_m}$$

where Δx_c is an effective model grid space $\sqrt{\Delta x^2 + \Delta y^2}$ and U_m is the mean wind speed in the cloud layer.

The closure approximations then state that all CAPE will be consumed in this timescale. By use of an iterative process, similar to FC, the updraft and downdraft areas can then be determined. The computation steps for the iterative process are as follows:

- The updraft and downdraft areas are determined.

$$A_u = \frac{M_u}{\rho_u w_u}$$

$$A_d = \frac{M_d}{\rho_d w_d}$$

However, since the updraft velocity from cloud base to the LFC was arbitrarily imposed, those areas are arbitrary. Therefore, a constant area from the cloud base to the vertical velocity maximum is used that is the vertical average of the areas computed from the above equation between those levels.

- The velocity of the compensating environmental subsidence and environmental area is found.

$$A_e = \Delta x \Delta y - A_u - A_d$$
$$w_e = \frac{-(M_u + M_d)}{\rho_e A_e}$$

With this subsidence, the θ profile of the environment is modified through vertical advection.

$$\frac{\partial \theta_e}{\partial t} = -w \frac{\partial \theta_e}{\partial z}$$

Because the timescale is usually on the order of an hour, this equation is handled numerically in an explicit time-split type of computation. The maximum Courant number of the subsidence ($w_e \Delta t / \Delta z$) is found and the number of smaller steps necessary to satisfy the stability criterion is found. A first order forward-upstream scheme is used over this number of smaller timesteps.

- An adjusted grid virtual potential temperature is found that is an area weighted average of the updraft, downdraft, and environment.

$$\theta_{v_g} = \frac{(\theta_u a_u + \theta_d a_d + \theta_e a_e)}{a_g}$$

- A new value of CAPE is computed. If this value is adequately close to zero (closer than 5% of the initial CAPE), then the convective parameterization will continue with these values. If the new CAPE is still greater than this value, then the updraft and downdraft mass fluxes are increased until the proper areas are attained.

This iterative process encompasses the most important calculations of the convective parameterization in determining the heating and moistening rates. In particular, the compensating subsidence is by far the most important effect in the heating profile. The actual structure of the updraft (aside from the detrainment in the anvil) has very little effect on the grid-averaged temperature because the updraft area is almost always very much smaller than the environmental area. For the same reason, the downdraft has very little effect on the heating rates except near the ground where the downdraft air may occupy a significant portion of the grid volumes. This is why the ice phase, for instance, in the updraft could be handled in an approximate way without affecting the accuracy in the scheme.

The parameter which controls the subsidence, and hence the heating profile, is the updraft mass flux profile. The detrainment modifications described above have a large effect on the subsidence since the updraft mass flux profile is altered. The updraft, especially with the steady state plume model, usually will penetrate the tropopause. Using only the specified mass flux profile (doubling from cloud base to top), the largest subsidence velocities will occur in the stratosphere where the stabilities are the highest. If this velocity is maintained for the entire timescale, the tropopause, in effect, will be advected downward. In some cases, this drop can be several kilometers. This is the reason Fritsch and Chappell's scheme produces extremely large heating rates and the sharp peak in the profile that occurs directly beneath the original tropopause.

The lateral detrainment of the updraft mass better simulates the actual physical process. As an updraft parcel ascends through a vertical level, applying mass continuity principles, another parcel must descend (assuming no lateral divergence). The subsident velocity of the parcel may have an instantaneous value similar to that computed by FC. However, it cannot maintain this velocity for the entire timescale because it will descend dry adiabatically and soon be positively buoyant compared to its environment and experience an upward acceleration. A gravity wave oscillation thus is created which transports mass and heat horizontally and vertically away from the convective circulation. Many of the difficulties with cumulus parameterization in general stems from the assumptions made regarding the effects of these propagating gravity waves and the horizontal and vertical distribution of the subsidence. While FC assume that their scheme is valid in grid volumes with horizontal dimensions on the order of 20 km, the assumption that all subsidence occurs within a grid volume is technically only completely valid if the horizontal grid spacing is greater than the Rossby radius of deformation.

After the above iterative process is complete, several other adjustments are made to the computed convective heating in the new scheme. The first involves a reduction of the updraft and downdraft mass fluxes due to a capping inversion. FC used the arbitrary temperature perturbation at the LCL in an attempt to account for an inversion from the LCL to the LFC. Aside from the arbitrariness, this method makes the FC scheme "all-or-nothing," either enough convection will occur to stabilize the grid volume or no convection will occur. This method also limits applicability of the scheme to smaller grid scales (about 20 km). As the grid scale becomes larger, less of the area is covered with convection, hence less of the conditional instability is consumed by the convection.

The new scheme treats the capping inversions in an entirely different fashion. In a manner somewhat similar to the convective parameterization scheme of Frank (1984), the first time convection occurs at a grid point, the resolved mass flux at the LCL is computed and "focused" into the computed updraft area. If the resulting vertical motion is adequate to break the inversion at cloud base, then the heating rates are not modified. If the resulting vertical motion is not strong enough, then the updraft area (and updraft and downdraft mass fluxes) is reduced until the vertical motion will overcome the negative buoyancy. The reduction will occur down to the minimum cell size of an updraft having the computed properties (taken to be 1 km radius). No convective tendencies will be computed if the radius is determined to be smaller than this. If convection has occurred at the previous convective time at this grid point, then the downdraft mass flux at cloud base will be added to the resolved mass flux in determining the adjusted updraft area.

The next computation step in the scheme is similar to FC. The downdraft mass flux is used to fill the bottom grid layers. Usually, only a few hundred meters are needed to contain all the downdraft air.

After this, the next major departure from the original scheme is done. In computing integrals of heating and moistening rates in the FC scheme, it was discovered that neither water mass or energy was conserved and that the discrepancies could be quite large. For instance, consider a situation where there were negligible downdrafts. In the FC scheme, all water mass used for the updraft (including precipitation and anvil evaporation) is not taken from the existing supply in the grid column, but instead is created. Even with downdrafts considered, the only drying tendency that can be computed with the scheme is in the air near the ground where the downdraft has occupied a significant fraction of the volume.

In an attempt to remedy this serious problem, at this point in the calculations of the new scheme, the entire water budget of the convection is recomputed so that water mass is conserved exactly. The steps that are taken are:

- Updraft and downdraft vapor entrainment are taken from the environment water mass.
- The downdraft mass started with some of the environmental vapor. The environment is decreased by this amount.
- The total amount of water mass in the downdraft air is computed. The total water mass evaporated by the downdraft is taken as the residual of the total mass minus the initial mass minus the entrained mass.
- The total condensate produced by the updraft is computed as the supply of vapor through cloud base plus the updraft entrainment minus the vapor that was needed to bring the updraft to water saturation.
- With the precipitation efficiency computed from the function given in FC, the amount of water mass evaporated in the anvil is the residual of the total condensate minus the precipitation minus the downdraft evaporation. If the anvil evaporation is not at least 10% of the vapor supply at cloud base, then the precipitation efficiency is reduced. This simply states that a particular structure of cloud (one with an

anvil) is expected. Since the function for the precipitation efficiency is very approximate, it is assumed that this is the source of error if the cloud does not exhibit a significant anvil. The condensate evaporated in the anvil is distributed by the same profile used to determine the detrainment. All condensate is assumed to evaporate and the temperature reduced accordingly; if this evaporation causes any grid volume to become saturated, the mesoscale model's explicit thermodynamic diagnosis will recondense the water and return the latent heat.

- Finally, the sub-cloud layer is depleted of the water mass that the updraft consumed. The method used to accomplish this is very approximate since in a convective situation, the boundary layer structure becomes quite complicated in the presence of updrafts, downdrafts, gust fronts, etc. Therefore, the method is to simply total the water mass present before the convection, deplete it by the amount consumed by the updraft, then replace any remaining water mass back into the grid volumes (proportional to volume) that are not occupied by the downdraft.

The above method will exactly conserve water mass, but nothing yet has been done about energy. Although a similar energy budget may be able to be devised that will conserve energy, it is not quite as clear as with the water budget because of the unknown relationships between sub-grid energy conversions. Therefore, a different procedure is used. It is assumed that the total moist static energy in the environment before the convection will be exactly equal to the total moist static energy afterwards. This neglects kinetic energy and sensible heat removed by the precipitation. If there then is an excess of energy (as is usually the case), the heating tendencies are reduced. There are three main regions in the vertical column where heating is significant, the downdraft cooling near the ground, the evaporated condensate in the anvil, and the subsidence warming from cloud base to cloud top. Because of the difficulties in determining accurately the subsidence warming and the fact that the cooling near the ground and in the anvil is due to evaporated condensate, it is assumed that any discrepancy in total energy before and after the convection is due to an inaccurate accounting of the subsidence. The subsidence profile is then shifted so that energy is conserved exactly.

All of the computations so far have been done on the higher resolution convective grid. The tendencies now can be transferred to the regular model grid by a volume weighting. This, however, will cause a small spatial truncation error in the tendencies. The tendency profiles are then readjusted so that the model grid integrated tendencies are equal to the convective grid tendencies.

5.3 Results and sensitivities of the convective parameterizations

This section will test the convective parameterizations described above by comparing the FC-type scheme with the Kuo-type scheme. In addition, several "tweaks" will be made to the FC-type scheme in order to show how sensitive the scheme is to changes in its implementation.

5.3.1 Initial conditions

The sounding used for the following tests was the Topeka, Kansas rawinsonde report for 4 August 1977 at 0000 UTC except that an additional 10% relative humidity was added up to 850 mb to make the sounding more conducive for convection. The actual sounding used is shown in Figure 5.2. The model grid spacing was assumed to 30 km in the horizontal dimensions. A grid-scale vertical motion of 10 cm/s at convective cloud base was assumed. For the modified FC scheme, it was assumed that the grid column would be stabilized in the computed convective timescale. The convective parameterizations were then run with these conditions and the predicted convective tendencies to potential temperature and mixing ratio were plotted.

5.3.2 Results of the modified Kuo scheme

The convective heating and moistening rates from the simple Kuo scheme for this sounding are shown in Figure 5.3. The magnitudes of the heating rates agree well with Lewis (1975) as does the shape of the profile. The downdraft cooling near the ground is several factors less than that predicted from the modified FC scheme described below, however. That scheme predicted that the downdraft would be about 10 K less than the environment near the ground while in this scheme the temperature deficit of 5 K is

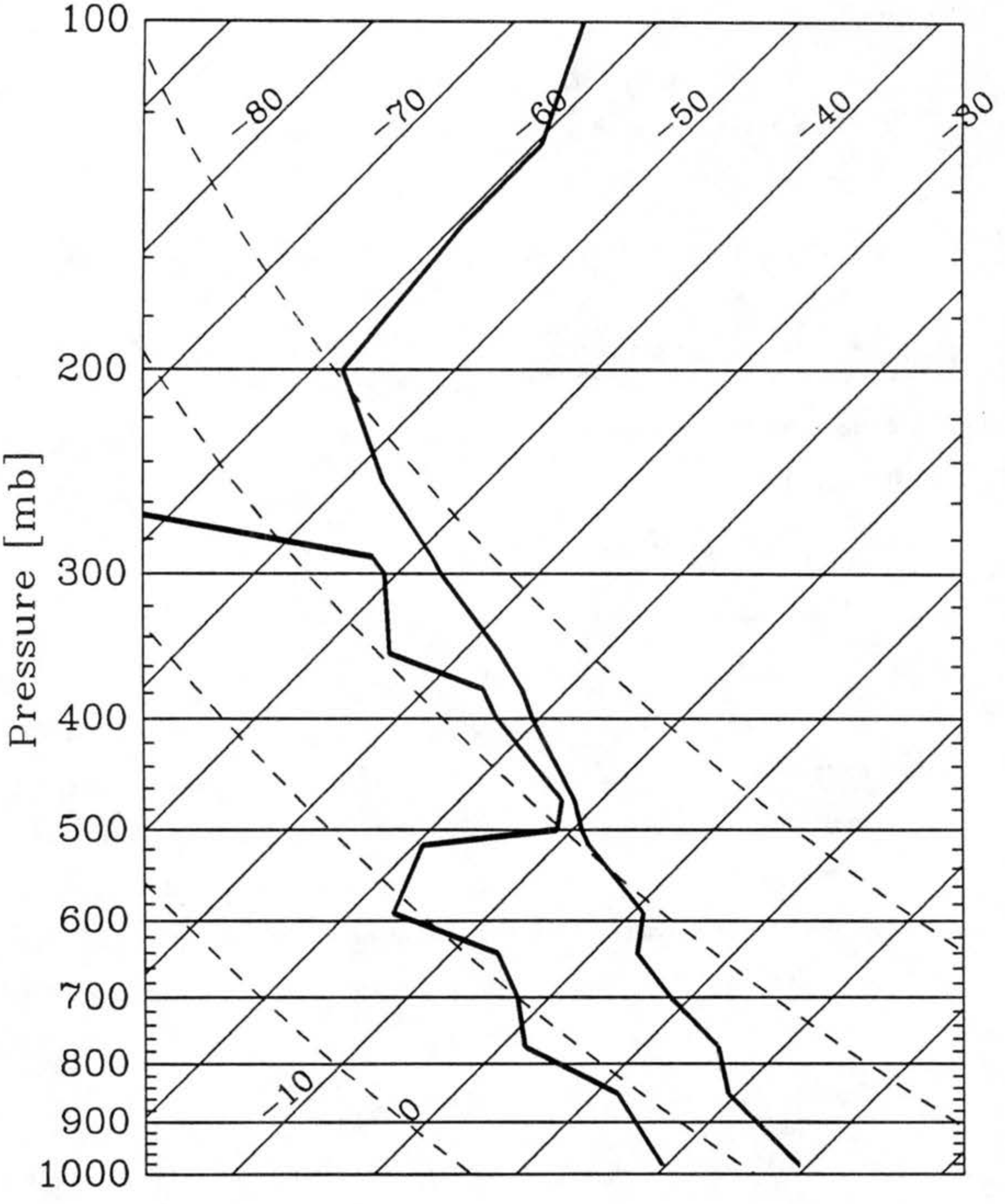

Figure 5.2: Sounding from Topeka, Kansas at 4 August 1977, 0000 UTC with 10% added relative humidity from the ground to 85 kPa.

specified. These profiles will be compared to the modified FC scheme in the next section.

5.3.3 Results of the modified Fritsch-Chappell scheme

In order to show that the new scheme, although greatly modified, can produce basically the same results as FC, a test was run without two of the most important modifications to see if the new scheme could produce a convective heating profile similar to Figure 11 in Fritsch and Chappell (1980b) (Figure 5.1). A profile of this shape was seen in almost all atmospheric profiles examined when run with the unmodified FC scheme. The two modifications in question are the lateral detrainment of updraft mass and the modification of the updraft vertical motion profile with the function of English (1973). The convective heating profile for this test is shown in Figure 5.4. The two profiles have many similarities; both have very high amplitudes of the heating rates just under the original tropopause and extremely high magnitudes of the cooling rates in conjunction with the overshooting tops. The shapes of the profiles are also very similar.

The lateral detrainment alone will not solve the problems with the heating profile. But with the addition of the lateral detrainment and the function of English which will lower the level of the updraft vertical velocity maximum to a level much more along the lines of many observational studies, the profile takes on a much more reasonable amplitude and shape (Figure 5.5). The heating maximum is not a sharp peak, but more of a broad region with a magnitude much closer to that of the observational studies of Lewis (1975). Comparing these tendency profiles also with the Kuo scheme described above, relatively close qualitative agreement between the shape and magnitude of the profiles can be seen. This test will be termed the "control" run for the remainder of this chapter.

This test indicates the modifications to the original FC scheme may produce more reasonable convective heating profiles.

Tests of the convective timescale

The basic premise behind the FC scheme is that convection will develop under certain conditions and will consume all of the existing CAPE in some convective timescale. The

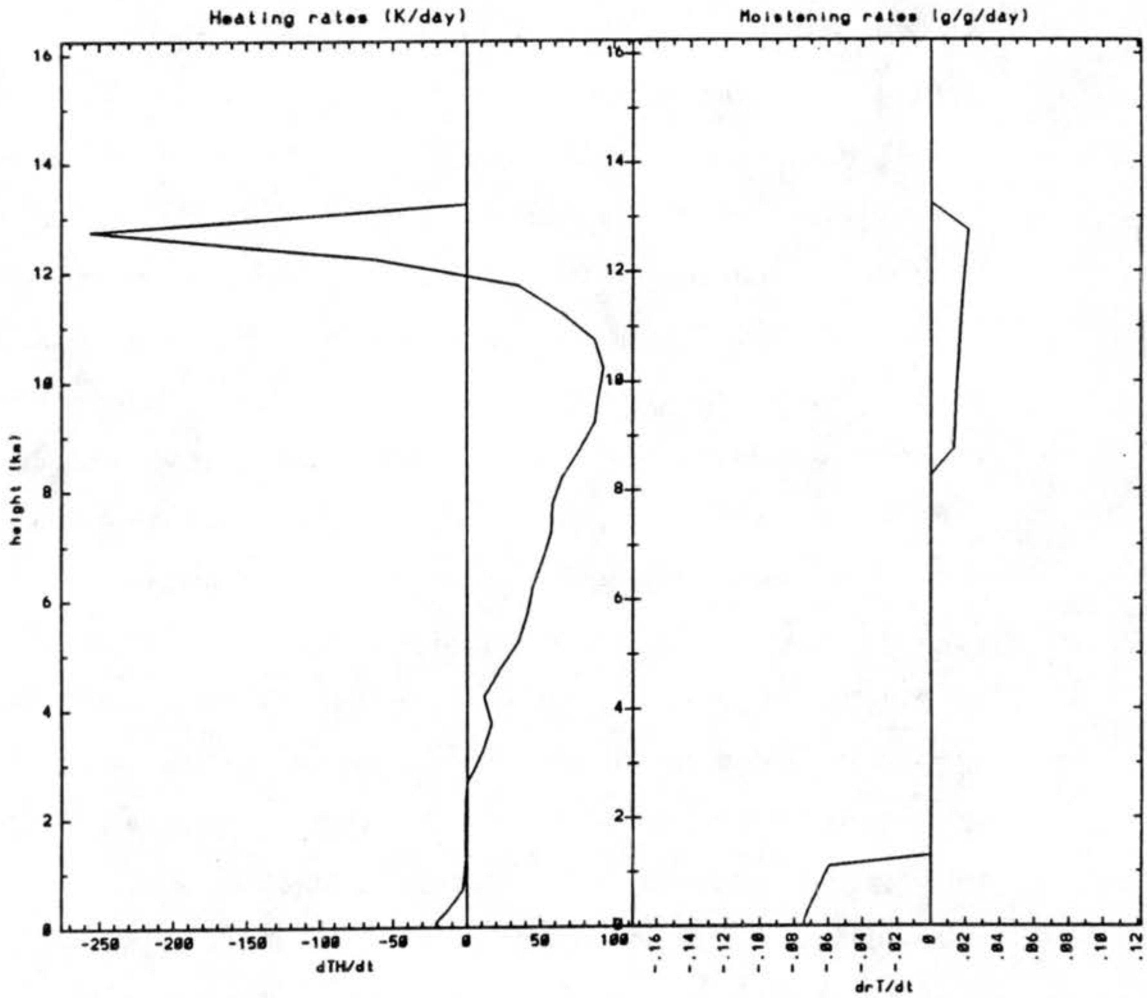

Figure 5.3: Convective heating and moistening rates from the simple Kuo-type parameterization.

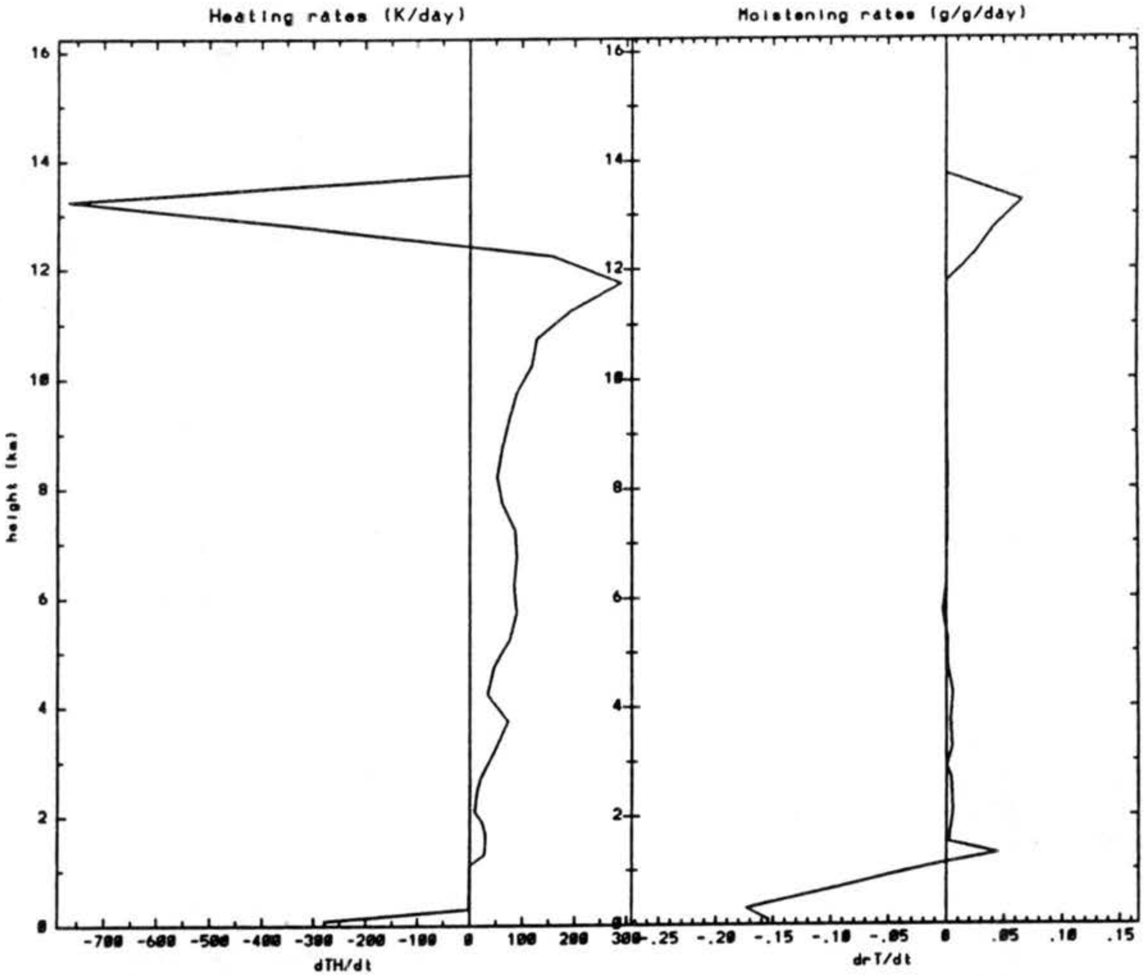

Figure 5.4: Convective heating and moistening rates from the new Fritsch/Chappell-type parameterization without lateral anvil detrainment and updraft velocity modifications.

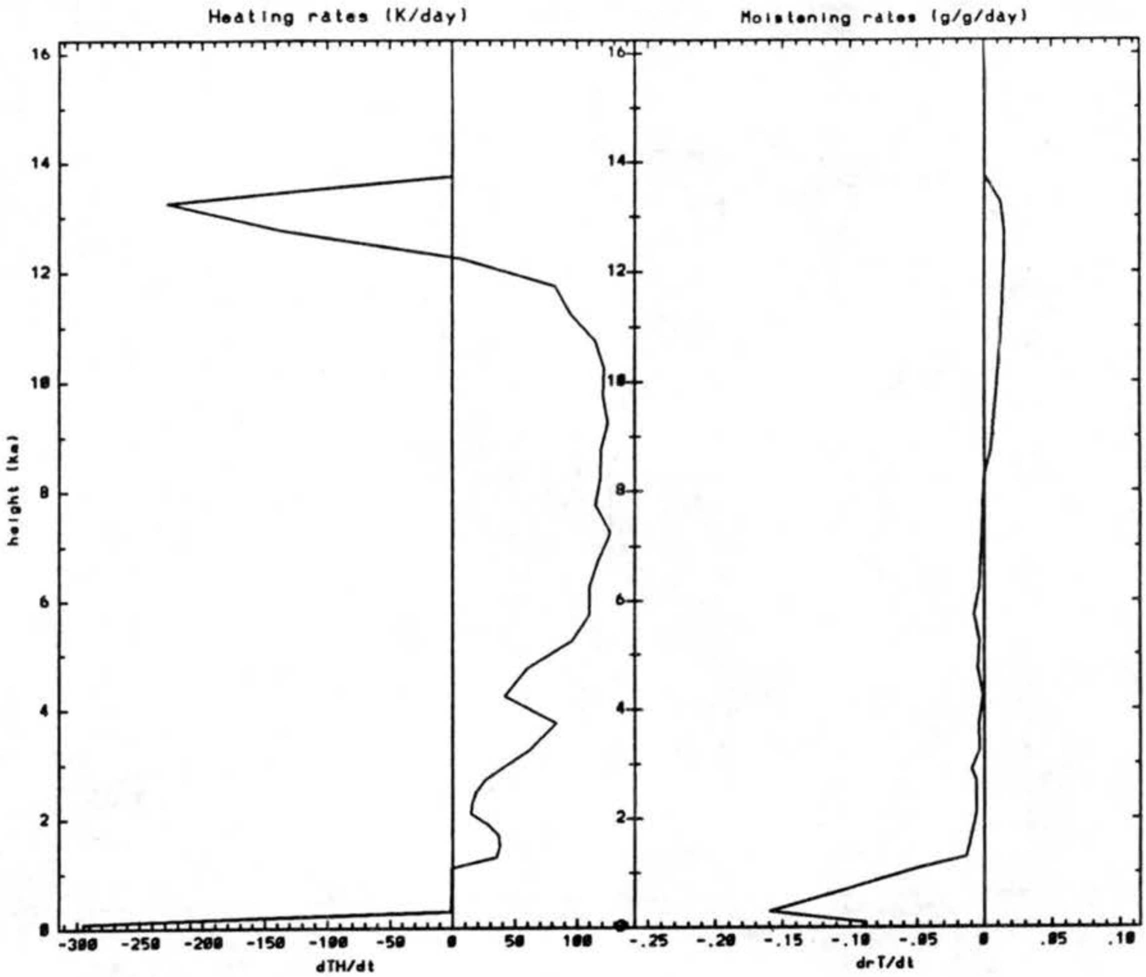

Figure 5.5: Convective heating and moistening rates from the new Fritsch/Chappell-type parameterization with all modifications.

specification of this timescale is taken to be the time that it would take the convective cells to move across the grid volume assuming they were moving at the mean wind speed in the cloud layer. However, a MCS or even individual cells can often move at speeds substantially different than advective speeds; in some cases they may be anchored to a stationary convergence line and continuously regenerate at the line, not showing much lateral displacement at all. In other cases, they may move at speeds faster than the wind velocity at any level in the troposphere (Fortune, 1989).

This next test modified the computed convective timescale of the control run which was 2771 seconds. Three other timescales were specified, 1200, 3600, and 7200 seconds. The resultant maximum heating rates are shown in Table 5.1. The magnitude of the rates are almost linear functions of the inverse of the timescale; a doubling of the timescale results in a halving of the heating.

Table 5.1: Convective timescale tests.

Timescale(s)	Max heating rate (k/day)
1200.	241.02
2771.	124.67
3600.	100.08
7200.	51.97
Kuo	92.60

The modification by Zhang (1985) of the original FC scheme where he specified that only 50% of the CAPE would be consumed in the convective timescale is also equivalent to saying that the timescale is doubled from its advective speed. In the light of these sensitivity tests, one can see that he cut his convective heating rates in half.

The rate at which the heating is applied to the mesoscale model can have an effect on the resultant circulation even if the time-integrated heating is the same. The faster that heating is applied the more likely it is that the model will develop an unbalanced, transient gravity wave response (depending, of course, on horizontal resolution and extent of the heating) where a slower heating rate can more easily lead to a more balanced circulation.

Tests of the energy conservation requirement

As was the case in almost all atmospheric profiles examined, the FC-type scheme added far more energy to the grid column than was actually released through condensation. Figure 5.6 shows the vertical heating profile for this test case without the conservation requirement exercised. The heating maximum and much of the profile was reduced by over 20 K/day when the scheme was constrained to conserve energy in the column.

5.4 Summary

To summarize this chapter on convective parameterization, many problems with the currently used convective schemes have been identified and described. Unfortunately, convective parameterization must still be used in meso-α scale numerical simulations today and for the foreseeable future because of lack of computer power. Two different schemes have been developed as part of this research, a simple, Kuo-type parameterization and a much more complex Fritsch/Chappell-type parameterization. Experience with the FC-type scheme showed that, because of many arbitrary assumptions and parameters that are common to the modified FC scheme and the original FC (1980a) scheme, the results were overly sensitive to small changes in the scheme. A comparison between the modified FC and the Kuo schemes was presented as an illustration of the problems that may be encountered. Since it is undesirable for the convective parameterization to be overly sensitive to other changes in the model physics in sensitivity runs, it was decided to use the simpler Kuo scheme in the actual model simulations.

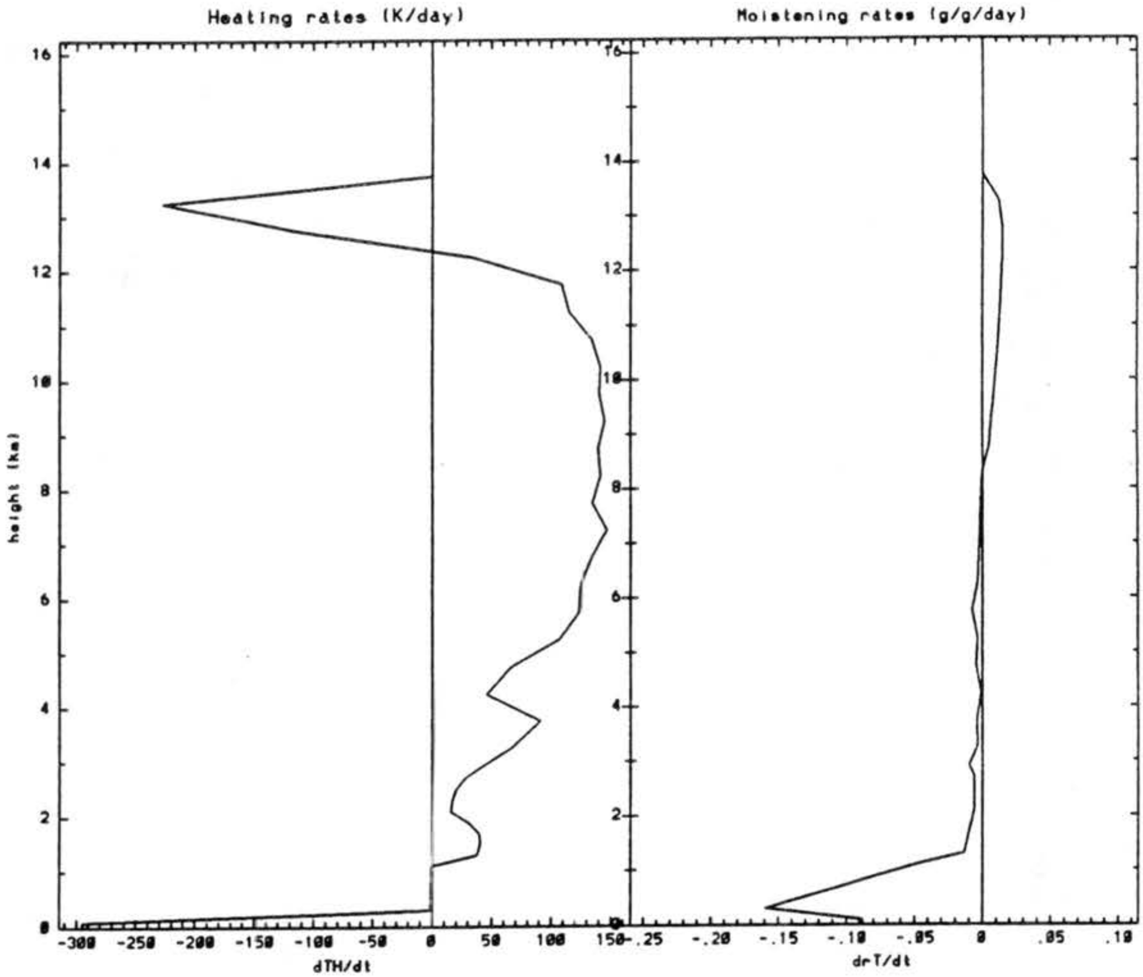

Figure 5.6: Convective heating and moistening rates from the new Fritsch/Chappell-type parameterization without energy conservation modifications.

Chapter 6

THE CCOPE MCC

During the Cooperative Convective Precipitation Experiment (CCOPE) in eastern Montana, a mesoscale convective complex (MCC) formed during the night of 2-3 August 1981 from convection originating in central Montana . This system did not produce much hail or flooding as it propagated through the Dakotas, but it was unusual in that the system formed in a baroclinic and highly sheared environment. This system may be classified as a derecho event (Hinrichs, 1888; Johns and Hirt, 1987) as there were numerous reports of strong straight line winds along the path of the convective system. This chapter will briefly describe the synoptic analysis of this MCC.

6.1 The observed convective system

As mentioned, this MCC formed in a highly baroclinic, sheared environment, unlike the more "classic" MCC environment described by Maddox (1981). The initial convection, which was quite severe, developed in central Montana about 2200 UTC and moved through the CCOPE observational network by 0000 UTC. As the convection reached the western Dakotas, it merged with weaker storms that had formed in northern Wyoming, probably due to a confluent mid-level (about 70 kPa) flow (Cotton et al., 1984). The deep mesoscale circulation of the system intensified after the merging (as is often observed) and the anvil shield reached Maddox's size criteria for an MCC shortly afterward. The system propagated through the Dakotas, reaching the Minnesota border by 1200 UTC on 3 August.

The upper level flow over the northern United States was generally from the west southwest to the east northeast throughout the period. A deep, relatively stationary trough was positioned over the eastern Pacific, providing a generating mechanism for short waves and the associated jet streaks. Figure 6.1a shows the mid-level Montgomery streamfunction and pressure fields on the 320 K isentropic surface while 6.1b shows these fields on the 340 K isentrope at 0000 UTC on 3 August. A general ridging in the mid and upper level flows can be seen over the MCC genesis region of eastern Montana although a weak trough in the 320 K streamfunction was evident in central Montana and Wyoming. This trough can be more clearly seen in the 70 kPa level analysis (Figure 6.2) performed by Cotton et al. (1984). This trough was not visible in the analyses 12 hours earlier. The isotach fields at the 320 and 340 K isentropic levels at 0000 UTC are shown in Figure 6.3. The MCC developed on the south side of the mid-level jet core and almost directly beneath the upper level core.

In the lower levels, a heat low centered in western Wyoming at 1200 UTC on 2 August moved toward the northeast during the morning and afternoon hours. By 1500 UTC, the low was far enough east to tap the high θ_e air that was on the plains and the moisture began to advect into southeast Montana. This, in conjunction with a weak front moving south from Canada, provided the low level lifting to trigger the initial storms in central Montana. The surface characteristics at 0000 UTC are shown in Figure 6.4.

Figure 6.5 shows the evolution of the precipitation features through the lifespan of the MCC with the NWS radar summaries. From the initial severe storms in east-central Montana at 2335 UTC, the convection weakened and became somewhat disorganized by 0135 UTC. Within the next few hours, perhaps partly due to the confluent mid-tropospheric flow, the convection again became organized and more widespread as the system attained MCC status. Schmidt and Cotton (1989) present a more complete analysis of the convective structure of the MCS just before the system reached MCC status around 0300 UTC. The MCC propagated across the Dakotas and by 1135 UTC was over the Minnesota border. It broke apart and lost its MCC status by 1300 UTC. Note also the change in orientation of the convective elements. From a line oriented parallel with the wind shear early in its life, the convection re-oriented perpendicular with the shear more like a squall line structure as the system crossed the Dakotas. In addition, the stronger convective elements extended throughout the north-south extent of the anvil shield. More

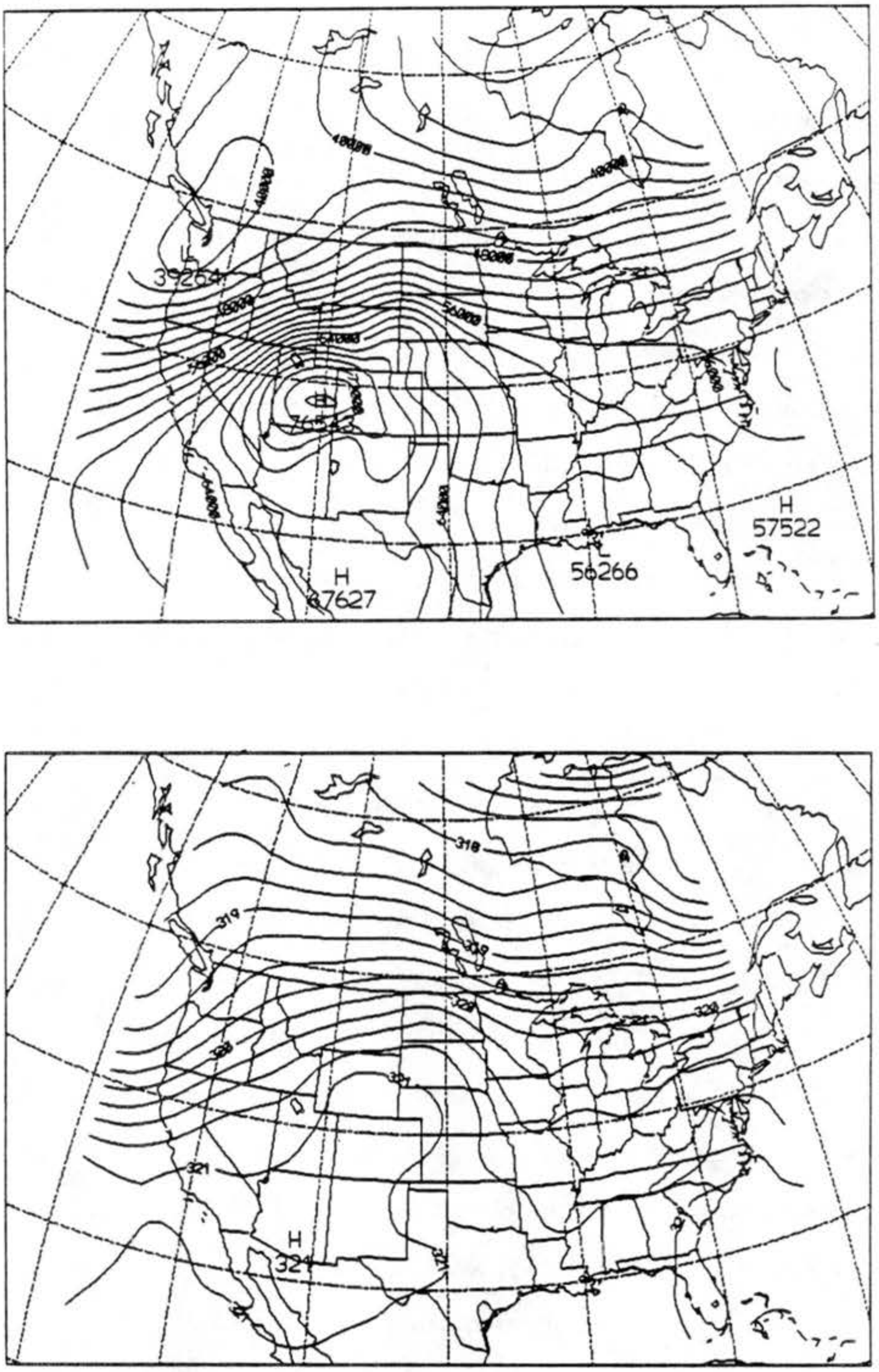

Figure 6.1: 3 August 1981 0000 UTC pressure and Montgomery stream function fields on the 320 K isentropic surface. Contour intervals are 2 kPa and 200 m^2s^{-2}.

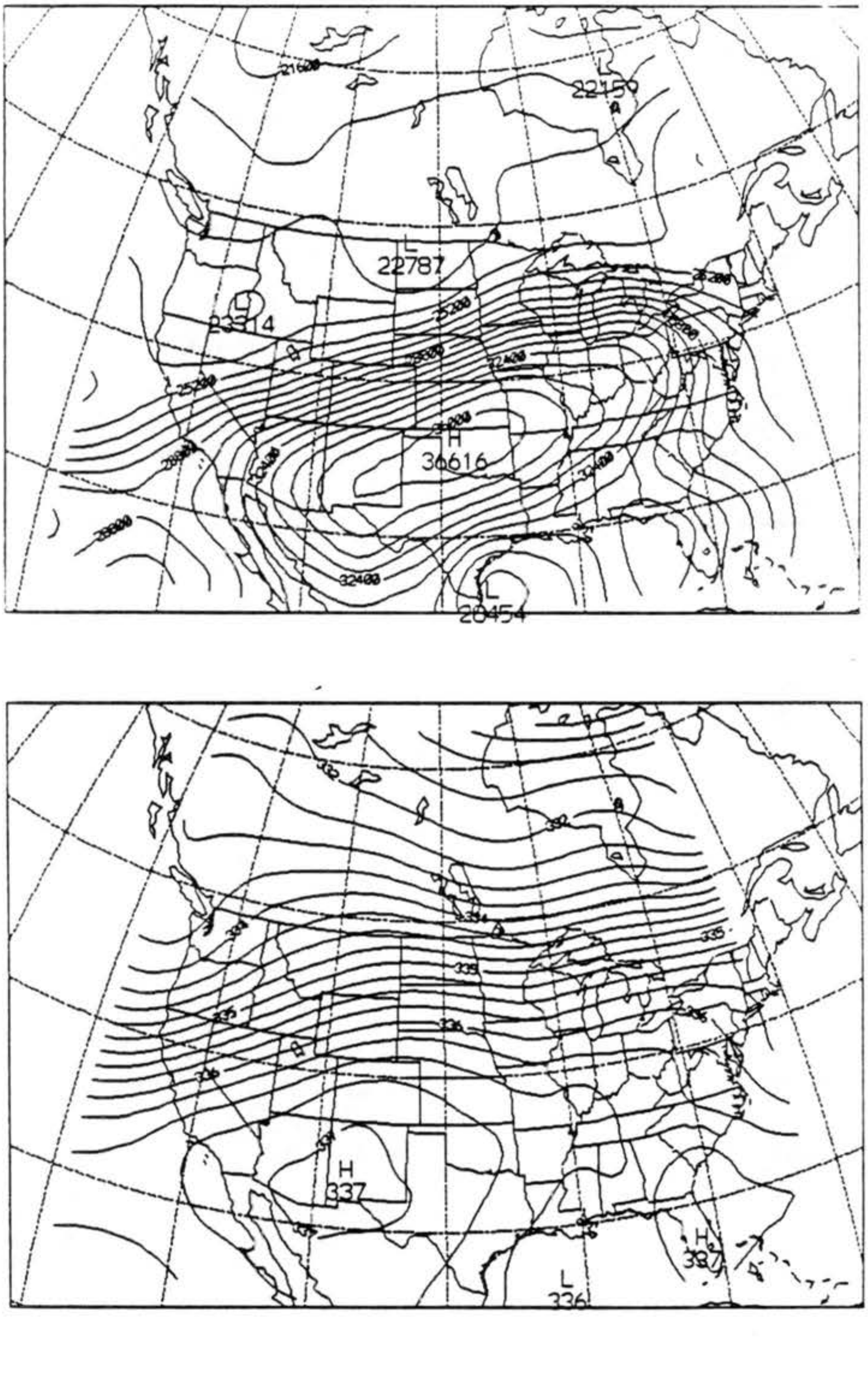

Figure 6.1: 3 August 1981 0000 UTC pressure and Montgomery stream function fields on the 340 K isentropic surface. Contour intervals are .9 kPa and 300 m^2s^{-2}.

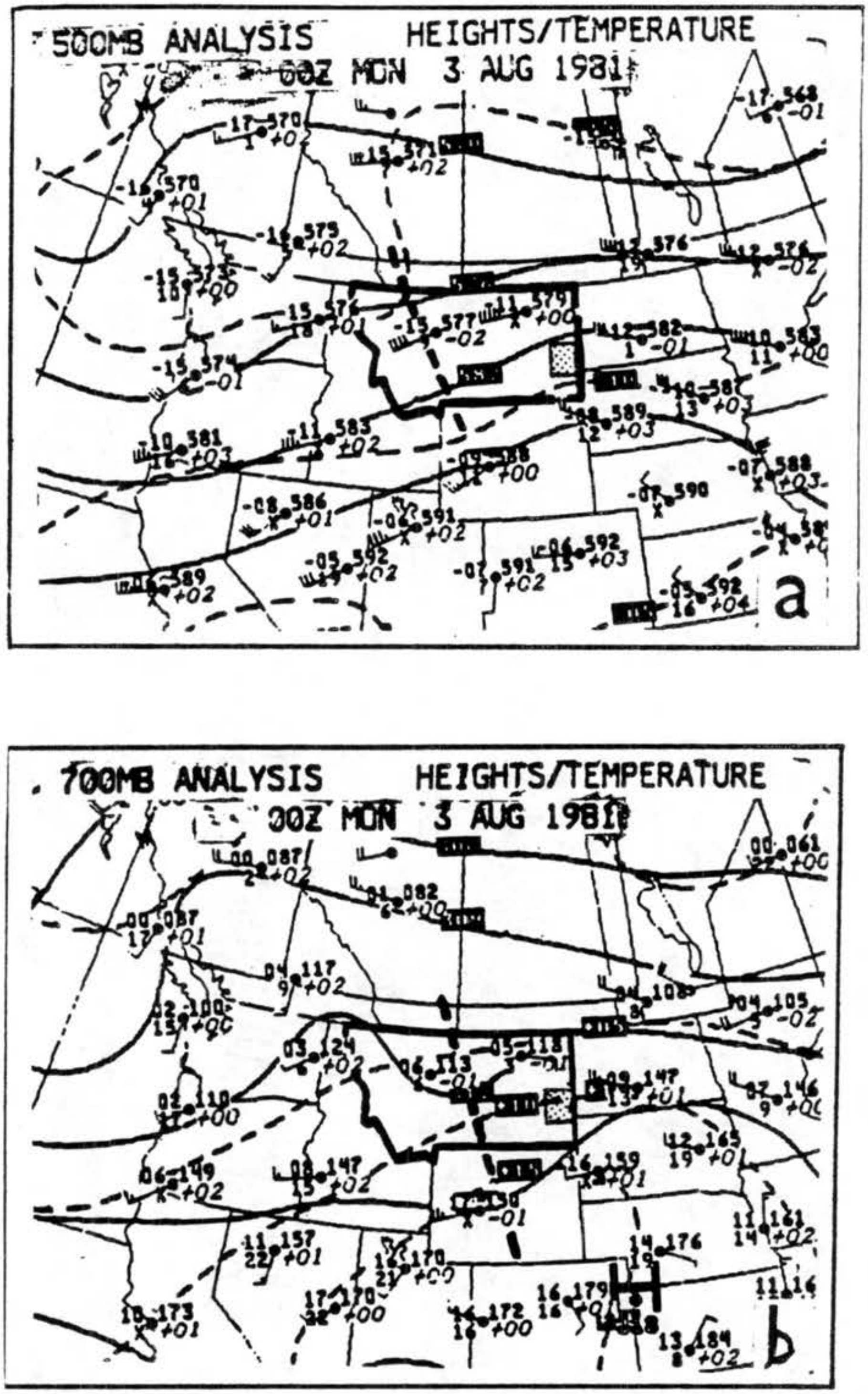

Figure 6.2: 3 August 1981 0000 UTC 50 and 70 kPa height and temperature analysis from Cotton et al., (1984).

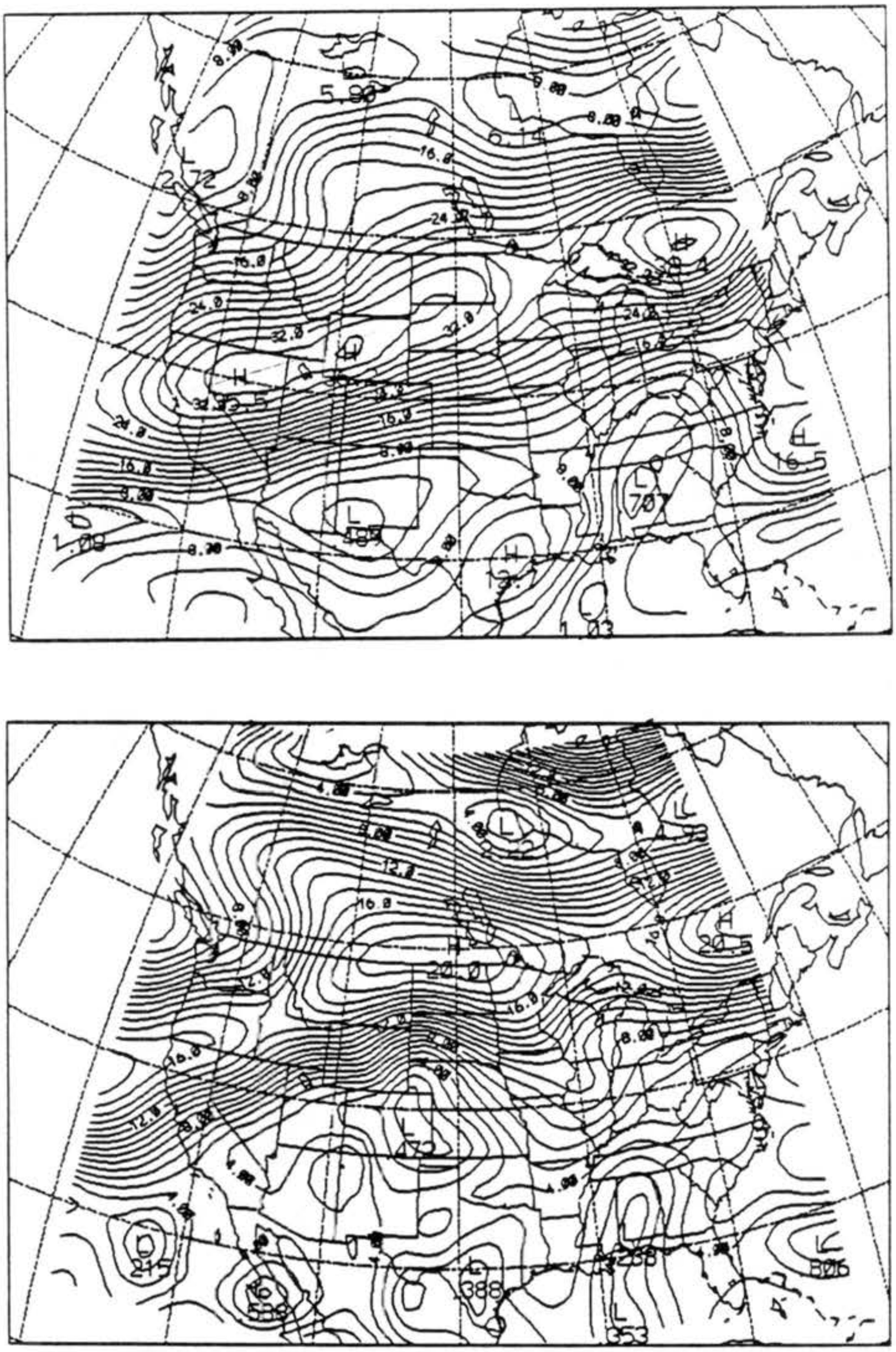

Figure 6.3: 3 August 1981 0000 UTC isotach analysis on a) 340 K isentrope with contour interval of 2 ms^{-1} and b) 320 K isentrope with contour interval of 1 ms^{-1}.

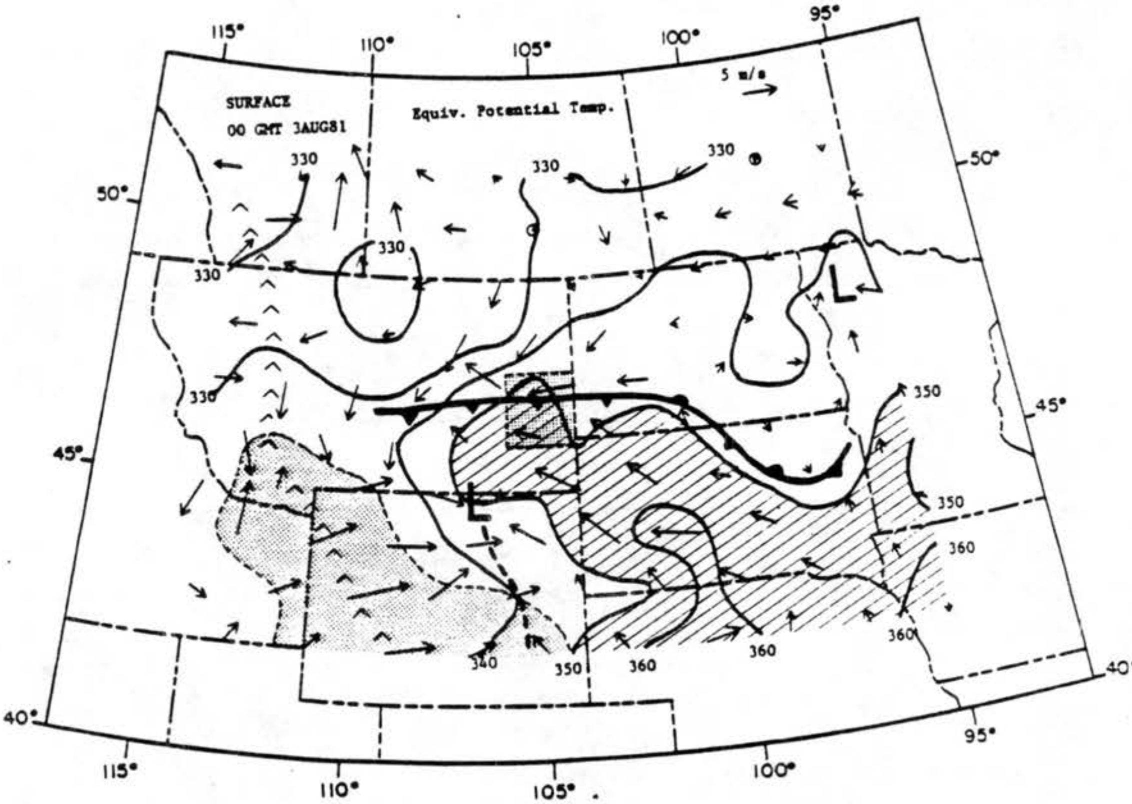

Figure 6.4: 3 August 1981 0000 UTC surface equivalent potential temperature analysis.

barotropic MCC's typically have the stronger convection located on the south side of the anvil shield in a more favorable location for inflow from the low level jet.

A.)

B.)

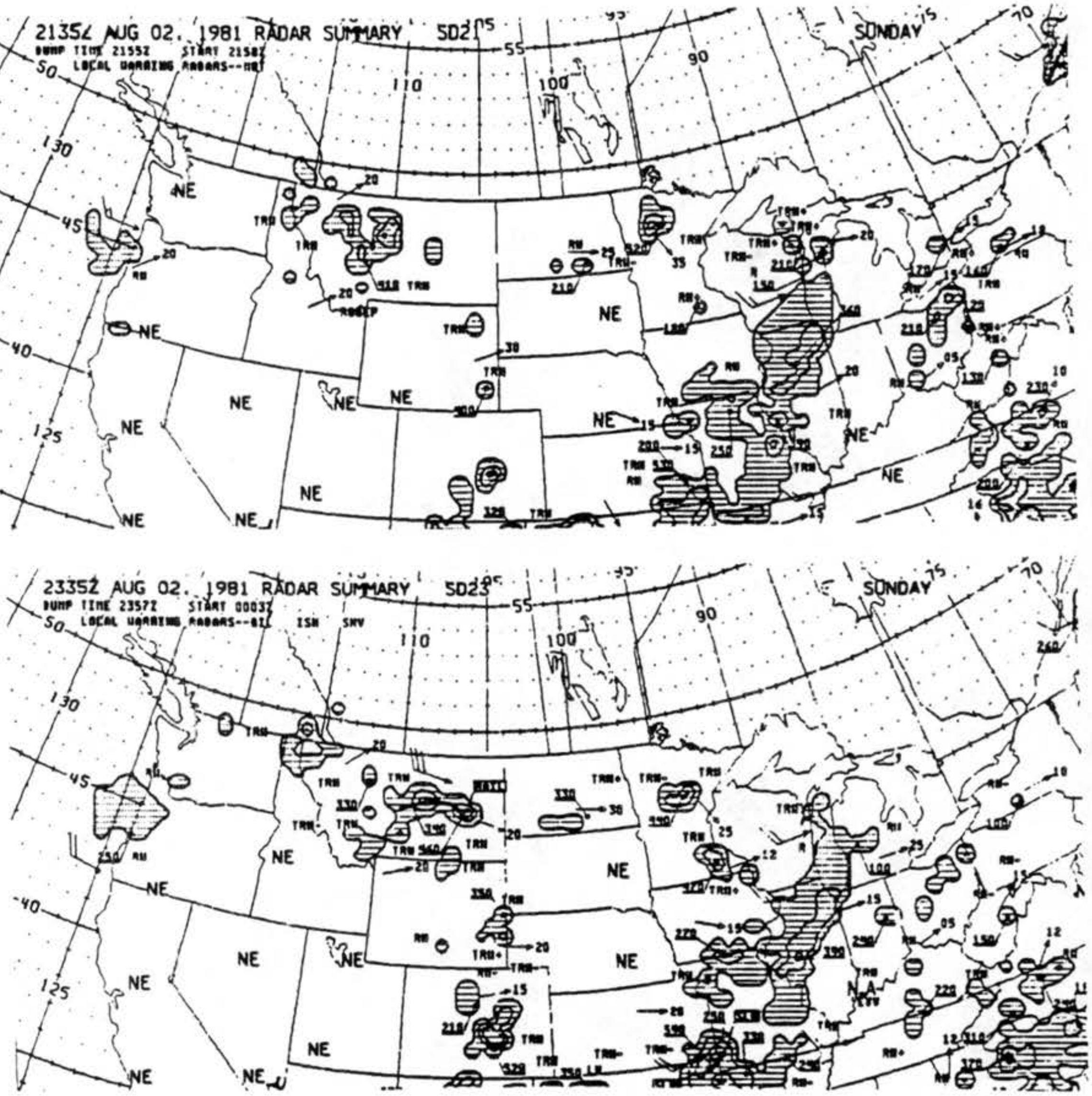

Figure 6.5: National Weather Service radar summaries from a) 2 Aug 1981 2135 UTC, b) 2 Aug 1981 2335 UTC, c) 3 Aug 1981 0135 UTC, d) 3 Aug 1981 0435 UTC, e) 3 Aug 1981 0935 UTC, and f) 3 Aug 1981 1135 UTC.

C.)

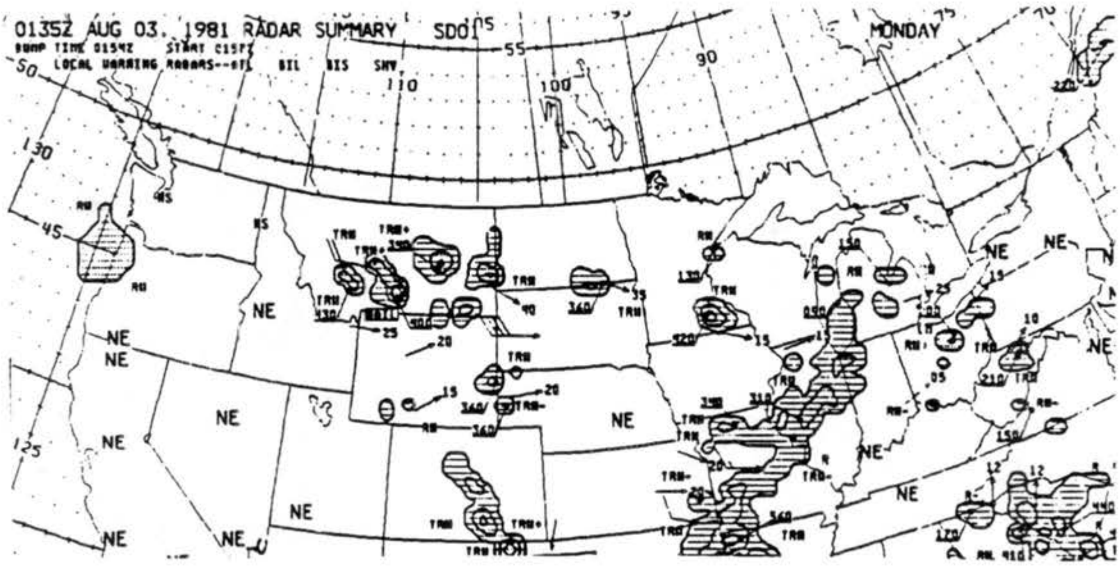

D.)

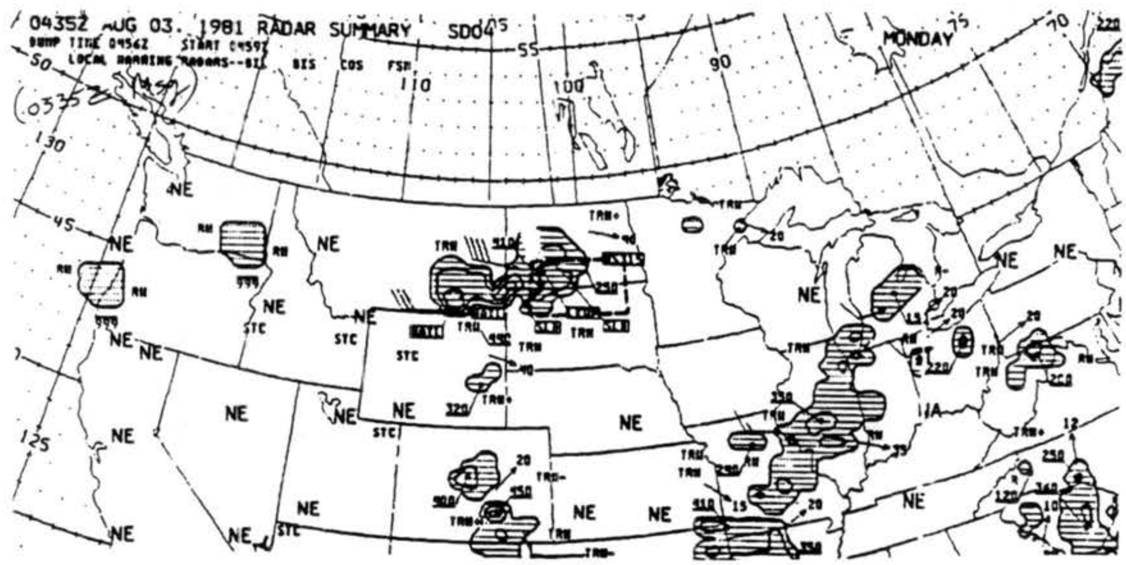

Figure 6.5: Continued.

E.)

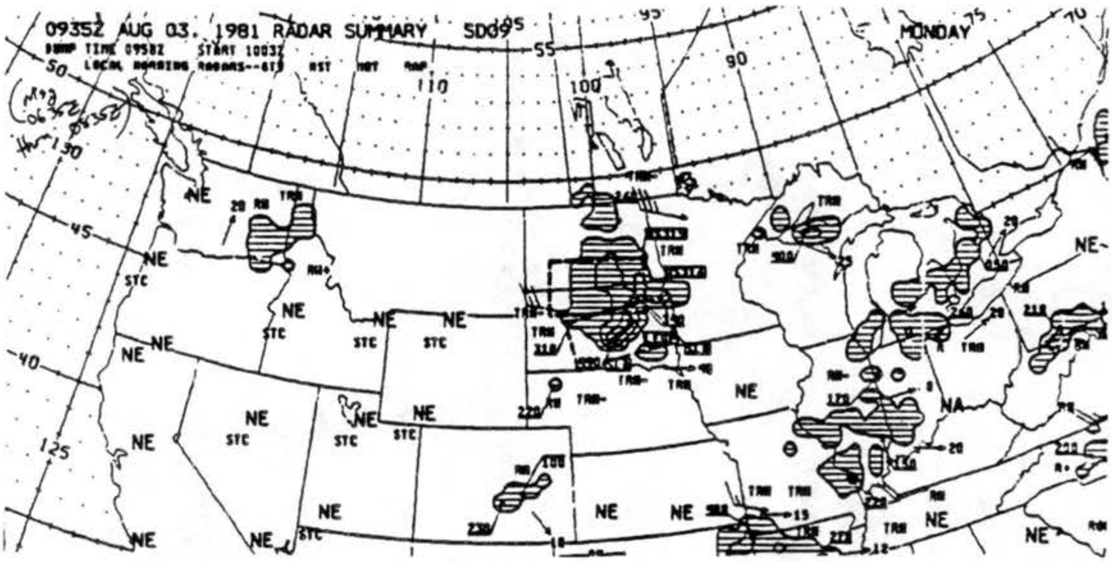

F.)

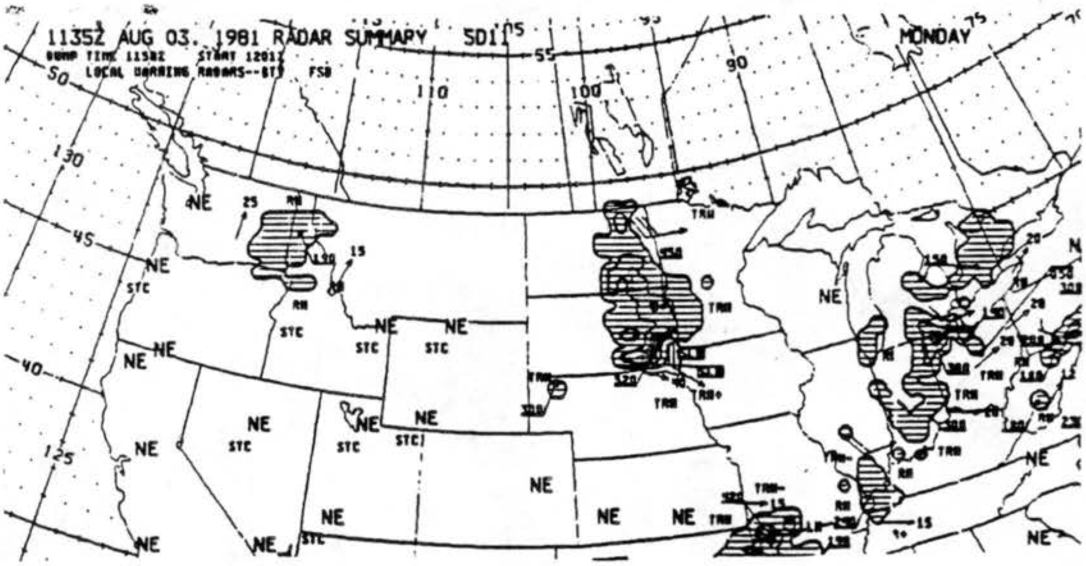

Figure 6.5: Continued.

Chapter 7

THE COARSE RESOLUTION NUMERICAL SIMULATIONS

7.1 The choice of the "control run:" a question of verification and predictability

As mentioned previously, the goal of this research is not to show that the model results can exactly mimic the observations of the particular case that was chosen for simulation. Indeed, the verification question is a difficult issue for those who need to show the forecast ability of a model. It has been standard practice in the past to verify model forecasts against the data analysis that has been performed by operational centers such as NMC or ECMWF. These analyses, though, are used by the centers for various purposes including the initialization of their synoptic scale operational models so that the analyses need to be relatively smooth. This is especially true if one is doing a historical case. In the case presented in this research (year 1981), the NMC analyses were truncated at global wavenumber 20, which corresponds to a horizontal wavelength of about 2000 km. Therefore, if an "S1" score or similar measure of model performance was computed for a model with even a relatively coarse resolution of 100 km, any mesoscale feature with a wavelength less than 2000 km that was produced by the model would be considered forecast error.

Rather than verify model forecasts against an analyzed dataset, an attempt could be made to compare against actual rawinsonde or surface measurements. The problem with this approach is that these measurements are point measurements while the model results, even if not explicitly stated in the model's derivation, need to be considered as areal or volume averages. Since the rawinsonde resolution is much coarser than the model resolution, an adequate observational sample is not taken of the atmosphere to compute the statistics. Even the surface observations only have an average of 2 or 3 points in each

100 km grid area. This is especially a problem in the summer season when forcing for the significant weather occurs on smaller spatial scales than often occurs in the winter.

Since the operational models today have resolutions of about 80 km (some are down to 30-40 km), the question of verification on the mesoscale will need to be addressed soon. Ideally, observational datasets of adequate spatial and temporal resolution and adequate spatial coverage are desired. However, this requires measuring systems of even higher resolution than those currently planned for the early to mid-1990's (wind profilers, etc.).

With these problems of model verification in mind, the goal of the current research is to provide a test vehicle to study various hypotheses about the development and propagation of MCCs. However, the question remains as to whether the model adequately simulates the atmosphere so that any conclusions drawn from the model results can be extended to the real atmosphere. The answer that will be given here is one of circumstantial evidence only. The model results will be compared only qualitatively with the available observations (radar, satellite, etc.). It is expected that the model is capable of producing mesoscale features, hence rendering the current quantitative synoptic-scale measures of model performance useless.

Along with the issue of verification of model performance, another question can be raised concerning the predictability of a particular event. The Lorenz type analysis which concluded that lack of information on scales smaller than observable will eventually feed upscale to all larger scales and destroy the predictability will not be addressed here. That analysis would produce a predictability time of 24-48 hours for mesoscale convective systems, which is longer than the simulation presented in this research. Another question, though, can be raised: "Will a slight change in initial conditions, boundary conditions, or aspects of the model formulation produce a significant change in the predicted event?"

In previous research, modellers have tested a model's sensitivity to initial conditions by introducing a random perturbation (which can be hypothetically viewed as measurement errors) into the initial fields (Anthes, personal communication). Anthes found that the model simulations, after a period of adjustment to the imbalanced perturbation, were not overly sensitive to the random forcings. This was probably due to the fact that many mesoscale events are forced by mesoscale variations in surface characteristics which can produce larger and more organized variations in the atmosphere than random forcings.

Unfortunately, a perfect atmospheric prediction model does not yet exist. In this study, a different class of predictability considerations will be examined. There are many uncertainties in the initial conditions and model formulation.There are many assumptions made in some of the model's parameterizations, where there is no physical basis for these assumptions, only circumstantial evidence and "intuition." Of the numerous simulations that have been made over the length of this research, two simulations showing the sensitivity of the model to numerical and initialization uncertainties will be shown. The first sensitivity simulation will present a test of the horizontal diffusion parameterization which also implicitly tests horizontal resolution. The second sensitivity simulation will vary the initial conditions for the run by modifying the initial soil moisture content which is not a quantity that is routinely measured. It has been shown in several studies that the daytime atmospheric boundary layer structure and depth is highly dependent on the soil moisture content. Since the boundary layer differences between the U. S. High Plains and Central Plains lead to the development of the nocturnal low-level jet and the structure of the mountain/plains solenoid, it could be expected that the initiation and behavior of an MCS that develops with forcing by the low-level jet could be affected by the initial soil moisture content which is used by several of the parameterizations currently employed in mesoscale models (Blackadar, McCumber and Pielke, Tremback and Kessler).

In choosing a particular simulation for this case study to use as the control run, these questions of verification and predictability must be addressed. In this work, simulations testing various aspects of some of the uncertainties in the parameterizations and initial fields have been run for the CCOPE 1981 case study. The simulation chosen as a control exhibited the best gross behavior of the convective system being studied as compared to the radar summaries. The following section will describe the control simulation in detail, comparing the results with the available observations, then present the predictability experiments mentioned above, comparing with the simulation chosen for the control run.

7.2 The control simulation and predictability experiments

This section will present the results from the simulation that was chosen as the control experiment and compare these results to the observations. Then the predictability tests covering two examples from the above discussion will be presented.

The model simulations were started at 1200 UTC on August 2. The coarse resolution simulations had a grid spacing of 1.4° in the east-west direction and 1° in the north-south direction which corresponds to about a 110 km grid spacing at 45° north. There were 56 grid points in the east-west and 46 in the north-south. The domain extended from 20° north to 65° north and from 140° west to 63° west. The long timestep length was 120 s with a small timestep length of 30 seconds.

7.2.1 The control simulation for the CCOPE case

As mentioned, the control simulation was chosen as the run which exhibited the best qualitative match between the modelled convective system and the observed behavior from the radar summaries. An additional consideration was one of economy. Since several sensitivity tests were to be run, only the coarser grid (about 110 km resolution) was run. The model configuration for this run was basically the model description as detailed in Chapter 3 except that the resolved precipitation processes were turned off. Resolved latent heating due to condensation was still included.

In a simulation such as this, there are a great many ways to look at the model results. Figure 7.1a-h shows the behavior of the convective system from the standpoint of the convective precipitation rate as computed by the convective parameterization. This rate can, in a qualitative sense, be compared to the radar summaries (Figure 6.5) especially when considering location of the active precipitating areas. Only a qualitative comparison can be made, however, since the radar will show both convective and much of the stratiform precipitation particles whereas the modelled convective precipitation rate is only the contribution from deep convection. Starting at 1800 UTC (Fig 7.1a), there is very little convective activity over Montana as observed. The convection predicted by the model to the southeast over Oklahoma, Kansas, Iowa, and Illinois was observed to occur at that

A.

B.

Figure 7.1: Convective parameterization precipitation rate from coarse resolution control run. a) 2 Aug 1800 UTC, b) 2 Aug 2200 UTC, c) 3 Aug 0000 UTC, d) 3 Aug 0400 UTC, e) 3 Aug 0600 UTC, f) 3 Aug 0800 UTC, g) 3 Aug 1000 UTC, h) 3 Aug 1200 UTC.

C.

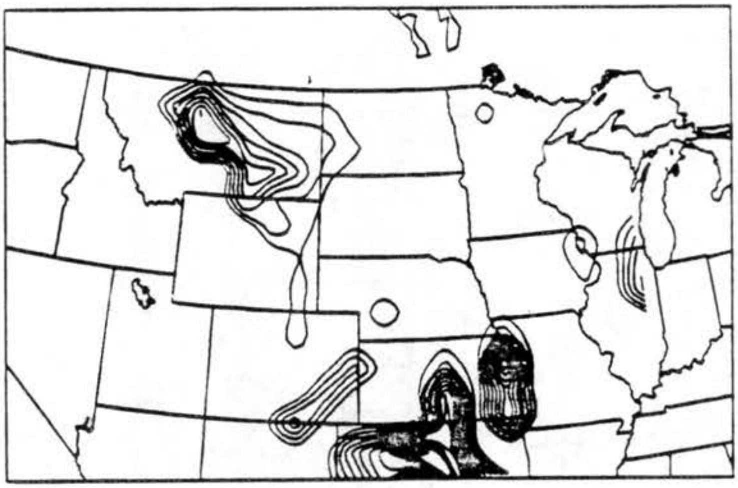

D.

Figure 7.1: Continued.

E.

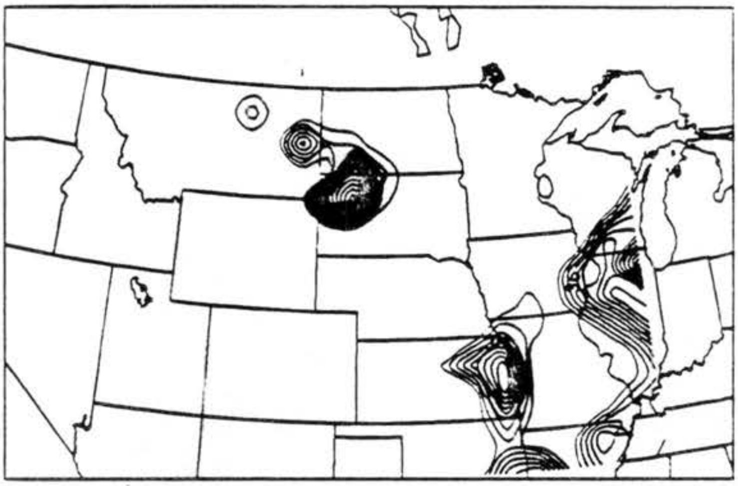

F.

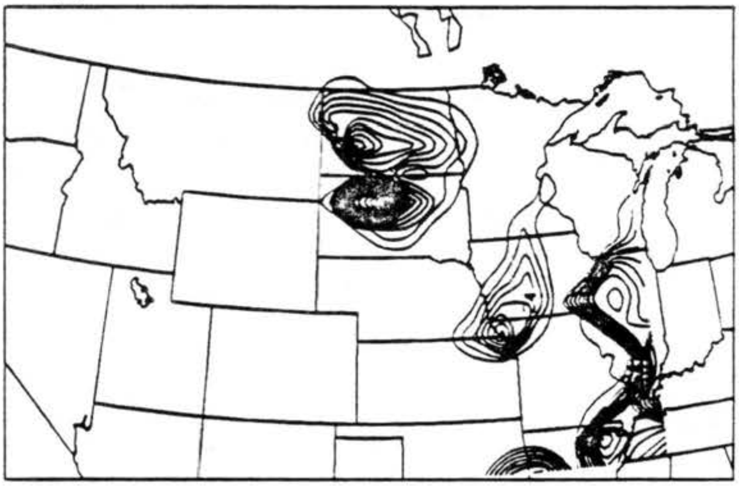

Figure 7.1: Continued.

G.

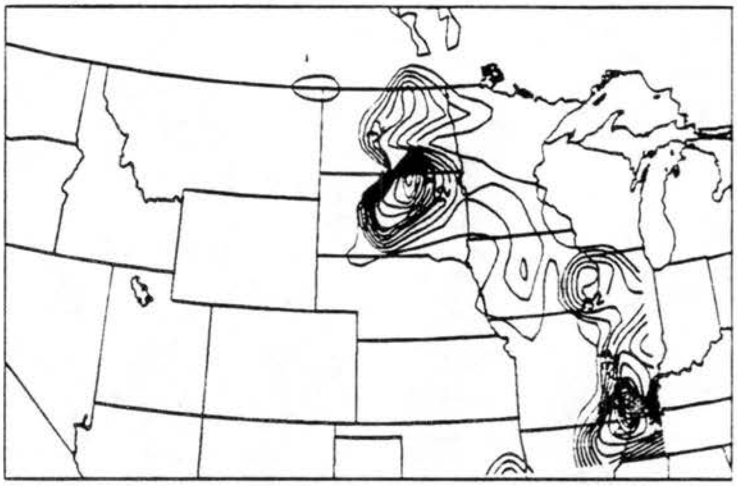

H.

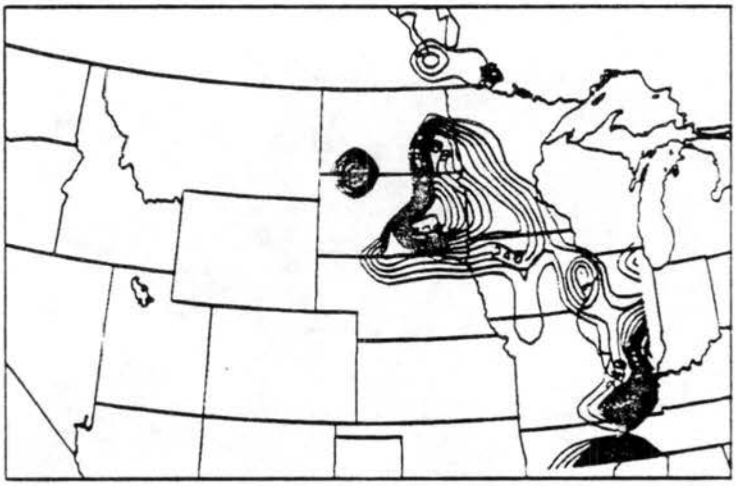

Figure 7.1: Continued.

time, although the model located the convection too far toward the northwest. By 2200 UTC (Figure 7.1b), the convection is beginning over Montana and northern Wyoming. The convection strengthened by 0000 UTC (Figure 7.1c) while the convective line over the central Plains weakened. The observed convective region in Montana weakened by 0200 UTC but reintensified by 0400 UTC. The location of the modelled system was good, but the simulated system continued to intensify from 0000 UTC to 0400 UTC (Figure 7.1d) and, by 0600 UTC (Fig 7.1e), moved out into the western Dakotas. The system continued to propagate through the Dakotas until the end of the simulation at 1200 UTC (Fig 7.1h) when it was located over the eastern Dakotas, lagging a bit behind the observations which placed it directly over the Minnesota border. This discrepancy, however, because of the relatively coarse model resolution, was lagged only by 1-2 grid points. The spatial orientation of the convective region of the system was also similar to observations. The system originally formed in Montana with the main convective areas elongated parallel to the mid and upper level winds. As the system propagated through the Dakotas, the main convective region of the system reoriented to be perpendicular to the upper level winds at a similar time as was observed. This transformation occurred rather abruptly (over a 2 hour period) and may have marked a change in the dynamics of the system. This transformation will be covered in more detail in the next chapter.

Focusing next on the surface characteristics of the circulation, the next figures show the low level fields following the lowest sigma-z coordinate surface which was about 150 m above the ground. Figures 7.2a-d show the perturbation Exner function field on this coordinate surface. The perturbation field is not reduced to sea level or other constant height level. At the beginning of the model simulation at 1200 UTC, two distinct areas of low pressure are evident over southern Montana and western Nebraska and Kansas. This regime continued up to about 2200 UTC when the southern low center dissipated. The low center over Montana then became dominant, moving slightly toward the east through the rest of the simulation.

Figures 7.3a-f show the time evolution of the low level isotachs and wind vectors through the 24 hour simulation. At 1200 UTC on 2 August, the low level jet is evident

A.

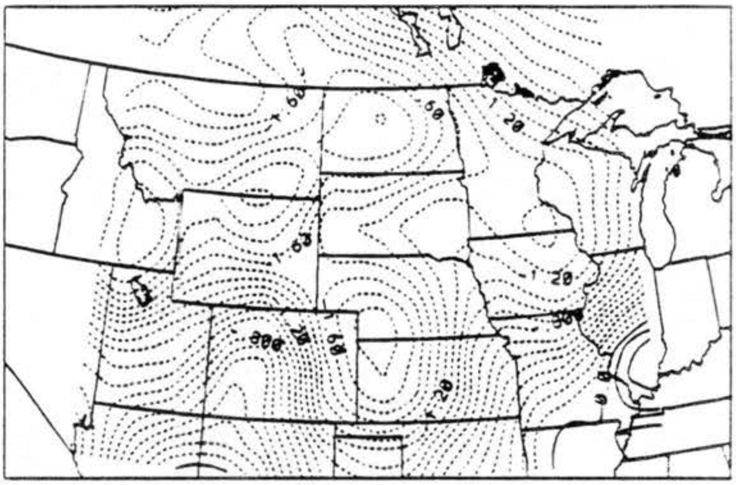

B.

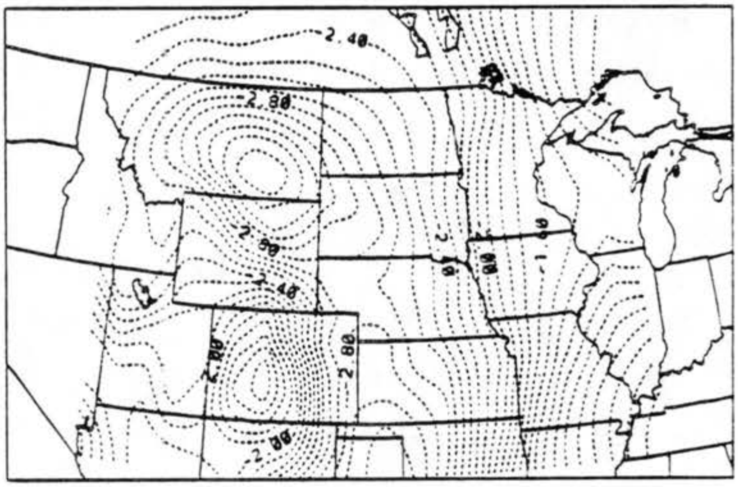

Figure 7.2: Perturbation Exner function on terrain following coordinate surface 150 m above ground from coarse resolution control run. a) 2 Aug 1200 UTC, b) 2 Aug 2200 UTC, c) 3 Aug 0600 UTC, d) 3 Aug 1200 UTC.

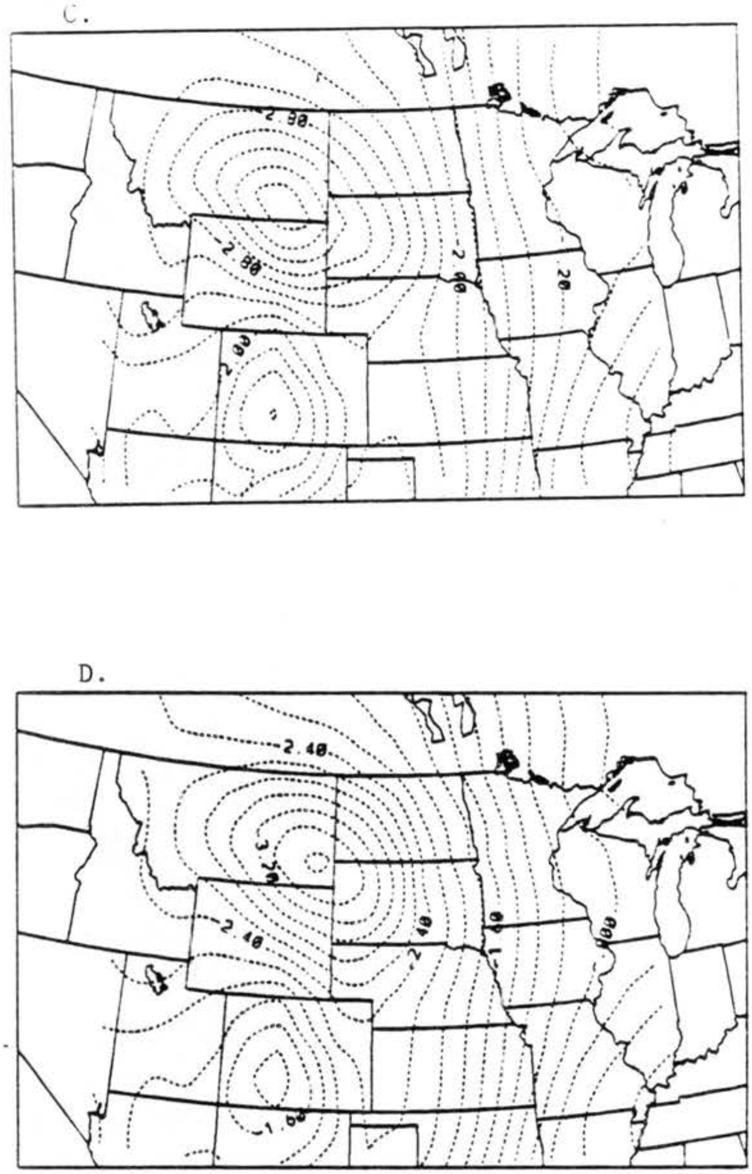

Figure 7.2: Continued.

A.

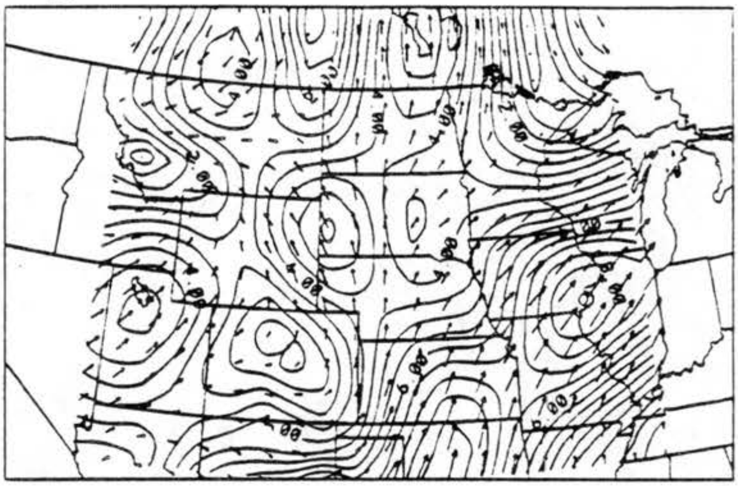

B.

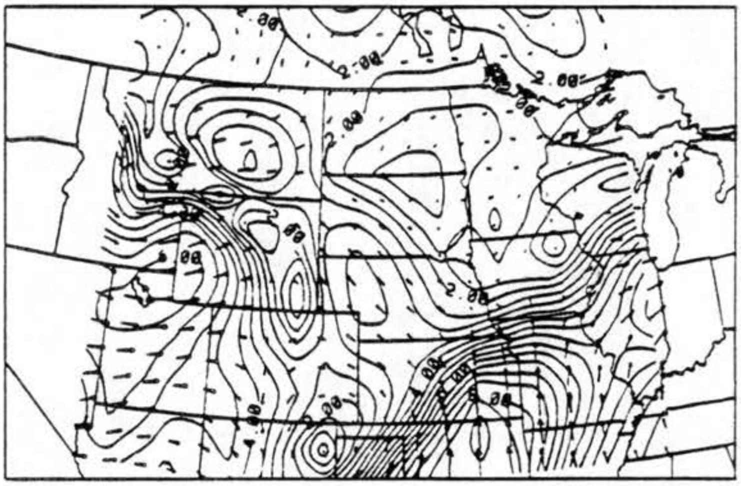

Figure 7.3: Isotachs and wind vectors on terrain following coordinate surface 150 m above ground from coarse resolution control run. a) 2 Aug 1200 UTC, b) 2 Aug 1800 UTC, c) 3 Aug 0000 UTC, d) 3 Aug 0400 UTC, e) 3 Aug 0800 UTC, f) 3 Aug 1200 UTC.

C.

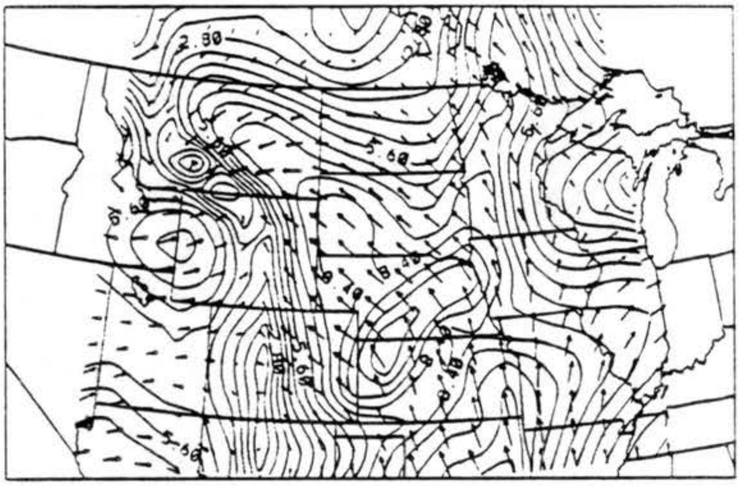

D.

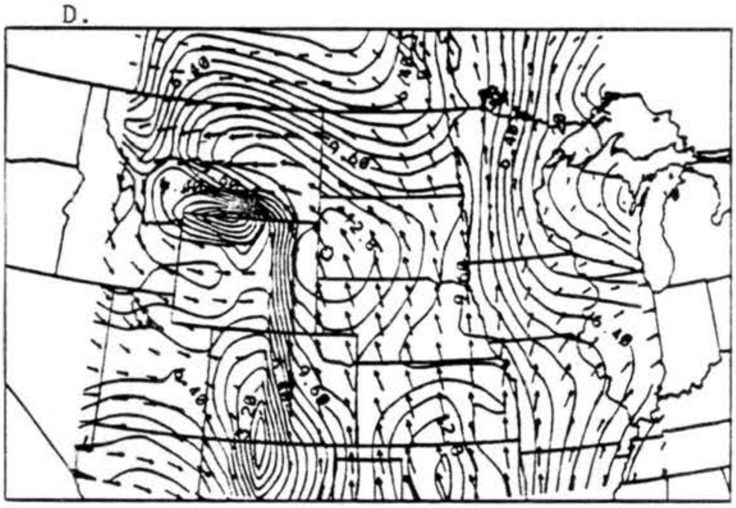

Figure 7.3: Continued.

E.

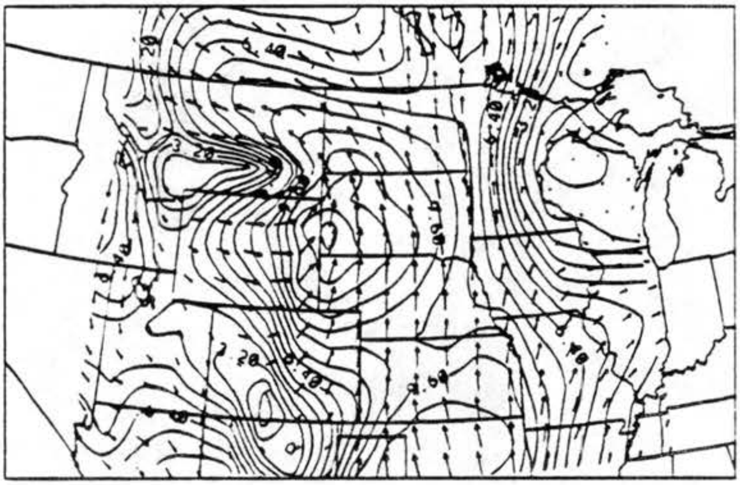

F.

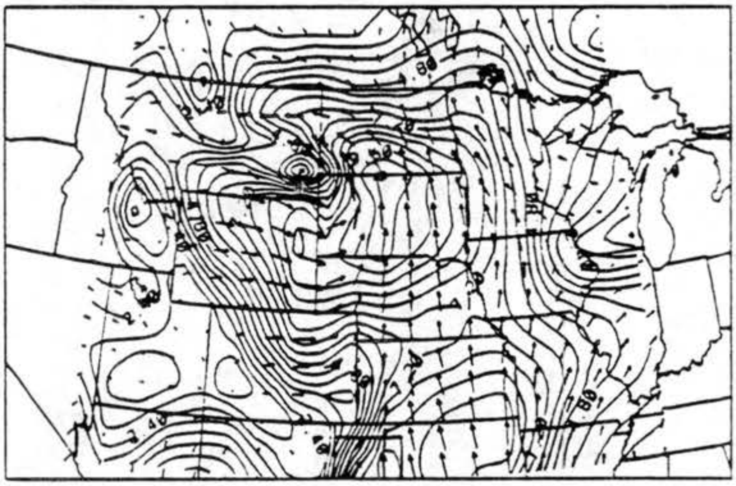

Figure 7.3: Continued.

through the central Plains with velocities up to 10 m/s. The jet weakened throughout the day, especially to the north and west of the convective line through the Plains. By 0000 UTC (Figure 7.3c) as the central Plains convective line weakened and the low pressure center over Kansas dissipated, the jet redeveloped toward the northwest, providing an energy and moisture source to Montana from the southeast. Comparing Figure 7.3c with a surface analysis of the area (Figure 6.4), good agreement again can be seen between the observations and the model results. Along with the southeasterly flow into Montana, the northeasterly flow from southern Saskatchewan can be seen behind the weak surface front. The low level jet continued to strengthen and veer throughout the night with the strongest convection occurring near the nose of the jet.

The low level moisture field is shown in Figures 7.4a-e. From the initial field at 1200 UTC, the mixing ratio decreased throughout the day as the boundary mixed out the moisture faster than the surface could act as a supply. From a morning value of about 12 g/kg at 1200 UTC, the moisture decreased to about 7 g/kg by 0000 UTC when the convective system was developing. This was much less than the observed values of 12-14 g/kg. Several factors could account for this discrepancy including inadequate initialization of soil moisture and neglect of local sources. Results from a sensitivity test of soil moisture initialization are presented below.

At the 5.16 km level, the isotachs are shown in Figures 7.5a-e. At the initial time (Figure 7.5a), a jet core was entering the Montana-Idaho region. During the day, the core propagated farther toward the east and dipped southward. By 0000 UTC, the core was located such that its nose was directly over the genesis region of the MCC. After the system developed, a small perturbation developed at the jet nose, most likely from enhanced inflow into the system (a rear level inflow jet). The inflow jet perhaps can be more easily seen in the relative vorticity field (0600 UTC, Figure 7.6) and is evidenced by a small positive vorticity perturbation over the extreme southeast corner of Montana. The jet and its perturbation accompanied the system throughout the night as the MCC crossed the Dakotas.

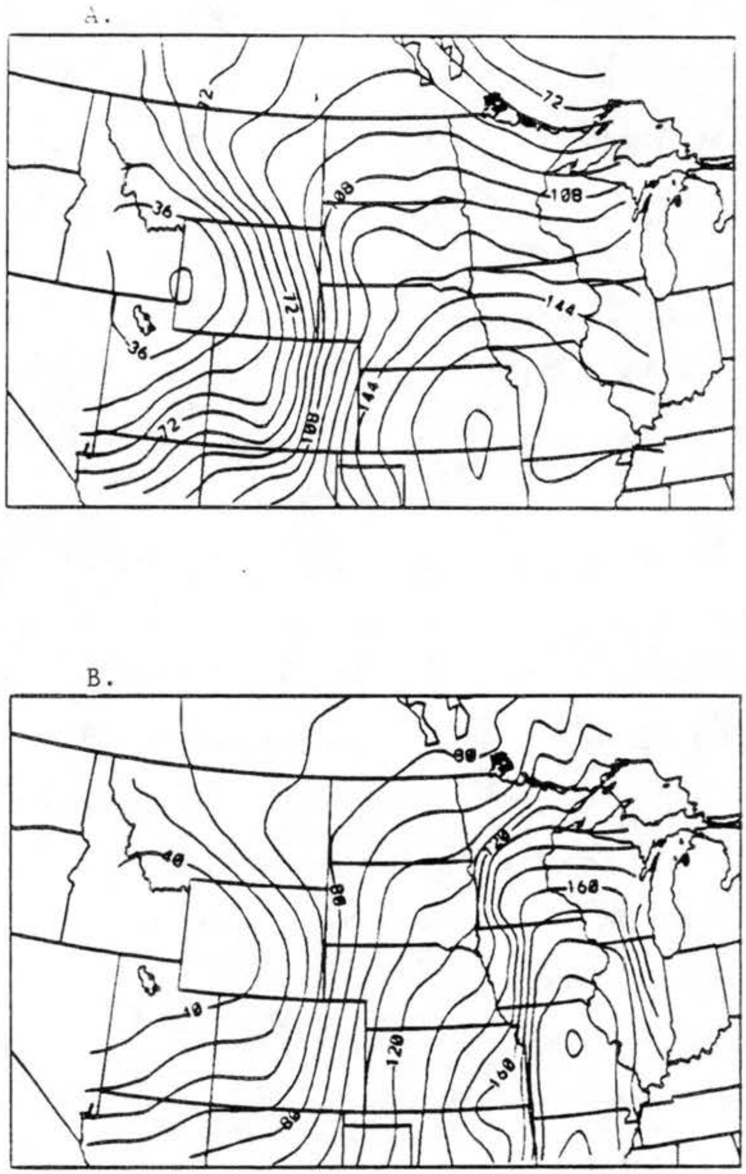

Figure 7.4: Total water mixing ratio field on terrain following coordinate surface 150 m above ground from coarse resolution control run. a) 2 Aug 1200 UTC, b) 2 Aug 1800 UTC, c) 3 Aug 0000 UTC, d) 3 Aug 0600 UTC, e) 3 Aug 1200 UTC.

C.

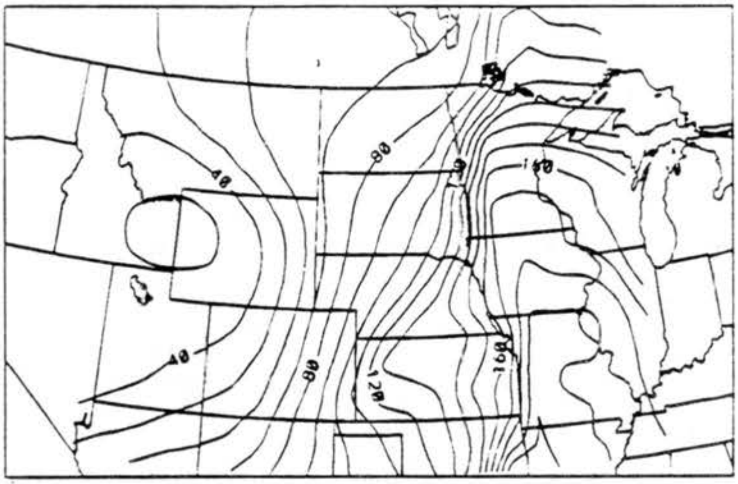

D.

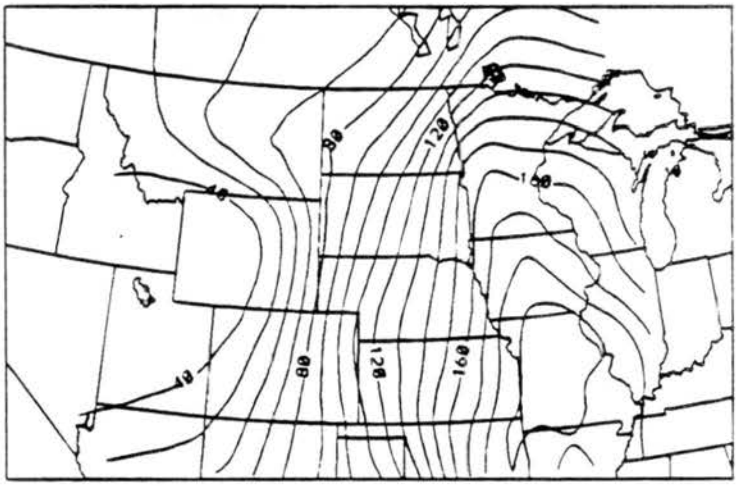

Figure 7.4: Continued.

E.

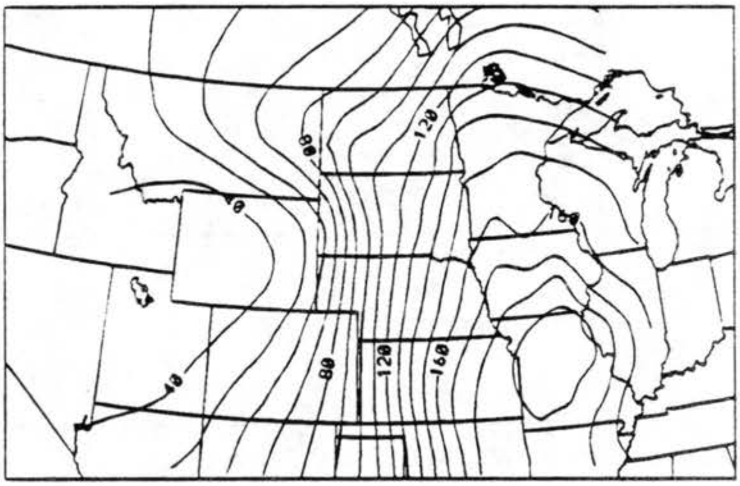

Figure 7.4: Continued.

A.

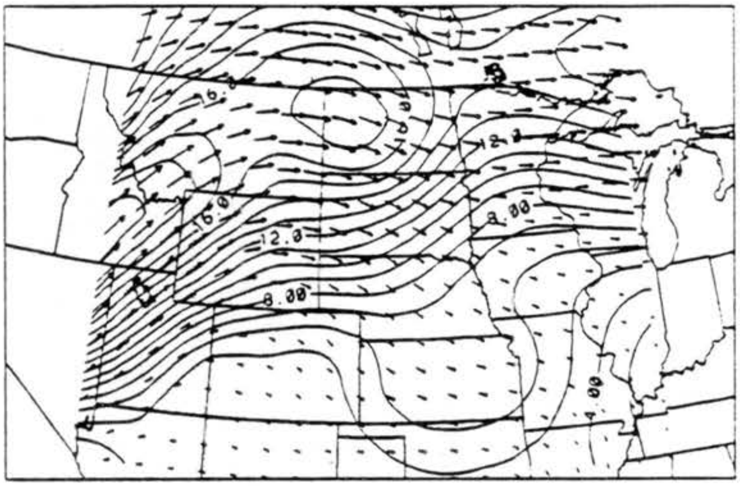

B.

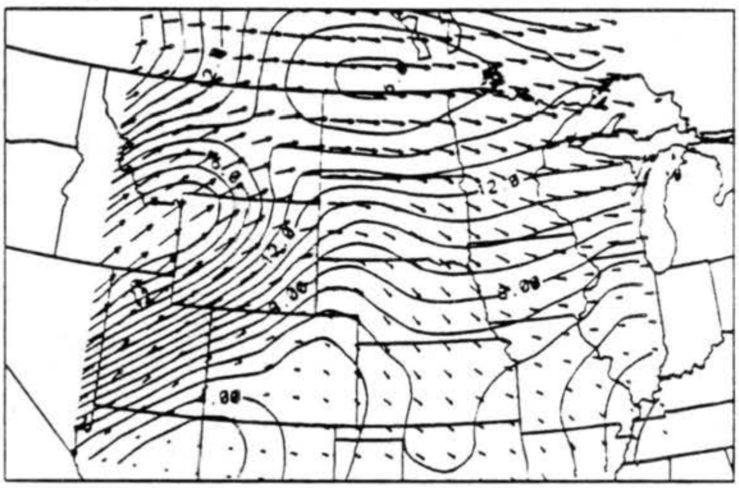

Figure 7.5: Isotachs and wind vectors at 5.16 km above sea level from coarse resolution control run. a) 2 Aug 1200 UTC, b) 2 Aug 1800 UTC, c) 3 Aug 0000 UTC, d) 3 Aug 0600 UTC, e) 3 Aug 1200 UTC.

C.

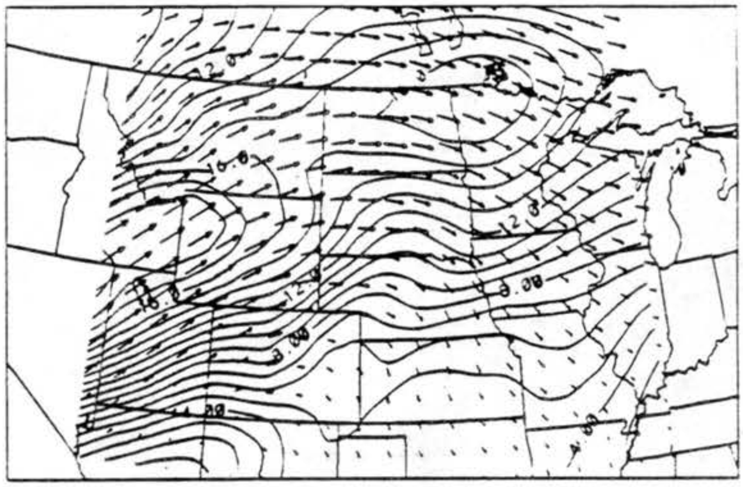

D.

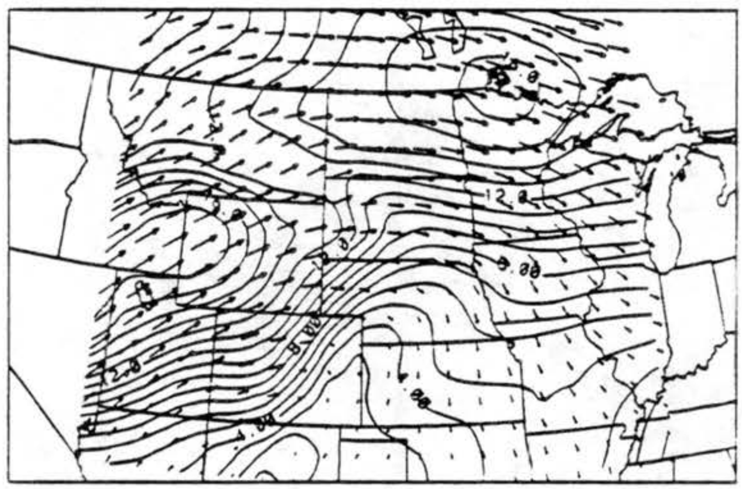

Figure 7.5: Continued.

E.

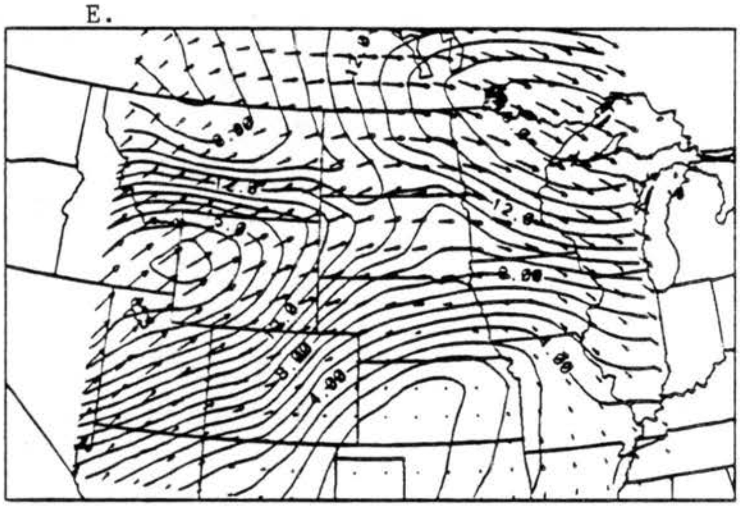

Figure 7.5: Continued.

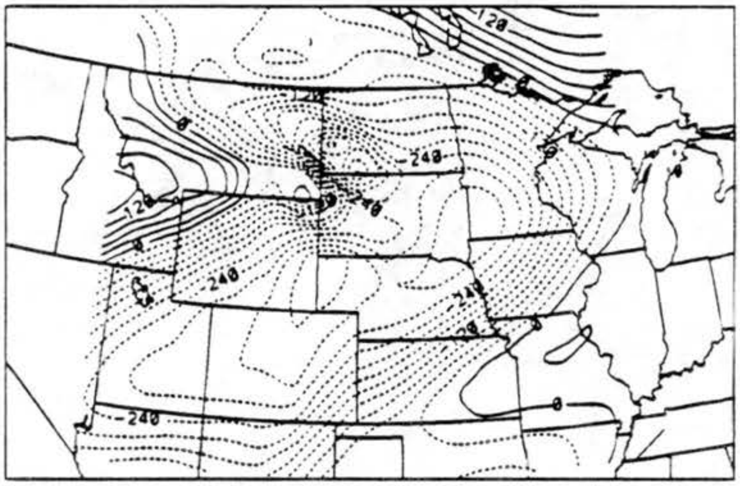

Figure 7.6: Relative vorticity field at 5.16 km above sea level from coarse resolution control run at 3 Aug 0600 UTC.

The mid-level pressure perturbation fields are shown in Figures 7.7a-d. At 0000 UTC, the Montana-Dakota region was under general ridging although a stationary wave seemingly associated with the topography was seen. This wave remained stationary throughout the simulation and no other evidence of a shortwave was found either in the pressure or the wind field. The relatively strong synoptic scale gradients may have obscured smaller perturbations, however.

The convective system can be seen in the mid-levels with the vertical motion (Figures 7.8a-d) and moisture fields (Figures 7.9a-f). At 1800 UTC, well before any strong convection developed in Montana, there was upward motion of over 4 cm/s over Montana that was apparently forced by synoptic scale dynamics. By 0000 UTC, after some convection had occurred, the upward motion became locally stronger, reaching about 10 cm/s. Later (0800 UTC), after the convection had become stronger and more persistent, the vertical motion became much stronger (over 20 cm/s) and more focused. By the end of the simulation (1200 UTC), the upward motion associated with the convective system again became weaker and more diffuse but organized in the bow-shaped pattern similar to the convective precipitation fields at the same time as the actual MCC was observed to begin its dissipation.

The moisture fields (total water mixing ratio) in Figures 7.9a-f show mostly the response of the moisture field to the advection by the resolved vertical motion. Although there is an additional source of moisture in this simulation from the convective parameterization, that moisture source is predominantly put higher into the atmosphere. Since resolved precipitation processes are not included in this control run, the moisture could only be advected and not precipitated. The moisture fields at 1800 and 0000 UTC show very little perturbation, as expected, over Montana since the resolvable circulations forced by the convection did not spin up by then. By 0200 UTC, however, a perturbation can be seen which grew larger as the simulation progressed. The region of higher moisture moisture moved with the system but somewhat lagged the upward vertical motion by the end of the simulation.

For a description of the upper level flow during the simulation, the 9.96 km level will be shown which was just under the tropopause in the Montana area. The isotach and

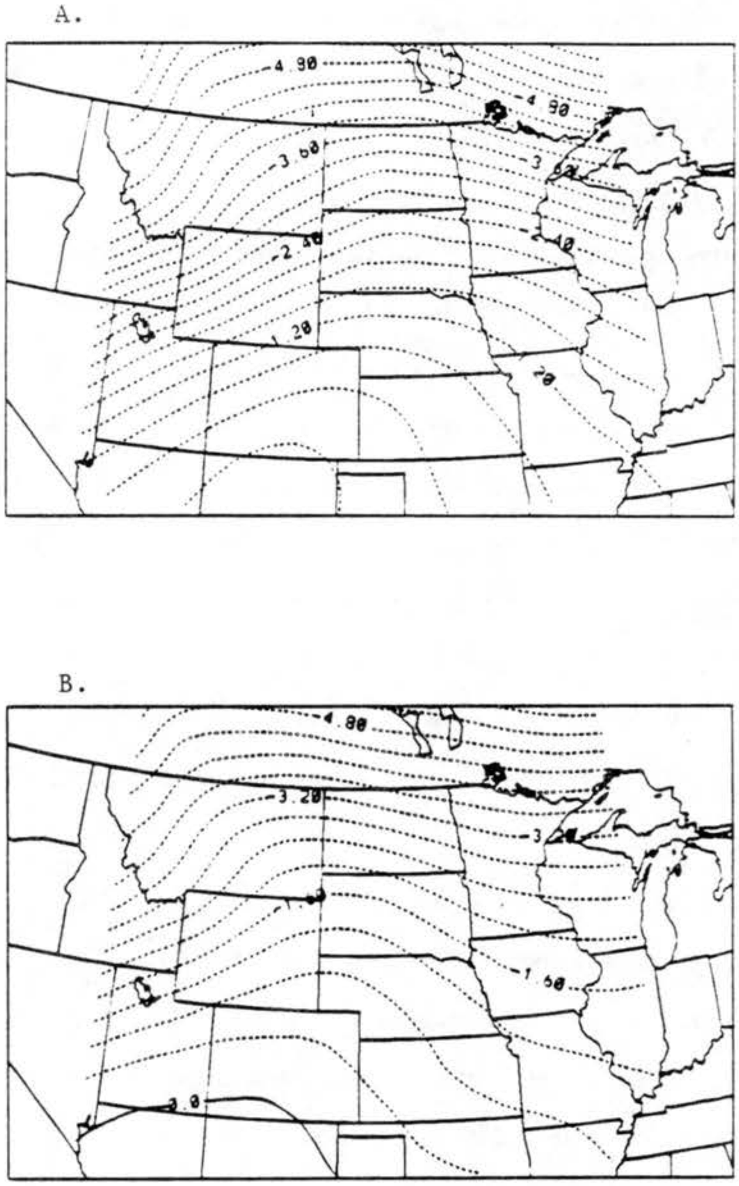

Figure 7.7: Perturbation Exner function field at 5.16 km above sea level from coarse resolution control run. a) 2 Aug 1200 UTC, b) 2 Aug 1800 UTC, c) 3 Aug 0000 UTC, d) 3 Aug 1200 UTC.

C.

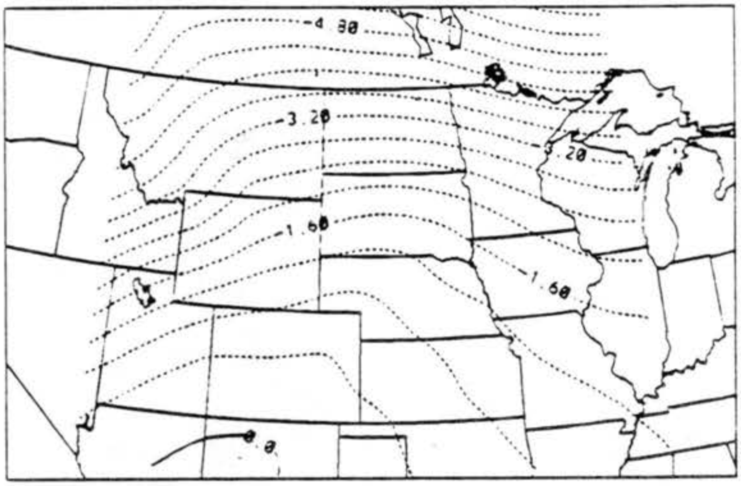

D.

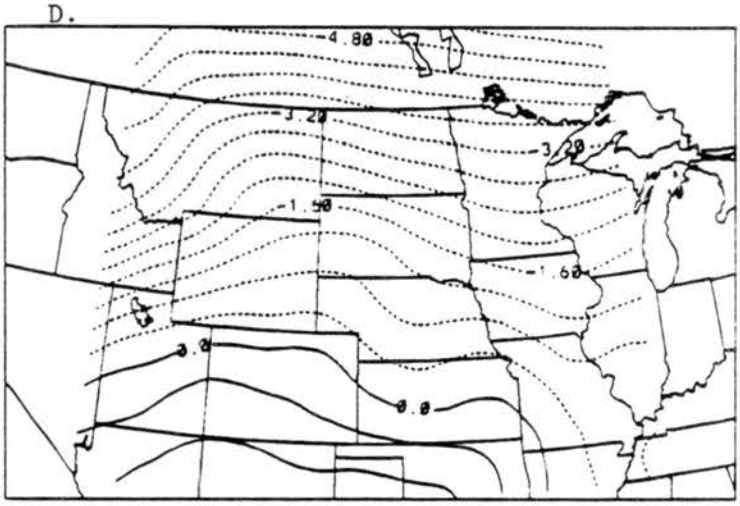

Figure 7.7: Continued.

A.

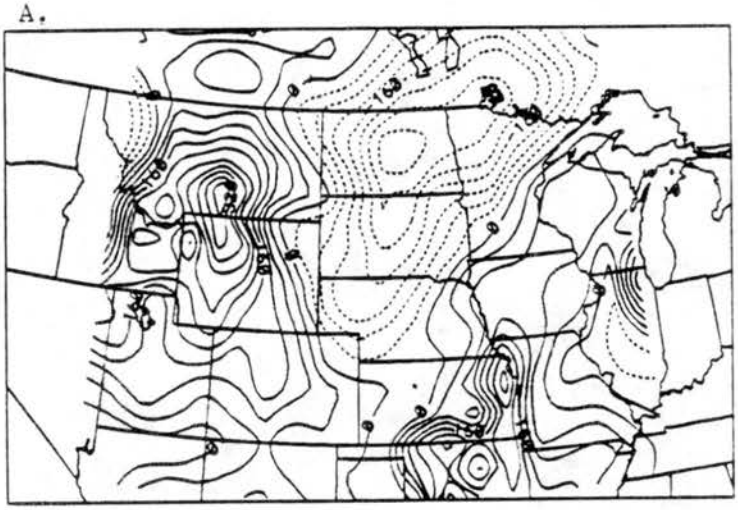

B.

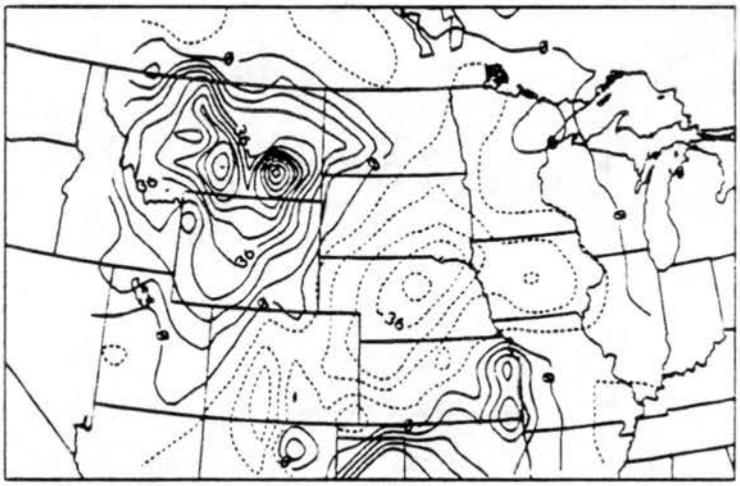

Figure 7.8: Vertical velocity field at 5.16 km above sea level from coarse resolution control run. a) 2 Aug 1800 UTC, b) 3 Aug 0000 UTC, c) 3 Aug 0800 UTC, d) 3 Aug 1200 UTC.

C.

D.

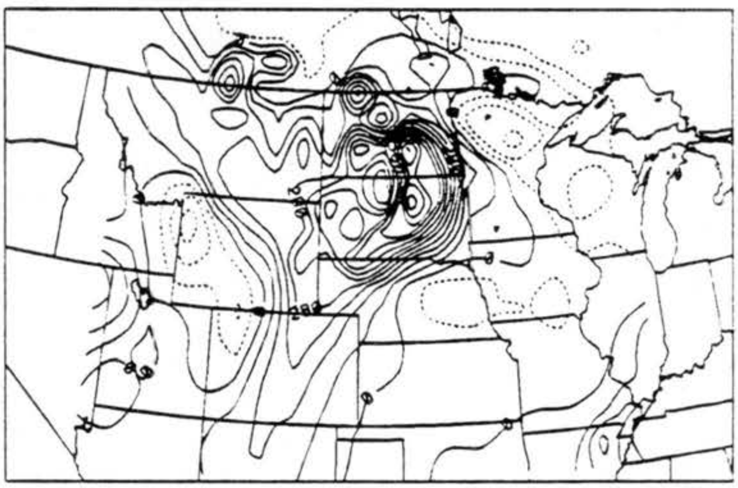

Figure 7.8: Continued.

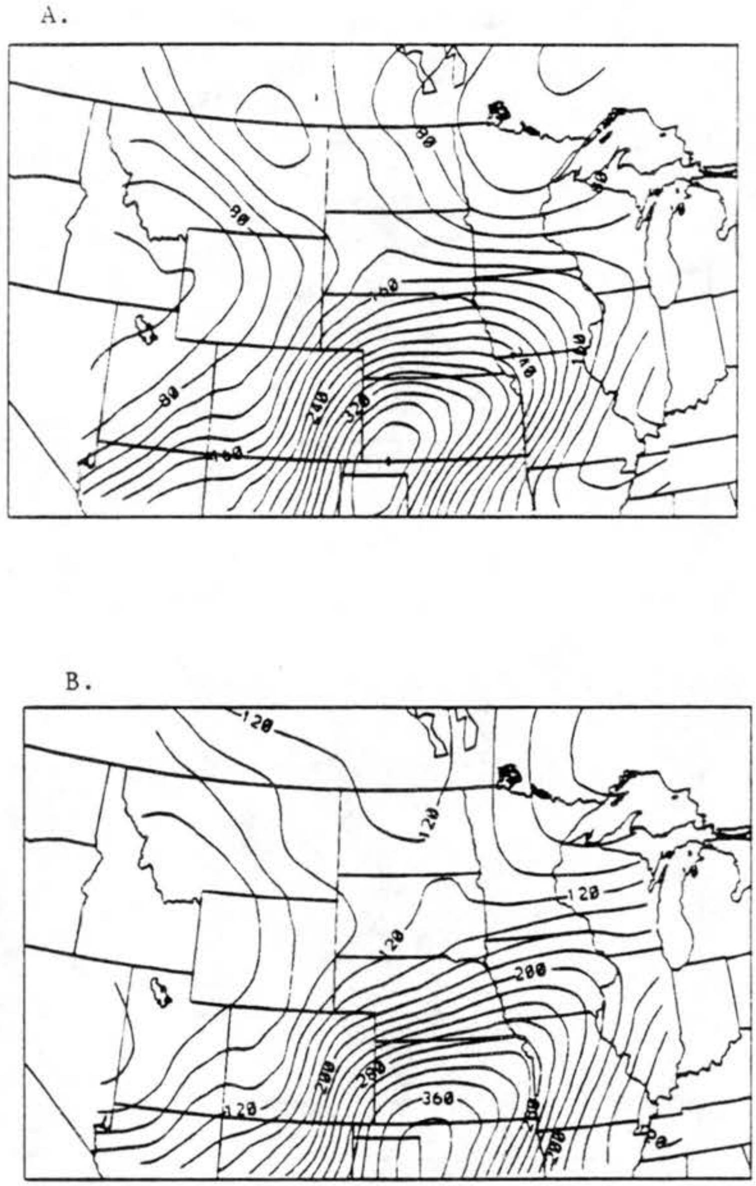

Figure 7.9: Total water mixing ratio field at 5.16 km above sea level from coarse resolution control run. a) 2 Aug 1200 UTC, b) 2 Aug 1800 UTC, c) 3 Aug 0000 UTC, d) 3 Aug 0200 UTC, e) 3 Aug 0600 UTC, f) 3 Aug 1200 UTC.

C.

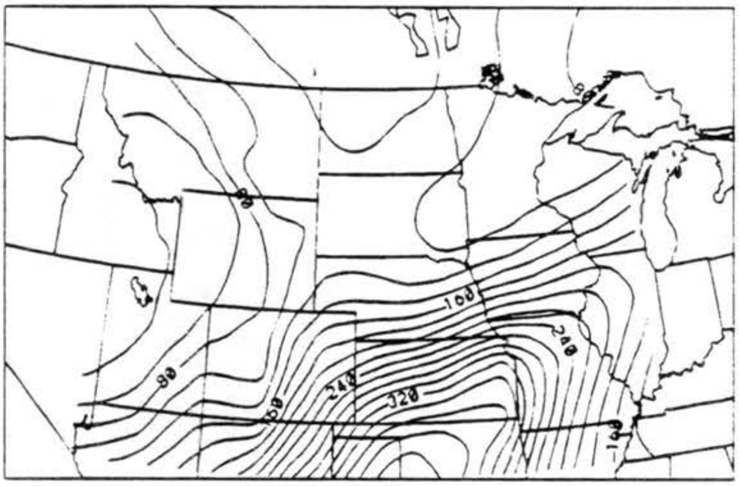

D.

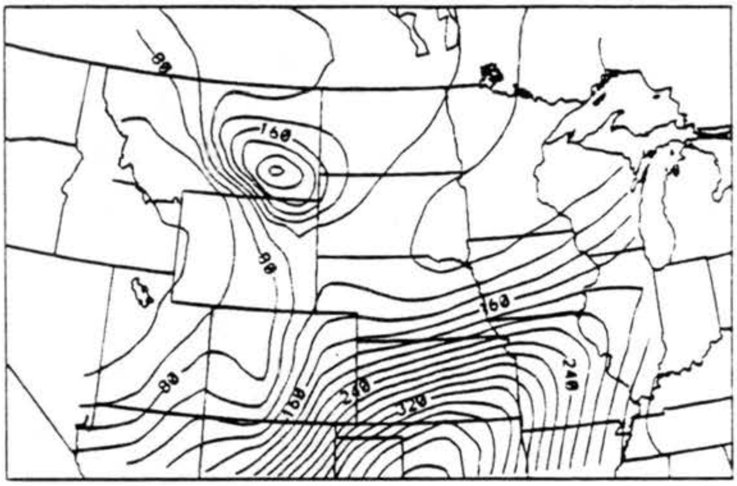

Figure 7.9: Continued.

E.

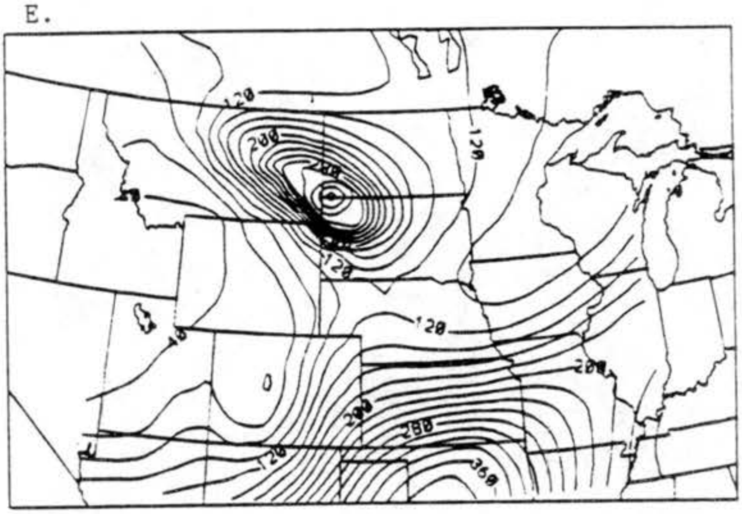

F.

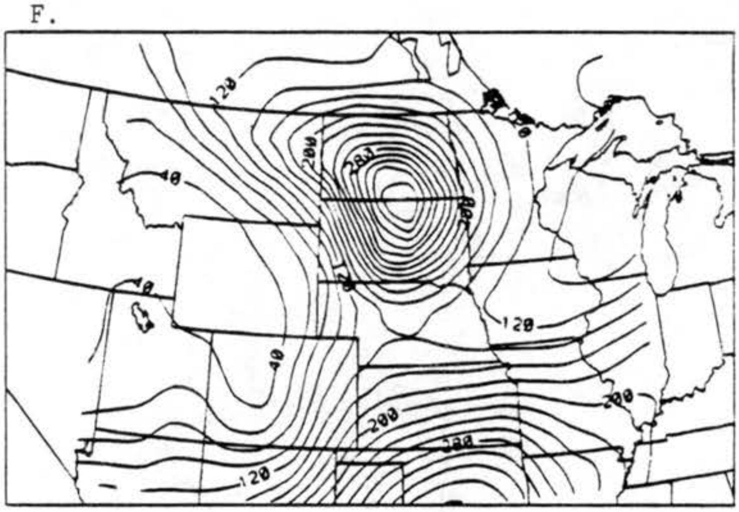

Figure 7.9: Continued.

velocity vector fields are shown in Figures 7.10a-e. Again, as in the mid-levels, a general ridging can be seen at the initial time (1200 UTC) with a strong jet core moving into the MCC genesis region. By 1800 UTC, this core had "split," with a slightly weaker core developing just downstream from the genesis region while the original core remained relatively stationary. Remember that there was no significant convection yet in the area. The primary core then began to propagate so that by 0000 UTC, there was mostly a single core structure again. The reason for this split or if it had any affect on the development of the original convection in Montana was not investigated with the model since it was not a focus of this study. By 0200 UTC, the upper level outflow jet associated with the MCC was beginning to develop in the same region where the secondary core had formed earlier. The outflow jet became very well developed by 0600 UTC and had moved downstream. Note also the retardation of the flow as it approached the system. This structure persisted through the remainder of the simulation. The outflow jet can also be seen in the relative vorticity field (Figures 7.11a-b). From a relatively innocuous ridge pattern at 0000 UTC, the negative perturbation associated with the anti-cyclonic outflow jet became quite pronounced by 1200 UTC.

The upper level vertical motion fields (Figures 7.12a-d) developed quite similarly to the mid-level fields. From general rising motion over Montana at 1800 UTC, the upward motion becomes stronger and more focused by 0000 UTC as the convection began. The upward motion becomes very focused by 0600 UTC before spreading out by 1200 UTC.

The upper level moisture fields (Figures 7.13a-d) were also similar to the mid-level fields, but because of the added contribution from the convective parameterization source, the perturbation associated with the Montana system can be seen earlier. By 0200 UTC, the resolved upward motion of the MCC had developed to enhance the perturbation. The perturbation moved with the resolved upward motion through the remainder of the simulation and, most likely because of higher horizontal advective speeds, was farther downstream at the end of the simulation than the mid-level moisture perturbation. Note also the reasonably circular shape of the perturbation.

In summary, the control simulation has reproduced many of the features of observed MCCs and the composite MCCs of Maddox (1980) and Cotton et al. (1989) in general

A.

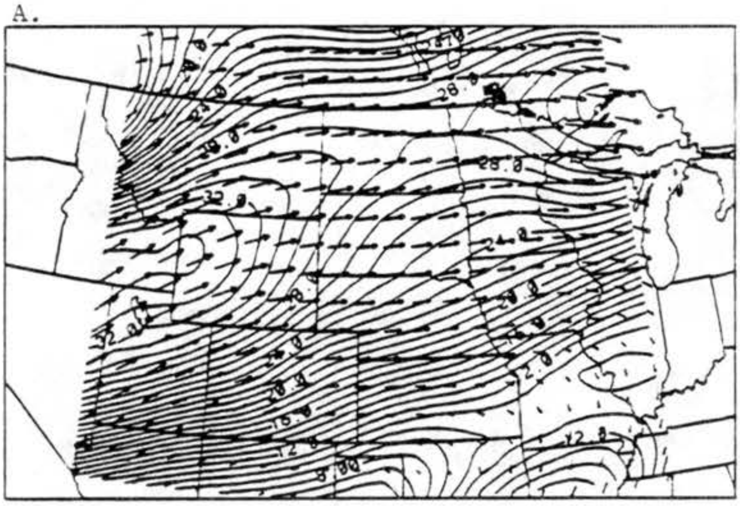

B.

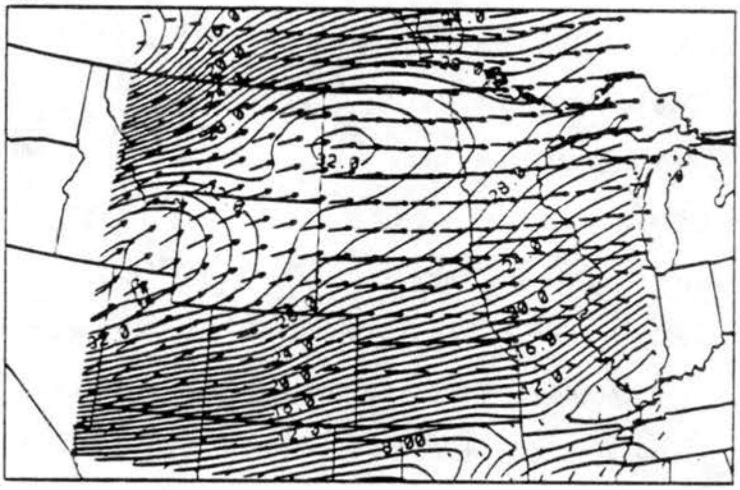

Figure 7.10: Isotachs and wind vectors at 9.96 km above sea level from coarse resolution control run. a) 2 Aug 1200 UTC, b) 2 Aug 1800 UTC, c) 3 Aug 0000 UTC, d) 3 Aug 0600 UTC, e) 3 Aug 1200 UTC.

C.

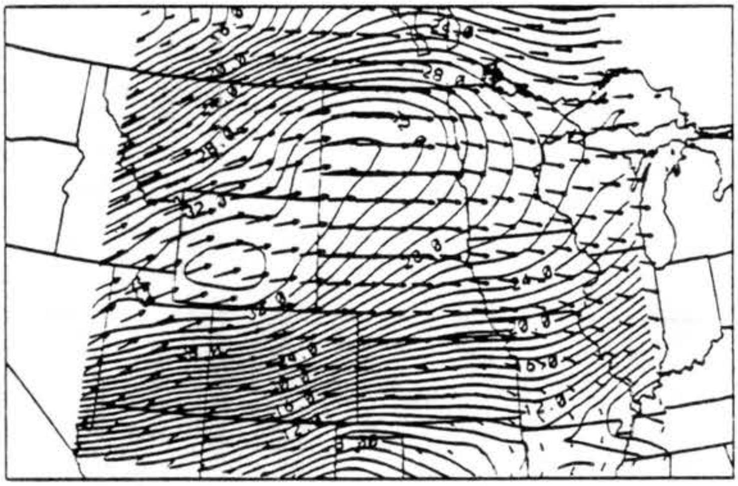

D.

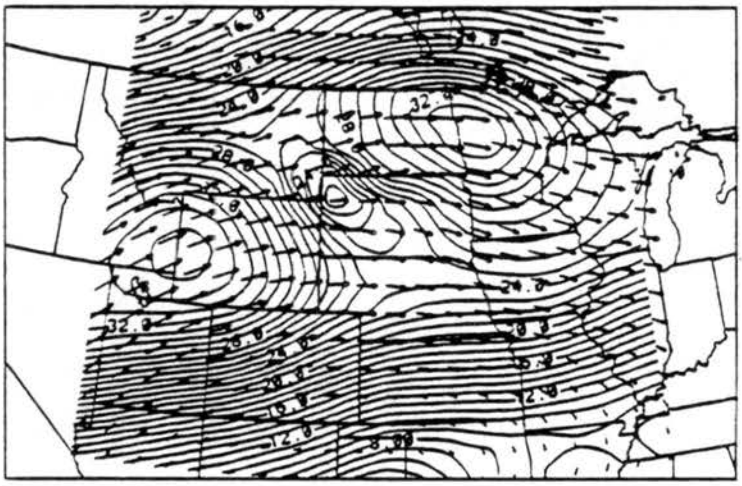

Figure 7.10: Continued.

E.

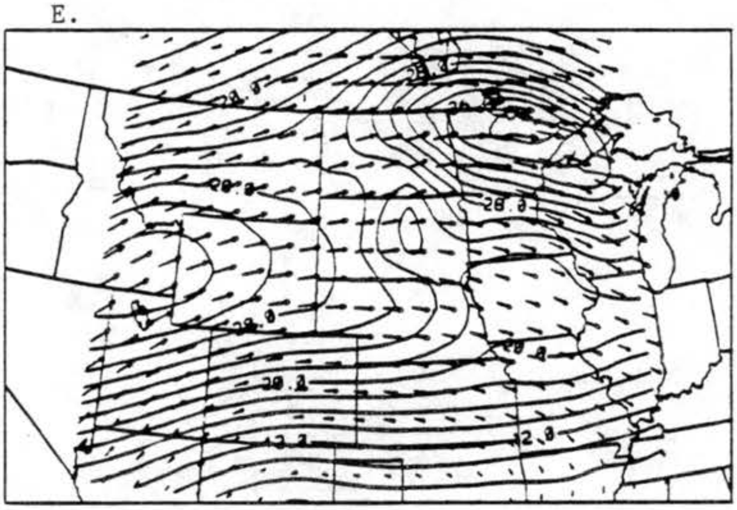

Figure 7.10: Continued.

A.

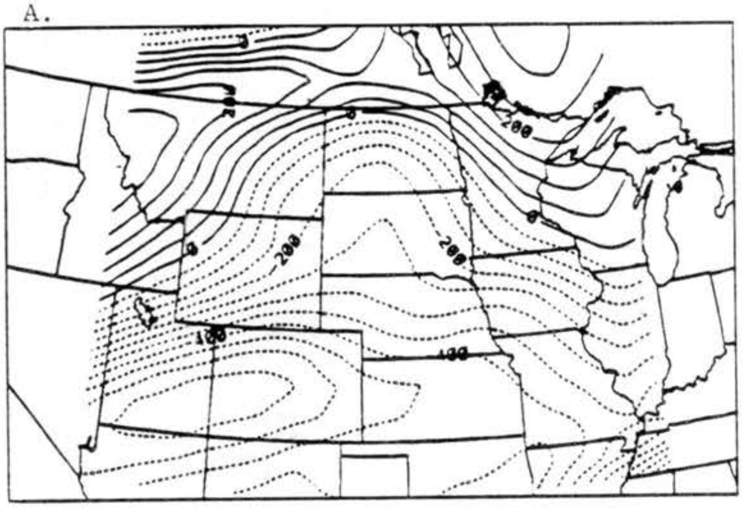

B.

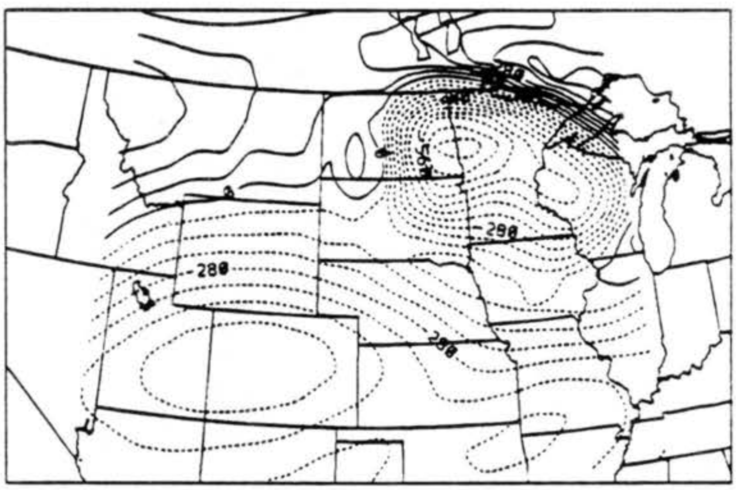

Figure 7.11: Relative vorticity function field at 9.96 km above sea level from coarse resolution control run. a) 3 Aug 0000 UTC, b) 3 Aug 1200 UTC.

A.

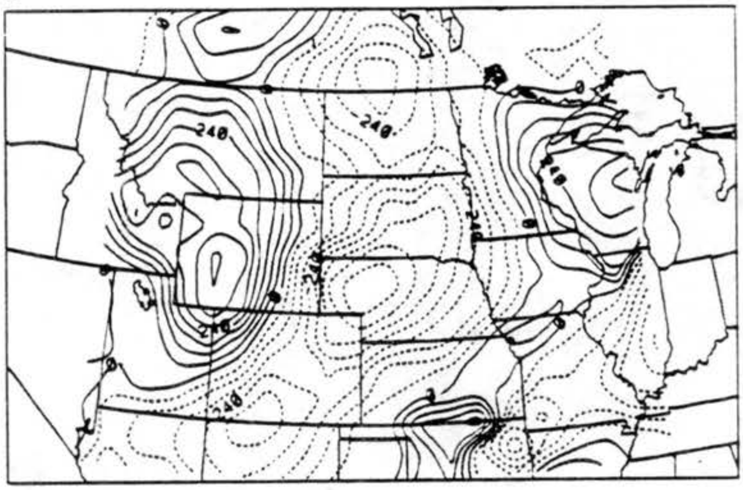

B.

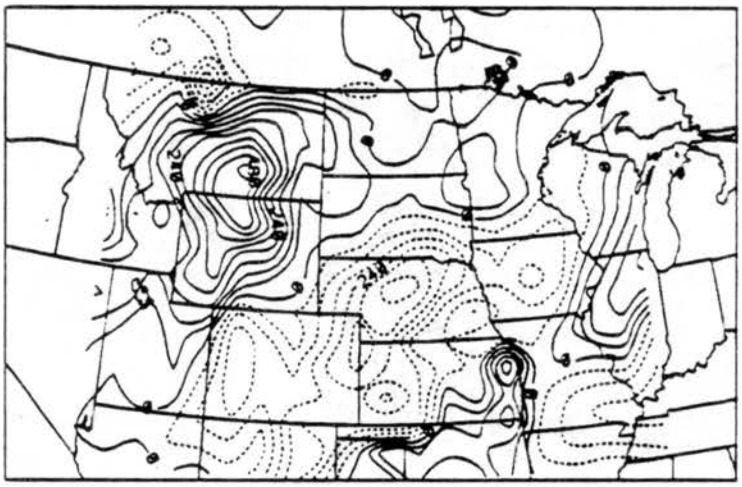

Figure 7.12: Vertical velocity field at 9.96 km above sea level from coarse resolution control run. a) 2 Aug 1800 UTC, b) 3 Aug 0000 UTC, c) 3 Aug 0600 UTC, d) 3 Aug 1200 UTC.

C.

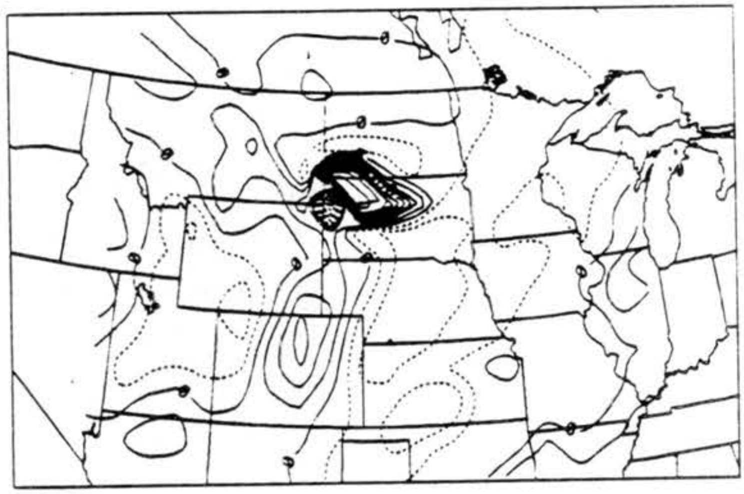

D.

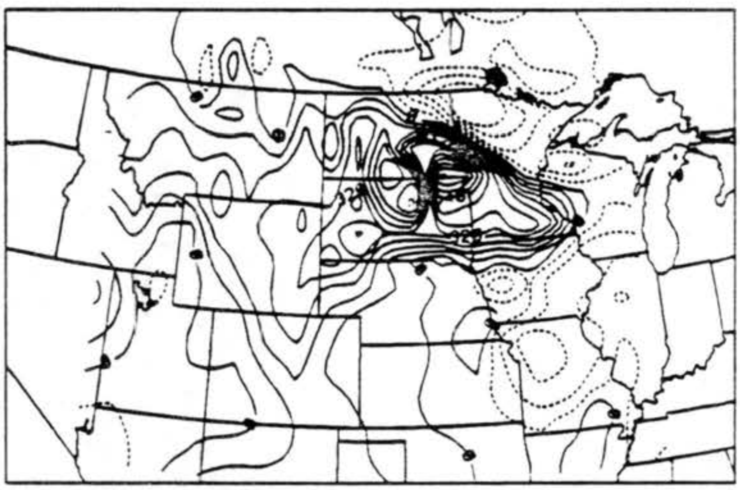

Figure 7.12: Continued.

A.

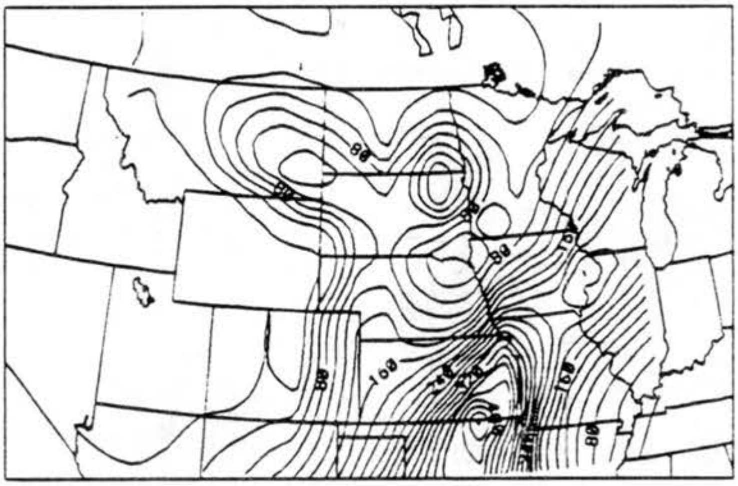

B.

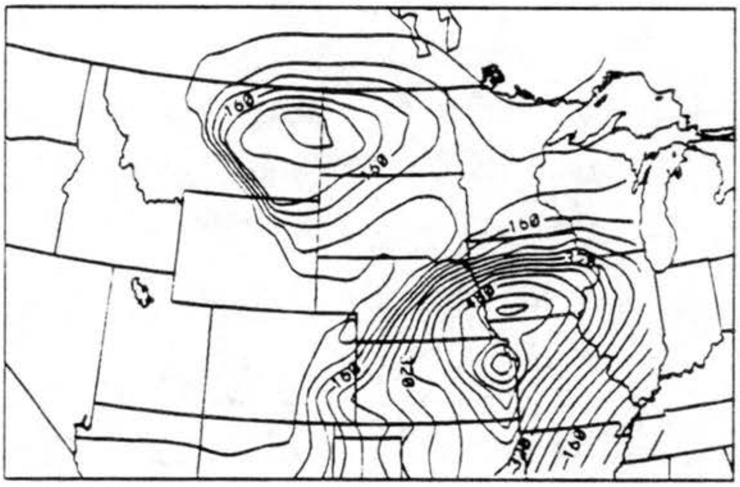

Figure 7.13: Total water mixing ratio field at 5.16 km above sea level from coarse resolution control run. a) 2 Aug 1800 UTC, b) 3 Aug 0000 UTC, c) 3 Aug 0600 UTC, d) 3 Aug 1200 UTC.

C.

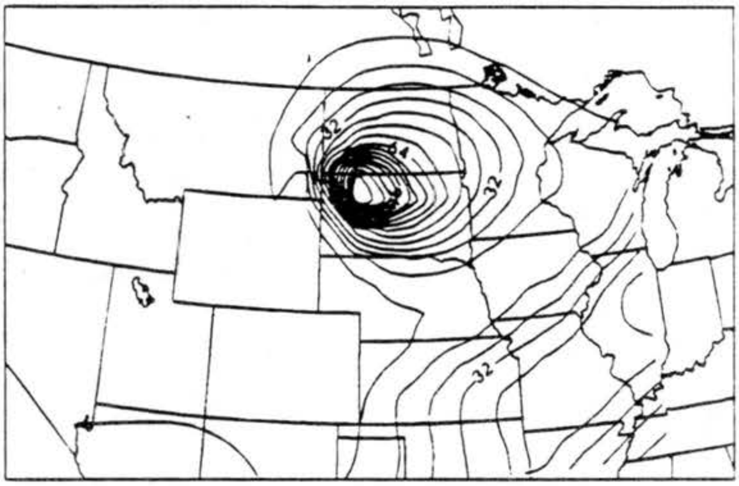

D.

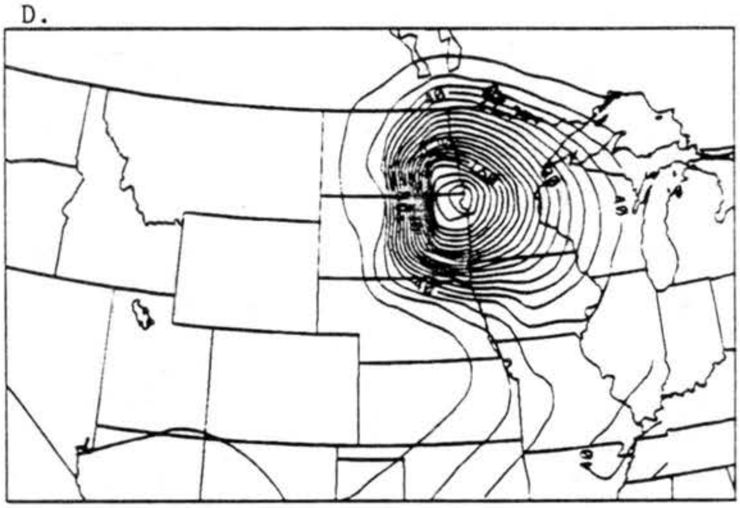

Figure 7.13: Continued.

and of the 2-3 August 1981 MCC in particular. Some of these features are the upper level outflow jet and the associated positive vorticity anomaly, mid-level inflow jet, circular mid- and upper-tropospheric moisture perturbations, re-orientation of the convective line, and, in general, an upscale development of the system from a sub-grid scale convective heat source to a meso-α-scale resolved circulation. Although there were many differences between the simulated and observed MCC, it is felt that conclusions based on the model results may be extended to the real atmosphere.

7.2.2 Variations in the horizontal diffusion coefficient

Horizontal diffusion in a larger scale model is commonly thought of as just a numerical filter on the fields since there is very little observational information or physical intuition on which to base a parameterization. The filter is used as a way to reduce the small wavelength features in the field so as to reduce numerical aliasing and "noise" in the model fields. Since there is little physical information to use, the strength of the diffusion is usually adjusted so that the model fields are "smooth enough." This obviously is a very qualitative measure and could vary from individual to individual. The following experiments have adjusted the strength of the horizontal diffusion to determine its effect on the simulation of the CCOPE MCC.

The horizontal diffusion coefficient for the model was defined as:

$$K_m = \frac{0.25}{\sqrt{2}} l^2 \sqrt{(D^2)}$$

$$K_h = 3K_m$$

where K_m is the exchange coefficient for momentum, K_h is the coefficient for heat and moisture, and D is the deformation. The turbulence scale length, l, is taken as $\sqrt{\Delta x^2 + \Delta y^2}$. For the horizontal exchange coefficients, only the horizontal components of deformation are used since vertical shear may have little to do with sub-grid scale processes on the meso-α-scale resolutions considered in this research.

This value is then checked against a minimum value to ensure that there is a background amount of diffusion to ensure "enough" smoothing for short wavelength features produced by numerical aliasing, etc. Since the horizontal deformation used in the formulation for K_m is usually small on a 110 km grid, the minimum value was used for virtually the entire simulation. The control simulation had the value of K_h/K_m set to 3 similar to the vertical diffusion formulation while the minimum value for K_m was $1.66 \times 10^{-5} l^2$ which corresponds to a value of the stability parameter for a second order diffusion scheme, $(K\Delta t/\Delta x^2)$, of about 0.002 (about 0.8% of the maximum damping value of .25). Two other simulations were run in which the value of K_h/K_m was set to 1. The minimum values for K_m were $2.5 \times 10^{-5} l^2$ in the weaker diffusion run and twice that value $(5.0 \times 10^{-5} l^2)$ in a stronger diffusion run which corresponds to a value of the stability parameter $(K\Delta t/\Delta x^2)$ of about 0.003 and 0.006, respectively (about 1/4 of 1% and 1/2 of 1% of the maximum damping value) which are still relatively small values for diffusion. These values are summarized in Table 7.1.

Table 7.1: Horizontal diffusion coefficients for sensitivity runs.

Run	K_m	$\frac{K_m \Delta t}{\Delta x^2}$	K_H	$\frac{K_H \Delta t}{\Delta x^2}$
Control	200,860	0.002	602,580	0.006
Weaker	301,290	0.003	301,290	0.003
Stronger	602,580	0.006	602,580	0.006

k_m and k_H are computed for a 110 km horizontal grid spacing.

Focusing first on the simulation with the weaker horizontal diffusion for the thermodynamic quantities (θ_{il} and total water), Figure 7.14a-b shows the convective parameterization precipitation rate at 0000 UTC. The Montana convective region was similar, however, major differences appeared in the southeastern Colorado region where the weaker diffusion run had a much stronger system. By 0600 UTC, the sensitivity run had a more focused, shorter wavelength system which is consistent with less filtering although the magnitude of the precipitation was less at this time. Again consistent with less diffusion, the mid-level vertical motion (Figure 7.15) is about twice as strong as the control run, as

A.

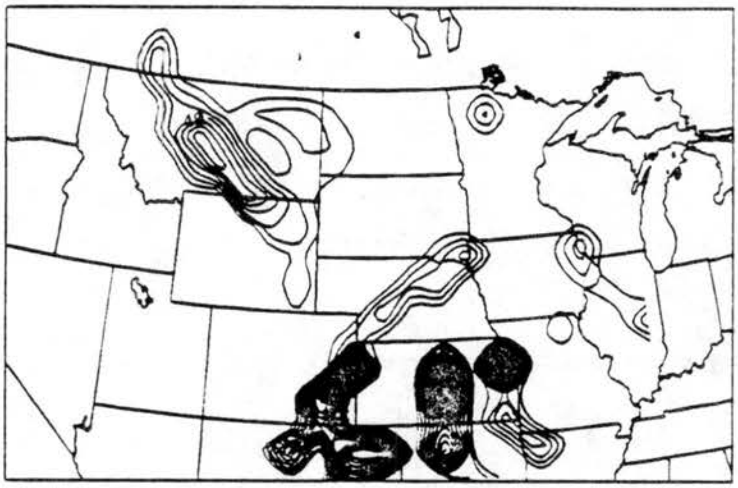

B.

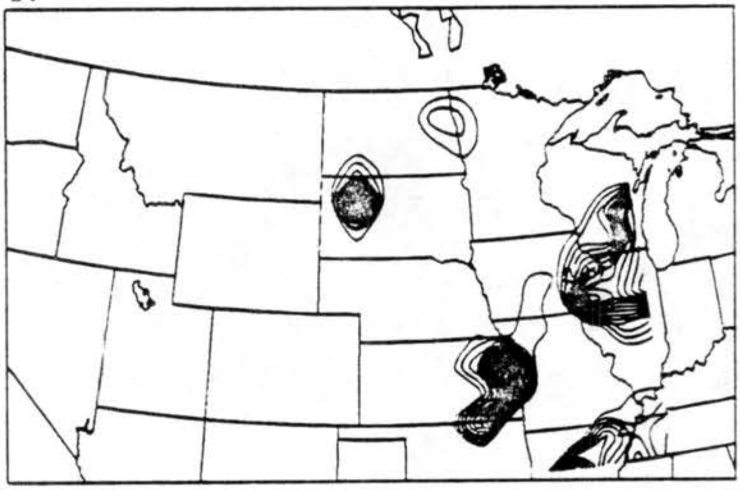

Figure 7.14: Convective parameterization precipitation rate from coarse resolution weaker diffusion run. a) 3 Aug 0000 UTC, b) 3 Aug 0600 UTC.

is the mid-level positive vorticity perturbation (Figure 7.16) associated with the system. The upper level vertical motion (Figure 7.17) is also much stronger and more focused, with the center starting to lag the control run. The total water field (Figure 7.18) is much greater also in the upper levels and also shows evidence of the slower propagation of the system. By 1200 UTC, the convective precipitation rate field (Figure 7.19) is similar between the control and sensitivity runs with the sensitivity run being somewhat stronger. The mid-level vertical motion (Figure 7.20) is significantly different, with the weaker diffusion run still lagging the control run and more focused and stronger. In addition, the center is lagging the convection as the system is becoming disorganized. The total water field (Figure 7.21) is again consistent with less smoothing as the sensitivity run's field is much stronger and focused. Mid-level vorticity in the sensitivity run (Figure 7.22) shows a much greater "spinup" of the system, with a large cyclonic perturbation. In the upper levels, the model fields are again substantially different between the two runs. The resolved mesoscale circulation is propagating much slower than the control run. The vertical motion (Figure 7.23) and total water (Figure 7.24) fields show that the center of the circulation is displaced to the northwest in the sensitivity run. Although the center of the negative vorticity perturbation (Figure 7.25) associated with the upper level outflow jet are located similarly between the two runs, the magnitude of the perturbation in the sensitivity run is about twice that of the control run.

The results of this simulation, in one sense, are intuitively expected. With less diffusion on the main forcing mechanism (convective heating), the circulation in general is more focused and stronger. However, the system did not move as fast in the sensitivity run.

The results of the second sensitivity run testing the horizontal diffusion are also somewhat intuitive. This run had the same minimum diffusion coefficient on the thermodynamic variables as the control run but the minimum coefficient for the u and v wind components was a factor of three higher. The resolved circulation of the MCC was more damped than the control run. Figure 7.26a-b shows the convective parameterization precipitation rate at 0200 UTC and 0600 UTC in the smoother run. At 0200 UTC, there

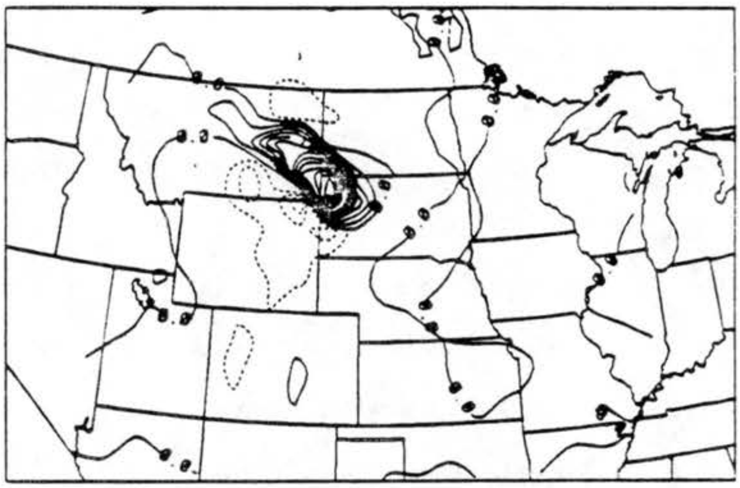

Figure 7.15: Vertical velocity field at 5.16 km above sea level from coarse resolution weaker diffusion run at 3 Aug 0600 UTC.

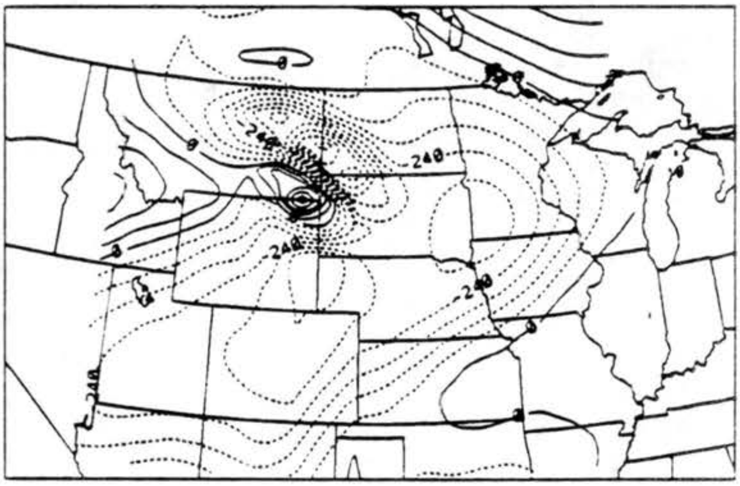

Figure 7.16: Relative vorticity field at 5.16 km above sea level from coarse resolution weaker diffusion run at 3 Aug 0600 UTC.

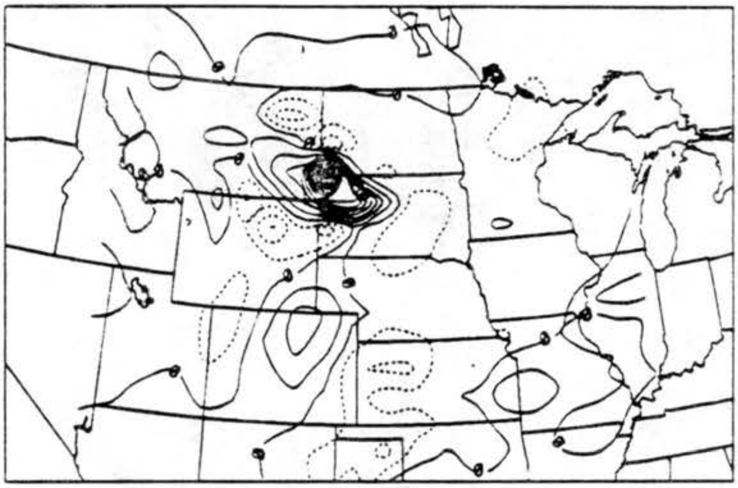

Figure 7.17: Vertical velocity field at 9.96 km above sea level from coarse resolution weaker diffusion run at 3 Aug 0600 UTC.

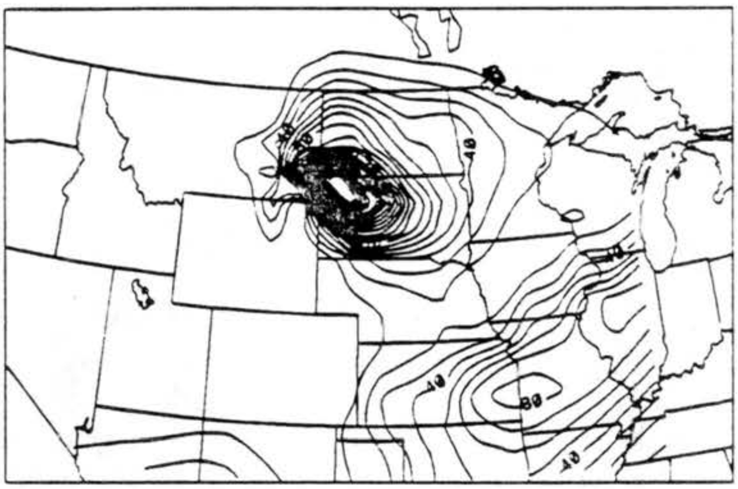

Figure 7.18: Total water mixing ratio field at 9.96 km above sea level from coarse resolution weaker diffusion run at 3 Aug 0600 UTC.

Figure 7.19: Convective parameterization precipitation rate from coarse resolution weaker diffusion run at 3 Aug 1200 UTC.

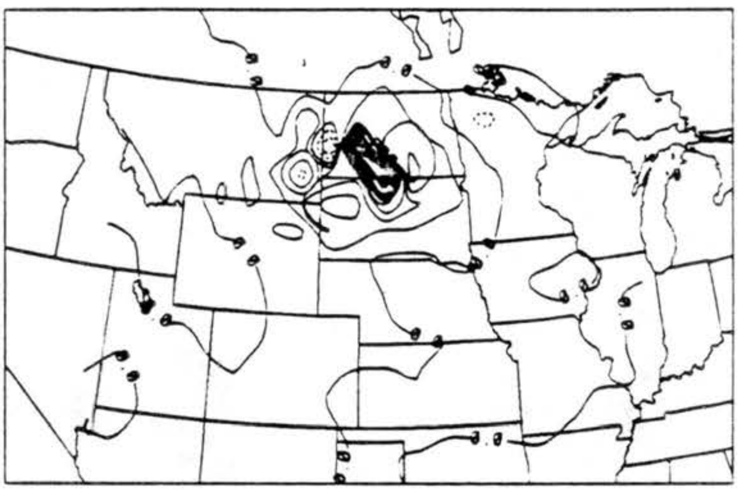

Figure 7.20: Vertical velocity field at 5.16 km above sea level from coarse resolution weaker diffusion run at 3 Aug 1200 UTC.

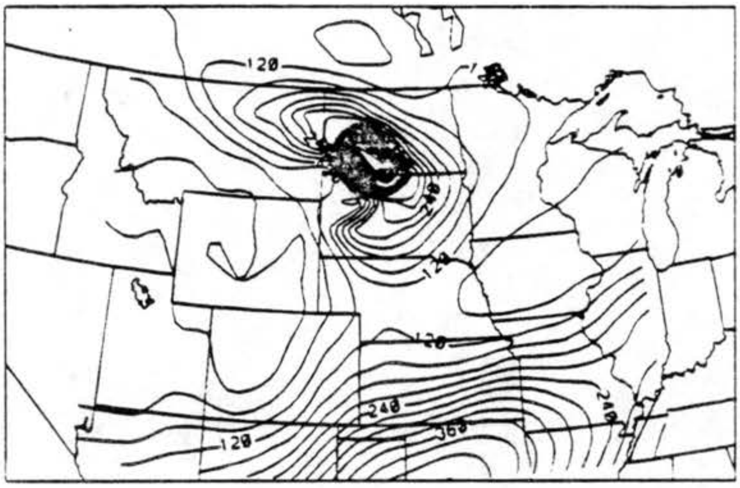

Figure 7.21: Total water mixing ratio field at 9.96 km above sea level from coarse resolution weaker diffusion run at 3 Aug 1200 UTC.

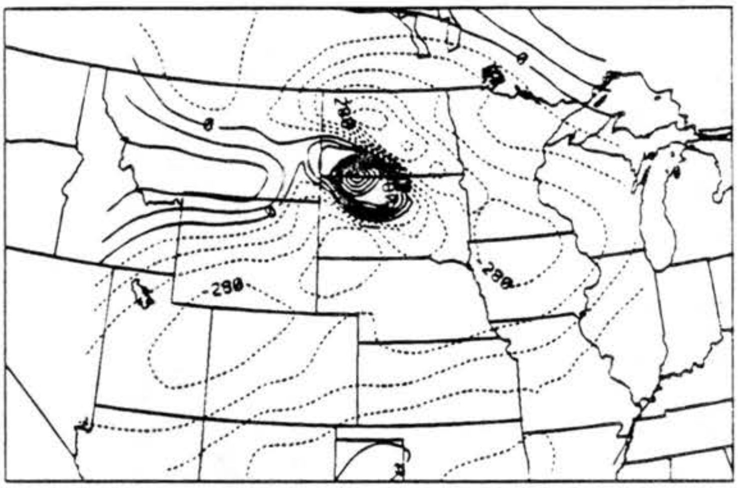

Figure 7.22: Relative vorticity field at 5.16 km above sea level from coarse resolution weaker diffusion run at 3 Aug 1200 UTC.

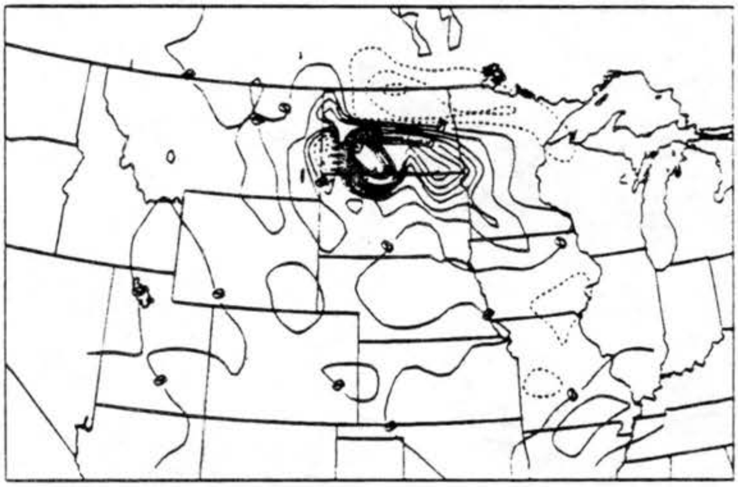

Figure 7.23: Vertical velocity field at 9.96 km above sea level from coarse resolution weaker diffusion run at 3 Aug 1200 UTC.

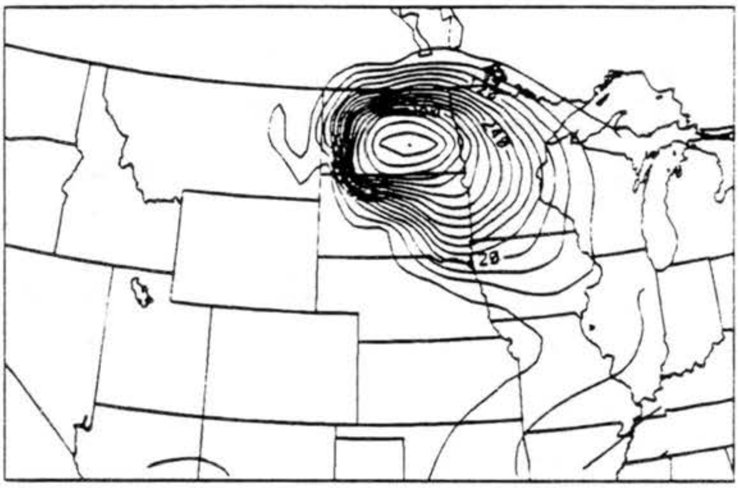

Figure 7.24: Total water mixing ratio field at 9.96 km above sea level from coarse resolution weaker diffusion run at 3 Aug 1200 UTC.

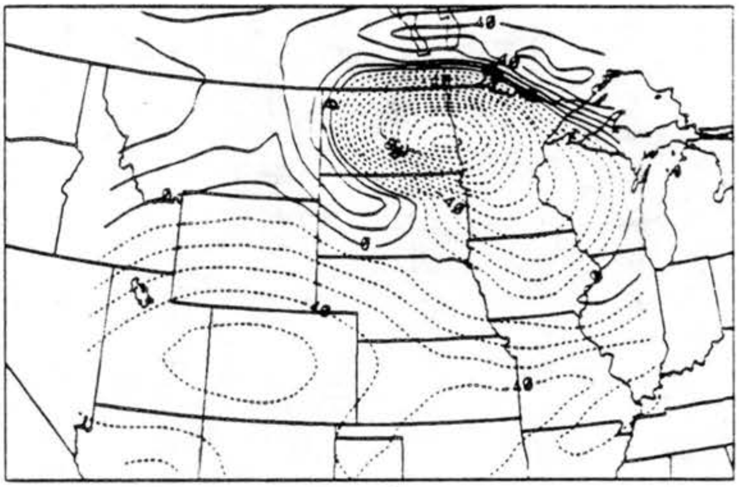

Figure 7.25: Relative vorticity field at 9.96 km above sea level from coarse resolution weaker diffusion run at 3 Aug 1200 UTC.

A.

B.

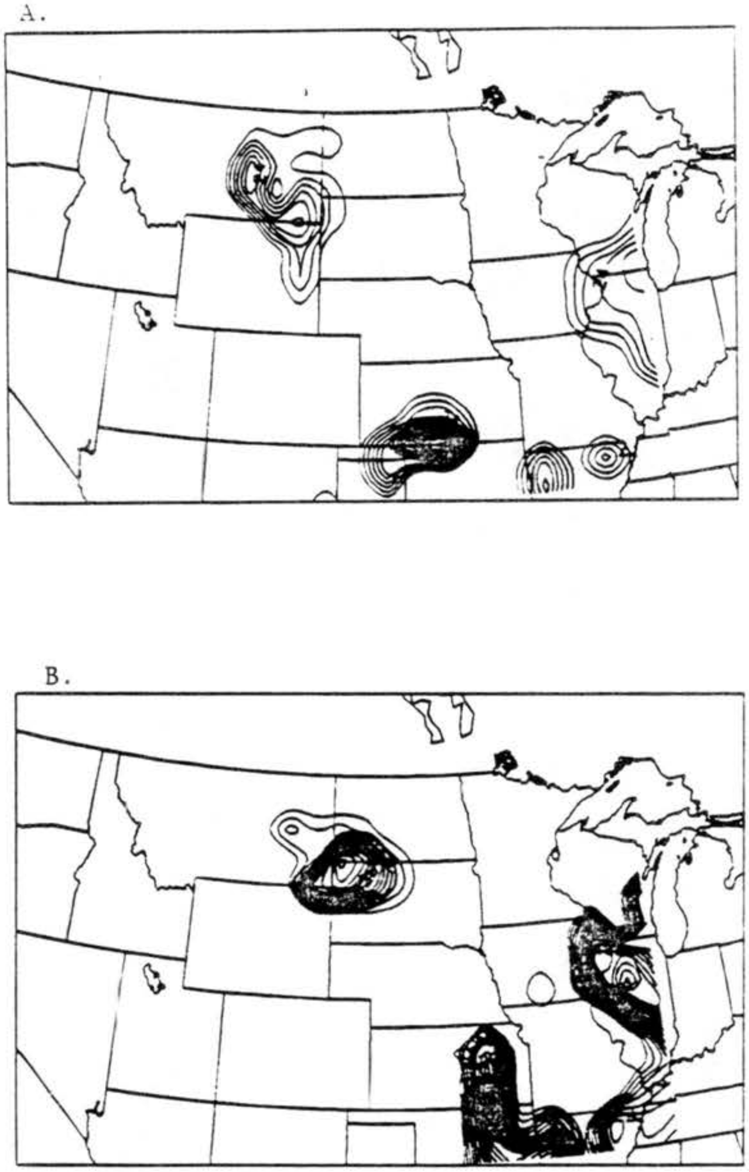

Figure 7.26: Convective parameterization precipitation rate from coarse resolution stronger diffusion run. a) 3 Aug 0200 UTC, b) 3 Aug 0600 UTC.

was significantly less precipitation falling in southern Montana while at 0600 UTC, there was still less and the convection in the smoother run began to lag the control run a bit. The 0600 UTC perturbation pressure fields (Figure 7.27) are very similar between the two runs, however. Total water fields in both the mid (Figure 7.28) and upper (Figure 7.29) levels begin to show this lag also along with a reduction in magnitude. Vertical motion (Figure 7.30) in the upper level is very disorganized at 0600 UTC, signifying that the system in the sensitivity run is not as deep. By 1200 UTC, these differences become more pronounced. The lag has become larger and can be seen in the convective precipitation rate (Figure 7.31) and mid-level vertical motion (Figure 7.32). The relative vorticity field (Figure 7.33) was significantly less perturbed in the mid-levels. In the upper levels, the weaker vertical motion field (Figure 7.34) was a different shape and located toward the southwest. The outflow jet strength (Figure 7.35), as expected, was also affected with the magnitude 4 m/s less than the control run.

These sensitivity simulations show that the strength and location of the convective system were altered significantly by relatively small changes in the magnitude of the horizontal diffusion, just one of the parameterizations present in numerical models. This points out that a need exists for further research into these parameterizations for the extension of the mesoscale numerical models into operational forecasting.

Another fairly obvious conclusion can be drawn from these simulations also. If the simulation results are strongly sensitive to the diffusion parameterization, then the model resolution is probably not adequate to simulate the atmospheric feature in question. However, in operational settings and even most of the time in research settings, compromises must be made between available computer resources and the desired "ideal" model configuration. For the current research, the CCOPE MCC simulation will be rerun with a 2.5 times increase in resolution (about a 44 km grid spacing) in the next chapter. Although this is still a compromise resolution, it should improve the integrity of the simulation.

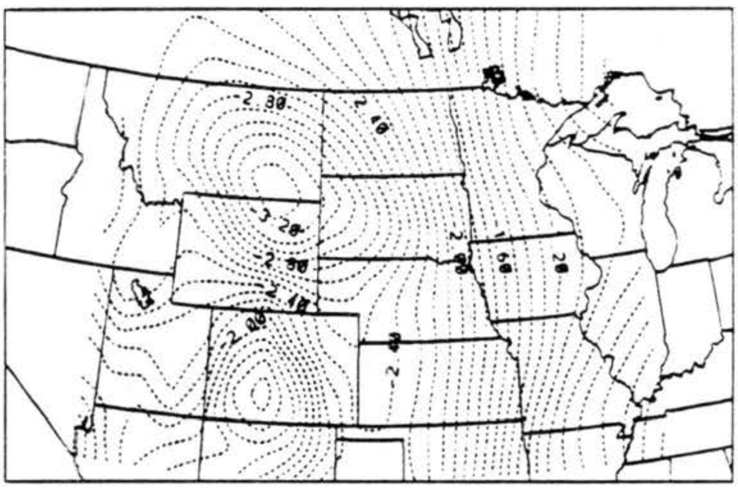

Figure 7.27: Perturbation Exner function on terrain following coordinate surface 150 m above ground from coarse resolution stronger diffusion run at 3 Aug 0600 UTC.

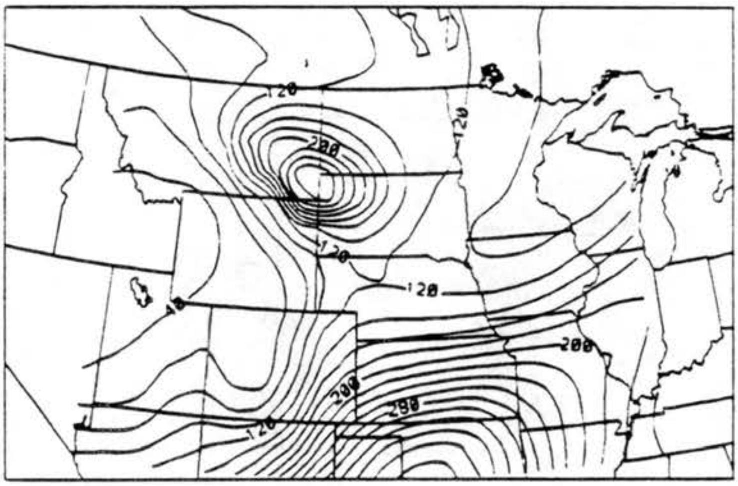

Figure 7.28: Total water mixing ratio field at 5.16 km above sea level from coarse resolution stronger diffusion run at 3 Aug 0600 UTC.

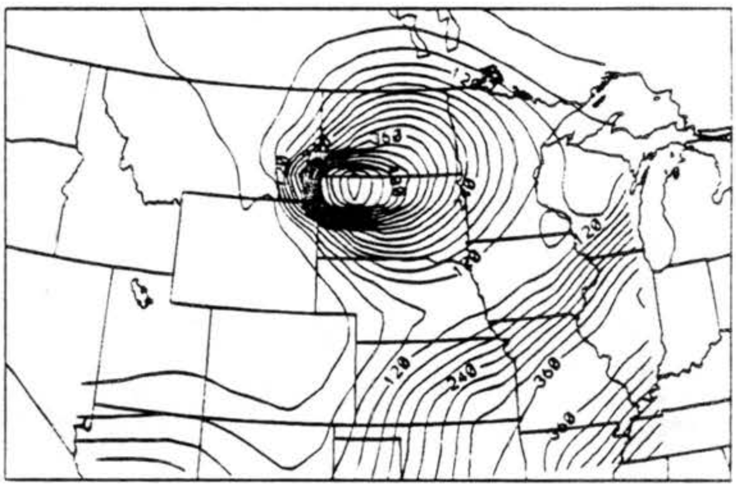

Figure 7.29: Total water mixing ratio field at 9.96 km above sea level from coarse resolution stronger diffusion run at 3 Aug 0600 UTC.

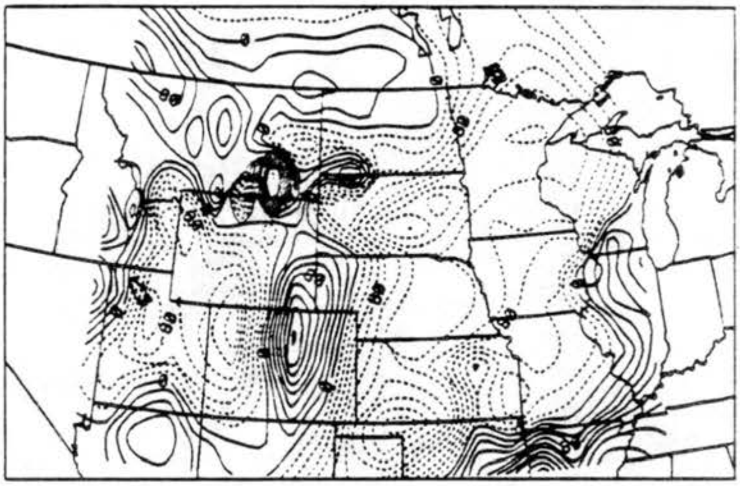

Figure 7.30: Vertical velocity field at 9.96 km above sea level from coarse resolution stronger diffusion run at 3 Aug 0600 UTC.

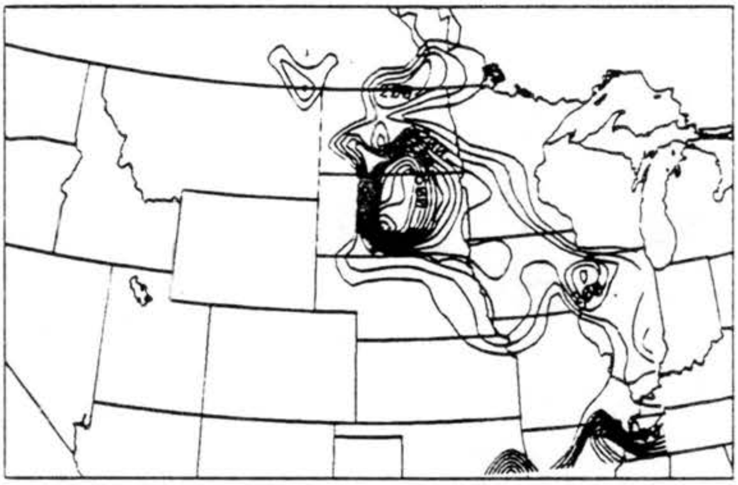

Figure 7.31: Convective parameterization precipitation rate from coarse resolution stronger diffusion run at 3 Aug 1200 UTC.

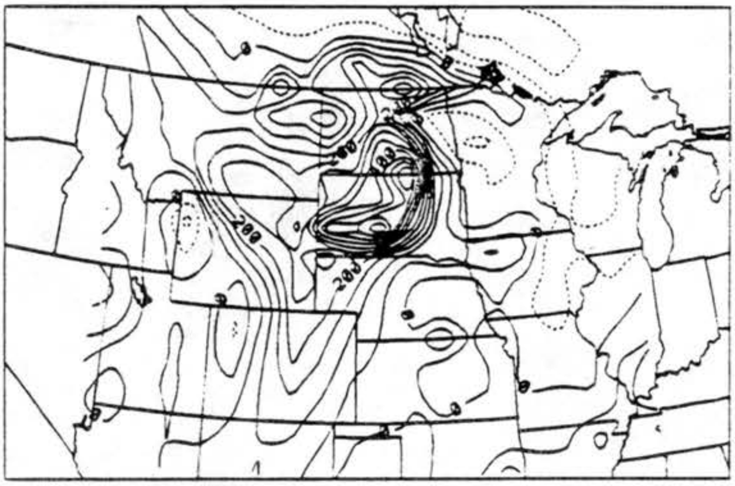

Figure 7.32: Vertical velocity field at 5.16 km above sea level from coarse resolution stronger diffusion run at 3 Aug 1200 UTC.

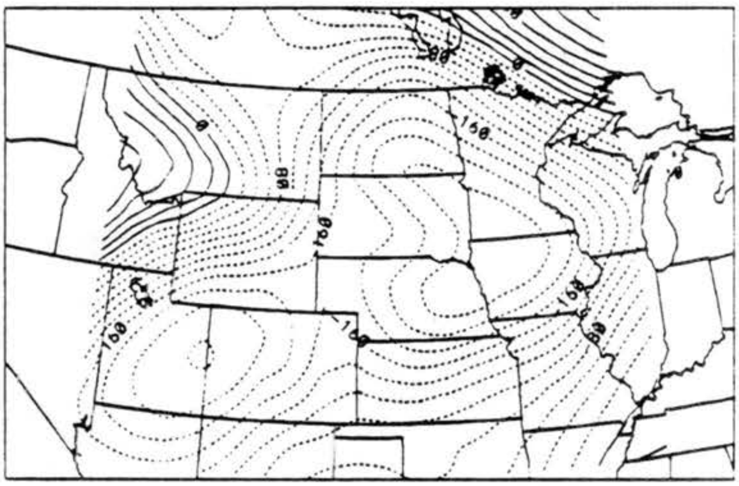

Figure 7.33: Relative vorticity field at 5.16 km above sea level from coarse resolution stronger diffusion run at 3 Aug 1200 UTC.

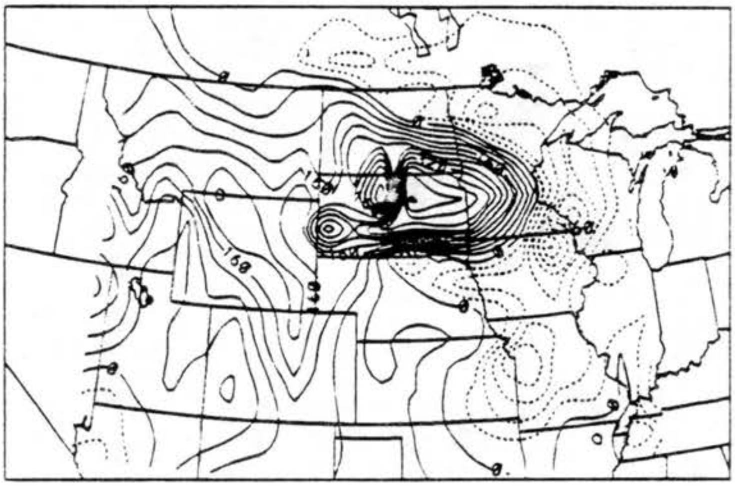

Figure 7.34: Vertical velocity field at 9.96 km above sea level from coarse resolution stronger diffusion run at 3 Aug 1200 UTC.

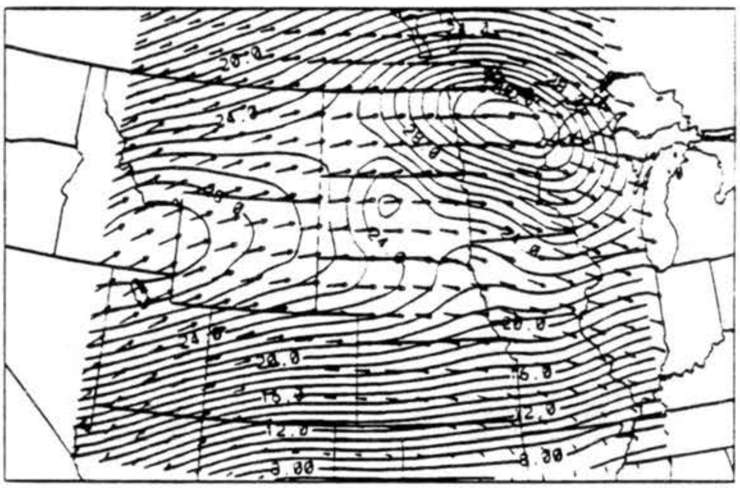

Figure 7.35: Isotachs and velocity vectors at 9.96 km above sea level from coarse resolution stronger diffusion run at 3 Aug 1200 UTC.

7.2.3 Variation in the soil moisture initialization

In the control run, the soil moisture content was computed by assuming the relative humidity in the top surface soil layer was equal to the relative humidity at the lowest atmospheric level. Because the functional form for recovering the soil moisture content from the relative humidity has a steep slope over a small range, the surface soil moisture was limited between a factor of 0.4 and 0.9 of the saturation value at the surface. Figure 7.36 shows the relationship between the moisture content and relative humidity for 4 different soil textural classes. The surface value was then increased to the lesser of twice the value or saturation to determine the value at a depth of 0.5 m. A run was made to test the sensitivity of these limits on the meso-α scale behavior of the MCC. In this run, the surface soil moisture content was limited between a factor of 0.7 and 0.9 of the saturation value. This produced a wetter than realistic soil especially over the mountain areas and high plains; this could lead to less of a "dry line" in the central plains and affect the behavior of the low level jet, thus changing the timing and placement of the MCC.

The behavior of the convective system was very different than the control run in this simulation. The convection started much earlier in the day (Figure 7.37a) at 2000 UTC and, by 0000 UTC (Figure 7.37b), was located much farther north than in the control run. Throughout the remainder of the simulation, the strongest area of convective precipitation remained in the Montana and Canadian Rockies (Figures 7.37c-d). The low level moisture field in this run at 0000 UTC is shown in Figure 7.38. Whereas the low level moisture over Montana in the control run was about 7 g/kg, this run had well over 14 g/kg. This increase in available moisture combined with the early forcing over the northern Rockies which was even evident in the control run, led to the convection forming when and where it did.

Further, the dynamics of the convective system was much different than the control run. The system did not become as "focused." Where the control run developed a rather circular moisture pattern in mid and upper levels, the pattern in this run (Figures 7.39 and 7.40) was more elongated downstream as the moisture was advected with the upper level flow. Moreover, the upper level moisture amount was much less due to the lack

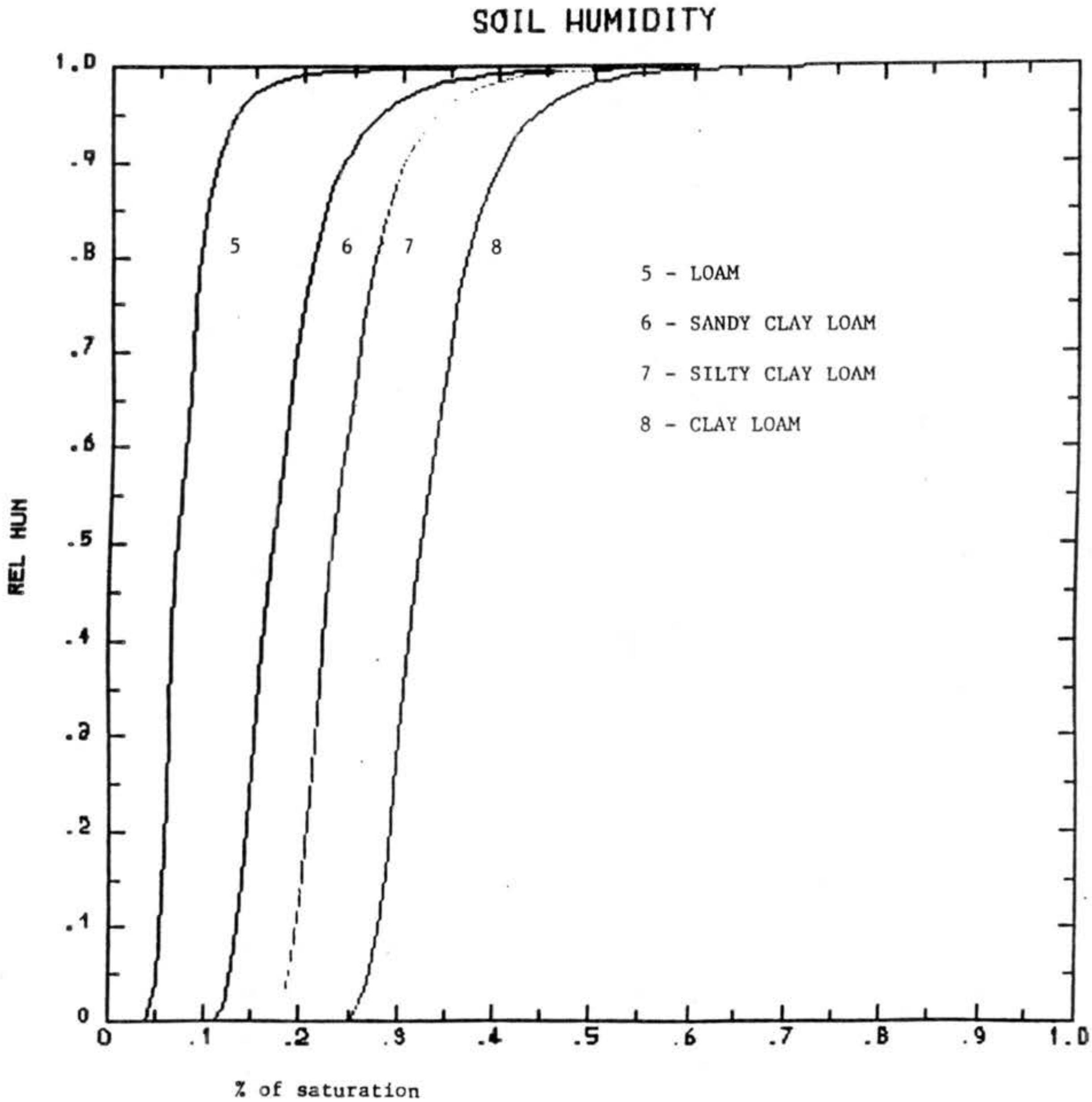

Figure 7.36: Relationship between soil relative humidity and moisture content expressed as percentage of the saturation value for the soil textural classes of loam (curve 5), sandy clay loam (curve 6), silty clay loam (curve 7), and clay loam (curve 8).

A.

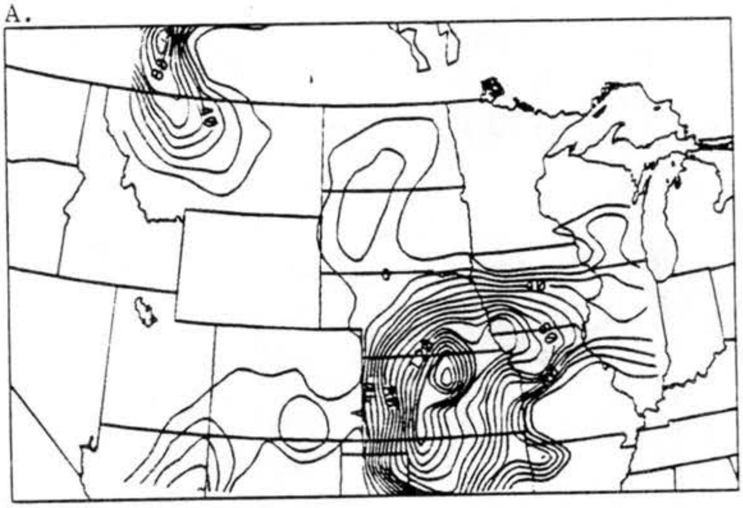

B.

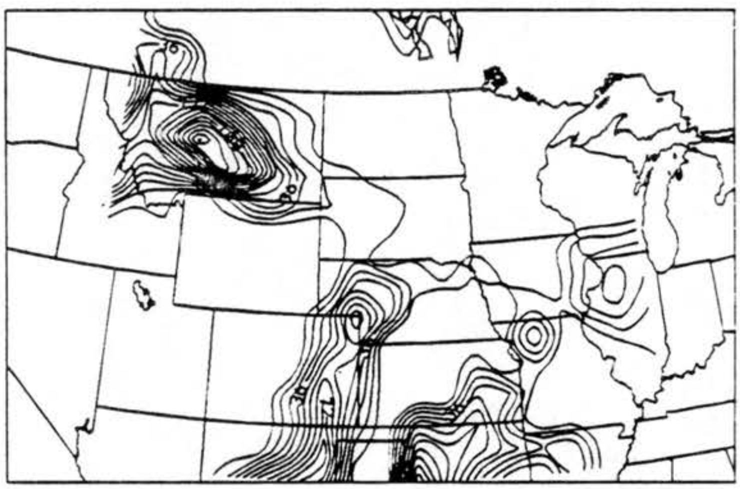

Figure 7.37: Convective parameterization precipitation rate from coarse resolution moist soil run. a) 2 Aug 2000 UTC, b) 3 Aug 0000 UTC, c) 3 Aug 0600 UTC, d) 3 Aug 1000 UTC.

C.

D.

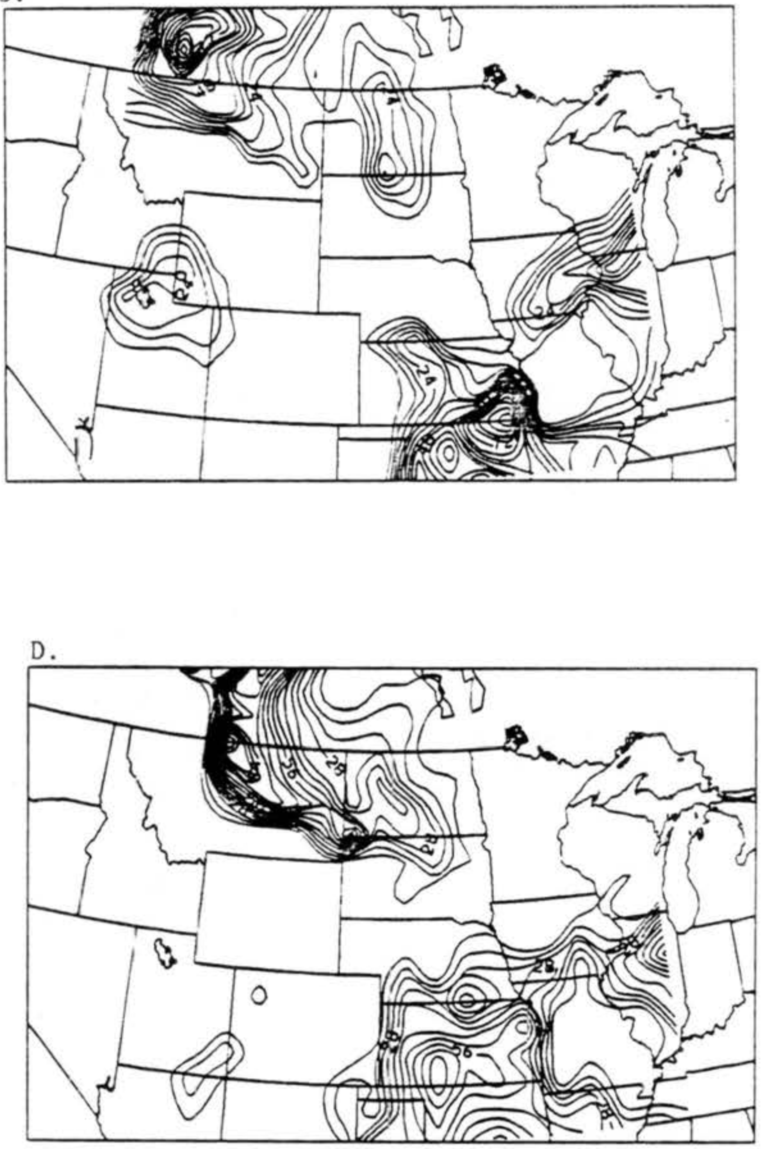

Figure 7.37: Continued.

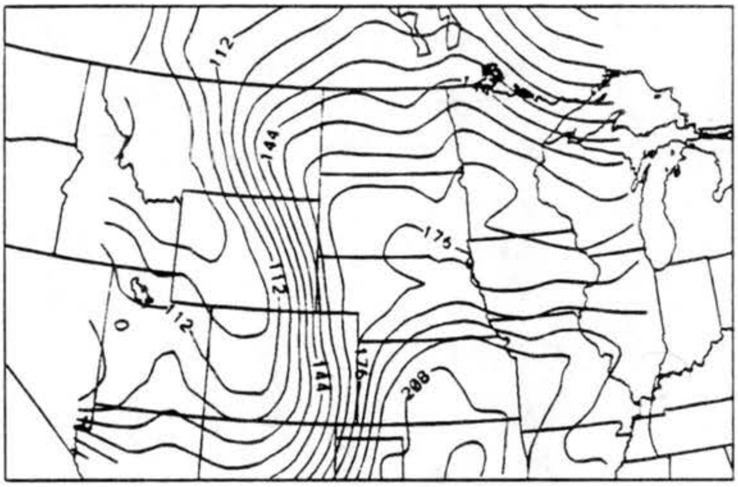

Figure 7.38: Total water mixing ratio field on terrain following coordinate surface 150 m above ground from coarse resolution moist soil run at 3 Aug 0000 UTC.

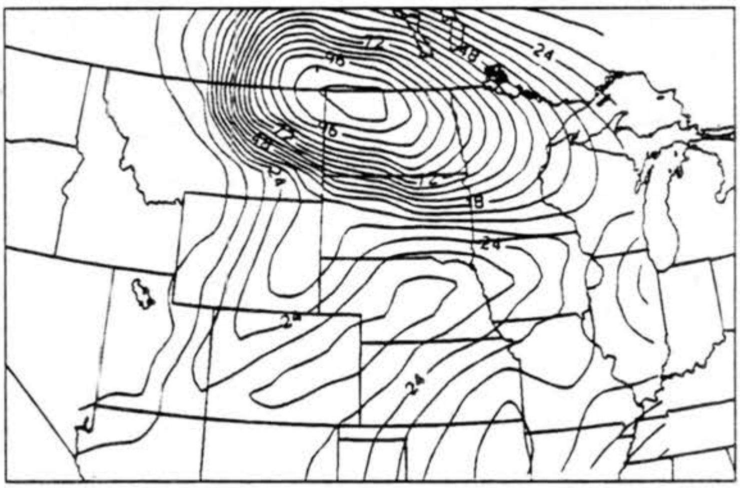

Figure 7.39: Total water mixing ratio field at 9.96 km above sea level from coarse resolution moist soil run at 3 Aug 1000 UTC.

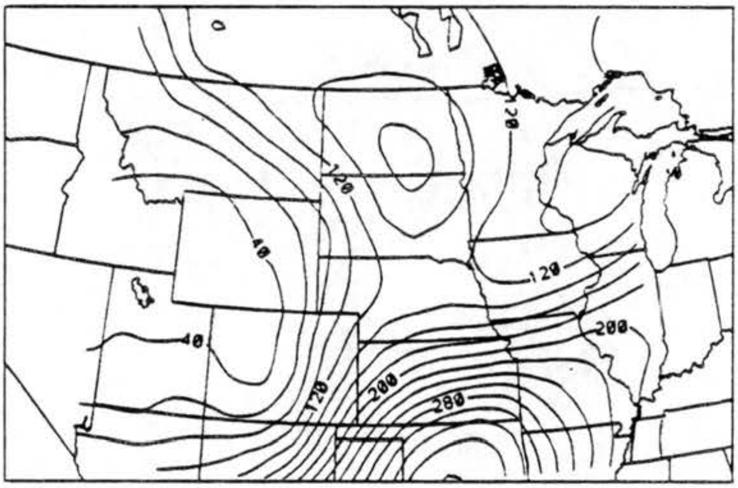

Figure 7.40: Total water mixing ratio field at 5.16 km above sea level from coarse resolution moist soil run at 3 Aug 1000 UTC.

of resolvable scale support. The system did not "spin up" as the control run did. This is evidenced by the resolved vertical motion fields (Figure 7.41 and Figure 7.42). The maximum upward motion at 1000 UTC in the control run at the 5.16 km level was 19 cm/s where the moist soil run was slightly over 5 cm/s. The upper level relative vorticity field at 1000 UTC (Figure 7.43) shows that the simulation did not develop a strong anticyclonic outflow jet as the control simulation did.

Although the soil in this sensitivity run was unrealistically wet, it does point out the importance of the soil moisture in affecting even the larger meso-α scales of motion. It is expected that if a simulation were made with a dry enough soil, the convective system would not have formed at all. Especially disconcerting is the fact that soil moisture contents are not measured or reported routinely. Even if these data were available, the parameterization of this process in current "state of the art" numerical models is lacking due mainly from resolution problems. The hydrologic cycle occurs on various spatial scales, from large scale evaporative processes and stratiform precipitation sources to small scale stream runoff and convective rainshafts, so that completely accurate inclusion of the cycle in forecast models of the foreseeable future will probably not be possible.

7.3 Summary

This chapter has been intended to show two main topics:

- that the numerical model developed as part of this research has adequately simulated an MCC so as to be able to attempt to draw some conclusions about the real atmosphere based on its results;

- that there still exists many uncertainties in the numerical modelling of these and other weather systems related to not only problems in adequately specifying the initial and boundary conditions, but also in the many assumptions required in the formulation of the model itself. These uncertainties greatly affect a model's predictability and its ability to be extended to an operational setting.

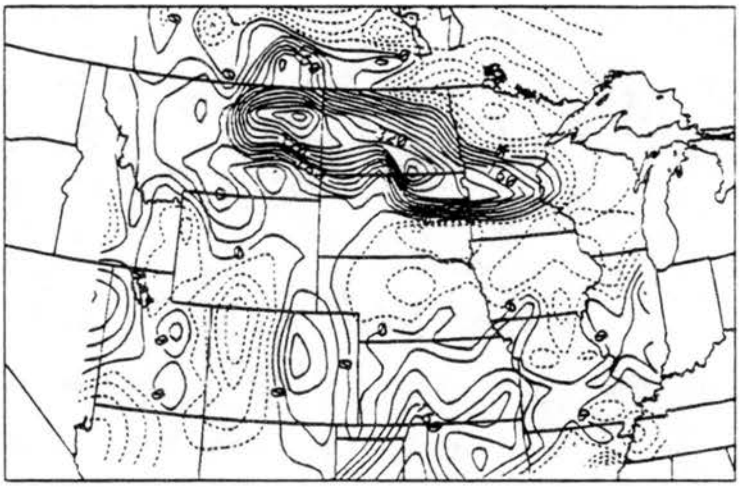

Figure 7.41: Vertical motion field at 9.96 km above sea level from coarse resolution moist soil run at 3 Aug 1000 UTC.

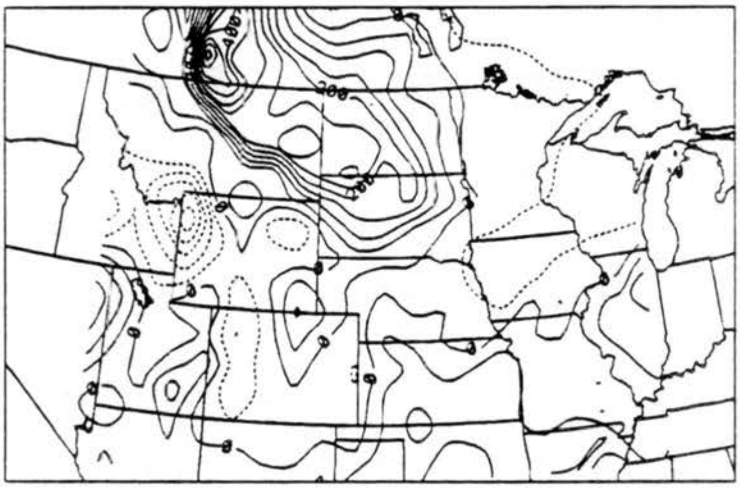

Figure 7.42: Vertical motion field at 5.16 km above sea level from coarse resolution moist soil run at 3 Aug 1000 UTC.

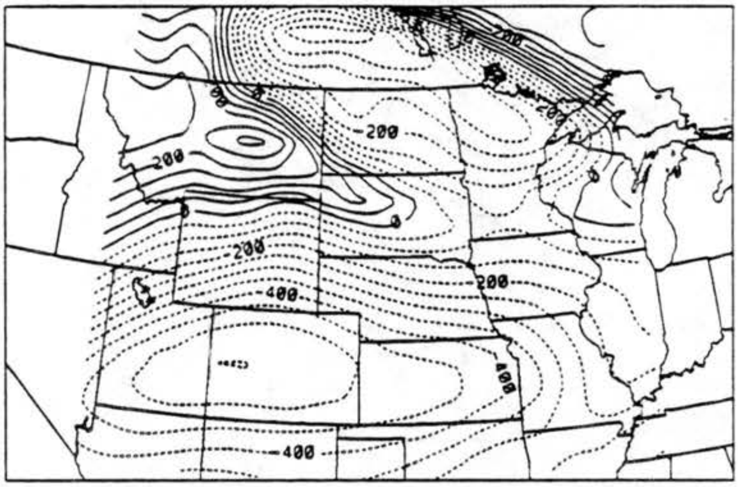

Figure 7.43: Relative vorticity field at 9.96 km above sea level from coarse resolution moist soil run at 3 Aug 1000 UTC.

Chapter 8

HIGHER RESOLUTION SIMULATIONS

The previous chapter presented simulations of the CCOPE MCC which used a rather coarse, 110 km grid spacing which can only crudely resolve even the meso-α scale of the circulation. In order to refine the meso-α circulations, further simulations using approximately a 45 km horizontal grid resolution were run. Additional sensitivity experiments were run with this resolution simulation to attempt to isolate the important forcing mechanisms of the convective system.

8.1 Description of higher resolution model simulations

The grid structure for the higher resolution simulations was configured with the following characteristics. In the east-west direction, there were 82 grid points with a 0.57° spacing with the westernmost point at 127° west longitude. In the north-south direction, 85 grid points with a 0.40° spacing starting at 26° north latitude were used. The vertical grid structure was the same as in the coarser resolution run. There were 27 levels with a stretched grid of 300 m resolution near the ground. Each level was stretched at a factor of 1.1 from the level below up to a maximum of an 800 m grid spacing.

All other aspects of the model physics were the same as the coarse resolution control simulation including no explicit resolved precipitation. The only minor changes to the model were: 1) the convective parameterization tendencies were updated every 20 minutes instead of every 30 minutes and, 2) the minimum horizontal diffusion coefficient was increased to $1.2 \times 10^{-4} l^2$ from $1.66 \times 10^{-5} l^2$. This value, as on the coarse grid, was chosen by trial and error to reduce short wavelength "noise" in the simulated fields.

8.2 Comparison with coarse resolution control run

This section will compare and contrast the simulation results between the coarse and fine resolution runs. Since the model physics are very similar, any differences can be attributed to just a few things. Along with the two changes to the model parameterizations mentioned above, two additional sources of differences are the change of resolution and the closer proximity of the lateral boundaries to the area of interest (which was necessitated from computer considerations). It is hypothesized that the latter had an insignificant effect and that any differences between the two simulations resulted from the increase in resolution.

Starting at 0000 UTC which was the time at which the severe convection in Montana was occurring, Figure 8.1 shows the vertical motion field at about 150 m above the ground. The pattern was very similar to the coarse resolution run with the high resolution run having a larger vertical motion (4.5 vs. 3.2 cms^{-1}) in south central Montana. The low level perturbation Exner function field (Figure 8.2) shows that the high resolution run had a slightly weaker low, but located similarly to the coarse run. The low level mixing ratio field (Figure 8.3) and the temperature field (Figure 8.4) were almost identical between the two simulations.

In the mid-levels (5.16 km ASL), the jet core was better resolved in the high resolution run (Figure 8.5) in northwest Wyoming bringing it closer to the area of active convection which led to the MCC development. The vertical motion field (Figure 8.6), as expected, shows more structure in the high resolution run.

The upper level (9.96 km ASL) isotachs and vertical motion field (Figures 8.7 and 8.8) show similar differences as the mid-level fields. The jet core is slightly stronger and located a bit closer to the convective region. The upward motion over Montana is actually weaker in the high resolution run and slightly farther east. This weaker upward motion at this level was consistent throughout the simulation. The resolved mesoscale circulation of the MCC did not extend quite as deep in the high resolution run. Possible reasons for the shallower system are 1) because of the higher resolution, a greater internal gravity wave response in the upper levels carried more heat away from the developing system and,

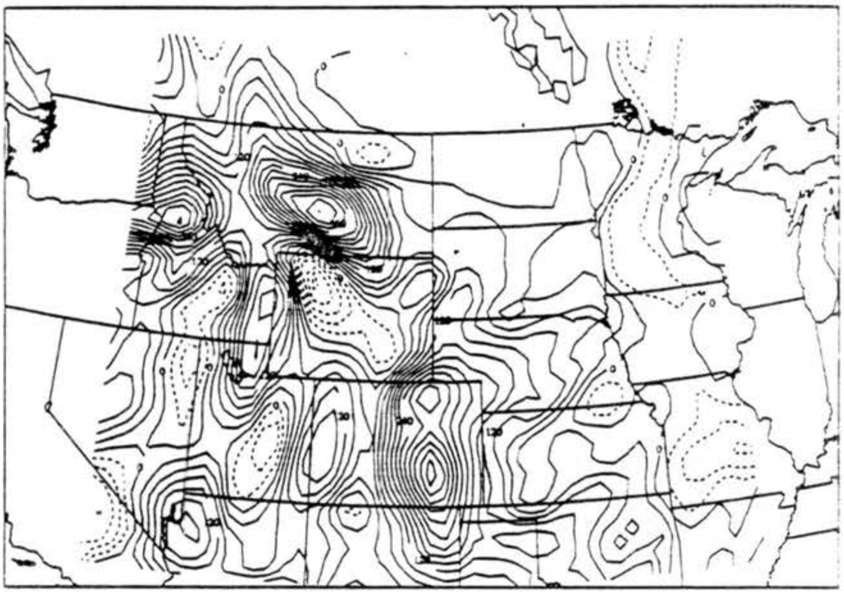

Figure 8.1: Vertical velocity field on terrain following coordinate surface 150 m above ground from higher resolution control run at 3 Aug 0000 UTC.

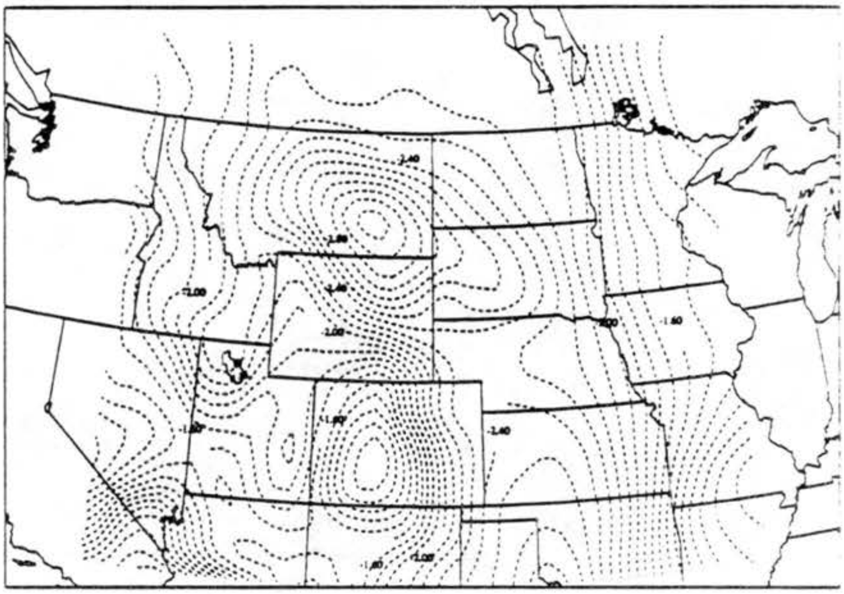

Figure 8.2: Perturbation Exner function on terrain following coordinate surface 150 m above ground from higher resolution control run at 3 Aug 0000 UTC.

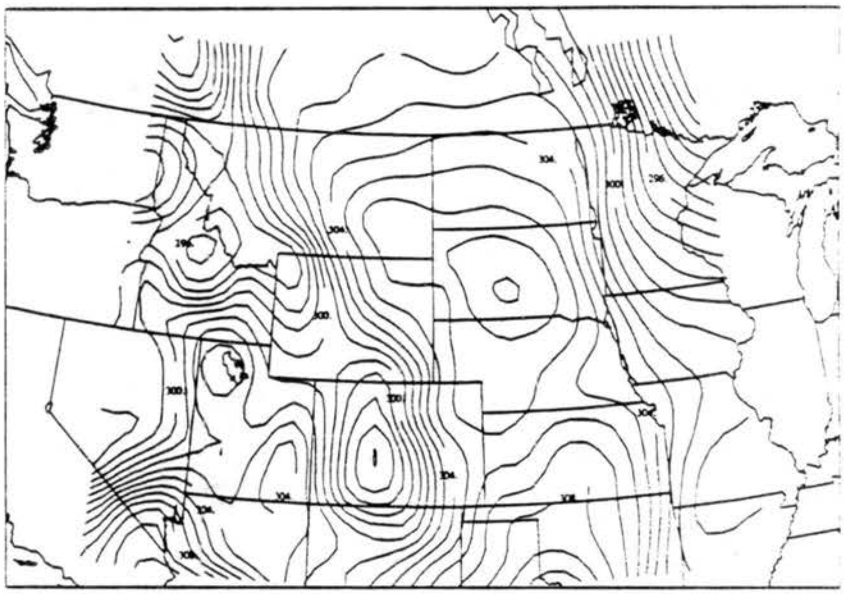

Figure 8.3: Temperature field on terrain following coordinate surface 150 m above ground from higher resolution control run at 3 Aug 0000 UTC.

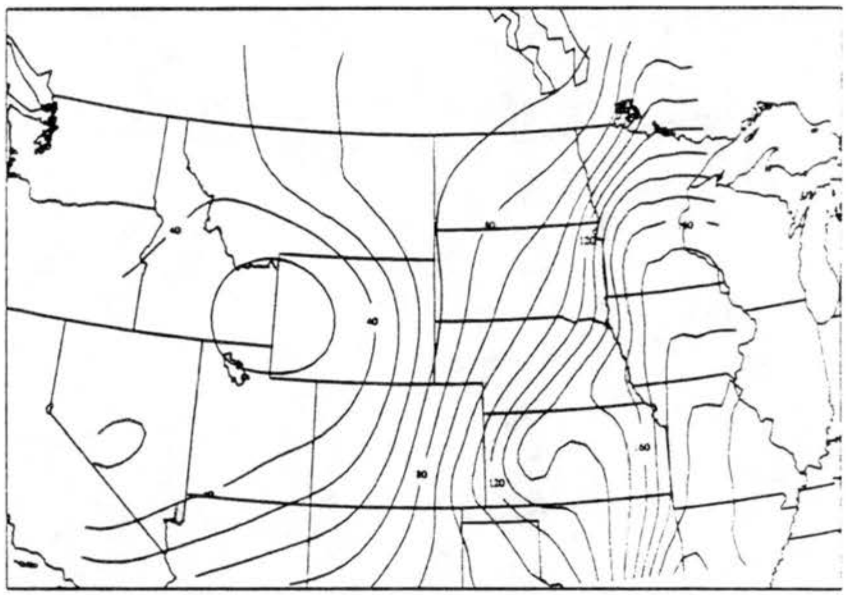

Figure 8.4: Total water mixing ratio field on terrain following coordinate surface 150 m above ground from higher resolution control run at 3 Aug 0000 UTC.

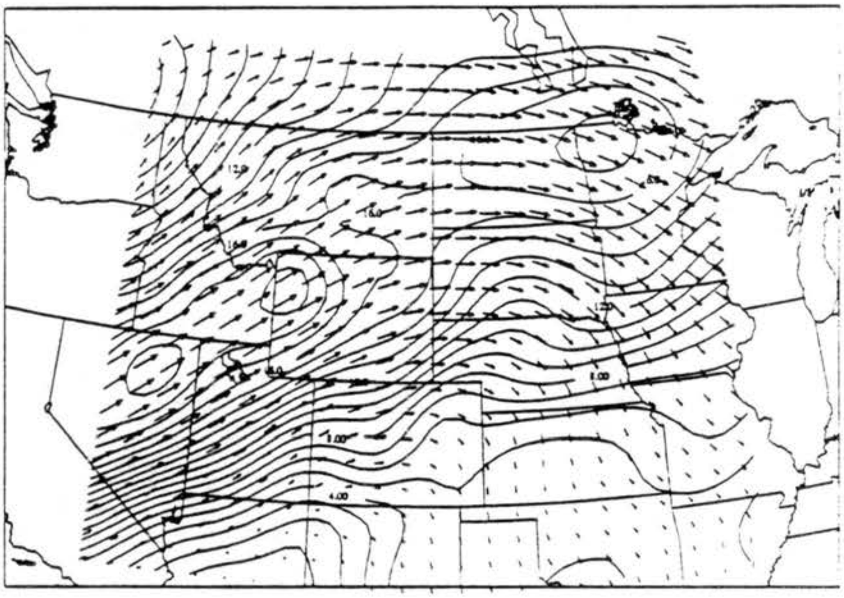

Figure 8.5: Isotachs and wind vectors at 5.16 km above sea level from higher resolution control run at 3 Aug 0000 UTC.

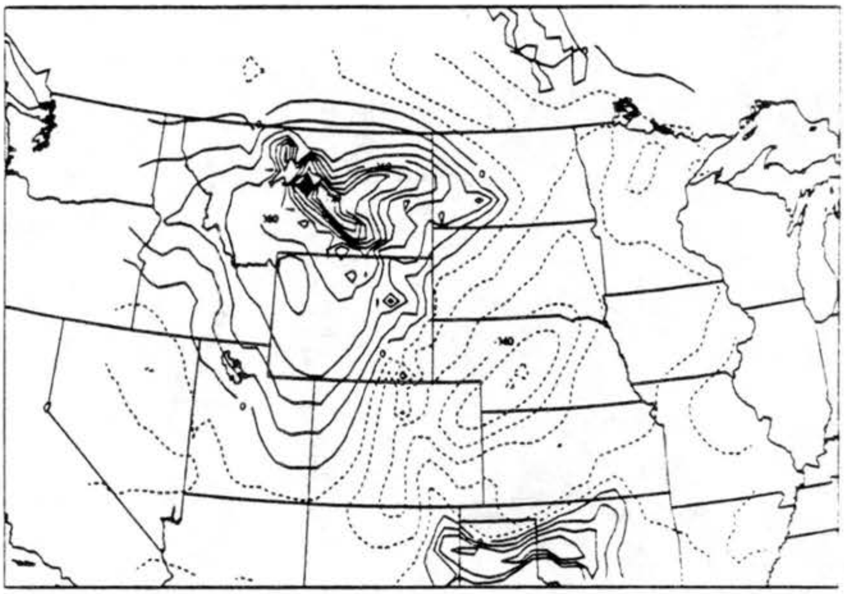

Figure 8.6: Vertical velocity field at 5.16 km above sea level from higher resolution control run at 3 Aug 0000 UTC.

2) the updating of convective parameterization tendencies every 20 minutes in the higher resolution run rather than 30 minutes in the coarse resolution run may, in some cases, reduce the integrated convective heating.

By 0600 UTC, the actual MCC had developed and moved into the Dakotas. The differences between the high and coarse resolution runs were again relatively minor at this time. The mid-level isotachs (Figure 8.9) show that the jet core was still located in northwest Wyoming and stronger than in the coarse run by about 10%. The mid-level vertical motion (Figure 8.10) was again similar although significantly stronger than in the coarse grid run. The upper-level isotachs (Figure 8.11) at 9.96 km show stronger perturbations in the coarse grid run which is consistent with the deeper circulation in that run.

The similarities between the two runs continued through the end of the simulation at 1200 UTC. The MCC had more time to develop and did become stronger at the 9.96 km level in the high resolution run. The isotachs at that level (Figure 8.12) show that the outflow jet core over northern Minnesota was the same strength in both runs. The upward motion (Figure 8.13) associated with the MCC was still stronger in the coarse run but the pattern and location were similar.

Figures 8.14, 8.15, and 8.16 show the comparison of the convective parameterization precipitation rates between the fine and coarse resolution runs at 0000 UTC, 600 UTC, and 1200 UTC, respectively. As can be seen from these figures, there again was very little difference between the two simulations except for the expected additional structure in the fine resolution fields. The timing and movement of the convective areas were very similar.

This section showed that the high resolution and coarse resolution control simulations produced very similar results in the formation and propagation behavior of the MCC. In fact, the close agreement in the simulation results was surprising given the convective nature of the forcing. The similarities were probably due to the strong synoptic forcing of the convection and the associated baroclinicity. The high resolution control simulation now will be used to examine various characteristics of the MCC. Afterward, two additional sensitivity experiments will be presented based on the high resolution control simulation.

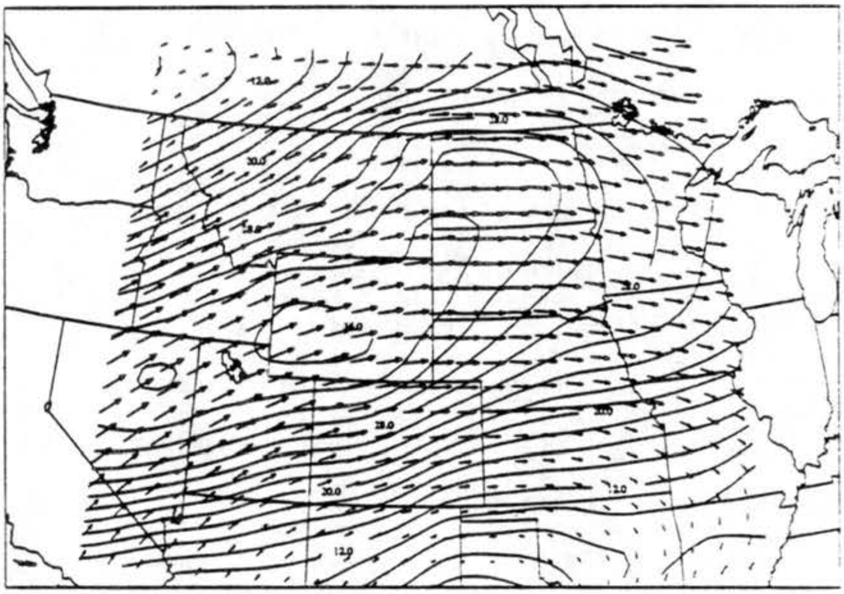

Figure 8.7: Isotachs and wind vectors at 9.96 km above sea level from higher resolution control run at 3 Aug 0000 UTC.

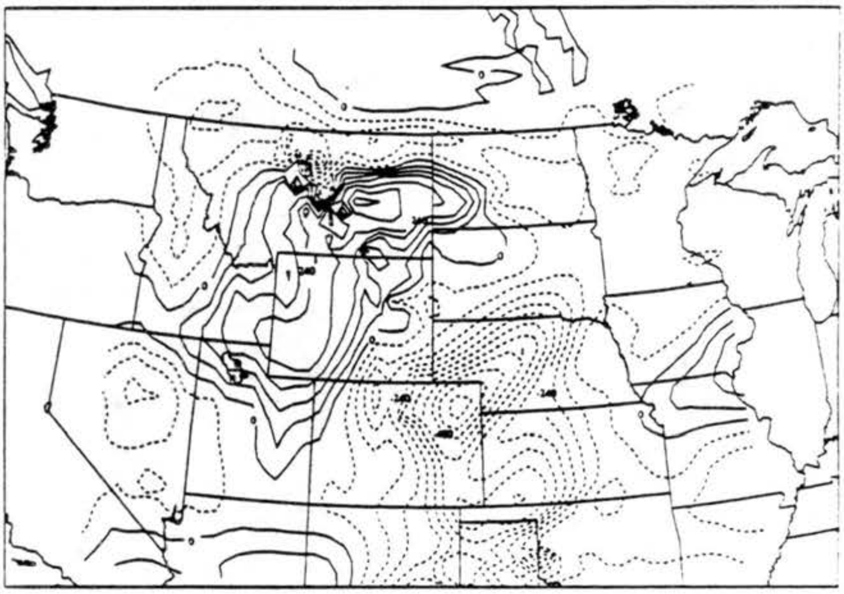

Figure 8.8: Vertical velocity field at 9.96 km above sea level from higher resolution control run at 3 Aug 0000 UTC.

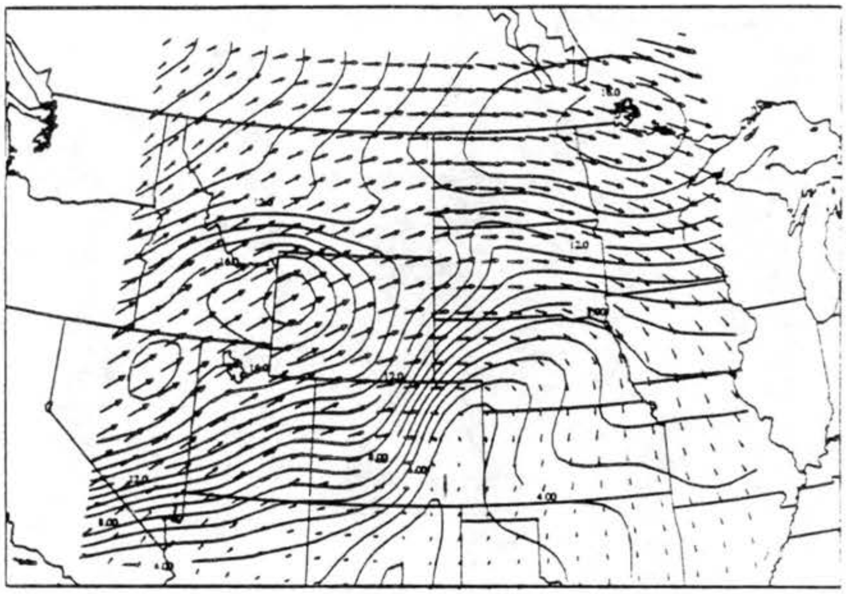

Figure 8.9: Isotachs and wind vectors at 5.16 km above sea level from higher resolution control run at 3 Aug 0600 UTC.

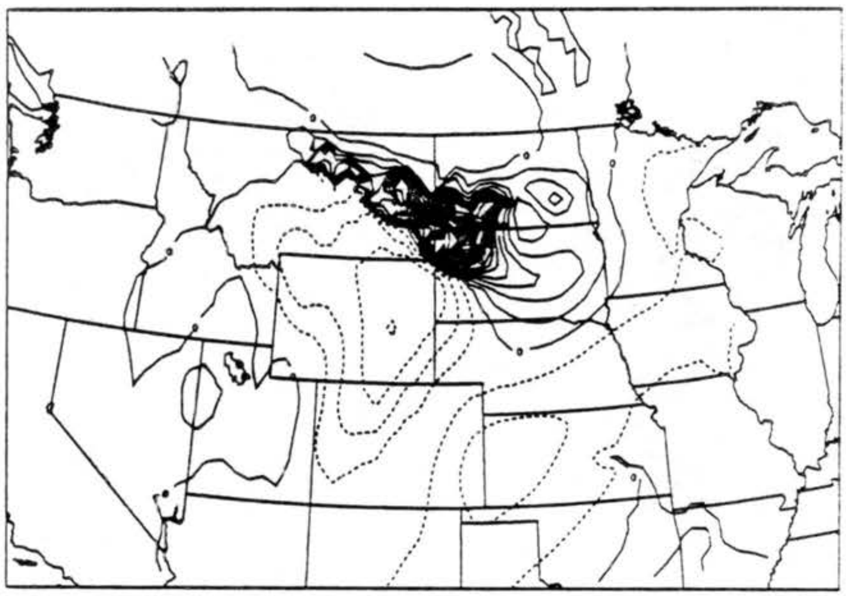

Figure 8.10: Vertical velocity field at 5.16 km above sea level from higher resolution control run at 3 Aug 0600 UTC.

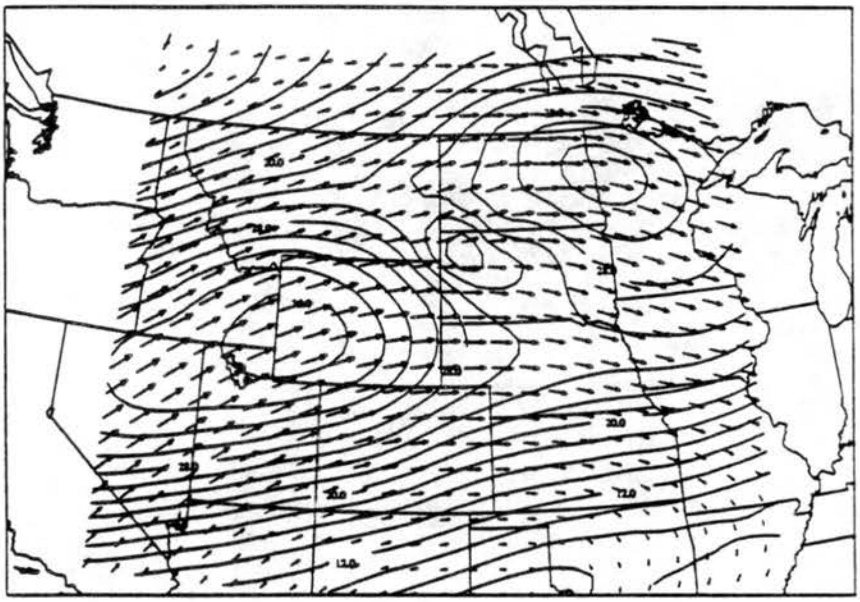

Figure 8.11: Isotachs and wind vectors at 9.96 km above sea level from higher resolution control run at 3 Aug 0600 UTC.

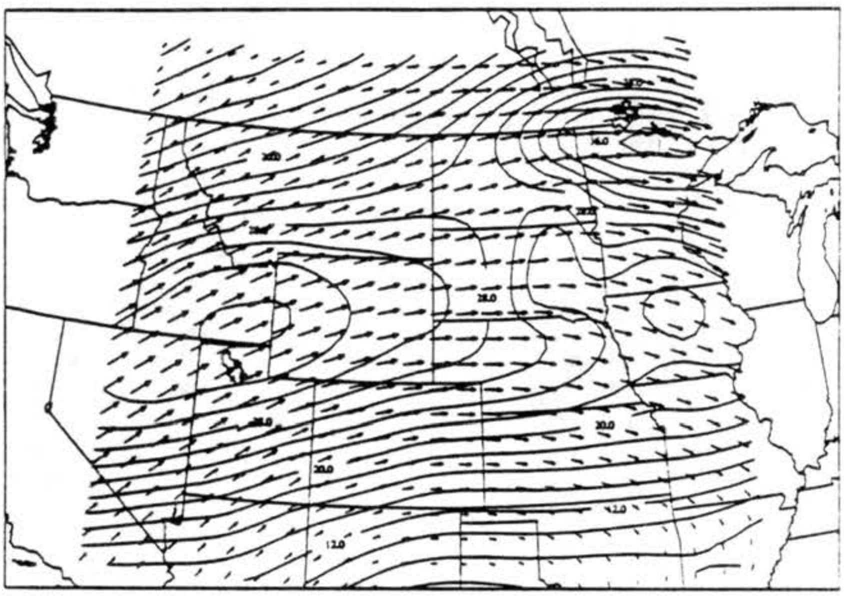

Figure 8.12: Isotachs and wind vectors at 9.96 km above sea level from higher resolution control run at 3 Aug 1200 UTC.

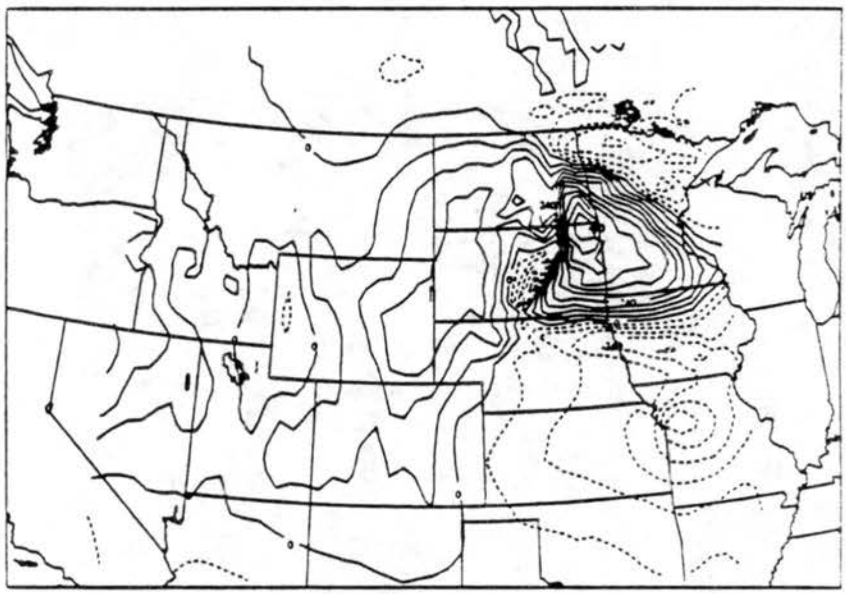

Figure 8.13: Vertical velocity field at 9.96 km above sea level from higher resolution control run at 3 Aug 1200 UTC.

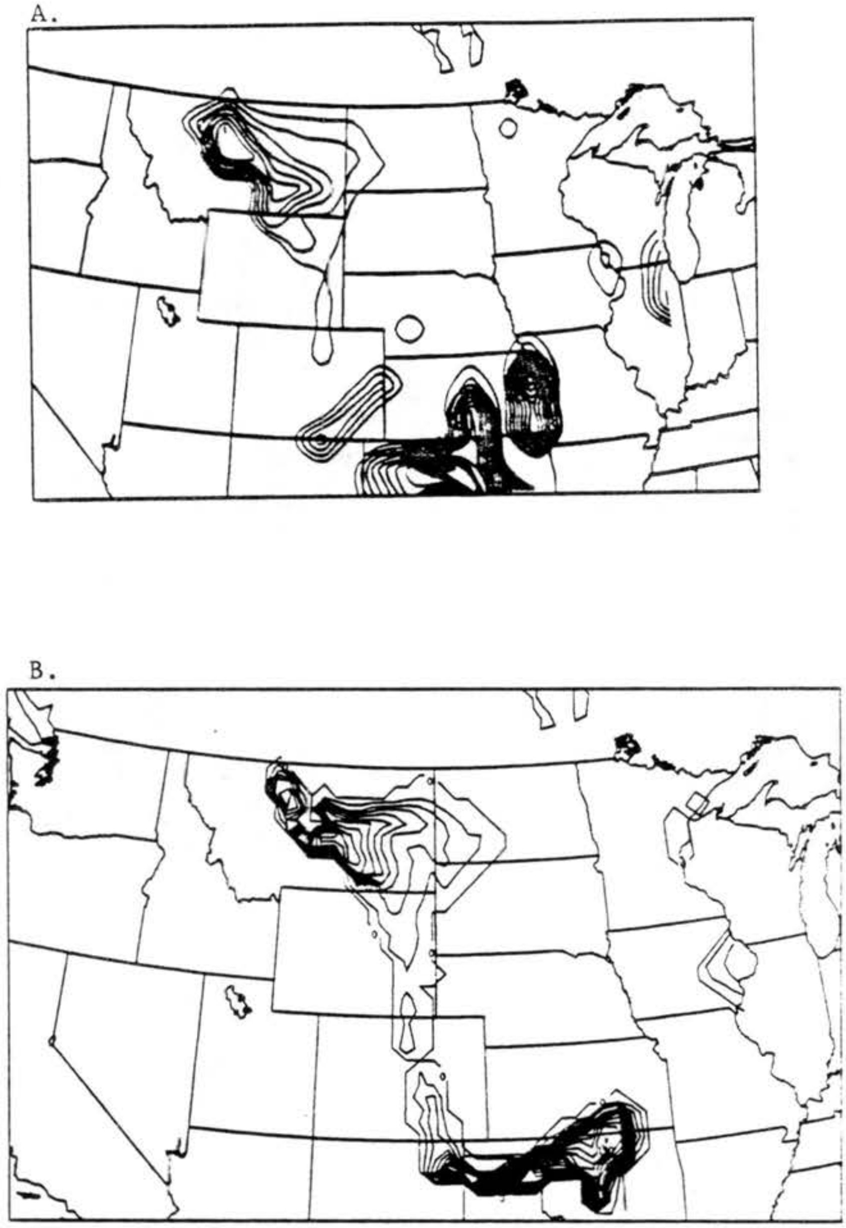

Figure 8.14: Convective parameterization precipitation rate at 3 Aug 0000 UTC. a) from coarse resolution control run. b) from higher resolution control run.

A.

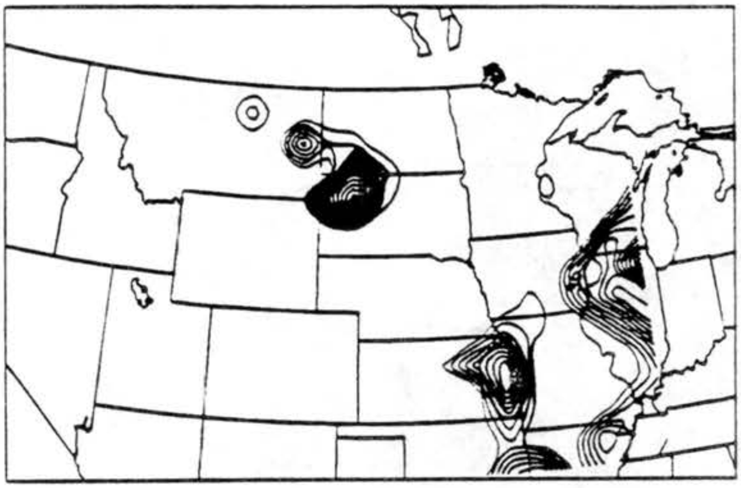

B.

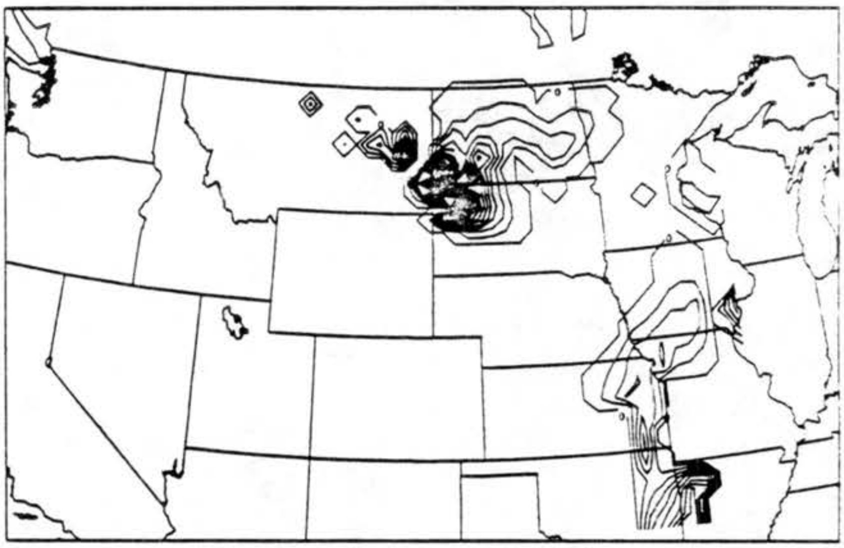

Figure 8.15: Convective parameterization precipitation rate at 3 Aug 0600 UTC. a) from coarse resolution control run. b) from higher resolution control run.

A.

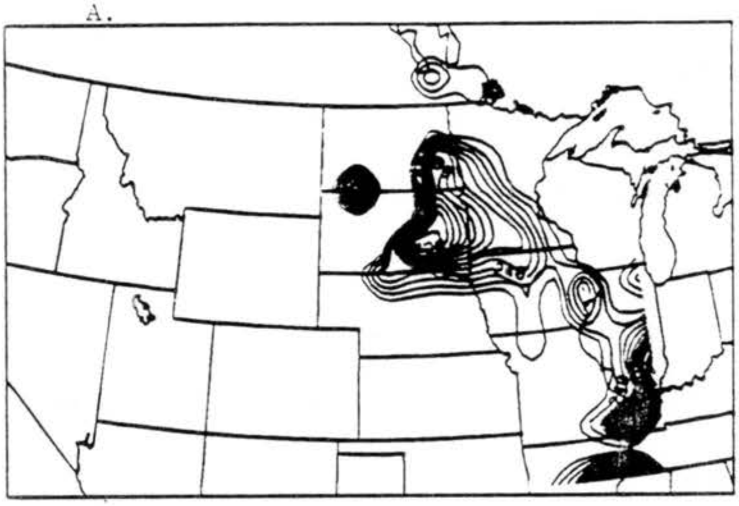

B.

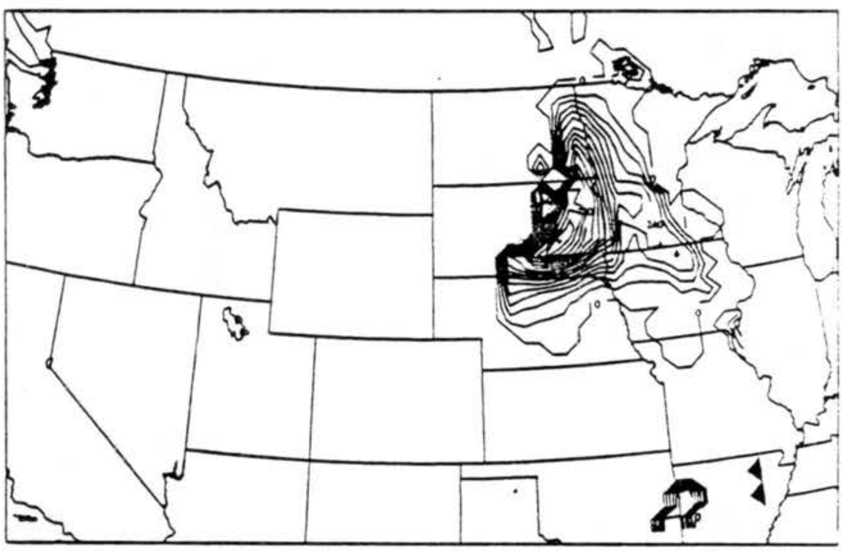

Figure 8.16: Convective parameterization precipitation rate at 3 Aug 1200 UTC. a) from coarse resolution control run. b) from higher resolution control run.

8.3 Identification of forcing mechanisms

This section will examine the development and evolution of the simulated MCC and attempt to identify the major physical forcing mechanisms responsible for determining the structure of the modelled convective system. One particular mechanism will be highlighted, that of the formation and propagation of the mountain/plains solenoid, which will be shown to be very important to the structure and behavior of the simulated MCC.

8.3.1 Initiation of the convective system

To review the synoptic situation in the Montana/Dakota region on the morning of 2 August, a surface low was present over the intermountain region of the western U.S. with a center in northwestern Wyoming. This low was a result of the longwave upper level trough over the eastern Pacific and the enhanced surface heating over the elevated terrain (a "heat" low). In addition in the low levels, the westward extension of the Bermuda high provided a favorable pressure gradient over the central U.S. plains for the formation of a strong nocturnal low level jet. The previous evening's jet and the circulation around the heat low center can be seen in the 1200 UTC low level isotach field in Figure 8.17. From the 1200 UTC fields, however, the two pressure patterns appeared to be "decoupled," with no strong direct feed of heat and moisture between the two systems. The low level jet, as is typical, veered toward the east. In the upper levels, the flow was generally anti-cyclonic and fairly strong for August, with speeds reaching 40 m/s near the tropopause. A mid and upper level jet core was moving into the Montana area. Because Montana was under the front left exit region of the jet core, a favorable situation for convection was set up as synoptic scale upward motion existed over the area most of the day.

As the day progressed, the planetary boundary layer developed. Because the soil and atmosphere was drier in the mountains and High Plains (Figure 8.18), in conjunction with the sloping topography, the mountain/plains solenoidal circulation was well developed. In the lower levels, this was manifested as an upslope velocity component, which can be seen in the vector field at 2000 UTC (Figure 8.19). From this figure also, the nocturnal low level jet can be seen to have backed to where it was directly from the south over

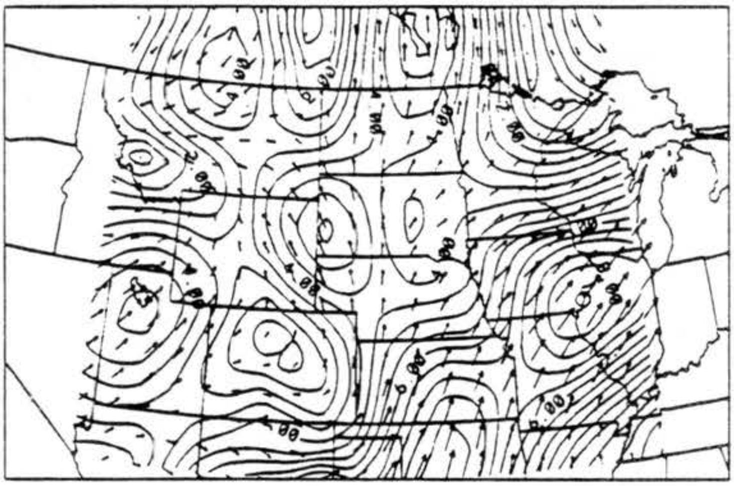

Figure 8.17: Isotachs and wind vectors on terrain following coordinate surface 150 m above ground from coarse resolution control run at 2 Aug 1200 UTC.

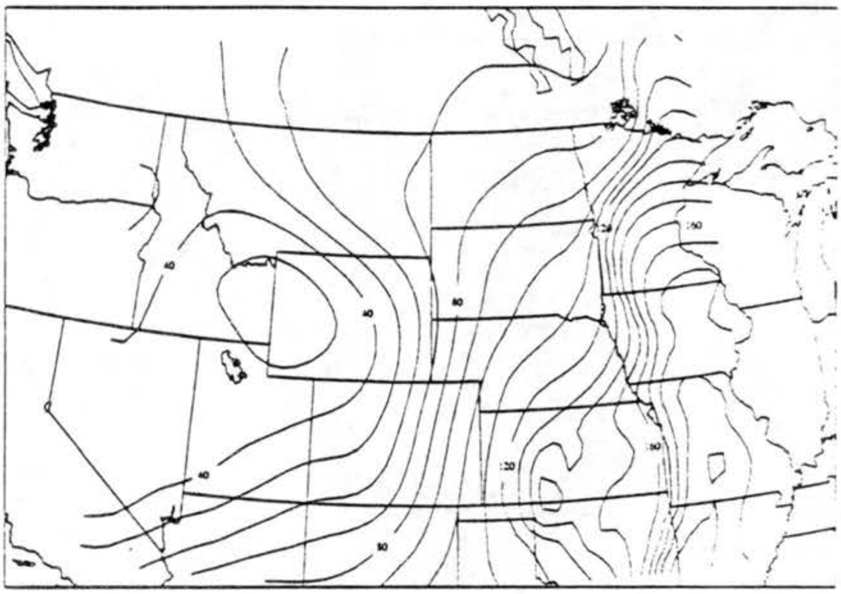

Figure 8.18: Total water mixing ratio field on terrain following coordinate surface 150 m above ground from higher resolution control run at 2 Aug 2000 UTC.

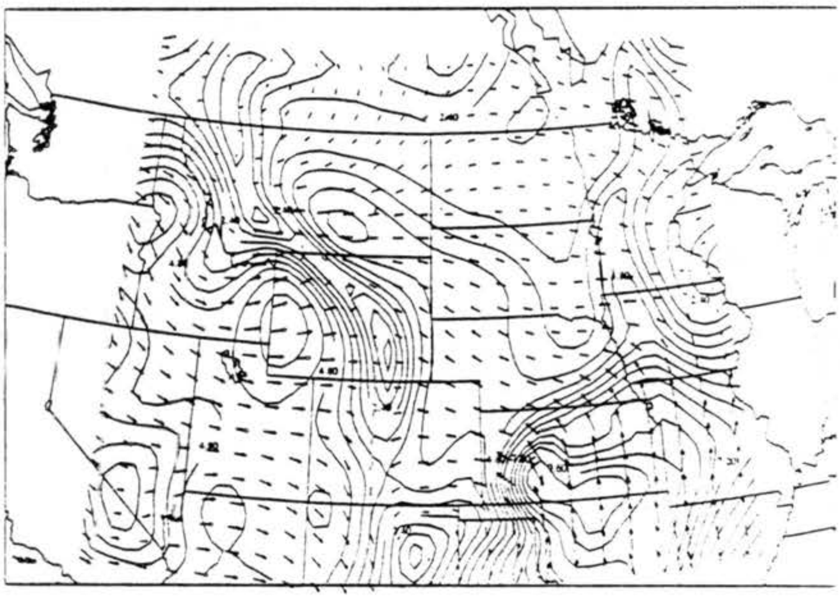

Figure 8.19: Isotachs and wind vectors on terrain following coordinate surface 150 m above ground from higher resolution control run at 2 Aug 2000 UTC.

Oklahoma then curving toward the west as a result of the solenoidal circulation. This was responsible for "coupling" the nocturnal jet with the heat low circulation, providing an energy and moisture source into the northern plains area for most of the afternoon hours. The boundary layer heating was also mostly responsible for deepening the heat low. Figure 8.20 shows the low level pressure fields at 2000 UTC and 0000 UTC. The perturbation Exner function had fallen from $-2.6JK^{-1}kg^{-1}$ to $-3.4JK^{-1}kg^{-1}$ which is over a 2 mb fall.

As mentioned earlier, the deep convection started over central Montana about 2200 UTC. The meso-α-scale conditions which helped support this convection were:

- A deepening surface low which provided a source of low level convergence along with moist upslope inflow from the southeast. The upslope component was forced also by the mountain/plains solenoid.

- A weak, mostly stationary front which was evident in the observations that moved southward from Canada providing an additional "trigger." This front was not modelled very well in the Dakotas where it was difficult to distinguish in the thermodynamic fields although a wind shift line could be seen.

- An upper level jet core that was in a favorable position to provide upper level divergence.

From this initial convection in Montana, the MCC developed as the convective system reached the border of the Dakotas. It is not known whether the simulated MCC had actually reached Maddox's (1980) isotherm size criteria by this time. Rather, the mesoscale convective system is termed an MCC at this time because it exhibits several of the features of observed MCCs, some of which will be discussed in the following paragraphs.

The isotach and vector fields in the low levels at 0400 UTC (Figure 8.21) show that there was still a good moisture supply from the newly developing nocturnal low level jet in the central plains as the boundary layer decoupled from the surface. Note, however, the double core structure of the jet with the southern core over Oklahoma. The northern

A.

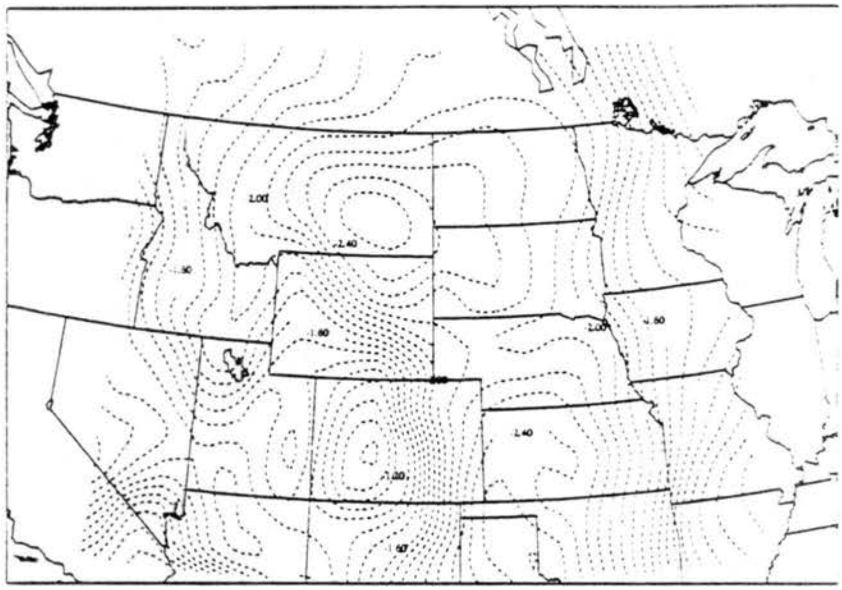

B.

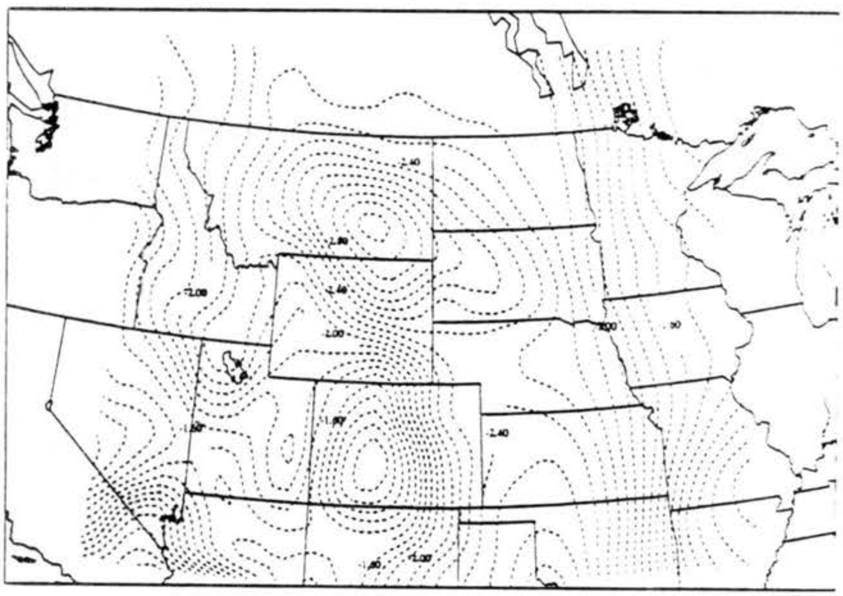

Figure 8.20: Perturbation Exner function on terrain following coordinate surface 150 m above ground from higher resolution control run at a) 2 Aug 2000 UTC, b) 3 Aug 0000 UTC.

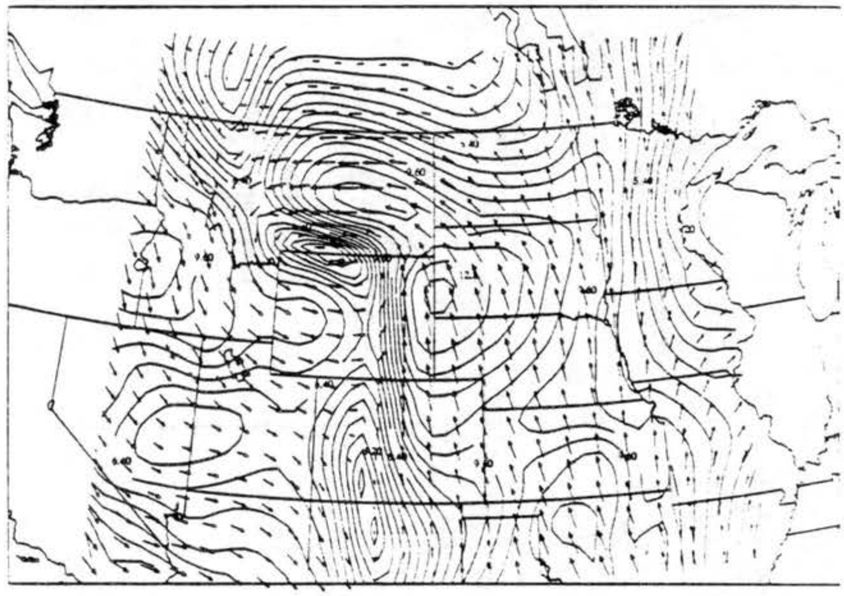

Figure 8.21: Isotachs and wind vectors on terrain following coordinate surface 150 m above ground from higher resolution control run at 3 Aug 0400 UTC.

core over the Wyoming/South Dakota border was actually stronger at this time due to the additional forcing from the heat low. The low level vertical motion at 0400 UTC (Figure 8.22) shows almost no upward motion near the surface directly under the convection (Figure 8.23), implying that most of the inflow into the system was not tied directly to the surface.

The mid-level vertical motion field (5.16 km) at 0400 UTC (Figure 8.24), shows the grid-resolved response to the convection system. Upward motion had reached about 20 cm/s, but, unlike the coarse grid simulations, a distinct rear inflow jet was not seen at this level (Figure 8.25), perhaps masked by the strong synoptic scale gradients. The resolved vertical moisture flux had become significant as the total water mixing ratio (Figure 8.26) had reached more than 2 g/kg by this time.

In the upper levels (9.96 km), an outflow jet was beginning to develop by this time (Figure 8.27) over eastern North Dakota. Note also the significant weakening of the flow directly over the system as the ambient flow is slowed down through the resolvable scale upward momentum transport and a high pressure perturbation above the system. The total water field (Figure 8.28) shows again the highly circular pattern associated with the MCC. The upper center is located slightly downstream from the mid-level center due to the differential advective velocities.

The grid-resolved response is a geostrophic adjustment process of the meso-α-scale circulations to the widespread and persistent heating from the cumulus convection. From numerous earlier sensitivity simulations which tested the convective parameterization schemes (results not shown), it was very obvious that the convective forcing needed to achieve an areal extent greater than the Rossby radius of deformation if a long-lived MCC was to develop. But additionally, the convective forcing needed to be persistent for the geostrophic adjustment of the MCC to occur. Even if the time-integrated convective heating was the same, applying the heating too quickly could force too much energy into the unbalanced gravity wave modes. Heating for a longer period of time can give the atmosphere and the Coriolis force more time to develop the balance. These results

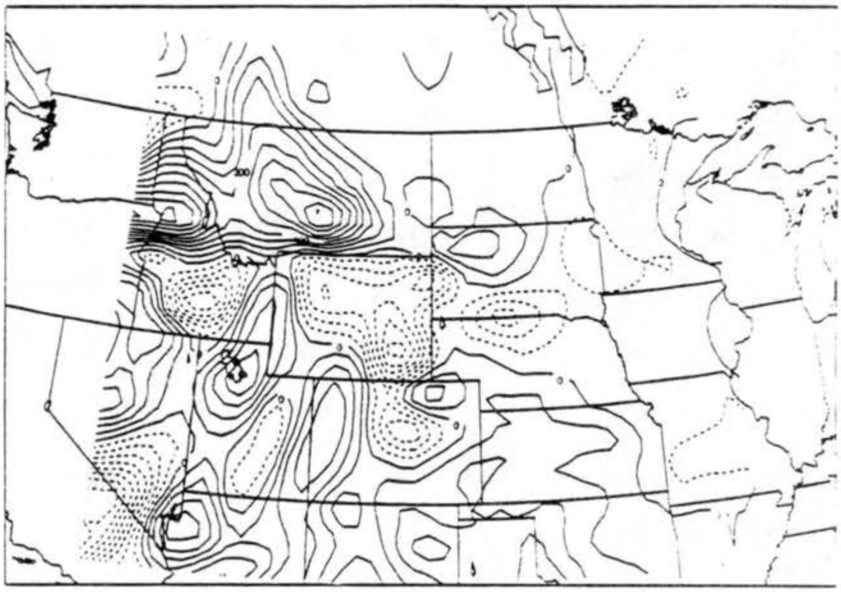

Figure 8.22: Vertical velocity field on terrain following coordinate surface 150 m above ground from higher resolution control run at 3 Aug 0400 UTC.

Figure 8.23: Convective parameterization precipitation rate from higher resolution control run at 3 Aug 0400 UTC.

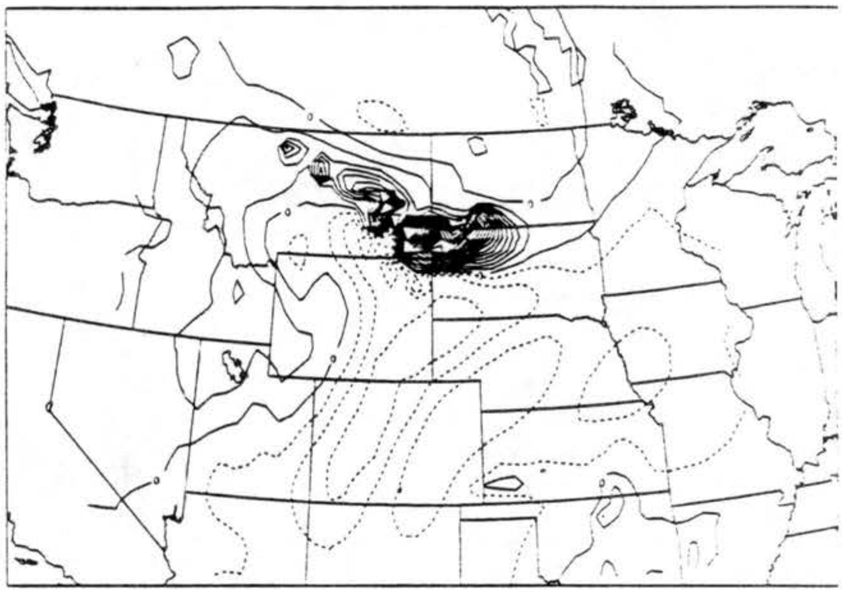

Figure 8.24: Vertical velocity field at 5.16 km above sea level from higher resolution control run at 3 Aug 0400 UTC.

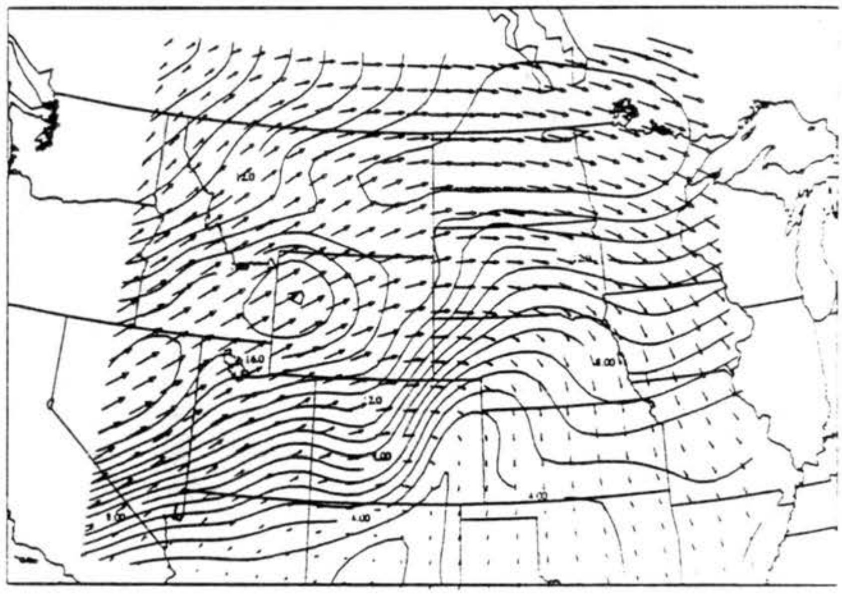

Figure 8.25: Isotachs and wind vectors at 5.16 km above sea level from higher resolution control run at 3 Aug 0400 UTC.

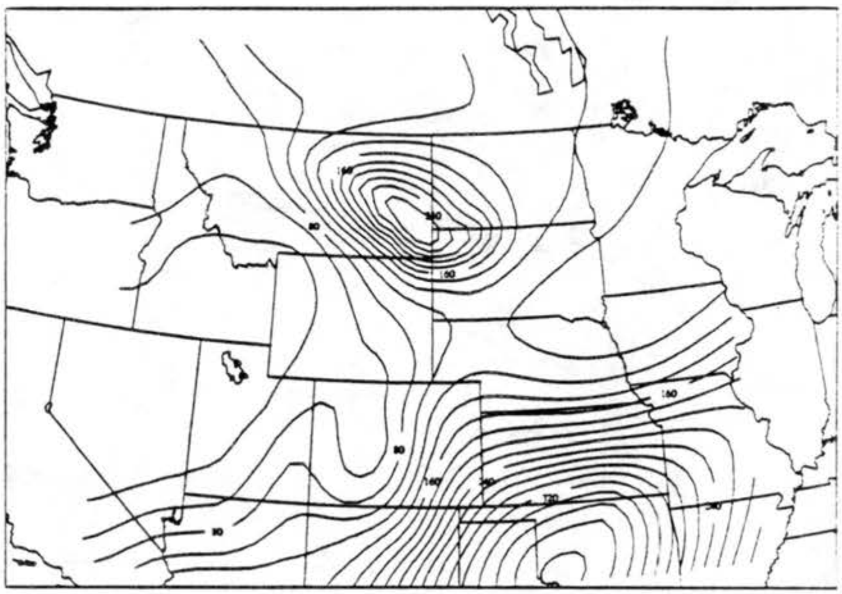

Figure 8.26: Total water mixing ratio field at 5.16 km above sea level from higher resolution control run at 3 Aug 0400 UTC.

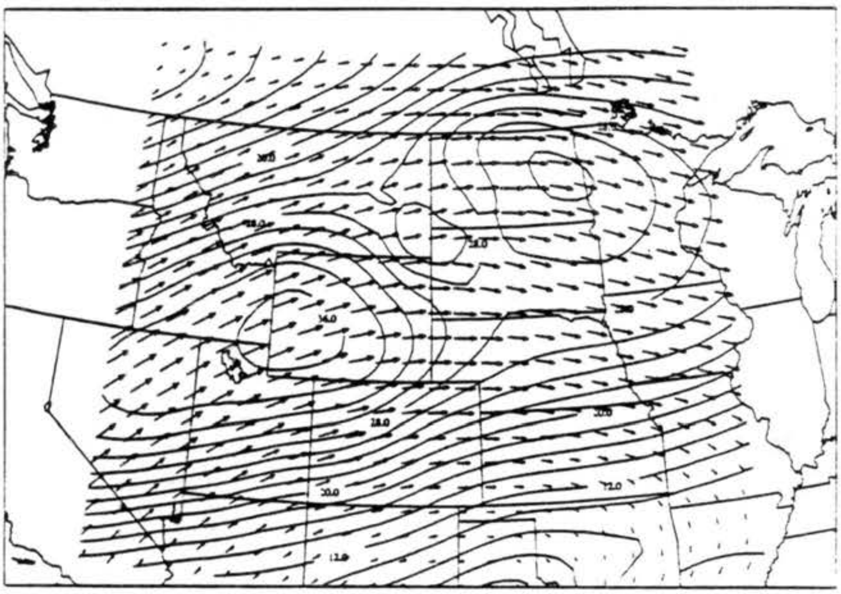

Figure 8.27: Isotachs and wind vectors at 9.96 km above sea level from higher resolution control run at 3 Aug 0400 UTC.

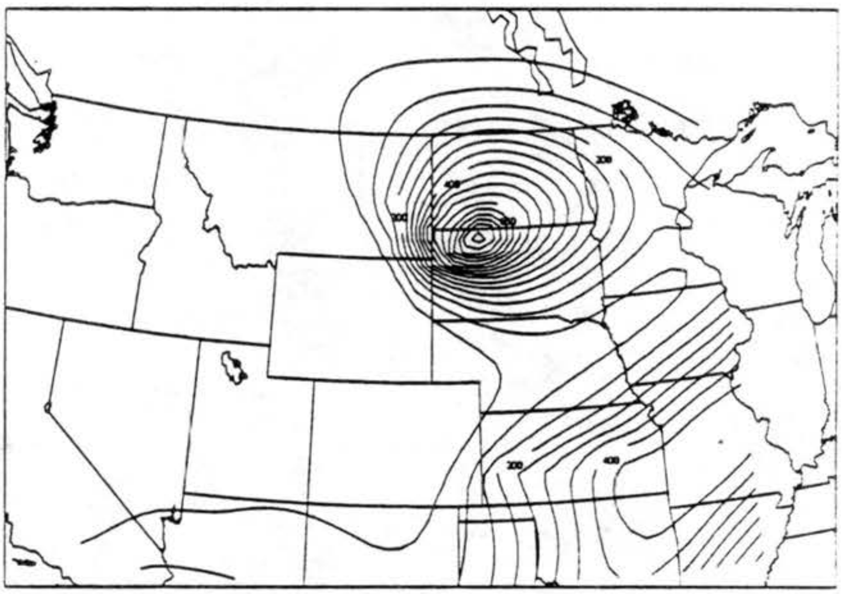

Figure 8.28: Total water mixing ratio field at 9.96 km above sea level from higher resolution control run at 3 Aug 0400 UTC.

are consistent with previous work reported by Schubert et al. (1980), Frank (1983), and Tripoli and Cotton (1989).

For the convection to be widespread and persistent, there must be some kind of synoptic or meso-α-scale organizing circulation. The convective available potential energy usually exists in the U. S. plains in the summer season, but a low-level convergence "source" and a supply of moisture are necessary. The low-level jet frequently serves as the mesoscale organizer in the central plains for mesoscale convective systems. However, a different mesoscale circulation which can provide low level convergence appeared to be more important in the CCOPE case and will be discussed in the following section.

As the convective system moved from central Montana to the western Dakotas, it became apparent from the model results that a "wave" in the potential temperature field was co-located with the system and perhaps providing forcing for the system. The wave was actually the temperature structure of the mountain/plains solenoid circulation that other researchers have mentioned in the past (e.g., Tripoli and Cotton, 1989). The solenoid is formed by two processes: 1) the sloping terrain forces differential heating between the mountains and plains, the same process described by many other researchers on smaller spatial scales (e.g., Defant, 1951, Banta, 1982, Bader and McKee, 1983), and 2) the elevated terrain in the simulation had usually drier soil than the lower plains thus creating a deeper planetary boundary layer. The simulated potential temperature fields and the corresponding vertical motion fields at 2000 UTC, 0000 UTC, 200 UTC, and 400 UTC are shown in Figures 8.29-8.32.

This solenoid appeared to be extremely important in creating favorable meso-α low-level vertical motion fields for the development and propagation of the convective system in addition to strengthening the low level jet (McNider and Pielke, 1981) which provided low-level heat and moisture convergence. In order to isolate the structure and behavior of the solenoid, a much simpler two-dimensional simulation was run to reduce the degrees of freedom in the full three-dimensional MCC simulation. The next section will describe this simpler simulation.

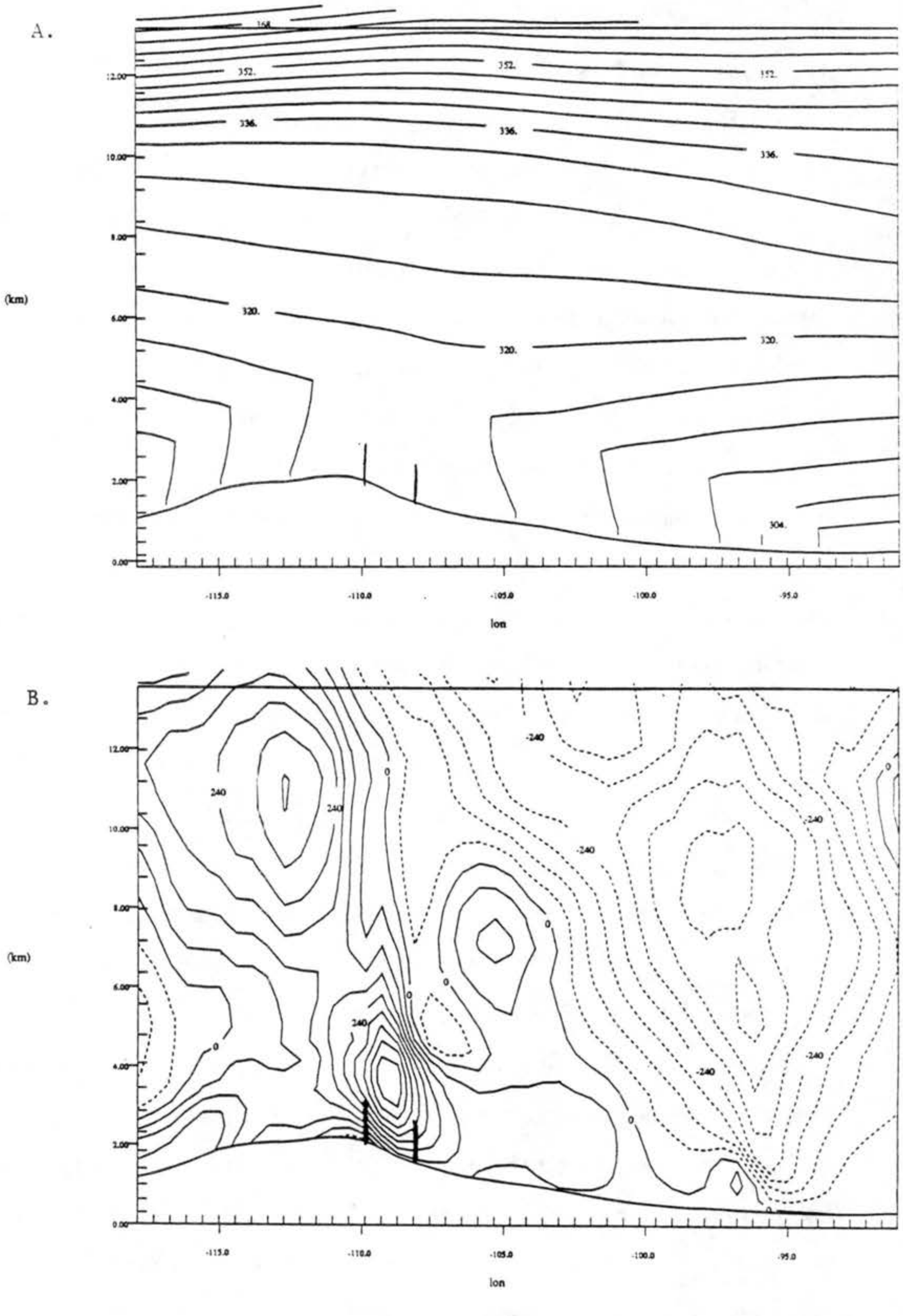

Figure 8.29: Vertical east-west cross section at 45.2° N from higher resolution control run at 2 Aug 2000 UTC. a) potential temperature, b) vertical velocity.

A.

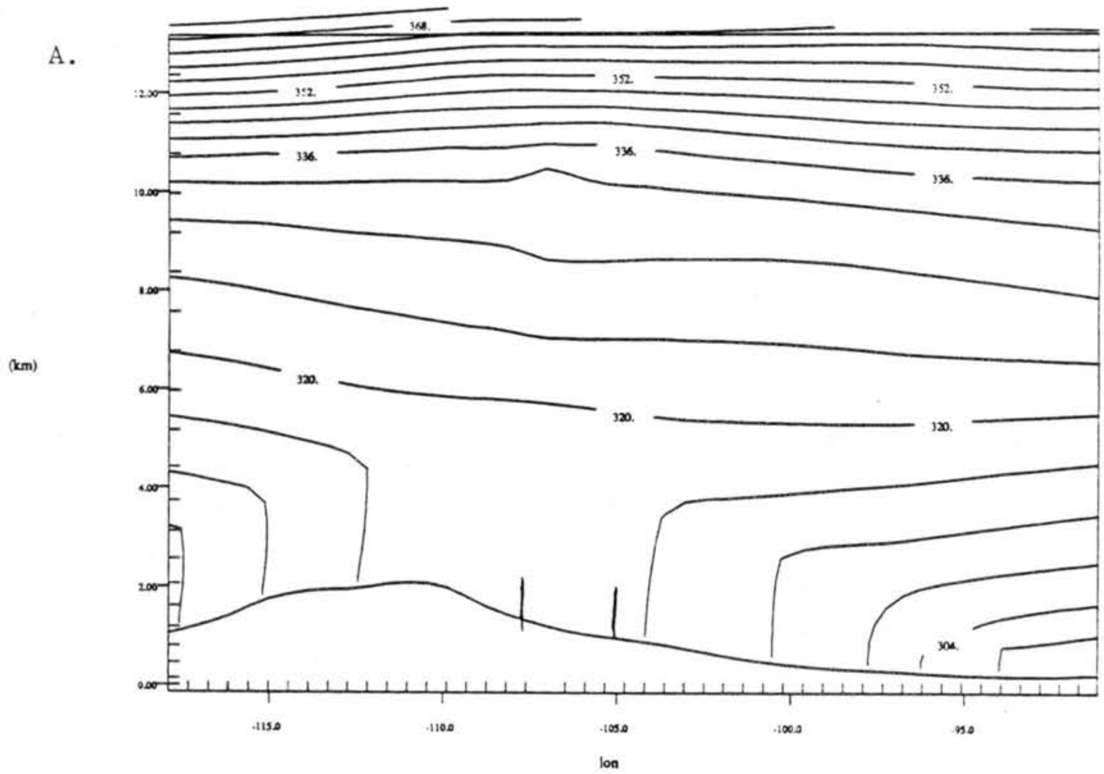

B.

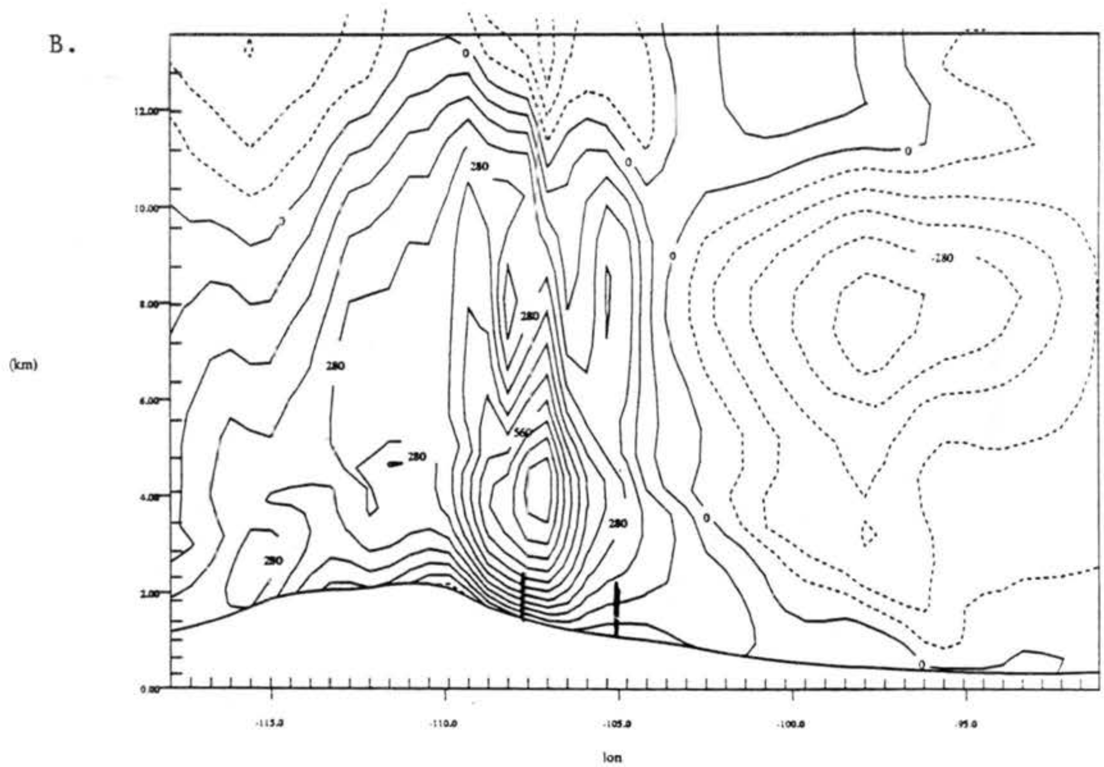

Figure 8.30: Vertical east-west cross section at 45.2° N from higher resolution control run at 3 Aug 0000 UTC. a) potential temperature, b) vertical velocity.

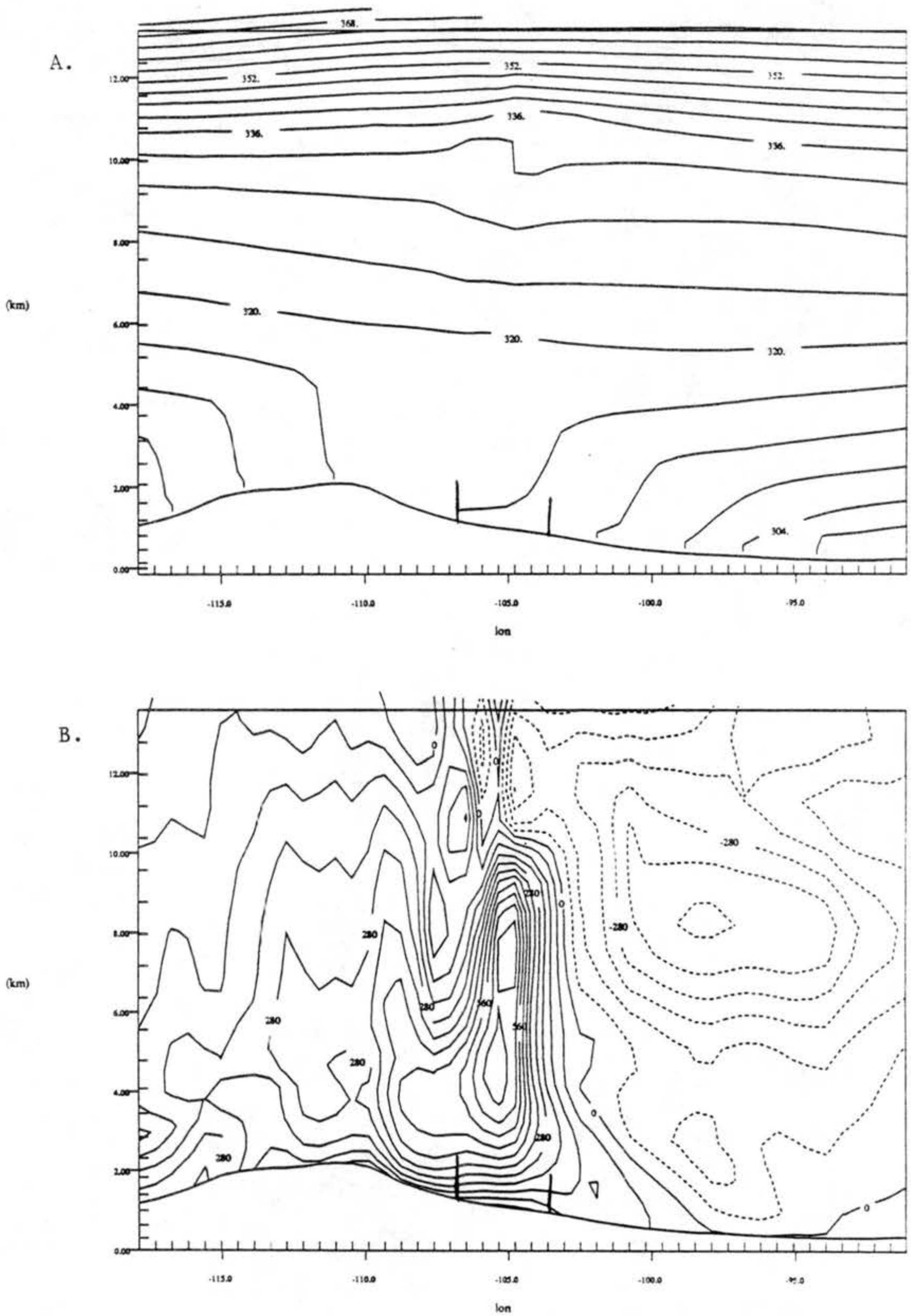

Figure 8.31: Vertical east-west cross section at 45.2° N from higher resolution control run at 3 Aug 0200 UTC. a) potential temperature, b) vertical velocity.

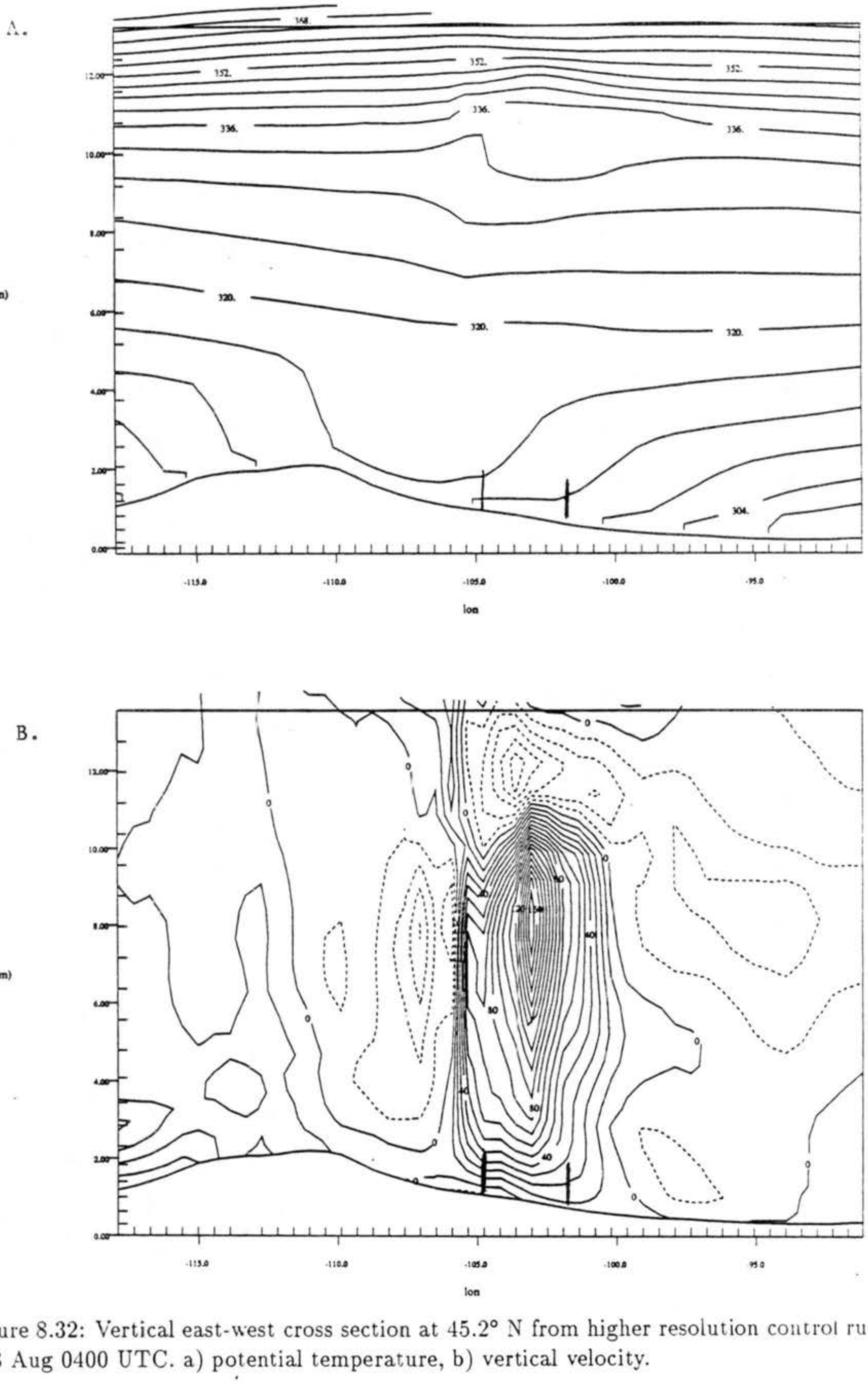

Figure 8.32: Vertical east-west cross section at 45.2° N from higher resolution control run at 3 Aug 0400 UTC. a) potential temperature, b) vertical velocity.

8.3.2 A simple 2-D illustration of the solenoid circulation

Although the solenoid could be seen in the full model run, several questions remained concerning the importance of various features on the structure of the circulation. In particular, the effects of the topography, convective heating, and resolved condensation could have been instrumental in creating and maintaining the solenoid. To eliminate these effects, a simpler two-dimensional simulation was run.

The simulation had 50 horizontal grid points at a 40 km grid spacing. The vertical structure had 25 levels with a 400 m grid spacing. The soil grid had the same structure as the three-dimensional runs, 11 levels extending from the surface to .5 m below. The simulation was forced by varying the soil moisture horizontally which created a "hot spot" in the western part of the domain to simulate one of the forcing mechanisms of the plains solenoid. The hot spot was approximately 300 km wide, about the scale of the Rossby radius of deformation. The entire domain had an initially constant 10 m/s westerly wind. No convection or condensation was allowed in this run throughout the 24 hours of simulation time. There was no topography in the model configuration. The simulation was started about sunrise.

Figure 8.33 shows the potential temperature and vertical motion fields at 4 hours of simulation time. From the potential temperature field, the size and location of the dry soil region can be seen. The vertical motion field shows that a "sea breeze-like" circulation had developed along both the eastern and western thermal boundaries with the western front weaker and moving toward the east into the hot spot faster than the eastern front which is stronger and anchored to the eastern boundary. At 8 hours of simulation time (Figure 8.34), the western front had almost overtaken the eastern front which remained relatively stationary. Note the much deeper boundary layer structure over the dry soil region extending well above the more stable boundary layer over the moist soil region which was at about 1 km AGL. The deeper boundary layer contributed to the vertical extent of the solenoidal mass convergence.

The front at 12 hours of simulation time (Figure 8.35) had still remained rather stationary. However, in the next 4 hours (Figure 8.36), a rather dramatic change occurred.

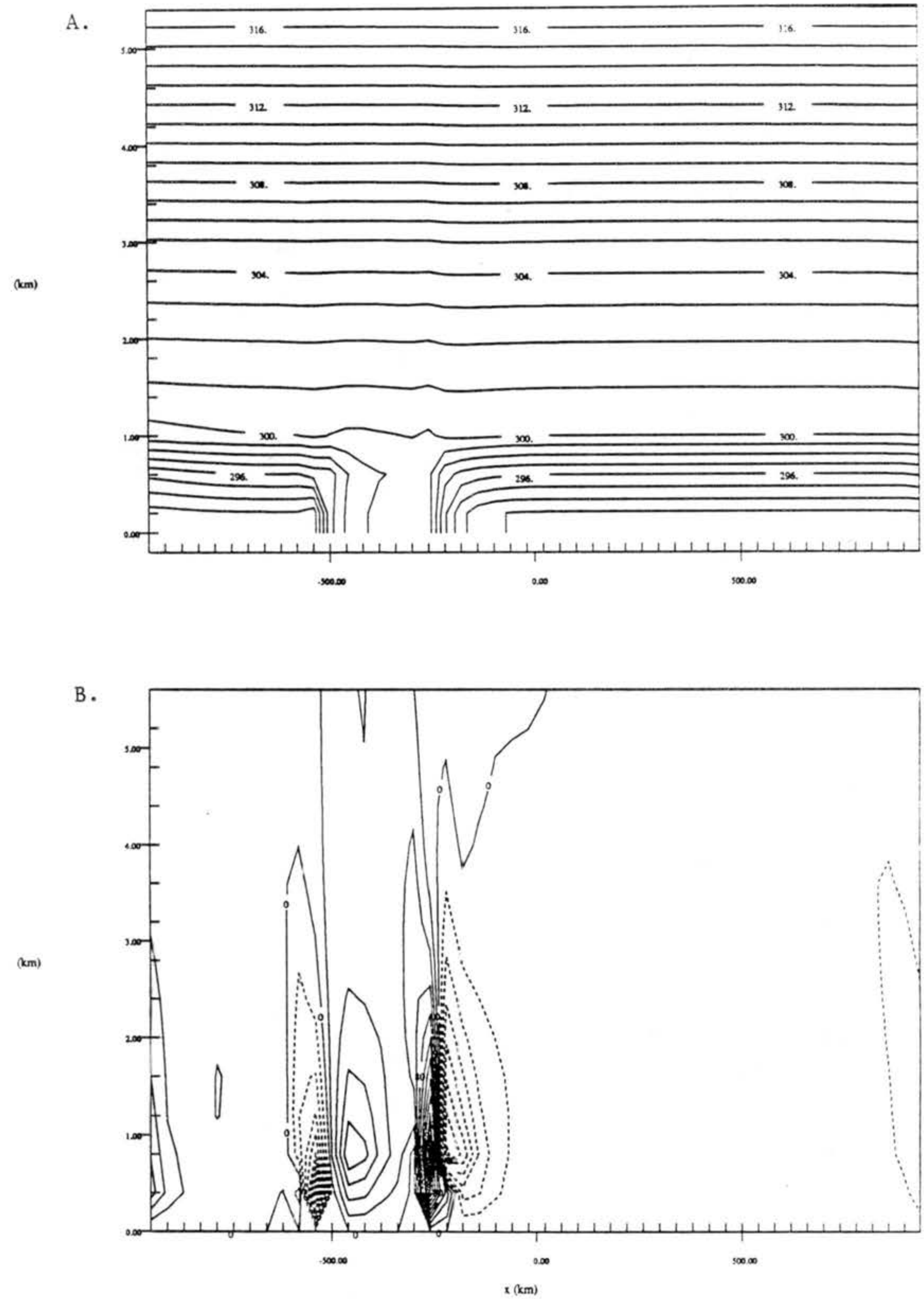

Figure 8.33: a) potential temperature and b) vertical motion from 2-D solenoid simulation at 4 hours simulation time.

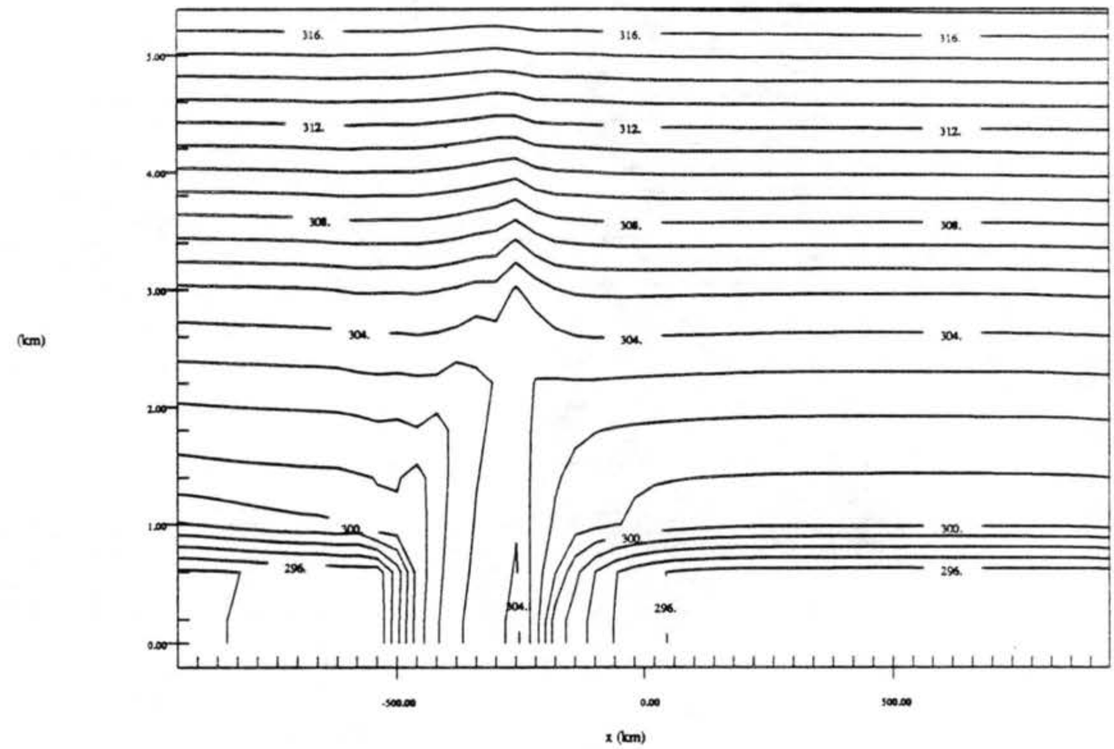

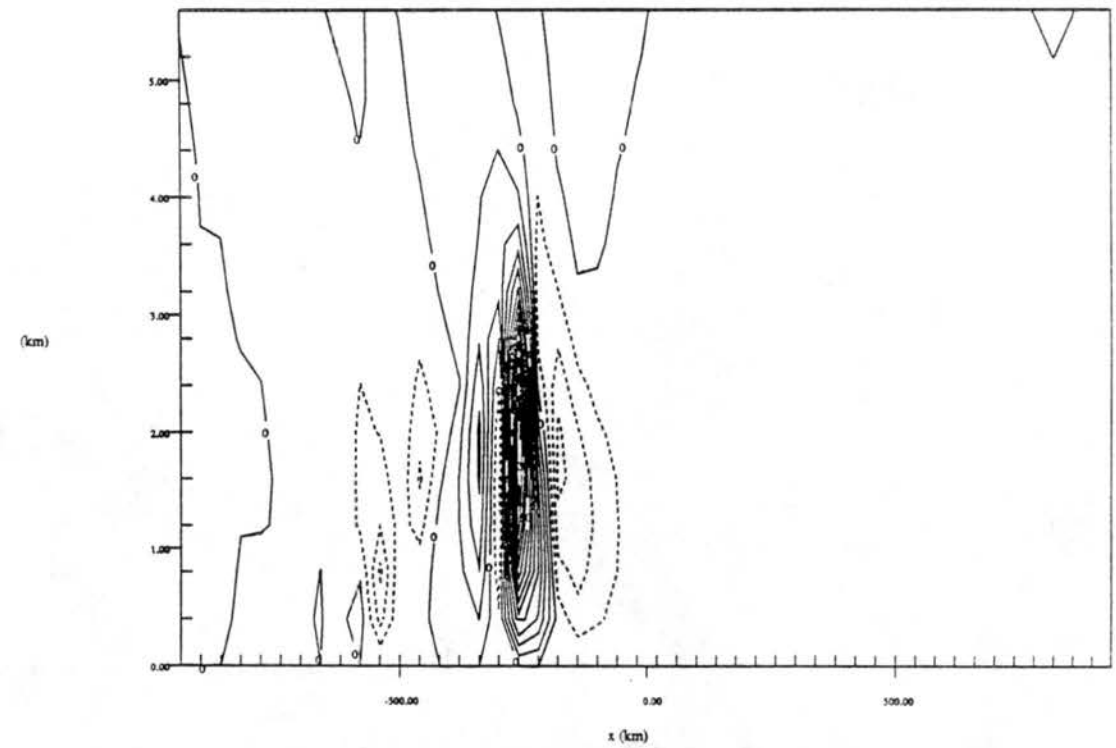

Figure 8.34: a) potential temperature and b) vertical motion from 2-D solenoid simulation at 8 hours simulation time.

As the surface cooled after sunset and the boundary layer decoupled from the ground, the solenoid itself was advected downstream toward the east. The vertical motion structure had changed significantly also.

The "overshooting tops" above the front were collapsing so that subsidence was evident which limited the upward motion only to the lower levels. The vertical motion continued to oscillate through the end of the simulation (Figures 8.37 and 8.38). The upward motion in the solenoid, as the heating is stopped near sunset, weakened as the solenoid underwent a geostrophic adjustment process, but an internal gravity wave response on the upstream edge of the advected solenoid continued to support an upward vertical motion branch at the leading edge.

Several points can be made about the solenoid structure and the relationship to the MCC:

- The solenoid can create favorable meso-α-scale lower level vertical motion fields for MCC development and support.

- The solenoid underwent a significant geostrophic adjustment during the simulation. A simulation without the Coriolis force activated (results not shown) produced a solenoidal circulation which collapsed right after sunset. The geostrophic adjustment was necessary for the long-lived structure of the solenoid. This also implies the spatial scales of the forcing, in this case the differences in surface characteristics, should be on the order of the Rossby radius of deformation for the forcing of a long lived solenoidal circulation. Raymond (1989) hypothesized that the conservative properties of potential vorticity may be advantageous to long-lived mesoscale convective systems. These properties will also contribute to a long-lived solenoid.

- However, the solenoid needs to exist only for six to twelve hours to support the MCC. It may, therefore, be possible for somewhat smaller scale solenoids (which are not completely geostrophically adjusted) to provide similar support structures for the MCC. Additional two-dimensional simulations (results not shown) suggested that even solenoids forced by a "hot spot" of 75 km radius produced similar gravity wave

A.

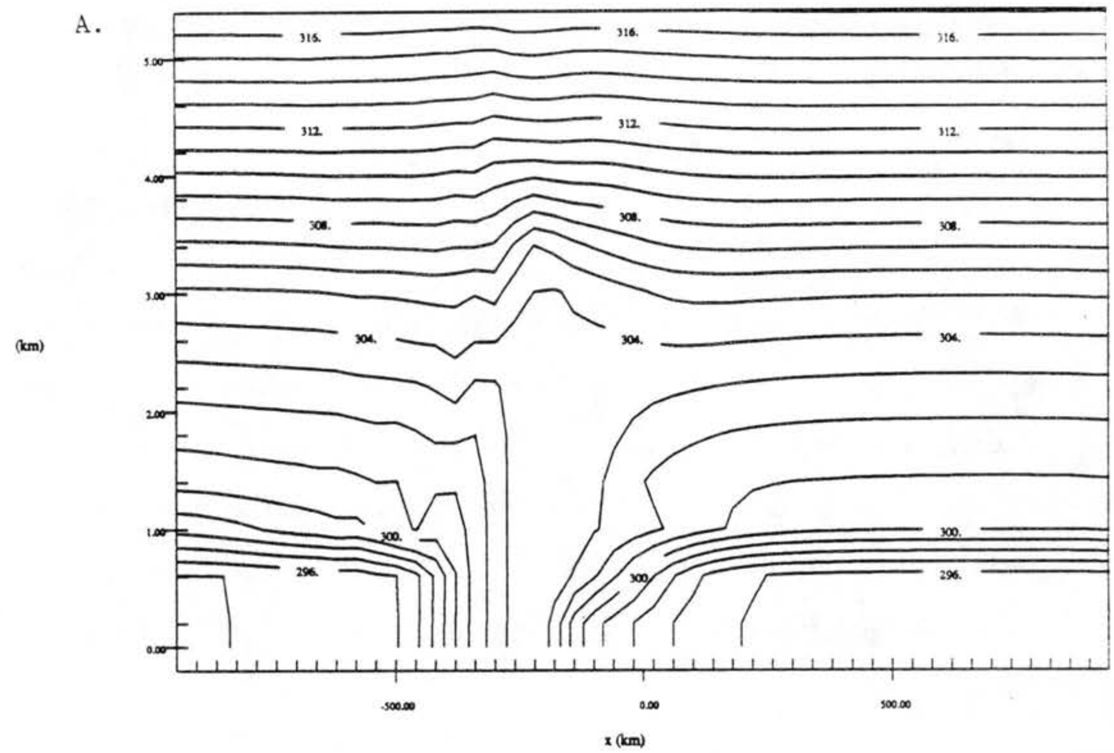

B.

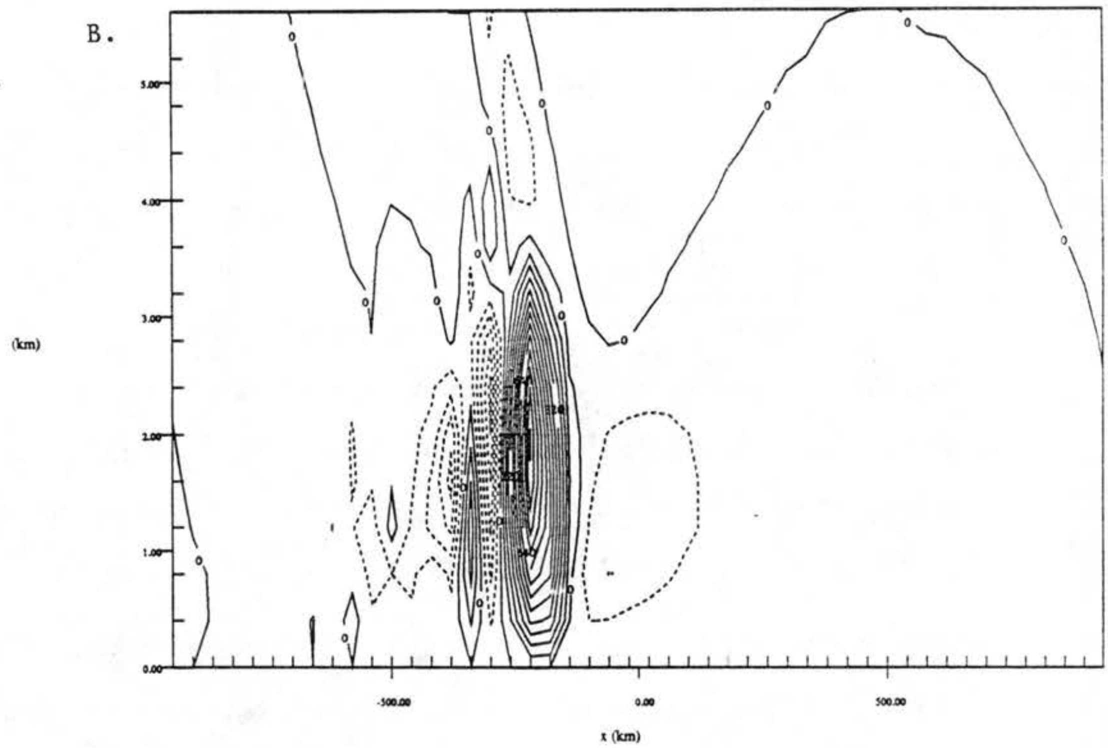

Figure 8.35: a) potential temperature and b) vertical motion from 2-D solenoid simulation at 12 hours simulation time.

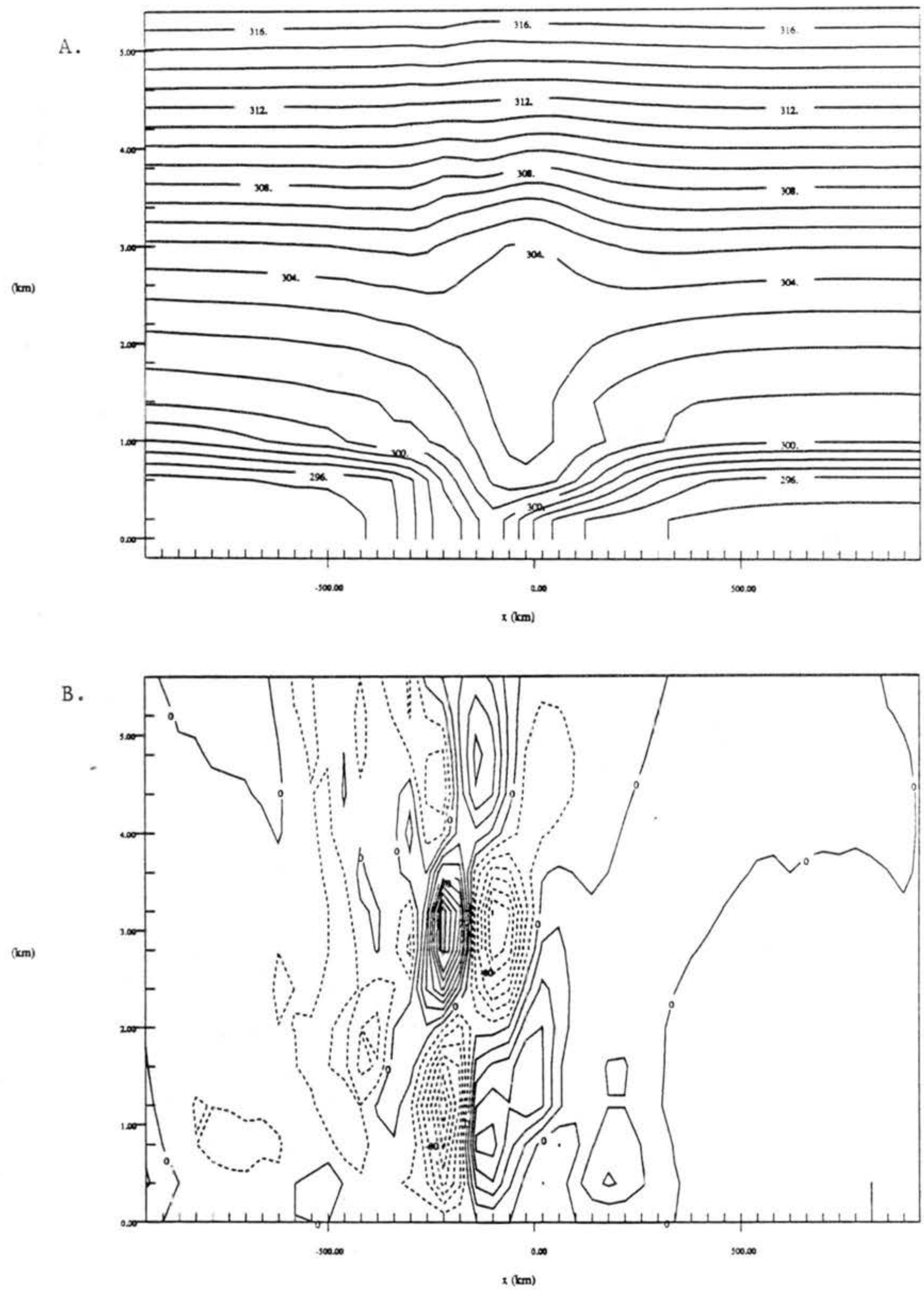

Figure 8.36: a) potential temperature and b) vertical motion from 2-D solenoid simulation at 16 hours simulation time.

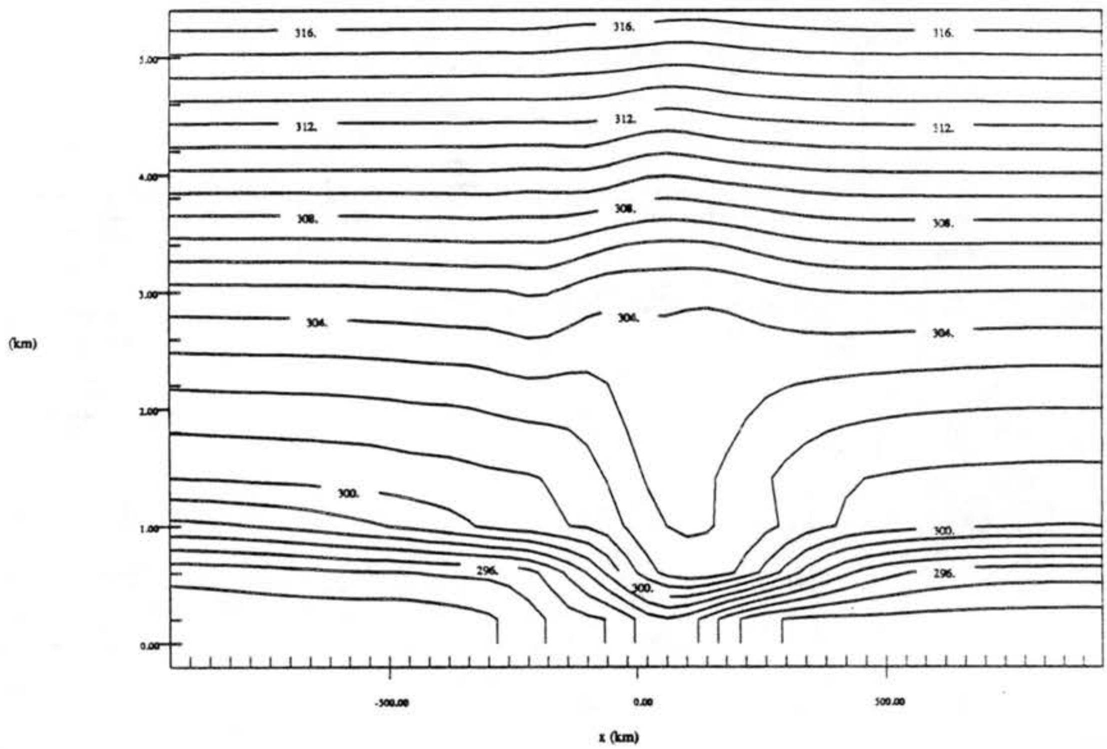

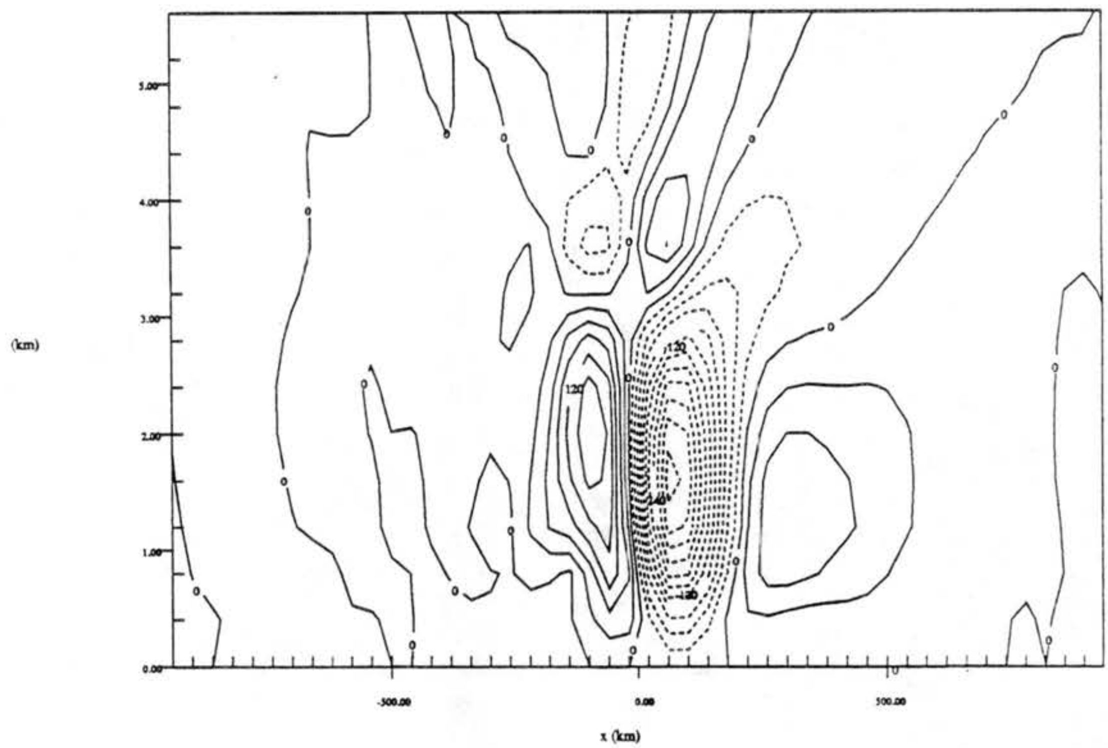

Figure 8.37: a) potential temperature and b) vertical motion from 2-D solenoid simulation at 20 hours simulation time.

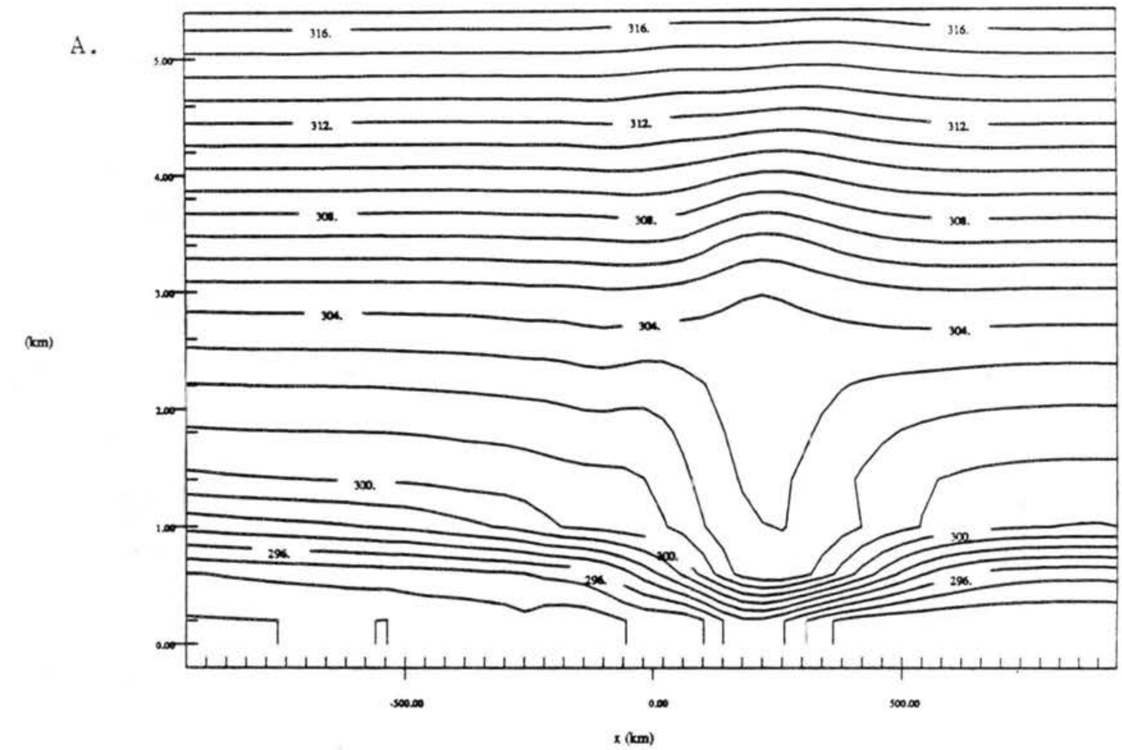

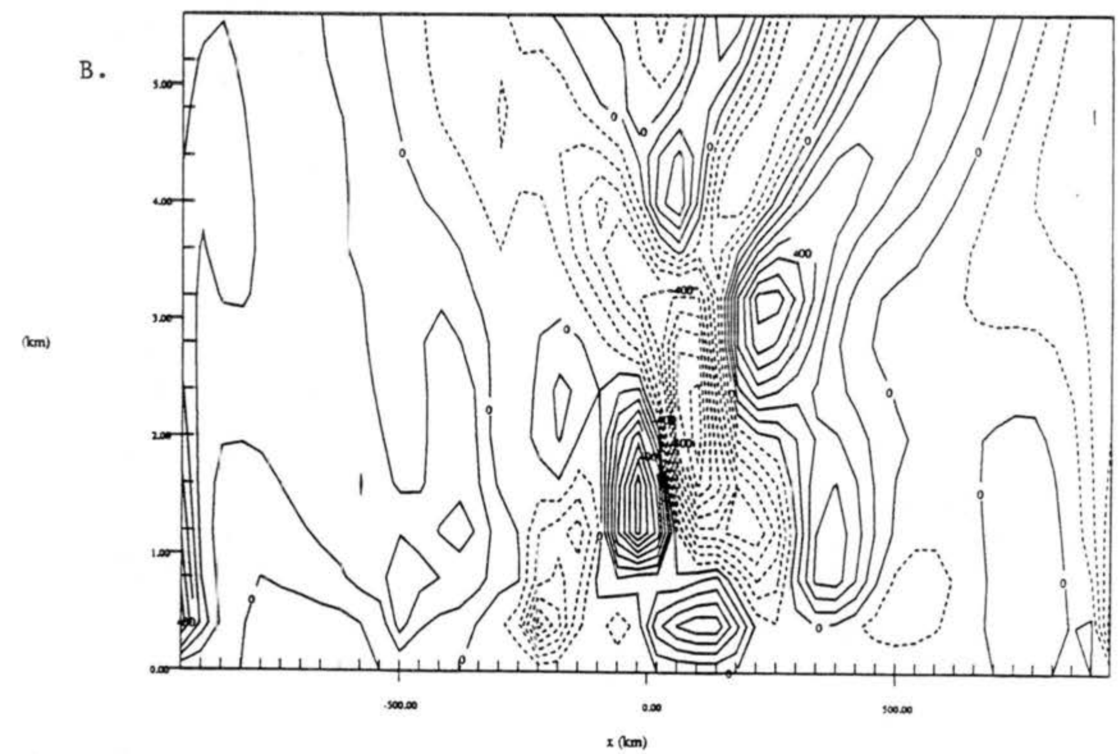

Figure 8.38: a) potential temperature and b) vertical motion from 2-D solenoid simulation at 24 hours simulation time.

responses through the night as the simulation shown here, although the wavelength of the gravity waves were shorter and the perturbations did not cover as large of an area.

- The structure of the solenoid is very similar to the meso-α-scale structure of an MCC. The lowest levels exhibit a cold perturbation due to the nocturnal cooling, the mid-levels are warm because of the advected elevated boundary layer, and the upper levels of the circulation have again a cold perturbation because of the upward motion at the top of the boundary layer. This temperature structure leads to the same circulations as an MCC also. From the v-component field (Figure 8.39), a mid-level cyclone and upper level anti-cyclone is evident. Note that this creates a potential vorticity structure (Figure 8.40) which is similar to an MCC also, so that the MCC in its initial stages has a potential vorticity source on which it may "feed."

- In the data composites performed by Maddox (1981) and Cotton et al. (1989), a mid-level shortwave was evident in the geopotential fields. It has heretofore been unexplained how and why this shortwave appears in the MCC genesis region at the proper time for MCC development. It is hypothesized that the shortwave is actually a reflection of the boundary layer solenoid structure, possibly modified by the deep convection and the MCS circulations. Since the solenoid has a low pressure perturbation up to the top of the boundary layer (which may be 600-700 mb or higher in the summer), a cross section through the mid-levels would show a shortwave feature. A 3.74 km pressure field at 0200 UTC from the 3-dimensional simulation (Figure 8.41) shows a shortwave that is coincident with the dry, elevated topography. This shortwave was not evident earlier in the simulation and could be seen to develop with the afternoon heating and the subsequent propagation of the solenoid. The vertical cross sections show that it is collocated with the warm perturbation of the solenoid.

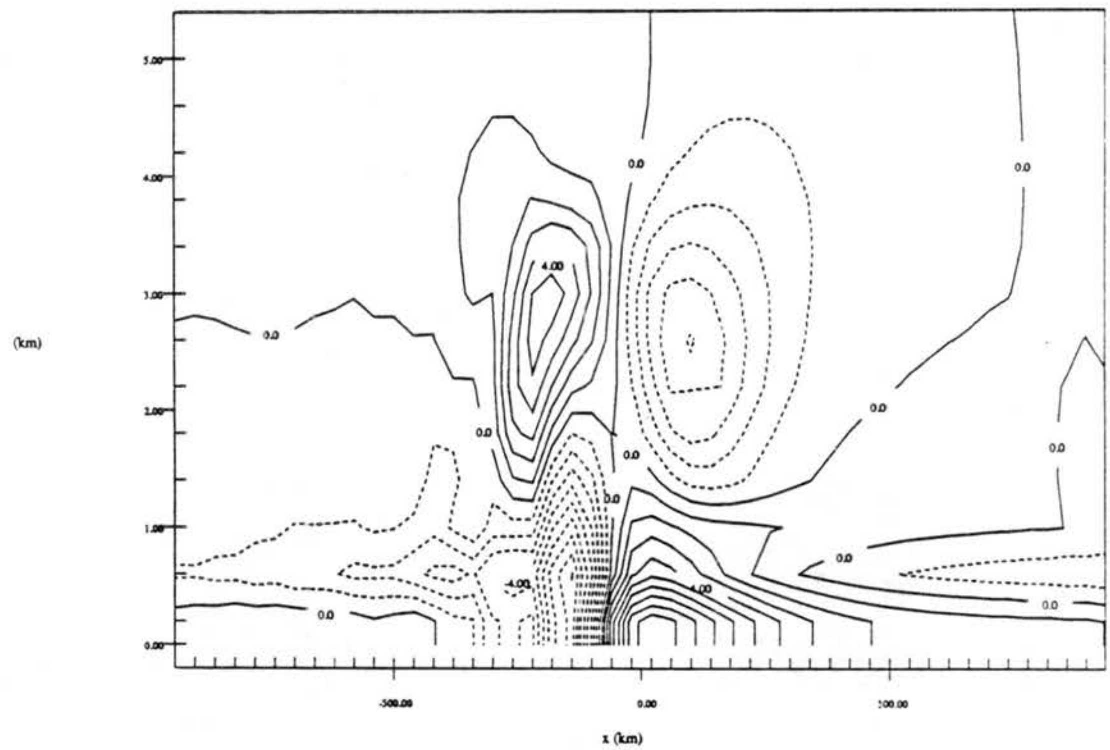

Figure 8.39: Normal wind component field from 2-D solenoid simulation at 16 hours simulation time.

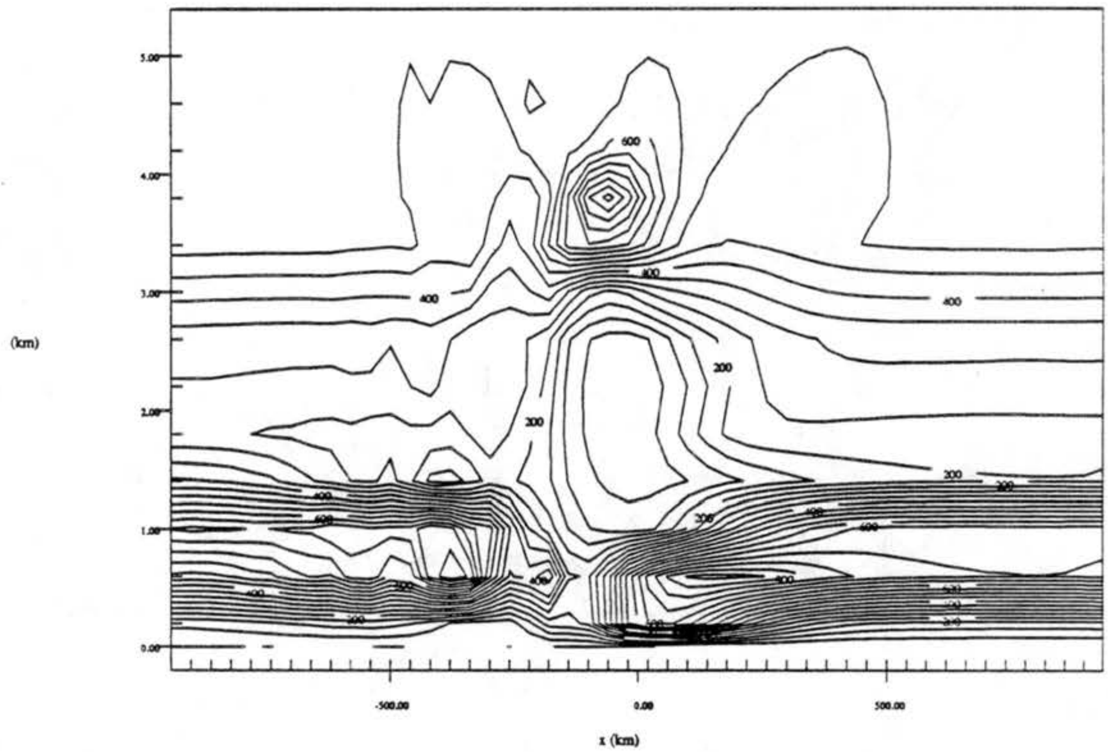

Figure 8.40: Potential vorticity field from 2-D solenoid simulation at 16 hours simulation time.

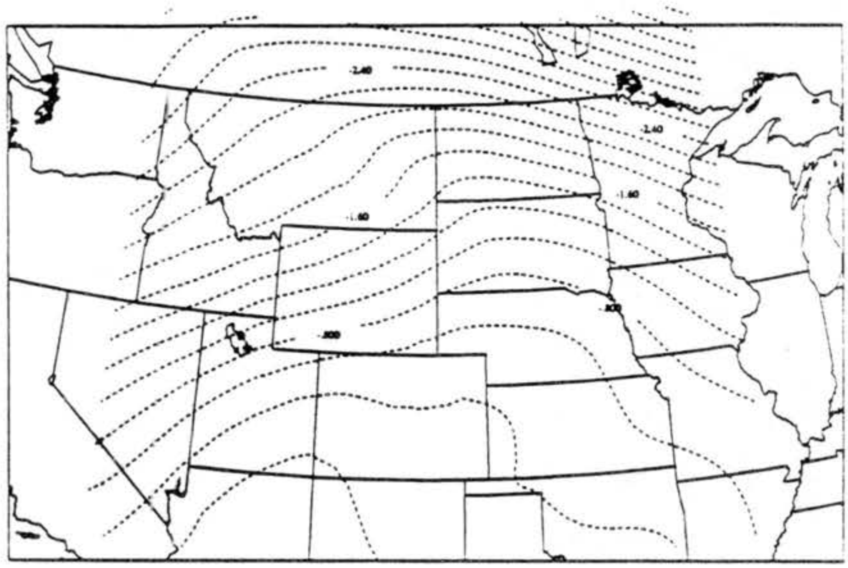

Figure 8.41: Perturbation Exner function at 3.74 km above sea level from higher resolution control run at 3 Aug 0200 UTC.

- This simulation also sheds some light on the moist soil sensitivity experiment discussed in the previous chapter. Recall in that simulation, all land areas were initialized with rather wet values of soil moisture content. The large differences in the results between the sensitivity experiment and control run were probably due to the lack of development of the solenoidal circulation since the soil heating differences between the mountains and plains were far less in the sensitivity run. This implies that the soil characteristics were more important than the topography in producing the simulated solenoid.

- The decoupling of the solenoid from the surface due to the nighttime cooling and its subsequent propagation toward the higher moisture supply of the lower plains may be one of the main reasons, along with the low-level jet, for the nocturnal preference of MCCs and MCSs over the U. S. High Plains.

- The mountain/plains elevation and surface characteristic differences are perhaps only one of the scenarios for producing a solenoid that could contribute to MCC development. Possibly the thermodynamic gradients across the central plain's "dry line" might be adequate to set up a solenoidal circulation. Differences in surface characteristics produced by previous convective systems, where large regions may have very wet soil adjoining areas where significant precipitation did not fall, could also set up conditions where solenoidal circulations might develop. Likewise, large irrigated areas next to non-irrigated areas such as in the Texas Panhandle could be large enough to produce the thermal anomalies necessary for a long-lived solenoid.

The next section will look at the remainder of the three-dimensional simulation as the mature MCC crossed the Dakotas.

8.3.3 Propagation of the MCC

By 0400 UTC, the MCC was reasonably mature. That is, the typical structure of an MCC had developed with a well resolved mean upward vertical motion region with mostly circular mid and upper level vapor and condensate fields. The MCC during the next

8 hours propagated from the western Dakotas to about the Minnesota border. Several interesting processes occurred during these 6 hours. The following will be focused upon: 1) a reorientation of the convective region from a line mostly parallel with the shear to a line perpendicular with the shear and, 2) the continued propagation of the solenoid.

8.3.4 Reorientation of convection

As the MCC crossed the Dakotas, the NWS radar summaries (Figure 6.5) showed that the strongest region of convection transformed from a line that was oriented parallel with the upper level winds in the western Dakotas to a line oriented perpendicular to the shear in the eastern Dakotas. The model also reproduced this behavior in the simulated convection and mid-level vertical motion fields. The mid-level vertical motion field is shown in Figure 8.42 for 0600, 0800, 1000, and 1200 UTC. The upward motion associated with the MCC appears more like a squall line although other aspects of squall line dynamics, such as a descending mid-level rear inflow jet, are not readily apparent possibly due to masking by the strong synoptic gradients.

Coincident with the reorientation, the speed of the convective system increased dramatically. In the western Dakotas, the center of the resolved vertical motion of the MCC moved eastward at 10-12 m/s consistent with the advective movement of the solenoid. During and after the reorientation starting about 0900 UTC, the speed increased to 20-22 m/s. There were no winds below 8 km above the ground in the vicinity of the MCC with an east-west velocity component of that magnitude.

A full dynamical explanation for this transformation is not clear. Several pieces of evidence, however, may shed some light on the change of orientation. The evidence may point to a shift of forcing for the convective system from the solenoid to an internal gravity wave response.

- The increased speed of 20-22 m/s was consistent with an internal gravity wave phase velocity.

- The meso-α-scale circulation of the MCC was weakening as it propagated into eastern South Dakota. This may have forced more of the latent heat release into the

A.

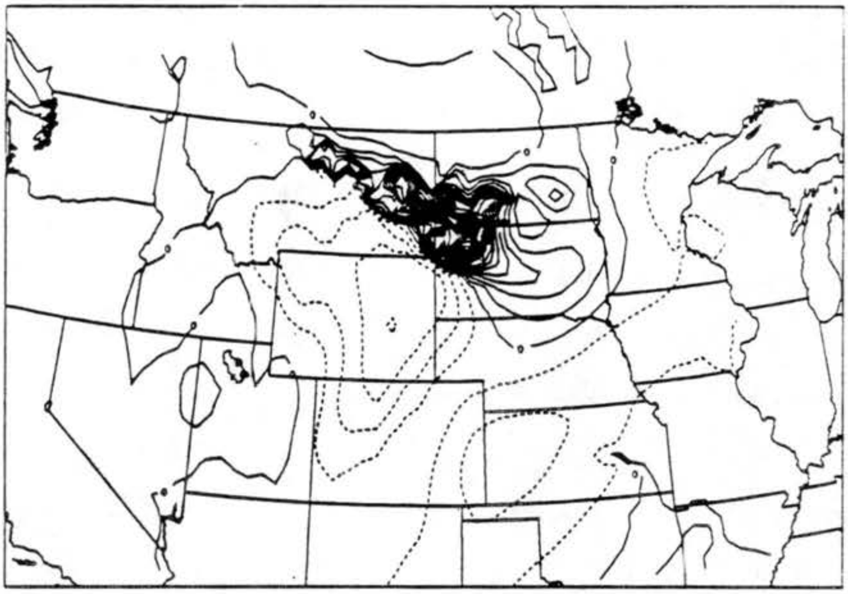

B.

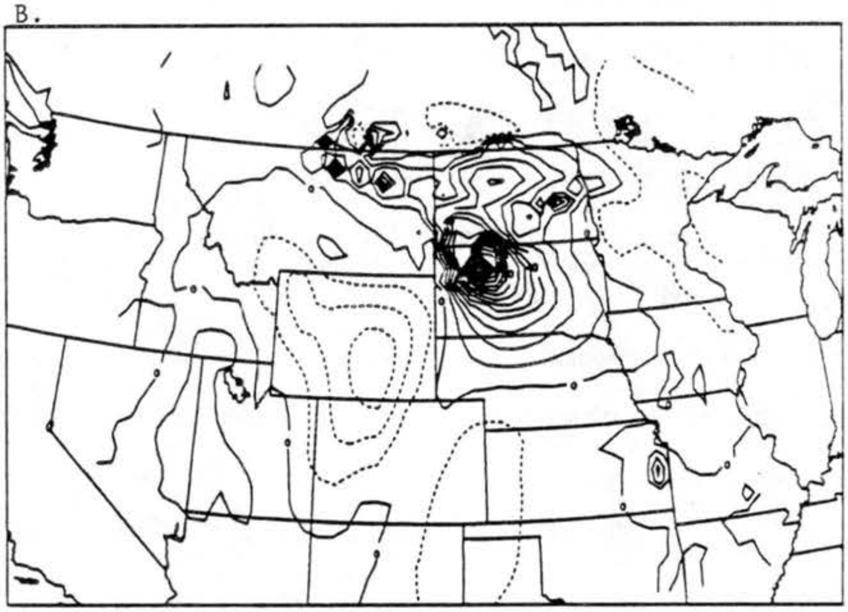

Figure 8.42: Vertical velocity field at 5.16 km above sea level from higher resolution control run at a) 3 Aug 0600 UTC, b) 3 Aug 0800 UTC, c) 3 Aug 1000 UTC, d) 3 Aug 1200 UTC.

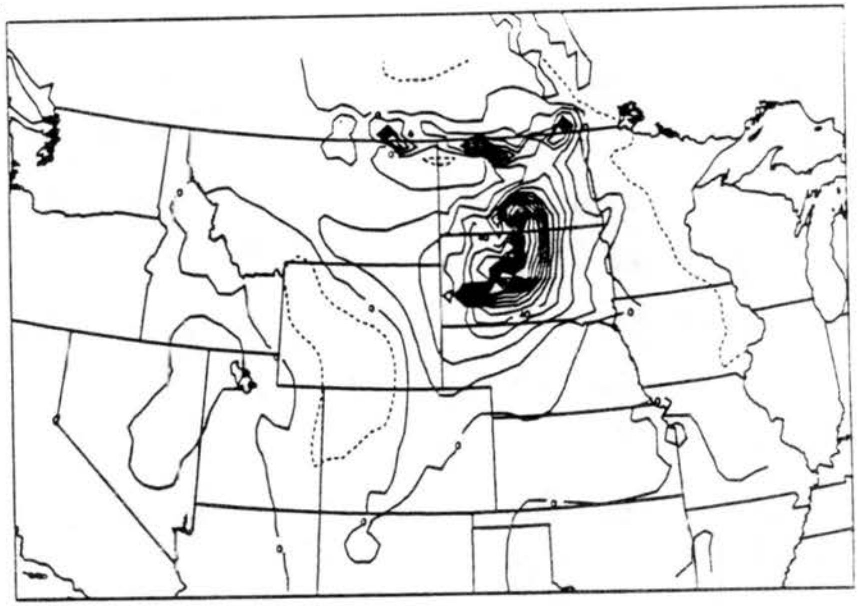

D.

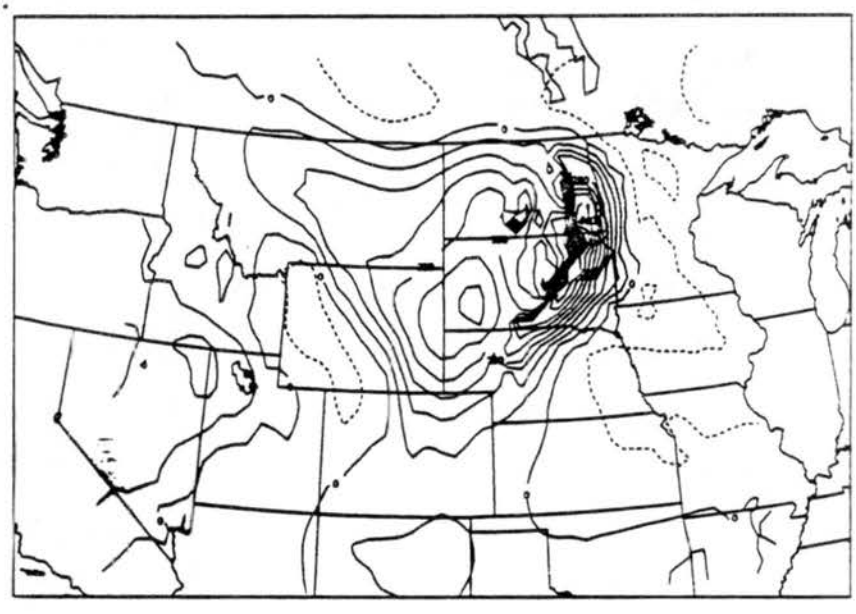

Figure 8.42: Continued.

convective scale, producing more of a transient gravity wave response, more typical of a squall line, which may have aided in the reorientation of the convection.

- A meso-α- to synoptic-scale mid-level thermal trough developed over the eastern Dakotas and Minnesota as the MCC propagated into the region (Figure 8.43). This would have increased the convective available potential energy (CAPE), possibly contributing to enhanced emphasis on the convective modes. The reasons for the development of this trough is not known; a possible explanation could be a thermally indirect forcing from the upper level outflow jet since the trough developed in the region and did not advect from the west.

8.3.5 Continued propagation of the mountain/plains solenoid

The solenoidal circulation produced by the elevation and surface temperature and moisture differences between the mountains and the lower plains continued to propagate across the Dakotas between 0600 UTC and 1200 UTC. The vertical cross sections of potential temperature and vertical velocity are shown in Figures 8.44-8.47. During the lifespan of the MCC, the location of the convection relative to the solenoid showed 3 distinct phases. The first phase, during the initiation of the system in central and eastern Montana, had the strongest convection near the center of the deeper mountain boundary layer where the low level upward motion was largest because of the convergence forced by the solenoid in conjunction with the upslope flow. In the second phase, after the solenoid had decoupled from the surface and moved into the western Dakotas, the strongest convection moved to the leading edge of the solenoid, where the strongest horizontal thermal gradients existed and where the "sea breeze-like front" should be expected the strongest. The third phase, as the MCC reached the eastern Dakotas, the strongest convection moved out in front of the solenoid, which probably led to the weakening of the resolved circulations. In addition, the faster propagation of the convection during the third phase may have led to the transformation to a line perpendicular to the shear as the convection outran the support of the solenoid.

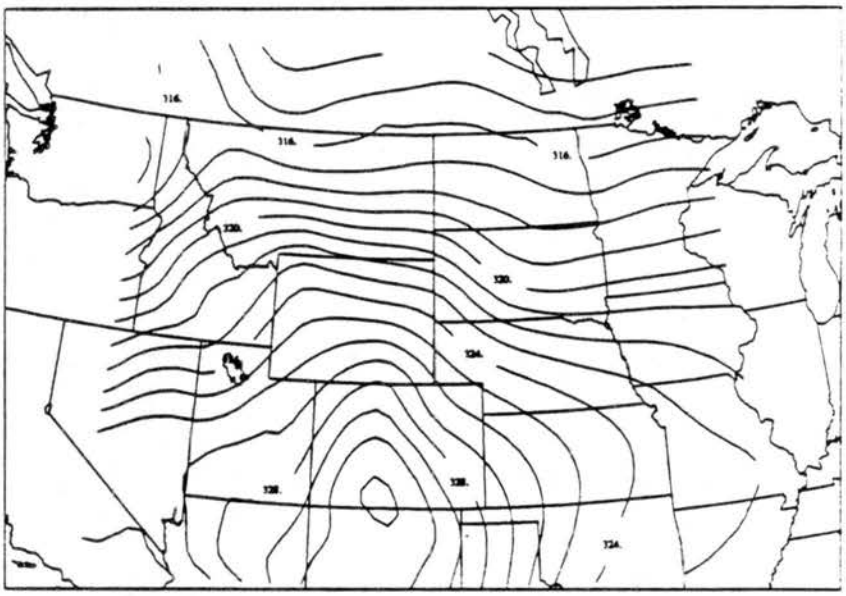

Figure 8.43: Potential temperature field at 5.16 km above sea level from higher resolution control run at 3 Aug 1000 UTC.

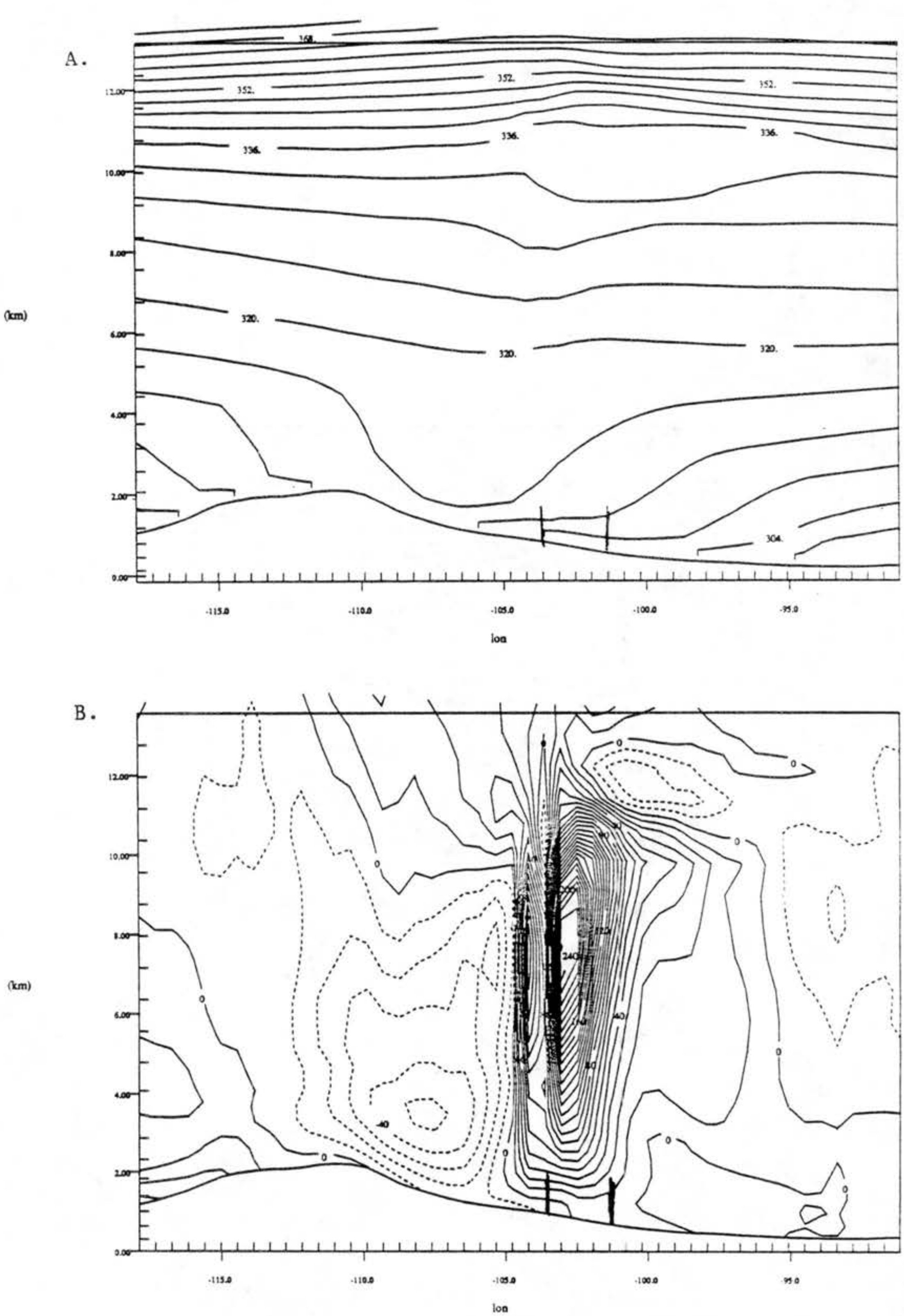

Figure 8.44: Vertical east-west cross section at 45.2° N from higher resolution control run at 3 Aug 0600 UTC. a) potential temperature, b) vertical velocity.

A.

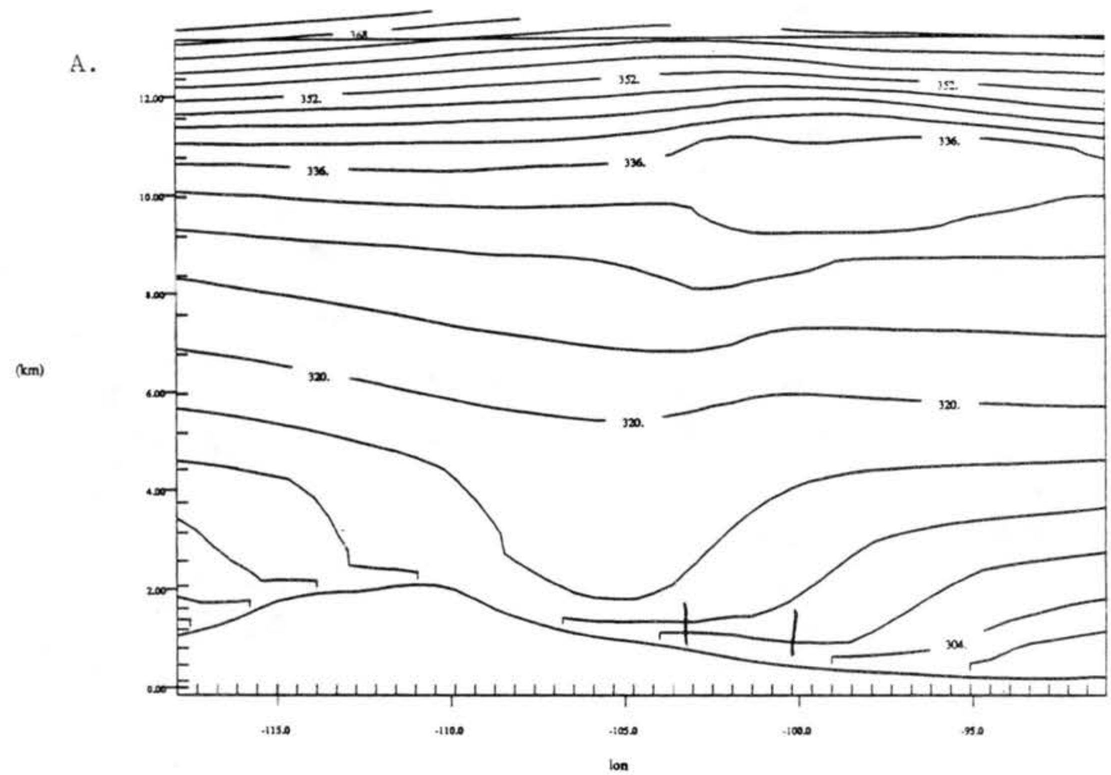

B.

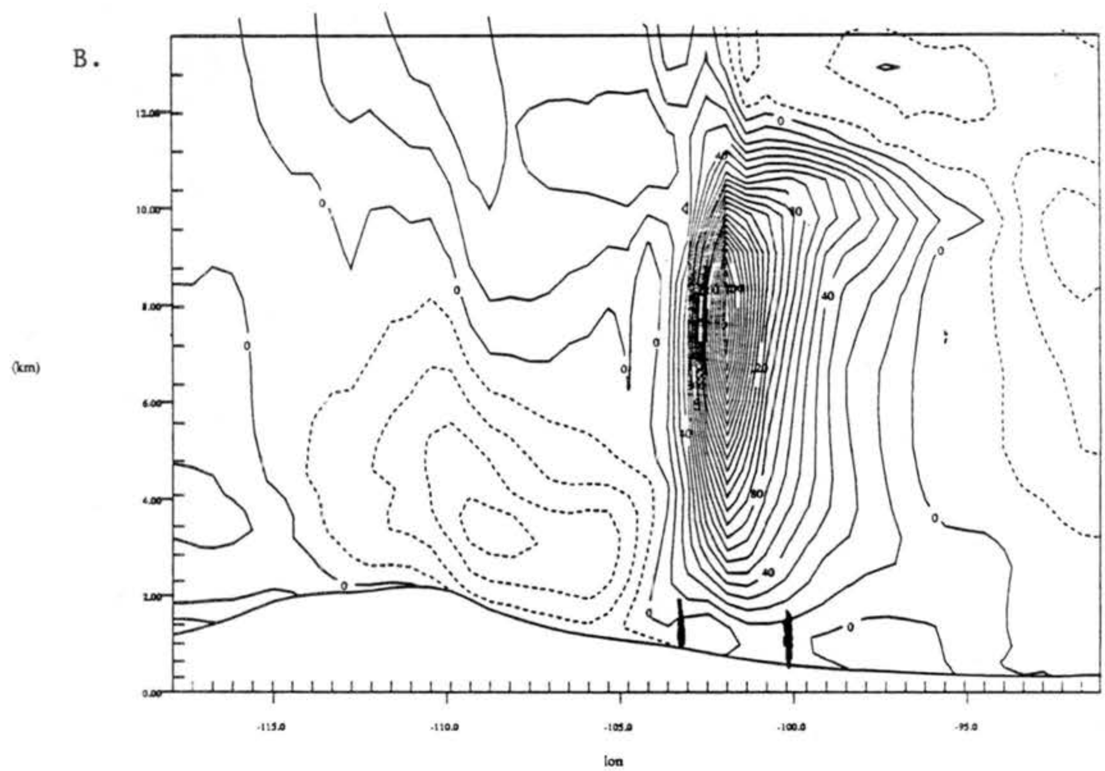

Figure 8.45: Vertical east-west cross section at 45.2° N from higher resolution control run at 3 Aug 0800 UTC. a) potential temperature, b) vertical velocity.

A.

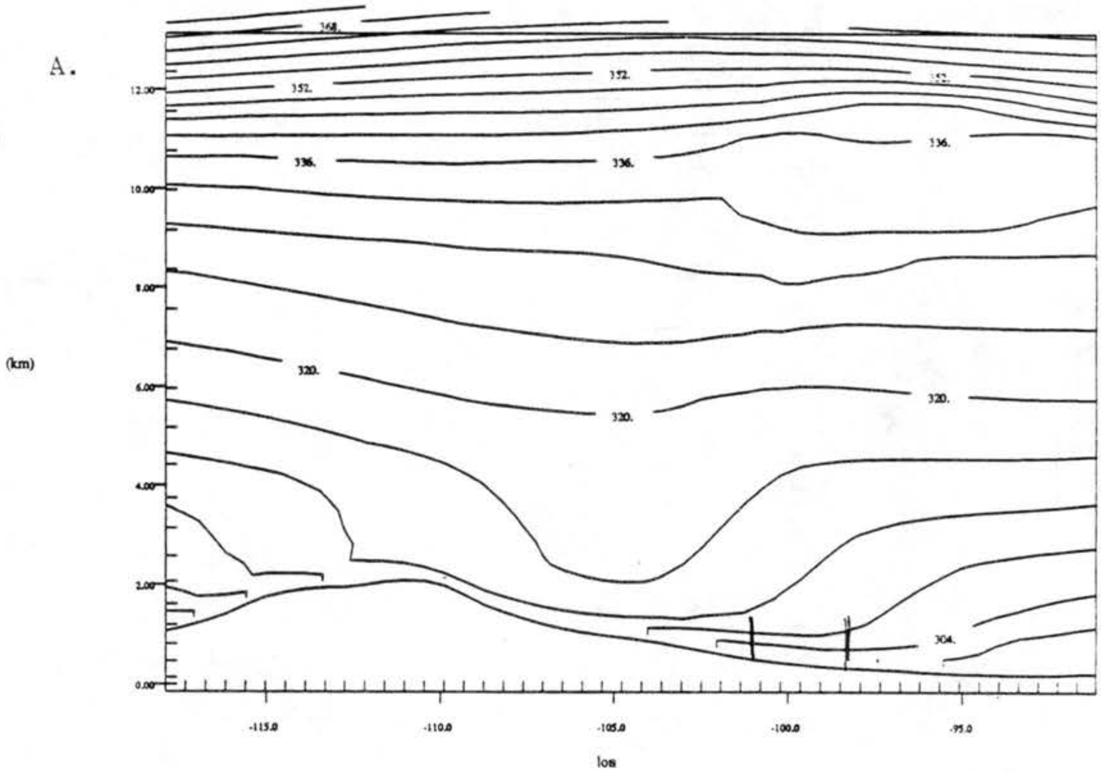

B.

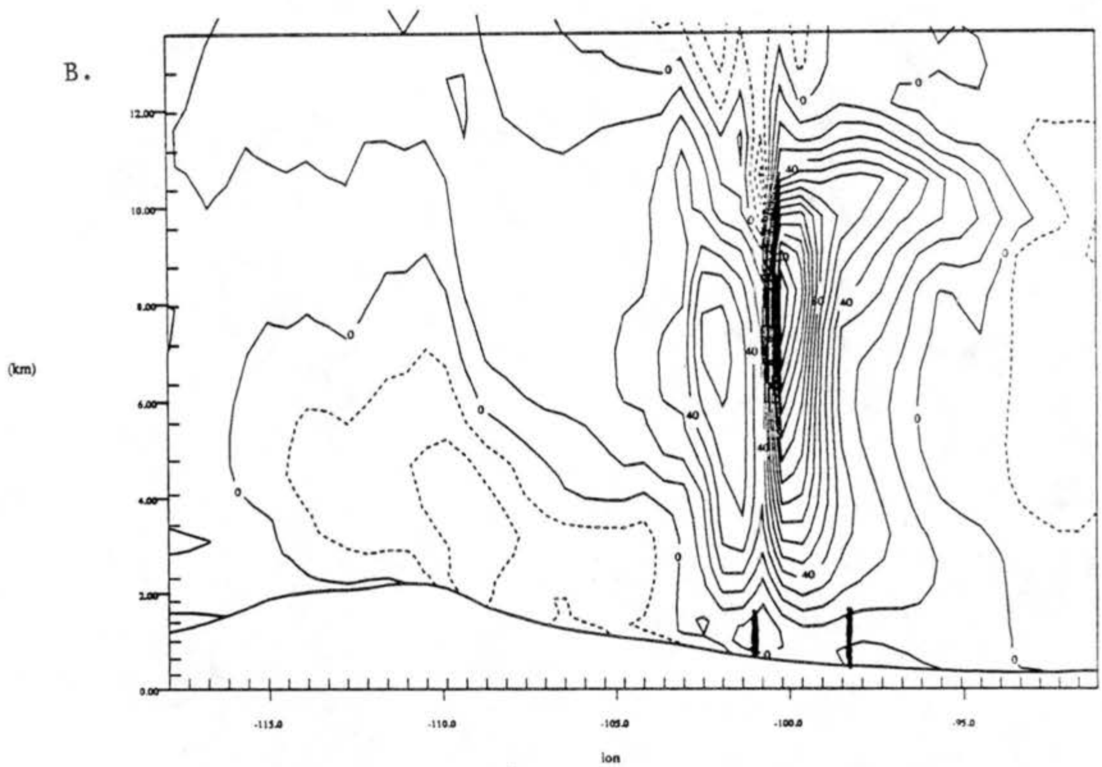

Figure 8.46: Vertical east-west cross section at 45.2° N from higher resolution control run at 3 Aug 1000 UTC. a) potential temperature, b) vertical velocity.

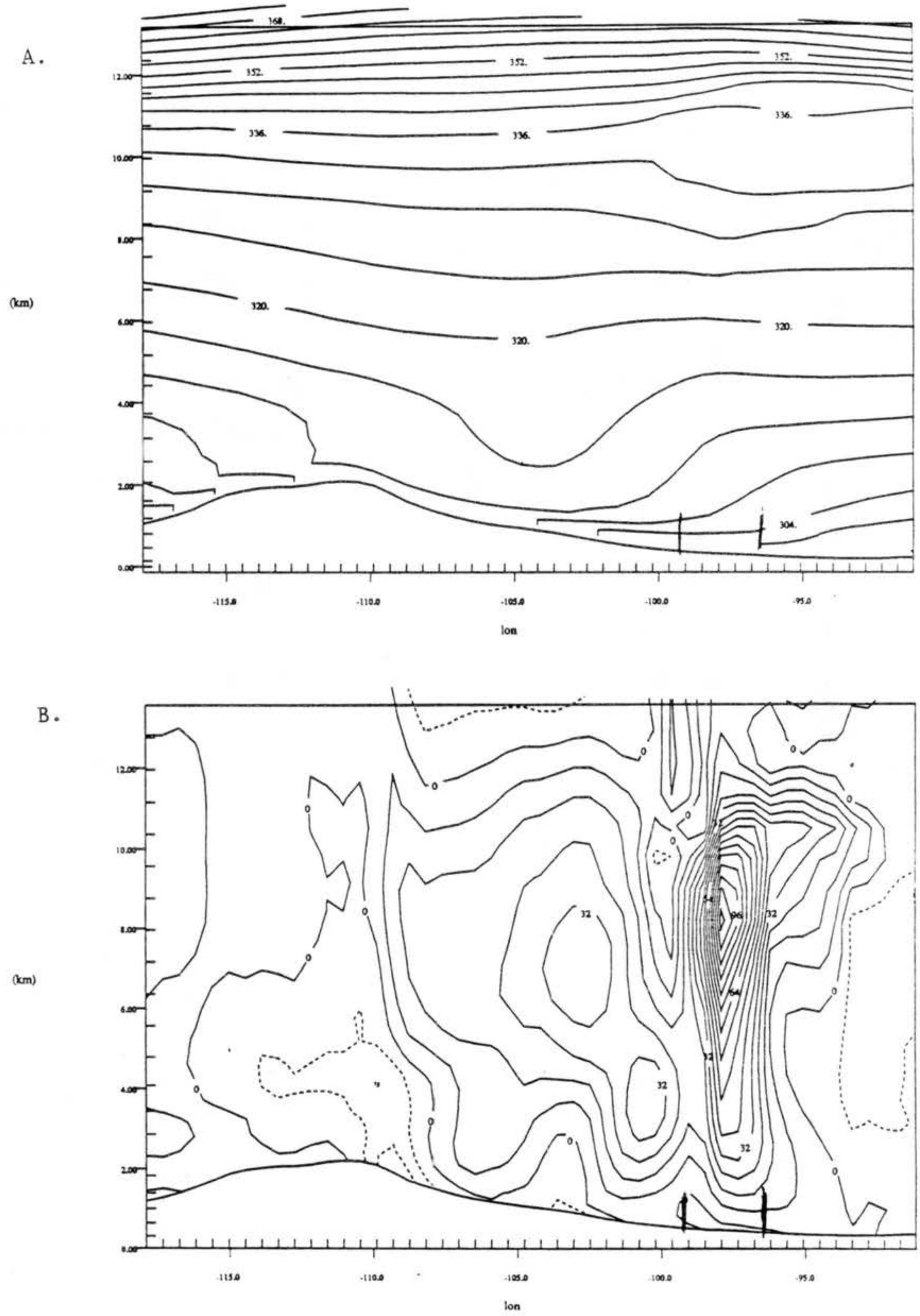

Figure 8.47: Vertical east-west cross section at 45.2° N from higher resolution control run at 3 Aug 1200 UTC. a) potential temperature, b) vertical velocity.

These 3 phases can be seen quite clearly from the vertical motion fields in conjunction with the convective precipitation rates. The first phase remained until about 0200 UTC, the second phase from 0200 to about 0900 UTC, and the third phase from about 0900 UTC on. Between each of the phases, a separation of the mesoscale mid-level upward motion into 2 distinct cores can be seen as the convection seemed almost to discontinuously propagate ahead of the resolved vertical motion. By the end of the simulation at 1200 UTC, a broad area of upward motion with a maximum at 4 km, was left well behind the leading edge of the convection and the much stronger updraft core associated with the MCC. Although the mid and upper level vertical motion is most likely a reflection of synoptic scale motions, the low-level center is probably forced from the remnants of the elevated solenoid.

The fact that the convection moved faster than the solenoid is not surprising since, because of the vertical shear, the advective speeds at low levels were weaker than the mid and upper levels. More surprising was the importance of the low-level forcing of the solenoid to maintain the coupling with the convective system through much of the MCC's lifetime in spite of the strong vertical shear.

8.4 Description of the dry sensitivity experiment

In analyzing the results of the MCC simulation, it is difficult to isolate cause and effect relationships among the various features of the simulation. For instance, the surface low over the Montana-Wyoming region deepened near the time of the development of the MCC. Did the deepening low increase convergence into the region to produce the convection or did the convection, along with possibly some feedback mechanism, help to deepen the low pressure? How did the convection affect the structure and propagation of the solenoid? Was the solenoidal low level forcing maintained without the interaction (downdrafts, pressure affects, etc.) of the convection? To attempt to isolate the effects of the convection on the mesoscale, the 45 km resolution simulation was repeated without the convective parameterization and its associated heating and moistening tendencies.

Everything else was identical including the resolved latent heat release. This was inconsequential, however, because the resolved scales did not produce significant amounts of condensate in this simulation.

Neither an MCC or any of the mesoscale circulations associated with the convective system developed in this simulation, implying that the meso-β scale convective heating was necessary for the production of the system. This is consistent with several other previous studies (e.g., Perkey and Maddox, 1985) where the convective parameterization tendencies were necessary to form a system with the characteristics of an MCC circulation.

It was interesting to track the propagation of the mountain/plains solenoid in this simulation and to compare it with the structure of the solenoid in the control simulation. At 0000 UTC, the vertical motion fields at 3.74 km ASL (Figure 8.48) were very similar between the two runs with the center of the upward motion located at about the same place with the same magnitudes. Two hours later at 0200 UTC (Figure 8.49), the control run had shifted the center toward the east along the axis of the dry simulation's upward motion. This was still the case for the next 6 hours (Figures 8.50-52) as the control run's convection and the dry simulation's solenoid maintained the same relationship to each other; the convection in the control run was located along the axis of the low-level upward motion near the leading edge of the solenoid in the dry run.

By 1000 UTC (Figure 8.53), the axis of the upward motion region of the solenoid in the dry simulation had shifted from a northwest-southeast configuration (perpendicular to the low-level jet) to a north-south configuration (perpendicular to the upper level jet) possibly due to differential advective velocities since there was north-south shear in the region. This also coincided with the time that the convective region in the control run had transformed to a north-south configuration, as discussed above, and had moved out in front of the solenoid. By 1200 UTC (Figure 8.54), the main upward motion region had clearly moved well out in front of the solenoid in the control run (Figure 8.54a). However, a secondary center can be seen behind the convective area, close to where the dry simulation placed the center of the solenoid (Figure 8.54b).

A series of vertical cross sections through 45.2° N shows the comparison of the vertical structure of the vertical motion between the dry and control runs (Figure 8.55-8.62). In

A.

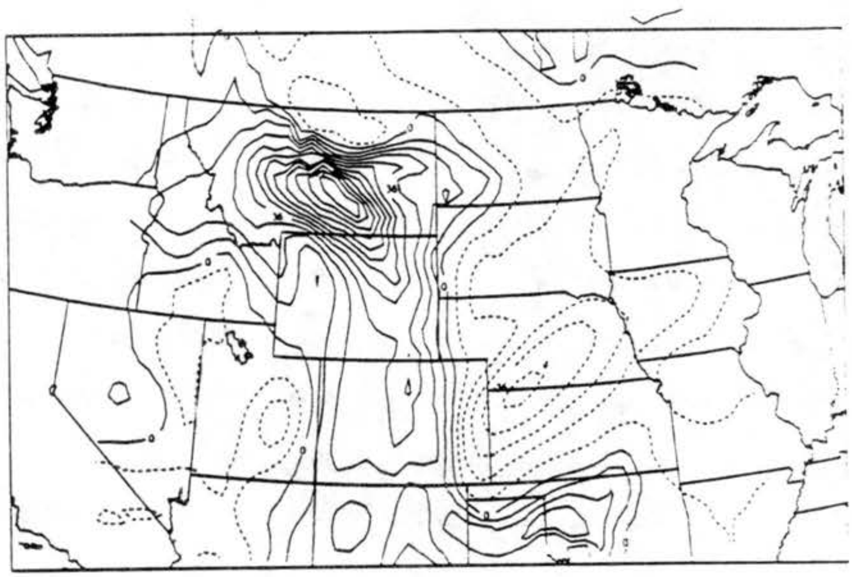

B.

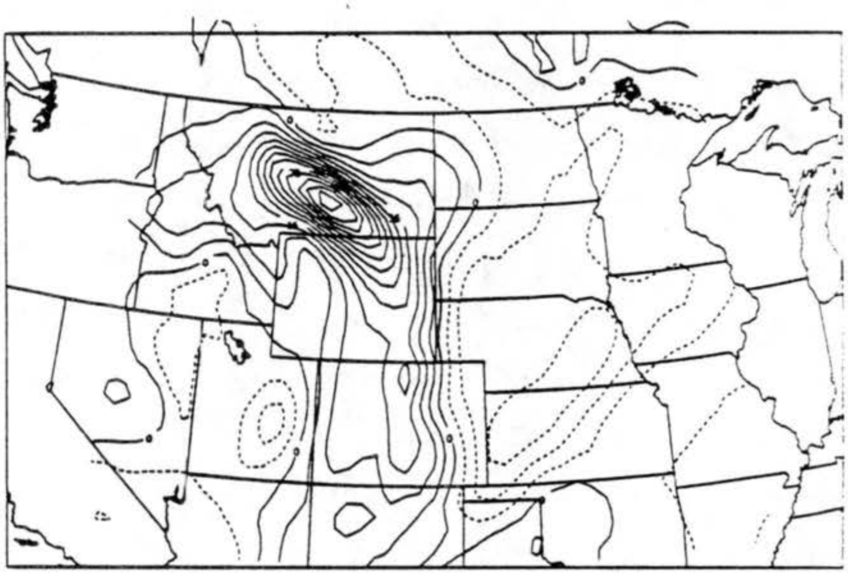

Figure 8.48: Vertical velocity field at 3.74 km above sea level at 3 Aug 0000 UTC. a) higher resolution control run, b) higher resolution dry run.

A.

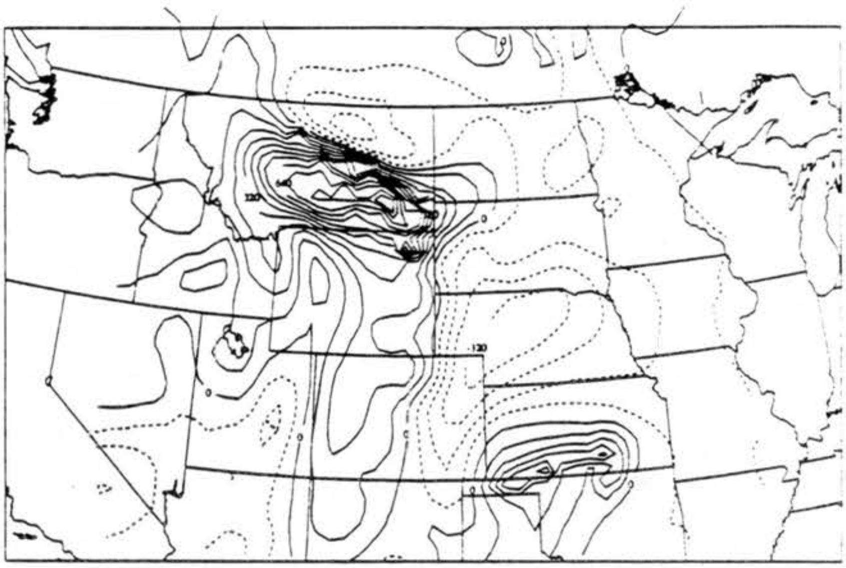

B.

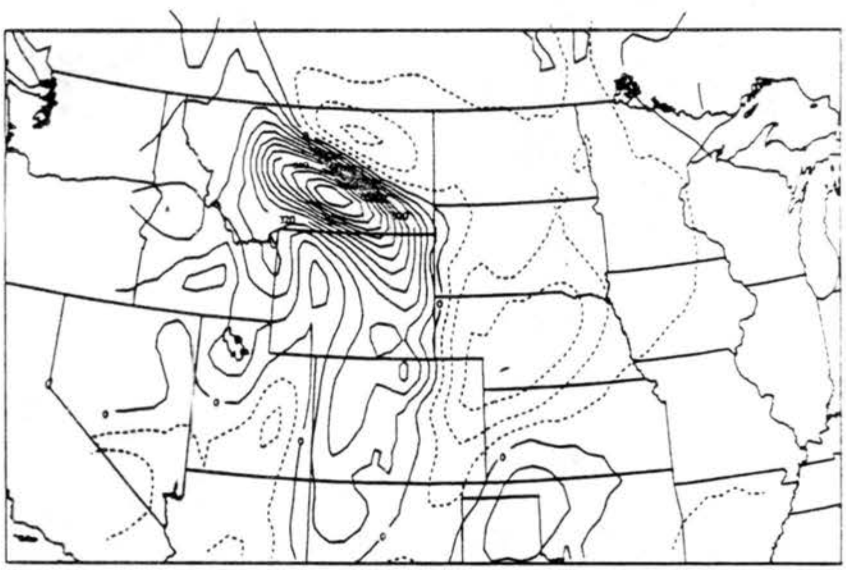

Figure 8.49: Vertical velocity field at 3.74 km above sea level at 3 Aug 0200 UTC. a) higher resolution control run, b) higher resolution dry run.

A.

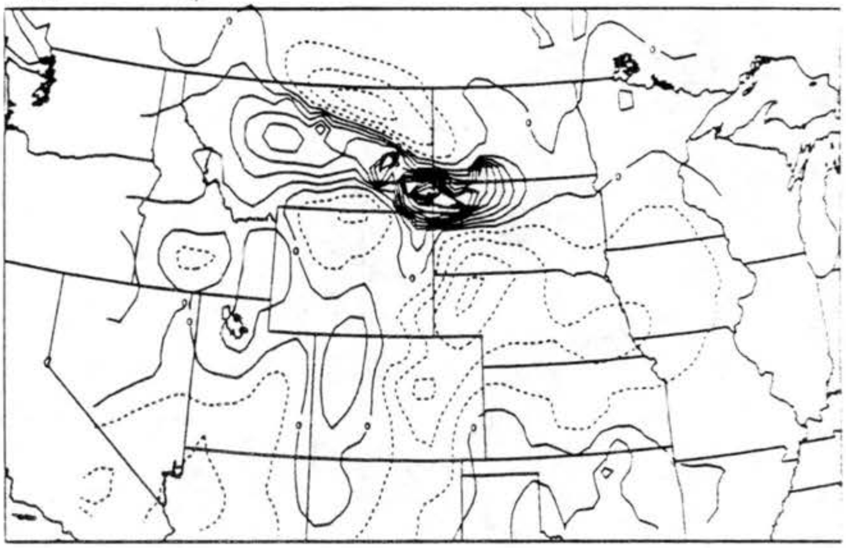

B.

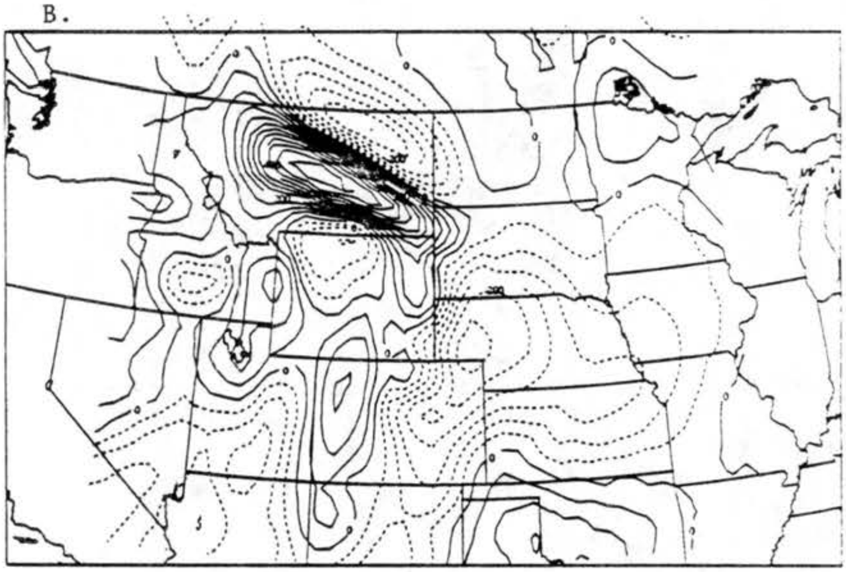

Figure 8.50: Vertical velocity field at 3.74 km above sea level at 3 Aug 0400 UTC. a) higher resolution control run, b) higher resolution dry run.

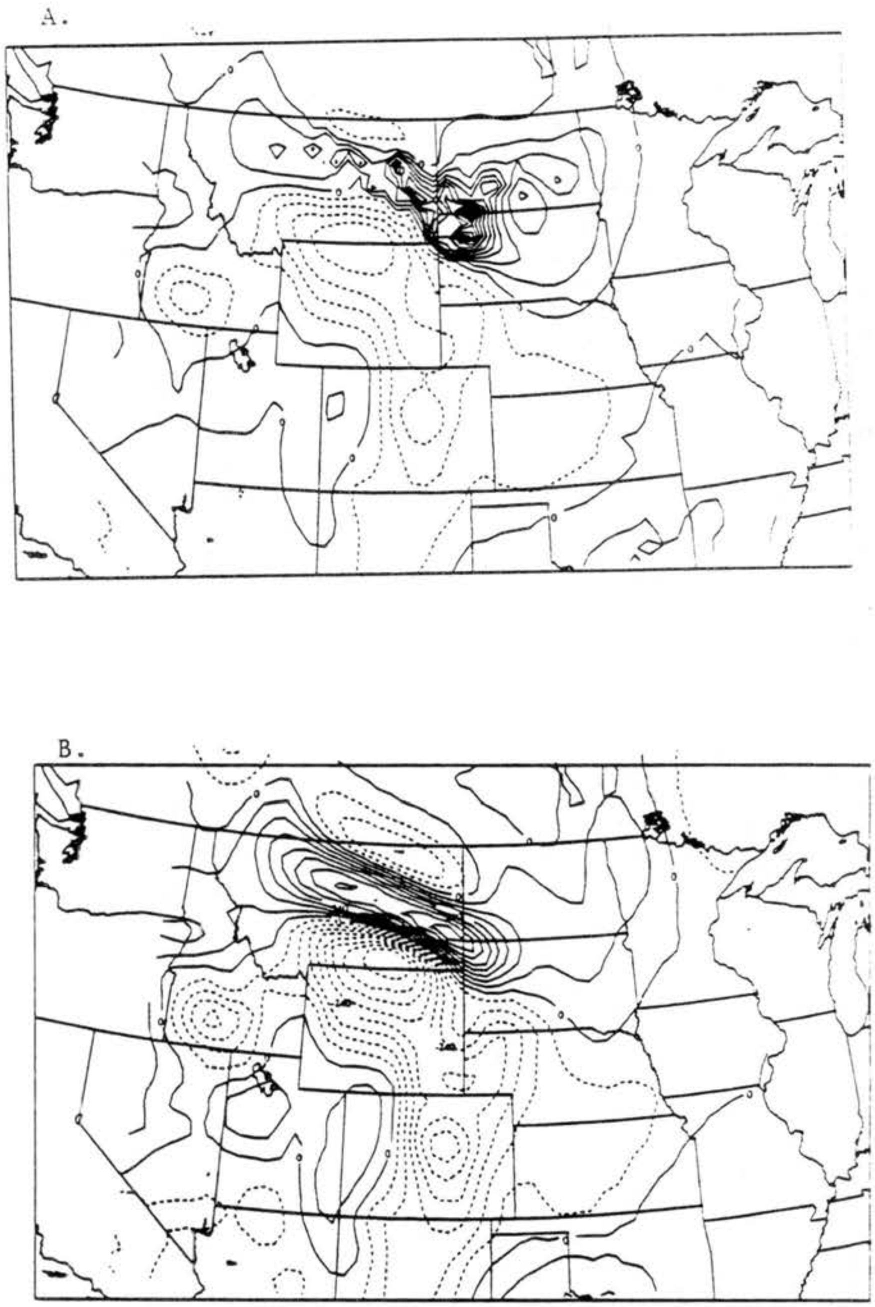

Figure 8.51: Vertical velocity field at 3.74 km above sea level at 3 Aug 0600 UTC. a) higher resolution control run, b) higher resolution dry run.

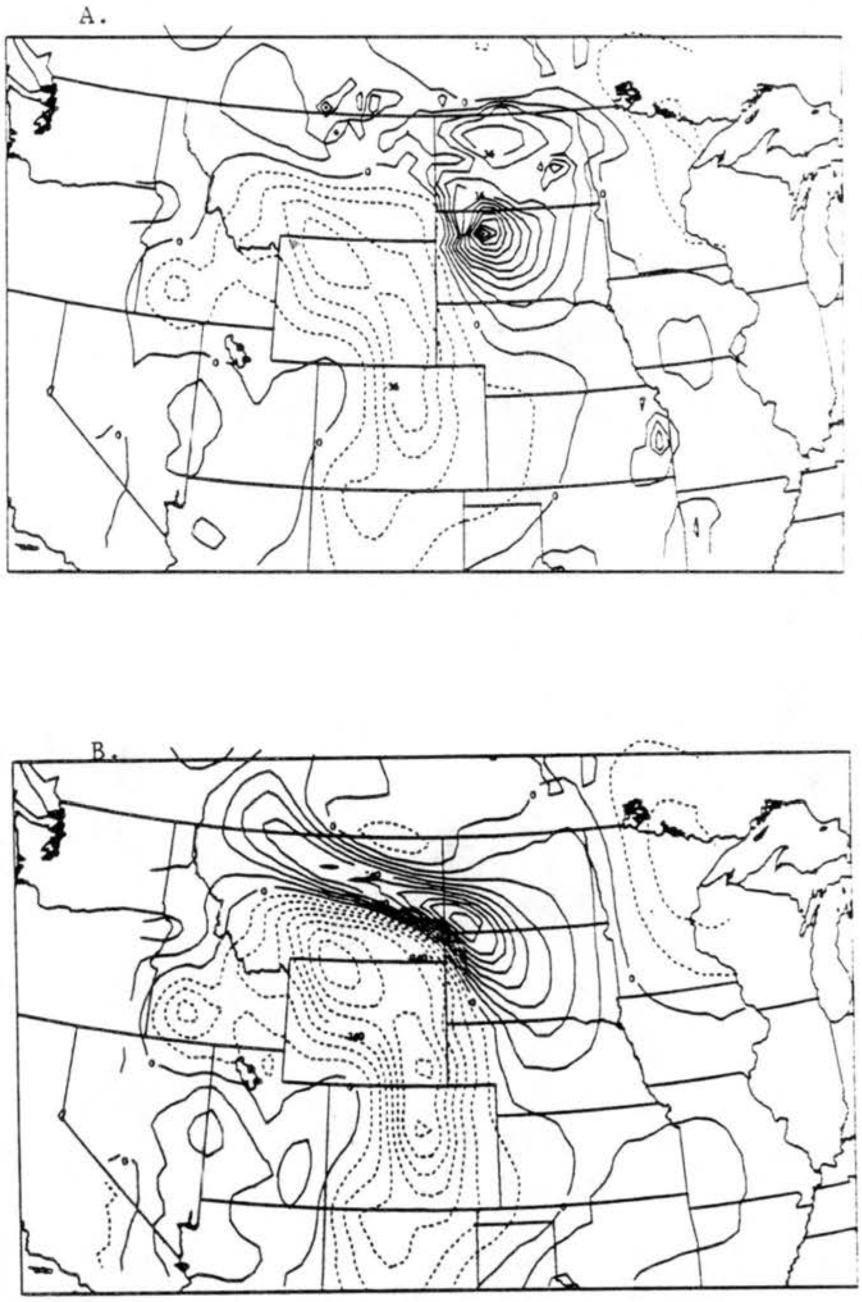

Figure 8.52: Vertical velocity field at 3.74 km above sea level at 3 Aug 0800 UTC. a) higher resolution control run, b) higher resolution dry run.

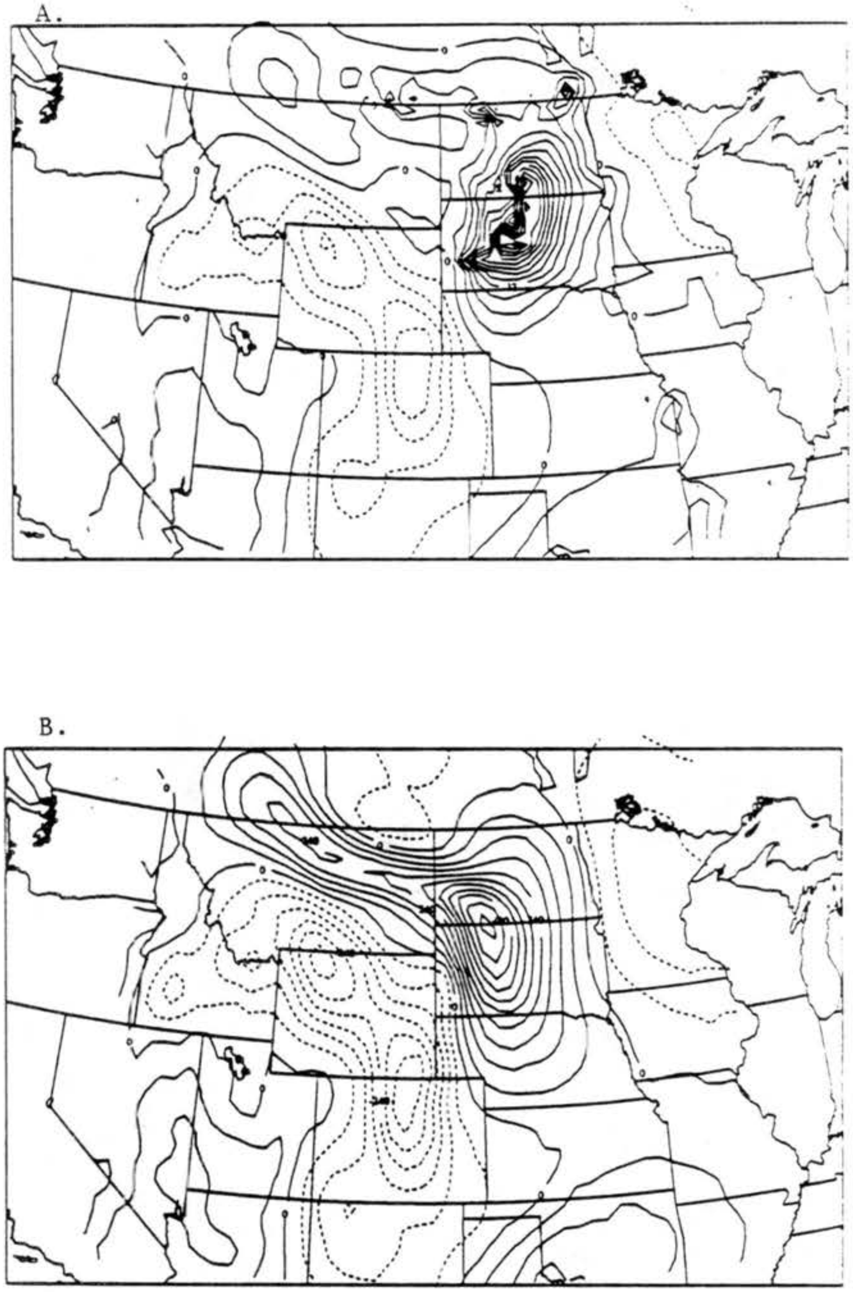

Figure 8.53: Vertical velocity field at 3.74 km above sea level at 3 Aug 1000 UTC. a) higher resolution control run, b) higher resolution dry run.

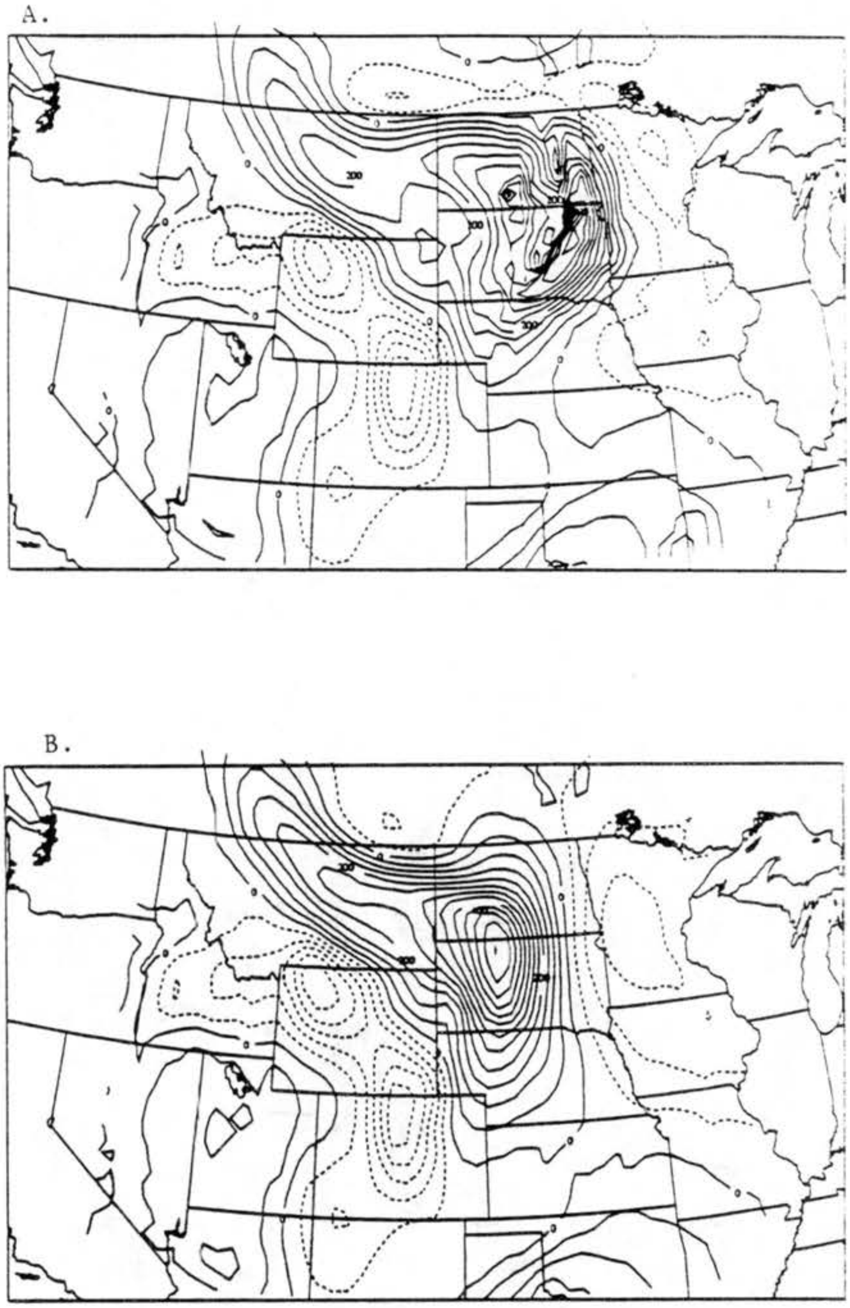

Figure 8.54: Vertical velocity field at 3.74 km above sea level at 3 Aug 1200 UTC. a) higher resolution control run, b) higher resolution dry run.

the control run between 0000 UTC and 0600 UTC, the upward motion center of the MCC was toward the leading edge of the region where the dry simulation placed the solenoid. The upward motion of the solenoid, modified by the convection in the control run, was much deeper than the upward motion in the dry run as was also shown by Tripoli and Cotton (1989) and Song (1987). By 1000 UTC, the split between the convective region and the solenoid was evident in the control run and at 1200 UTC the split can be seen clearly. The MCC in the control run left behind a low and mid-level vertical motion structure that closely resembled the solenoid produced by the dry run both in shape and location (about 101° W). The upward motion in the low and mid-levels of the solenoid was weaker in the control run.

The main focus of this sensitivity experiment was to show that the simulated MCC in the control run, at least during the first eight hours of its life, tracked very closely with a mountain/plains solenoid produced by a simulation without convective effects. As the control run's MCC outran the support of the solenoid, it left behind a circulation which closely resembled the solenoid in the dry run which was unmodified by the convection.

8.5 Microphysics sensitivity

All of the previous simulations that were described did not have the resolvable microphysics and precipitation processes activated. Any supersaturation was condensed and the latent heat was released, but the condensate did not precipitate. This section will present results from the 45 km resolution simulation with these grid-resolved processes activated.

The microphysical parameterizations will not affect the simulation until there is a significant amount of condensate present, that is, cloud water will not be converted to other species until enough cloud water exists. Obviously, the actual amount is dependent on various factors such as which species to be converted to, temperature, diagnosed nuclei concentrations, etc. This simulation was restarted from the control run at 0000 UTC, before there was significant condensate developed from the convection in the Montana region. The condensate species from the microphysical parameterizations used in this

A.

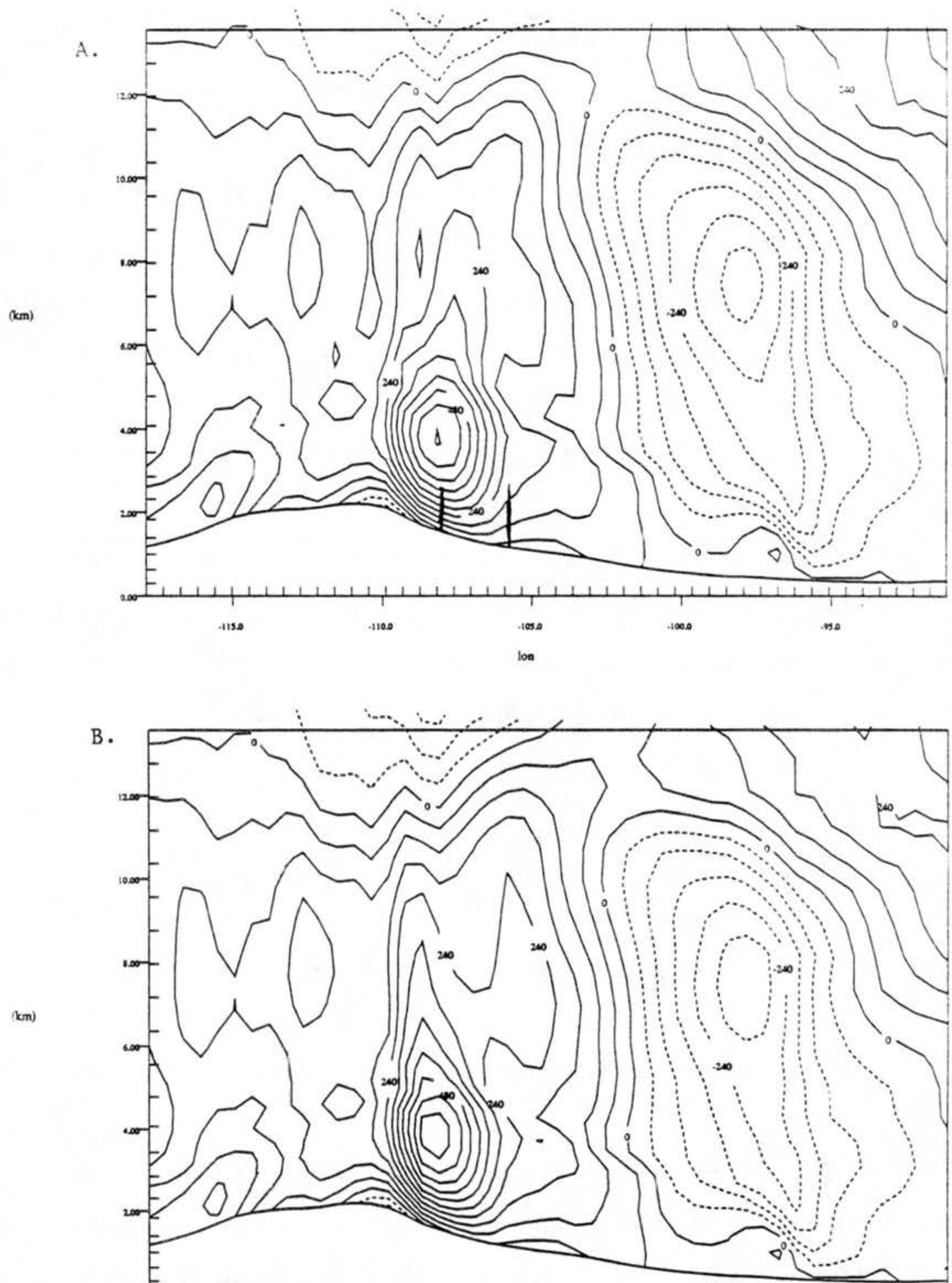

B.

Figure 8.55: Vertical east-west cross section of vertical velocity at 45.2° N from at 2 Aug 2200 UTC. a) higher resolution control run, b) higher resolution dry run.

A.

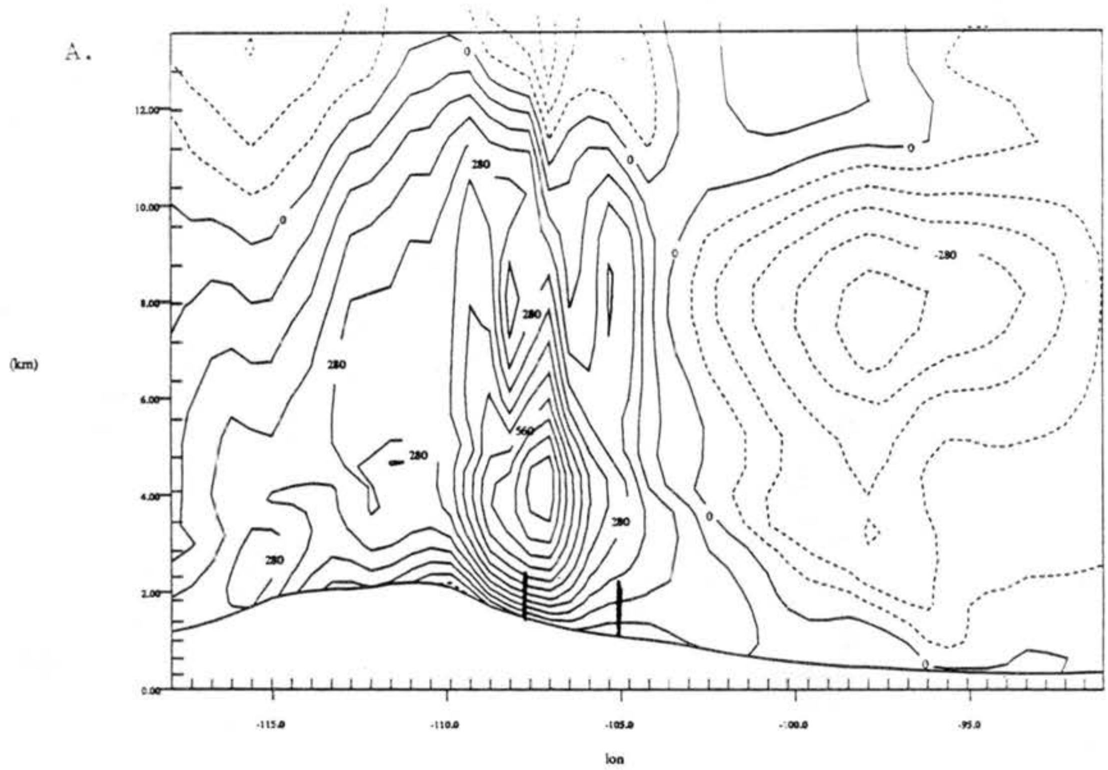

B.

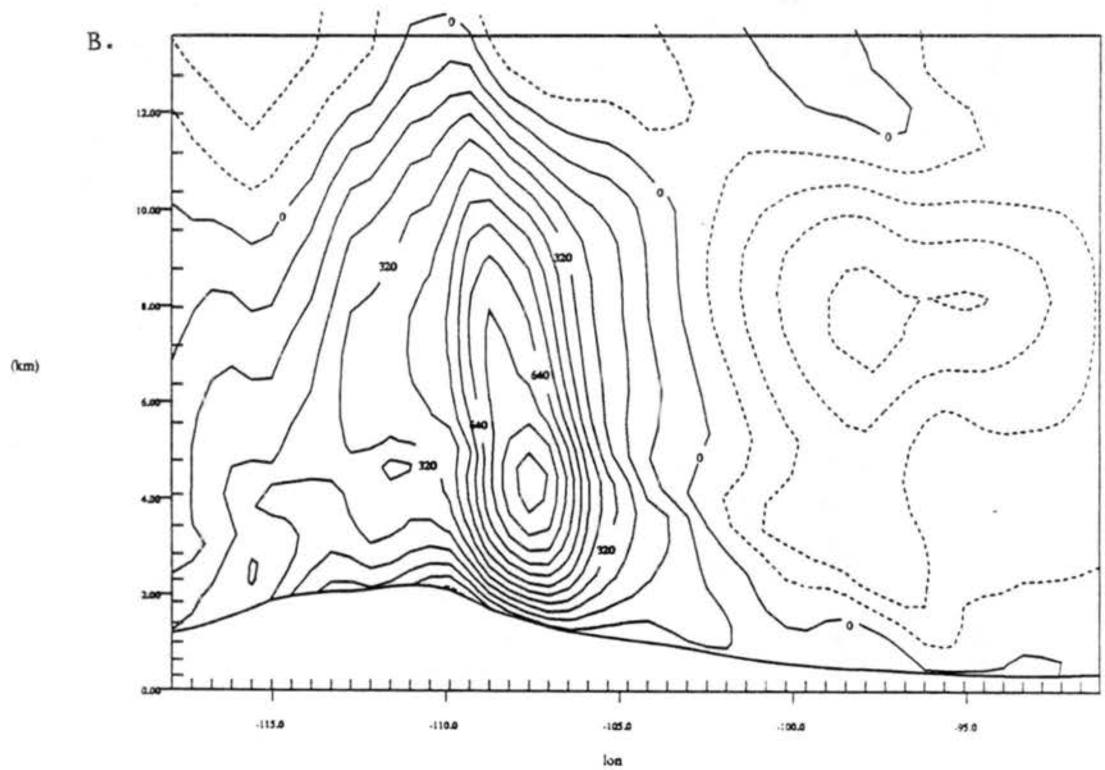

Figure 8.56: Vertical east-west cross section of vertical velocity at 45.2° N from at 3 Aug 0000 UTC. a) higher resolution control run, b) higher resolution dry run.

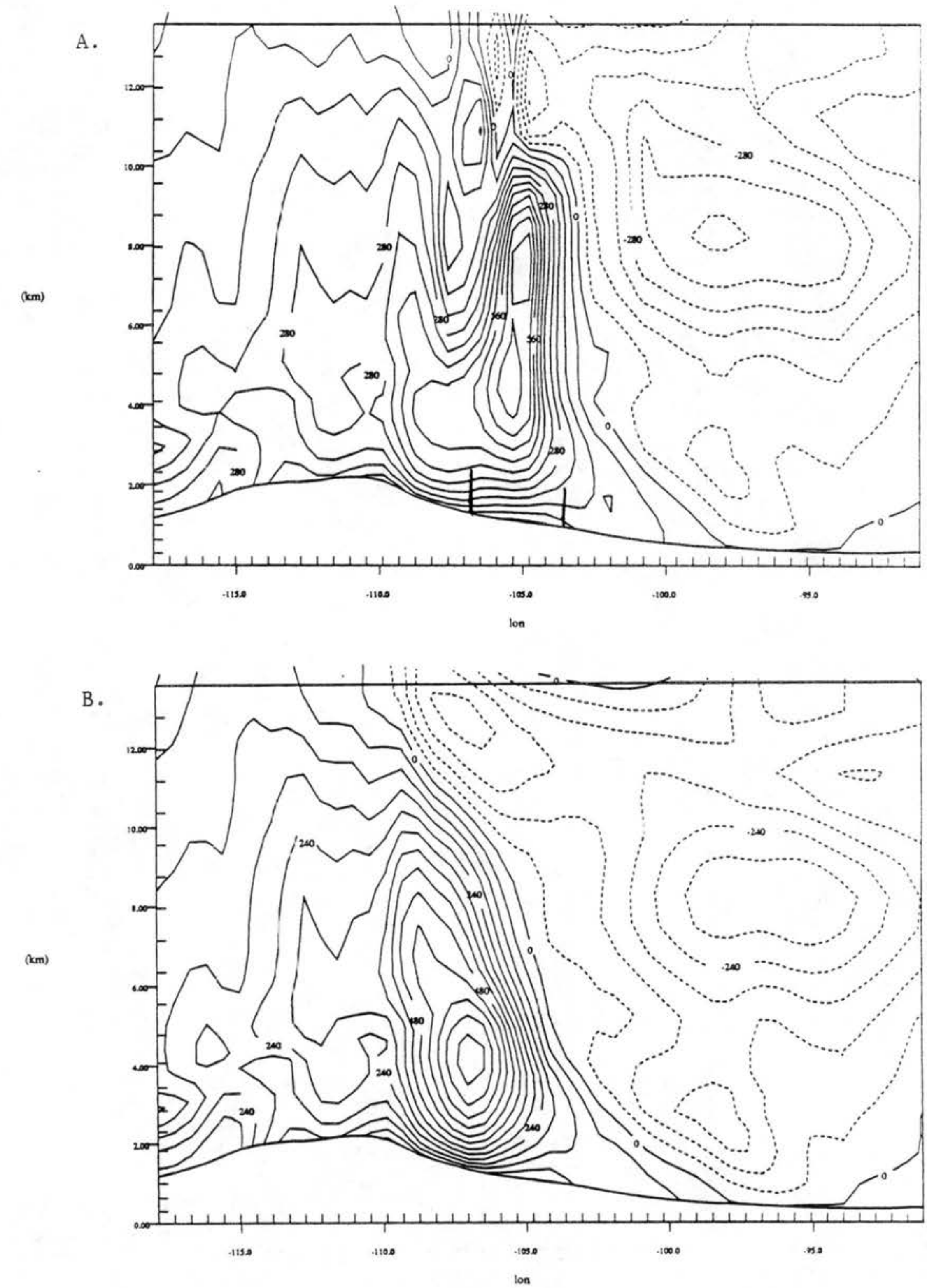

Figure 8.57: Vertical east-west cross section of vertical velocity at 45.2° N from at 3 Aug 0200 UTC. a) higher resolution control run, b) higher resolution dry run.

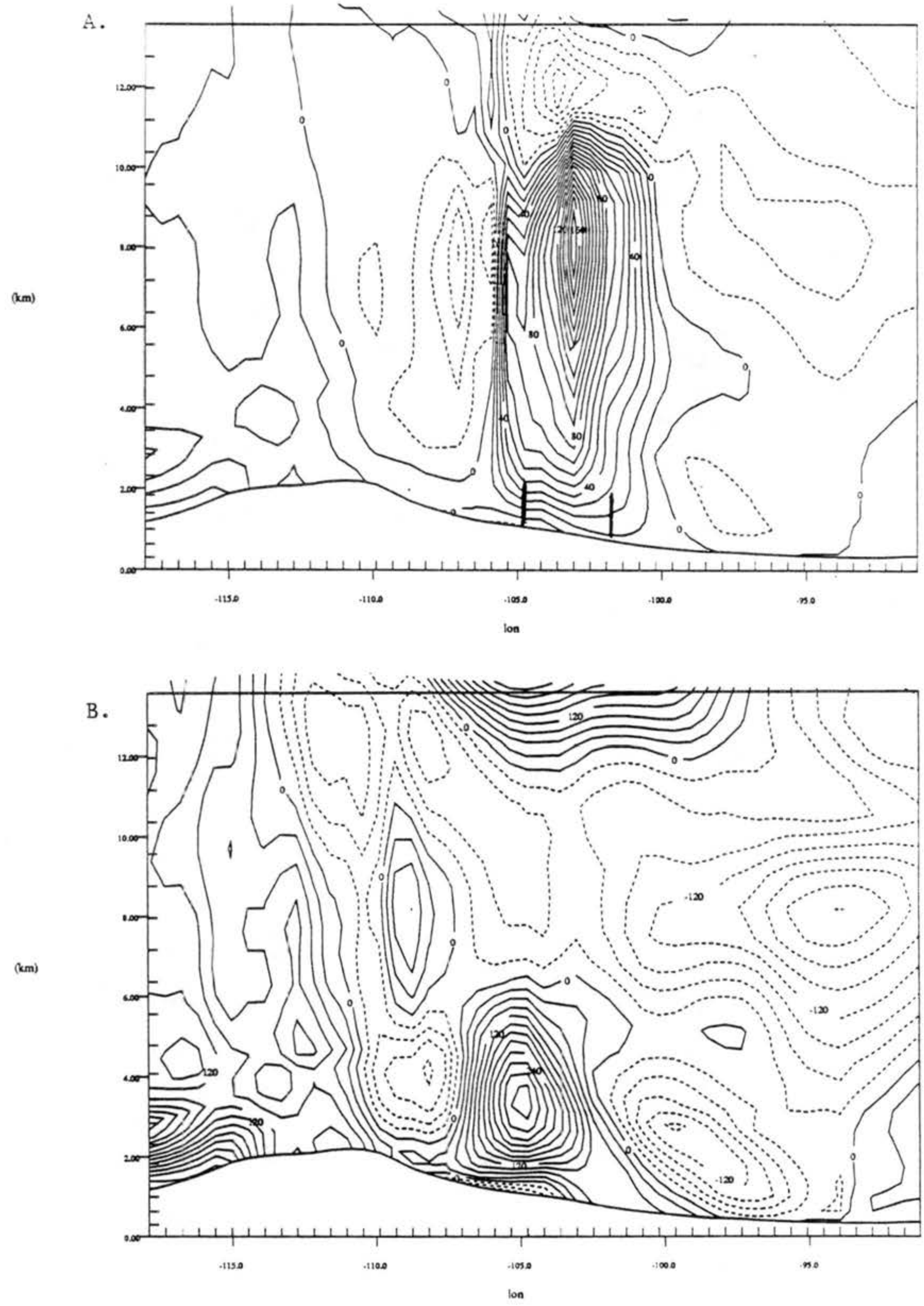

Figure 8.58: Vertical east-west cross section of vertical velocity at 45.2° N from at 3 Aug 0400 UTC. a) higher resolution control run, b) higher resolution dry run.

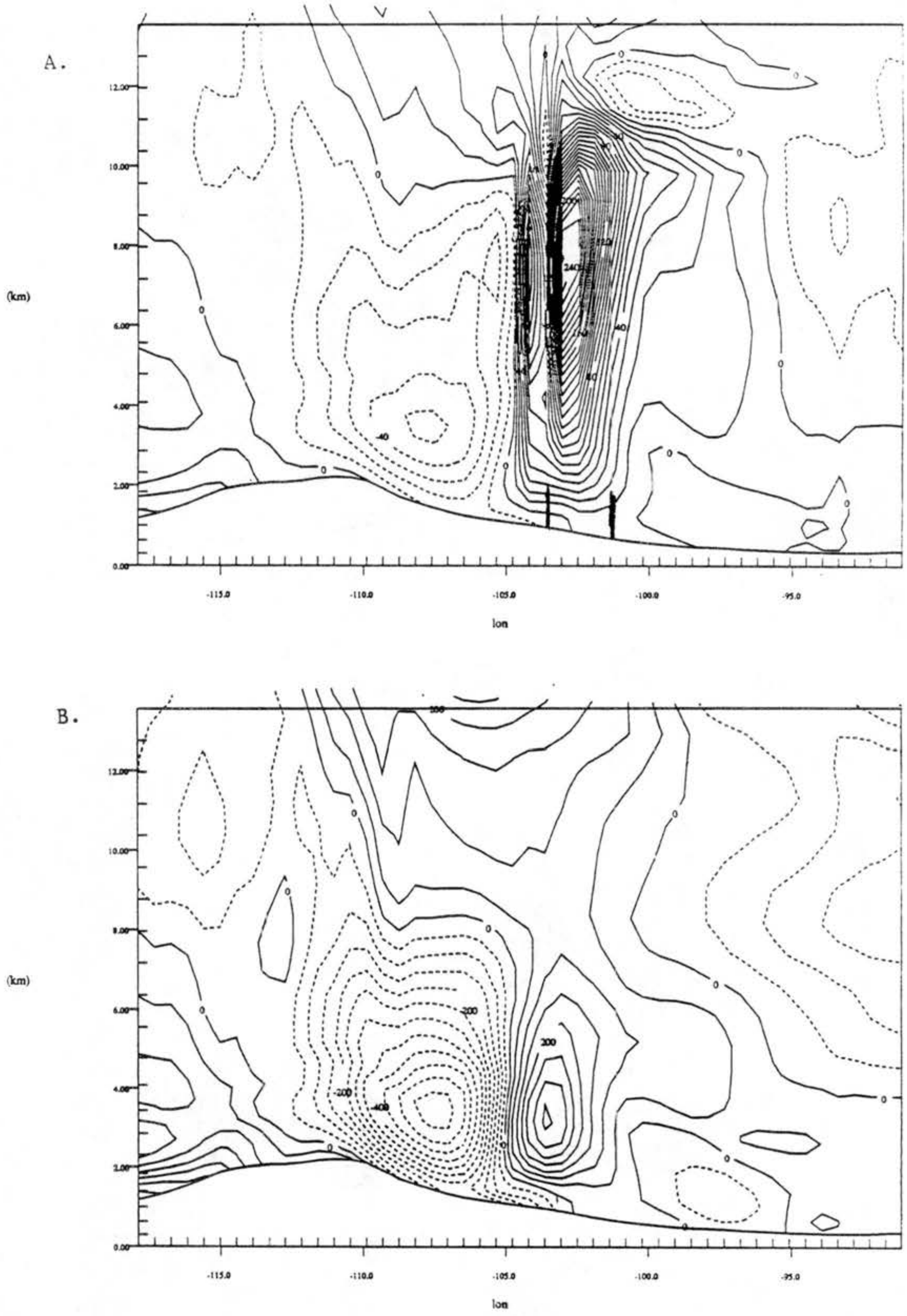

Figure 8.59: Vertical east-west cross section of vertical velocity at 45.2° N from at 3 Aug 0600 UTC. a) higher resolution control run, b) higher resolution dry run.

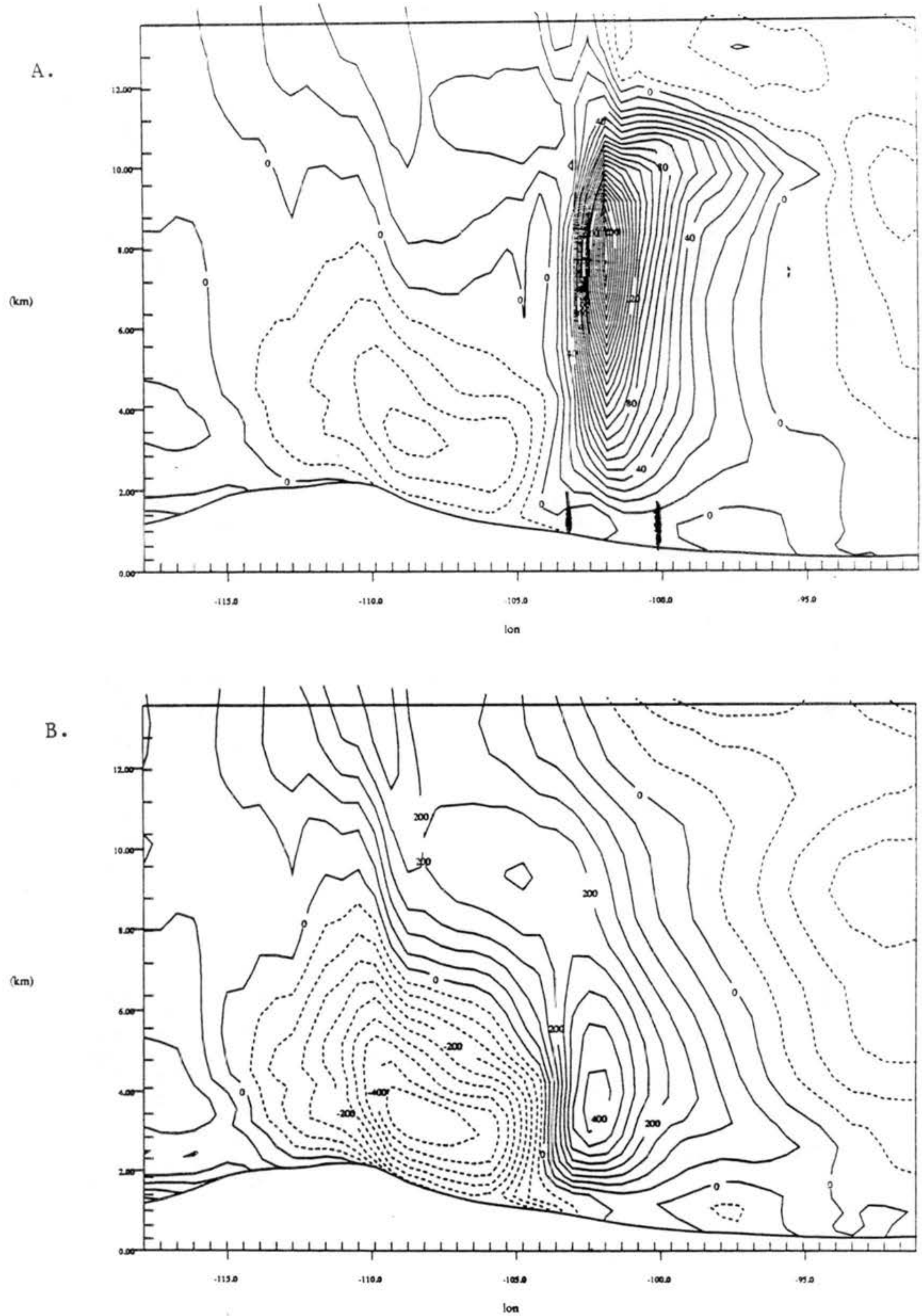

Figure 8.60: Vertical east-west cross section of vertical velocity at 45.2° N from at 3 Aug 0800 UTC. a) higher resolution control run, b) higher resolution dry run.

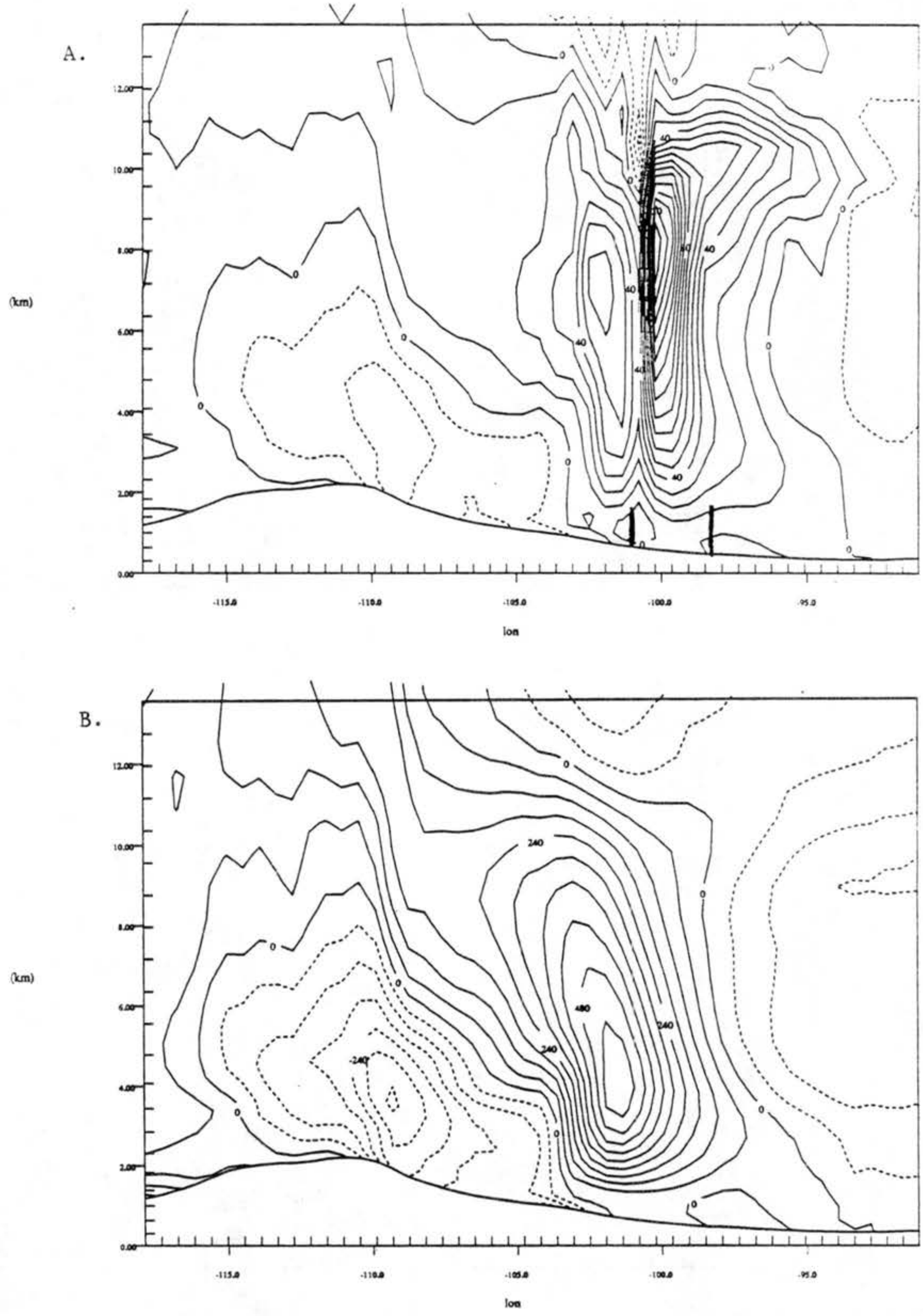

Figure 8.61: Vertical east-west cross section of vertical velocity at 45.2° N from at 3 Aug 1000 UTC. a) higher resolution control run, b) higher resolution dry run.

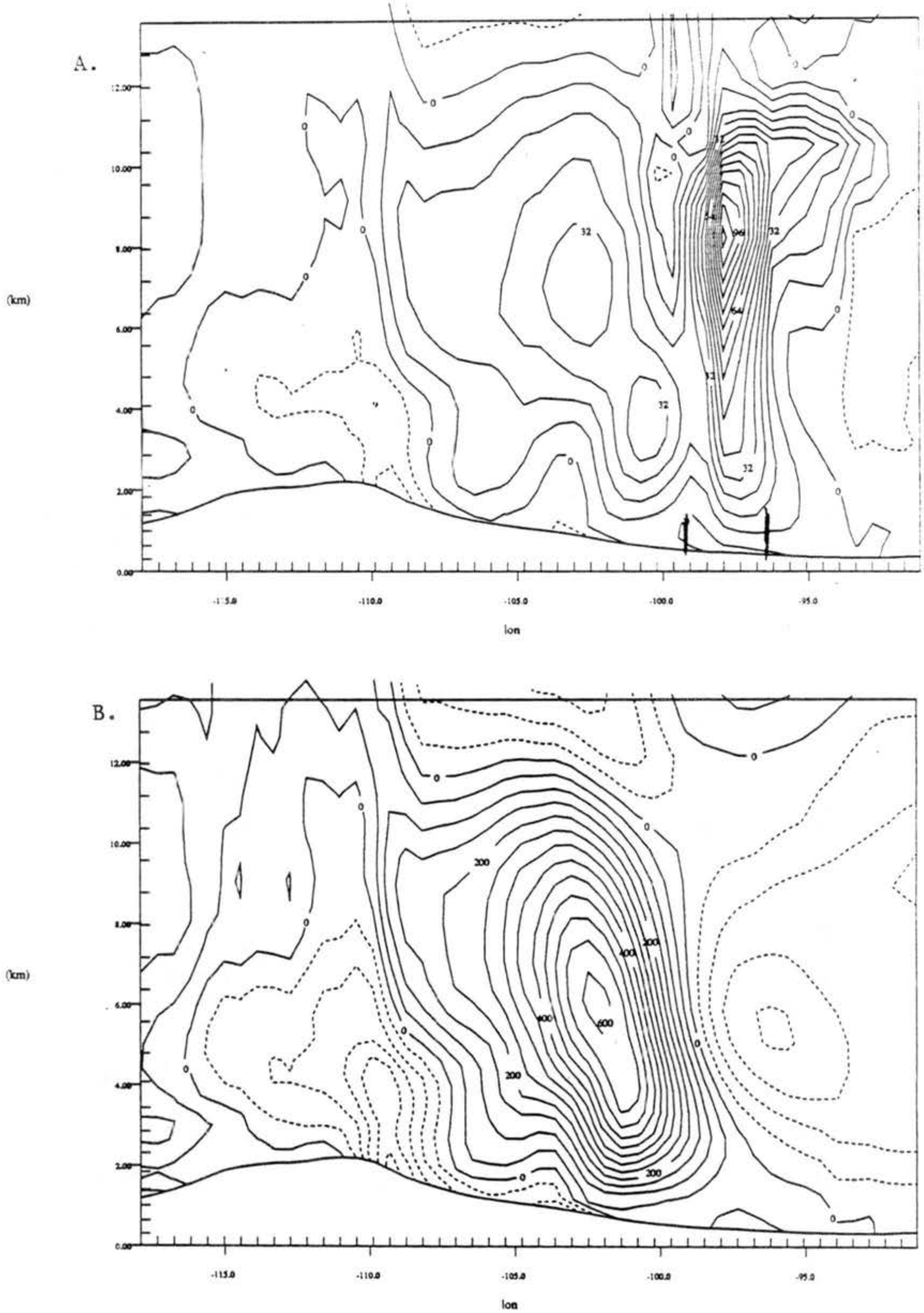

Figure 8.62: Vertical east-west cross section of vertical velocity at 45.2° N from at 3 Aug 1200 UTC. a) higher resolution control run, b) higher resolution dry run.

simulation were rain water, pristine crystals, snow, and aggregates. Graupel was not used because it is mainly formed in the active convective updrafts which are parameterized in this resolution simulation.

In the first few hours after 0000 UTC during the developing phase of the meso-α-scale system, there was very little difference between the control run and the sensitivity simulation. The convective system developed in the same location and propagated similarly during this phase. This is not surprising considering that the system at this phase was dependent on the convective heating for its forcing before the mesoscale aspects of the circulation developed. The main source of condensate at this point was the convective parameterization moistening tendencies which supply water to the upper troposphere. Because of the cold temperatures and large ice nuclei concentration diagnosed from the modified Fletcher concentration formula, this condensate first is converted to pristine crystals which, because of their small size, have a very small terminal fall velocity.

As the mesoscale circulation of the MCC became stronger, the amount of condensate produced became greater. In addition, the condensate is produced at lower levels, since the source of the supersaturation is from vertical advection from low and mid-levels. Since temperatures at these lower levels are warmer, the other ice phase species were produced. These other species, because of the higher terminal velocities, could then precipitate and eventually melt into rain water.

There were two main differences between the control run's MCC and the microphysical run's MCC as they matured and propagated through the Dakotas. First, because of the increased latent heat release from the inclusion of the ice phase, the MCC circulation was slightly deeper in the sensitivity run. Second, and more importantly, the evolution of the spatial distribution of the convection underneath the MCC anvil was different.

Figure 8.63 shows the convective parameterization precipitation rates from 0700 UTC to 1200 UTC in the microphysical run at hourly intervals. The northerly extent of the convection was greater than in the control run at 0700 UTC. By 0800 UTC, two distinct centers of convection can be seen in the both runs; the southern center was in northwestern South Dakota and the northern center was in central North Dakota. The northern center was stronger and persisted longer in the sensitivity run and could still be seen clearly at 1000 UTC near the Canadian border in northeastern North Dakota. The northern center also propagated faster than the southern part of the convective system. In addition, at 1000 UTC in the microphysical run, a second development of convection could be seen over the North Dakota/South Dakota border. This convection persisted through the end of the run and, at 1200 UTC, the convection of the MCC displayed somewhat of a horseshoe shape which actually matches the observed radar precipitation pattern (Figure 6.5f) better than the control run. The strongest mid-level vertical motion at 1200 UTC (Figure 8.64c) also shows this horseshoe shape. The MCC as a whole propagated a little slower in the sensitivity run.

The reasons for the differences in convection between the control and microphysics runs are not completely understood. With the microphysical parameterizations activated, the physical differences that existed between the two runs were: 1) additional latent heat release from the ice phase with a different vertical distribution of heating causing a slightly deeper system, 2) precipitation of resolvable scale condensate which unloaded some of the suspended condensate in the control run and, 3) evaporation and melting of the precipitation at mid and low levels. As the convective system in the microphysical run reached the central Dakotas (1000 UTC) and developed the split structure, a mid-level subsident region developed behind the system (Figure 8.64b), possibly forced from either low and mid-level evaporation or melting. The subsidence, though, developed with the split of the convection and did not cause it. The vertical motion at 0800 UTC (Figure 8.64a) shows no downward motion associated with the MCC although the split can be seen at that time. Examination of the pressure fields revealed very little information, however, because of the masking by the strong synoptic-scale gradients. In addition, as with the control run, no mid-level rear inflow jet could be seen throughout the entire life of the system.

8.6 Higher resolution simulations summary

By using a higher resolution grid (about 45 km), the simulations for the CCOPE MCC were repeated. The high resolution control simulation had an almost identical

A.

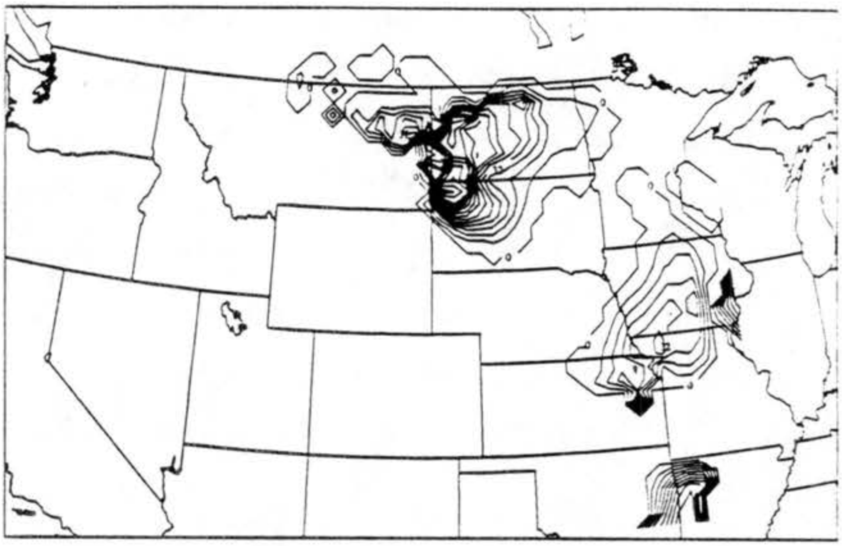

B.

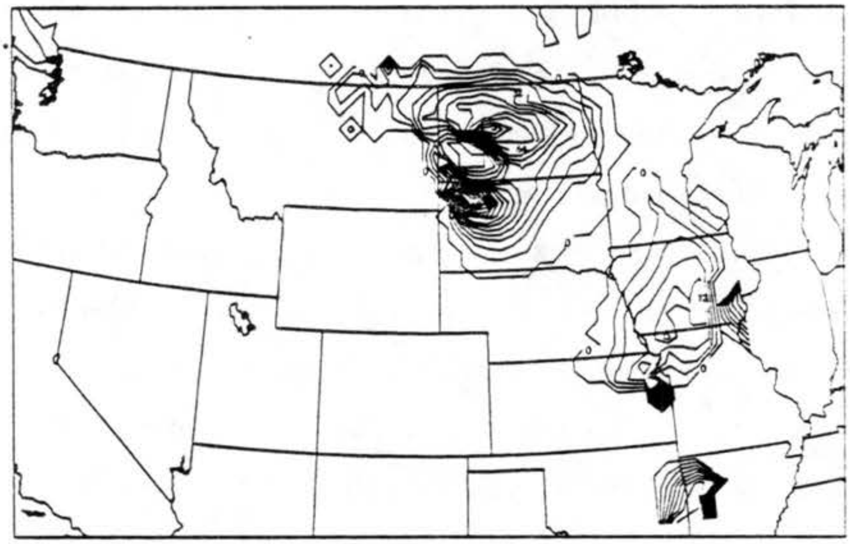

Figure 8.63: Convective parameterization precipitation rate from higher resolution microphysics run at a) 3 Aug 0700 UTC, b) 3 Aug 0800 UTC, c) 3 Aug 0900 UTC, d) 3 Aug 1000 UTC e) 3 Aug 1100 UTC, f) 3 Aug 1200 UTC.

C.

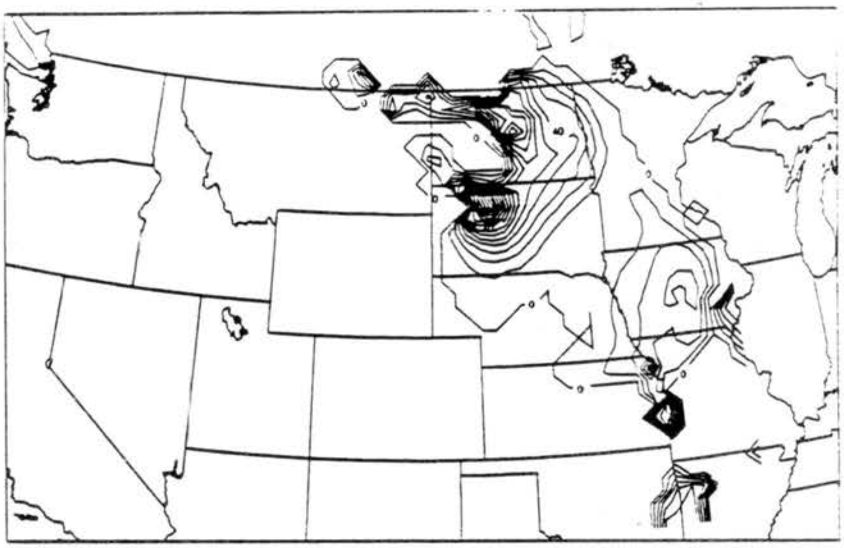

D.

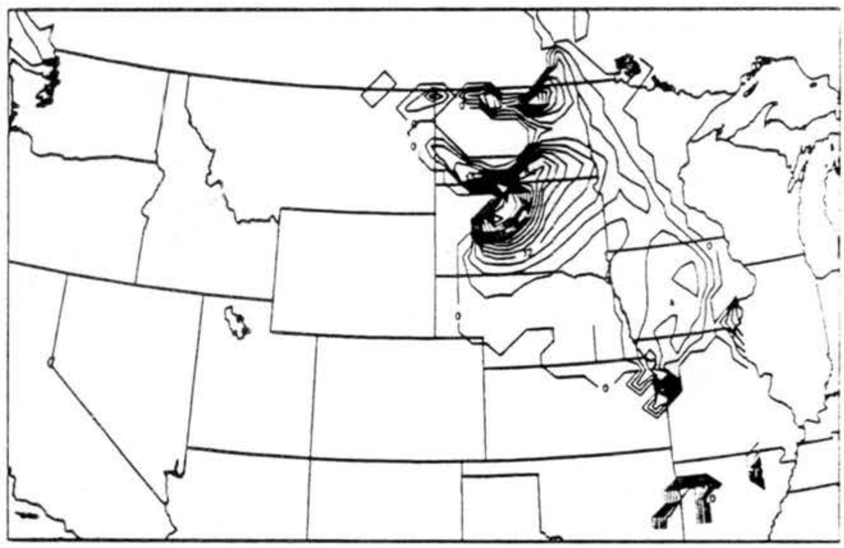

Figure 8.63: Continued.

E.

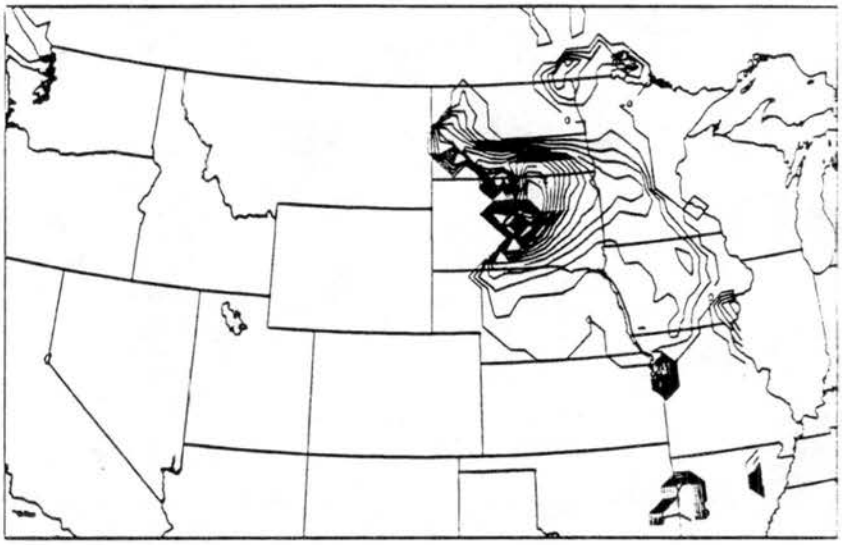

F.

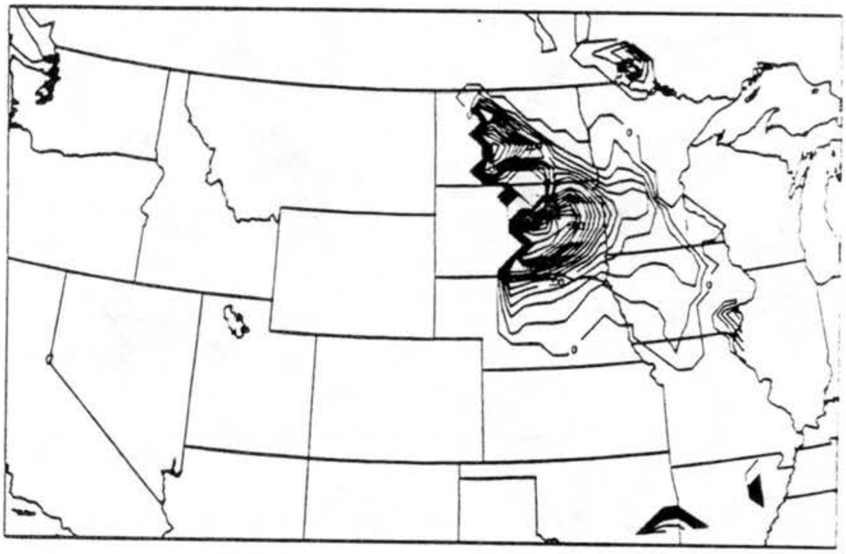

Figure 8.63: Continued.

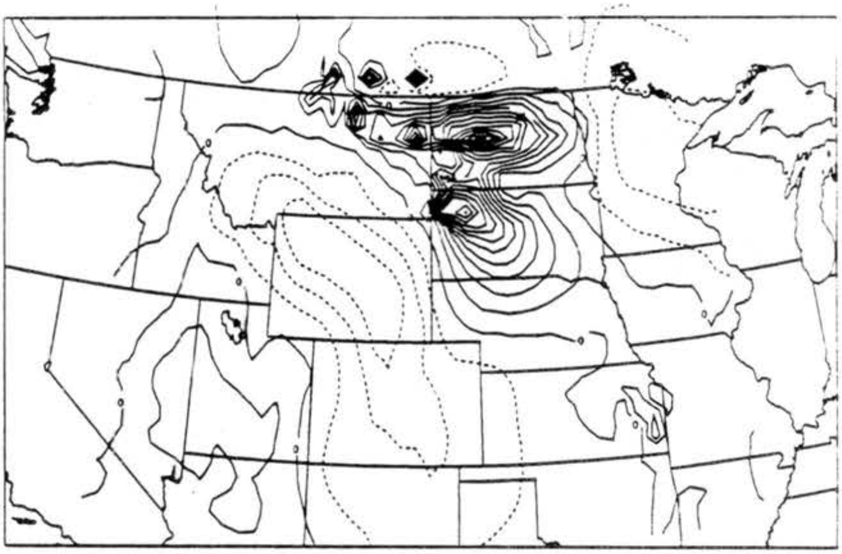

B.

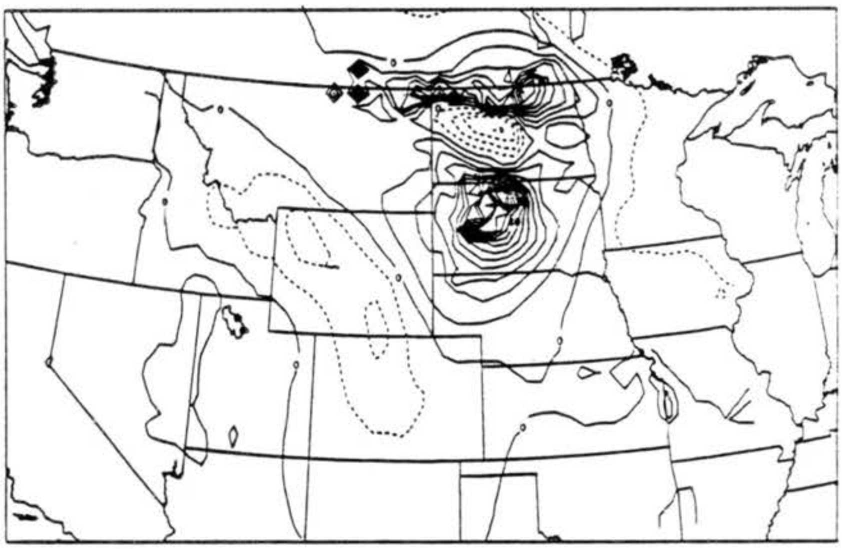

Figure 8.64: Vertical velocity field at 5.16 km above sea level from higher resolution microphysics run. a) 3 Aug 0800 UTC, b) 3 Aug 1000 UTC, c) 3 Aug 1200 UTC.

c.

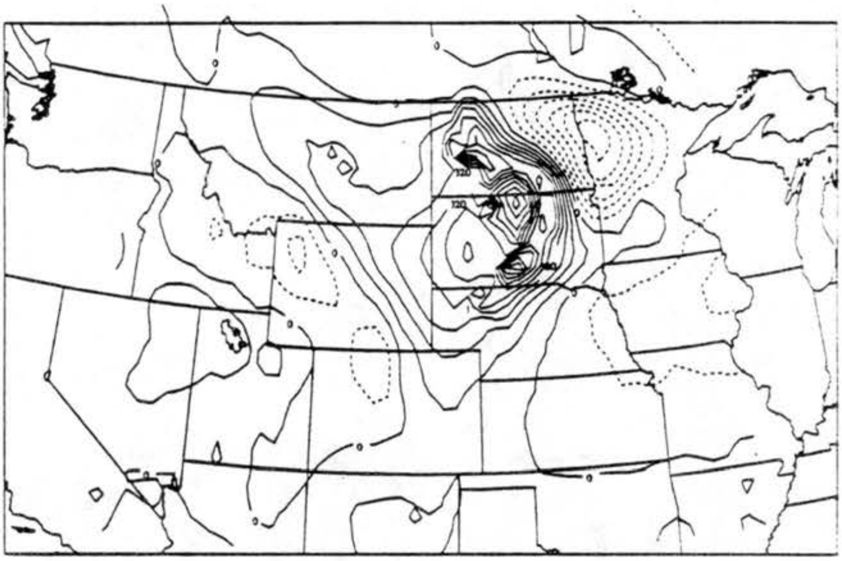

Figure 8.64: Continued.

model configuration to the coarse resolution control simulation described in Chapter 7. A comparison of the results between the coarse resolution and higher resolution runs showed surprisingly good agreement for this convectively-forced simulation, adding to the credibility of the numerical model.

The higher resolution results were then examined for the major forcing mechanisms of the simulated MCC. Important features for the development of the MCC were a low-level "heat low" in the Montana-Wyoming region, the Bermuda high providing a favorable pressure gradient over the central plains for the development of a strong nocturnal low-level jet, a weak front moving southward from Canada, and an upper level jet core in a favorable position to provide upper-level divergence. But also important was the development and propagation of the mountain/plains solenoidal circulation which was formed by topography slope and differing soil characteristics. The solenoid helped to support the low-level heat and moisture inflow into the heat low in Montana during the afternoon hours. As the surface cooled, the solenoid decoupled from the mountains and advected into the central plains, creating favorable low-level vertical motion fields as it moved. Results from a simple two-dimensional simulation in which the solenoid was re-created verified many of these features. The solenoid may also be responsible in many cases of MCC development for the nocturnal preference for MCCs and the frequently observed mid-level shortwave that often accompanies the convective systems.

As the MCC moved into the central Dakotas, it outran the support of the solenoid and almost doubled its propagation speed. The convective region reoriented to a squall line structure although several features of classic squall line dynamics were absent. It is hypothesized that an internal gravity wave response may have been responsible for this transformation.

Two sensitivity simulations were presented based on the higher resolution run. In the run made with no convective parameterization, the MCC did not develop. This run produced a low-level solenoidal circulation which propagated across the Dakotas. At the end of the simulation, the dry solenoid looked very similar to the solenoid in the control run after the MCC had left its support. The sensitivity experiment with the resolved microphysical parameterizations activated showed that the gross behavior of the MCC was similar to the control run although there were differences in the details of the convection underneath the anvil.

Chapter 9

SUMMARY AND CONCLUSION

This dissertation has dealt with the development of a mesoscale numerical model and its use to study the complex circulations of a baroclinic environment which supported the development of a mesoscale convective complex. A summary of the research and the major findings will be detailed in the section below. This will be followed by suggestions for further research.

9.1 Summary of model development

The hydrostatic numerical model developed as part of this research was first written as a separate version of the CSU cloud/mesoscale model (Tripoli and Cotton, 1982). The non-hydrostatic cloud model and the hydrostatic meso-/synoptic-scale model were combined in 1983 to form the first versions of the CSU Regional Atmospheric Modelling System (RAMS). A subsequent restructuring of RAMS was started in 1986 to allow for the inclusion of two-way interactive nesting and several of the physical models and parameterizations from the mesoscale model of Dr. Pielke's research group. This led to the current form of RAMS which was used for the simulations described in this research, although most of the developmental simulations were run with the older versions. Listed below are some of the aspects of RAMS which were developed during the coarse of this research.

- A hydrostatic "time-split" time differencing scheme (Tremback et al., 1985) was developed which allows the model to run with a longer time step by splitting those terms which control the propagation of the Lamb and external waves off on a smaller timestep.

- A prognostic soil temperature and moisture model (Tremback and Kessler, 1985) which consists of a modified form of the soil model described by McCumber and Pielke (1981) was coupled to the atmospheric model.

- A new form of the higher ordered forward upstream advection scheme (Tremback et al., 1987) was derived and the sixth-order flux conservative form of this scheme was implemented in RAMS.

- The two most popular convective parameterization schemes used in mesoscale modelling were examined. An improved version of the Fritsch and Chappell (1980a) scheme was developed which corrected several severe problems with the original scheme such as non-conservation of energy and water mass and inconsistent vertical profiles of convective heating. For the purposes of this research, the new scheme, like the original Fritsch/Chappell scheme, was too sensitive to small changes in various parameters so a simple form of the Kuo (1974)-type scheme was developed and used in the simulations.

- An isentropic data analysis package was written which combines data from several different sources and performs an objective analysis on isentropic coordinate surfaces.

- Finally, all of the "engineering" aspects of creating a large computer code were developed for which little or no credit is given in this field. Everything from input/output schemes (often relatively more complicated than physics or numerics) to the visualization of model and data analysis results must be considered in the development and construction of a numerical model.

9.2 Summary of CCOPE MCC simulations

- The goal of this research was to employ the numerical model to study an MCC with higher space and time resolution than is available through observational means, not primarily to reproduce the observations that were available. The model results still must be compared with the observations, however, to examine the credibility of the model so that conclusions drawn from the simulation could possibly be extended to the real atmosphere.

- The issues of model verification and predictability are discussed. Verification of mesoscale results are very difficult since observational datasets of similar or higher resolution to the model resolution are required. Comparing model results with coarser resolution analyses will show simulated mesoscale circulations as forecast error. In examining the predictability aspects of an atmospheric event, the problems of inaccuracies in the model formulation and initial and boundary conditions were discussed. The initial and boundary conditions are usually provided to the model from an analysis of much coarser resolution. Many of the model parameterizations rely only on intuition for basic physical processes since the physics are frequently not adequately understood.

- A control run for the coarse resolution (about 110 km) simulations was chosen and compared with the observations. While there were many differences, the control run simulated an MCC whose convective structure evolved similarly with the observed convective system. The simulated MCC did not travel as far by 1200 UTC as the observed MCC and the atmospheric boundary layer moisture in the simulation was less than the observed. Overall, the behavior of the simulated system compared favorably with the behavior of the observed system and established the credibility of the numerical model.

- Two simulations testing the predictability aspects of the model formulation and initial conditions were presented. The first simulation tested the horizonal diffusion parameterization and showed that small changes in a parameterization that is employed as a numerical filter can make significant differences in the behavior of the MCC circulations. It also suggested that the 110 km resolution was too coarse to adequately resolve the MCC. The second simulation varied the initialization of soil moisture (for which no observational data exists) by making the U.S. High Plains and the Rocky Mountain region wetter than the control run. The simulated convection in this run bore almost no resemblance to the control run. These simulations showed more research still needs to be done on basic modelling problems, including diffusion schemes and surface heat and moisture fluxes, for the extension of these models to the operational forecasting arena.

- Higher resolution simulations (about 45 km) were made to increase the spatial resolution. A comparison between the coarse resolution and higher resolution runs showed only small differences in the gross behavior of the simulated MCC.
- The results of the higher resolution control run were examined for the important forcing mechanisms of this MCC. Important was the development and propagation of the mountain/plains solenoidal circulation which was formed by topography slope and differing soil moisture contents. The solenoid helped to support the low-level heat and moisture inflow into the heat low in Montana during the afternoon hours. As the surface cooled, the solenoid decoupled from the mountains and advected into the central plains, creating favorable low-level vertical motion fields as it moved. Other factors present in the simulation that are thought to be important to the development of the MCC were a low-level "heat low" in the Montana-Wyoming region, the Bermuda high providing a favorable pressure gradient over the central plains for the development of a strong nocturnal low-level jet, a weak front moving southward from Canada, and an upper level jet core in a favorable position to provide upper-level divergence.
- Results from a simple two-dimensional simulation in which the solenoid was recreated, forced only by varying the soil moisture, verified many of these features. The solenoid may also be responsible in many cases of MCC development for the nocturnal preference for MCCs and the frequently observed mid-level shortwave that often accompanies the convective systems.
- In the two-dimensional simulation, the solenoid underwent significant geostrophic adjustment during the simulation. The simulation implied that the spatial scales of the forcing, in this case the differences in surface characteristics, should be on the order of the Rossby radius of deformation for the forcing of a long lived solenoidal circulation. However, the solenoid needs to exist only for six to twelve hours to

support the MCC. It may, therefore, be possible for somewhat smaller scale solenoids (which are not completely geostrophically adjusted) to provide similar support for the MCC.

- The large differences in the results of the wet soil coarse resolution simulation compared to the control run were due a weaker development of the mountain/plains solenoid, implying that, in this case, the differences in soil characteristics were more important than topography slope in creating the simulated solenoid.
- Other scenarios, for instance the "dry line" in the central plains, might also set up adequate thermodynamic gradients to form a solenoidal circulation which could impact MCC and MCS development.
- For the first eight hours of its life (0000 UTC - 0800 UTC), the simulated MCC and solenoid propagated together across the western half of the Dakotas moving at a low level advective velocity of about 12 m/s. As the MCC reached the central Dakotas, the convective region reoriented to a north-south line configuration, appearing more like a squall line, although other aspects of squall line dynamics were absent. At this time also, the MCC almost doubled its propagation speed (from 12 m/s to 22 m/s) and left the support of the solenoid. It was hypothesized that an internal gravity wave response caused this reorientation and increased propagation speed.
- A higher resolution sensitivity simulation in which the convective parameterization was not used showed the expected result that no convective system or other mesoscale circulations developed that exhibited the characteristics of an MCC. This dry run, as with the control run, produced a low-level solenoidal circulation which propagated across the Dakotas. At the end of the simulation, the dry solenoid looked very similar to the solenoid in the control run after the MCC had left its support.
- The sensitivity experiment with the resolved microphysical parameterizations activated showed that the gross behavior of the MCC was similar to the control run although there were differences in the details of the mesoscale vertical motion fields and convection underneath the anvil.

9.3 Suggestions for further research

9.3.1 Numerical modelling suggestions

There is almost no aspect to numerical modelling that can be considered a solved problem. Everything from the coordinate system to the basic equation set to time differencing needs continued research and study. As the "best" scheme is found, computer capabilities are increased which change the model resolution so that even the basic model aspects need to be re-examined. But obviously, the largest efforts should be expended in the model's parameterizations of various physical processes. For the purposes of this research, the convective parameterization was the most crucial and the most approximate of the many parameterized processes. Research concerning the convective parameterizations should concentrate on their ability to handle the higher grid resolutions that are becoming common because of the advances in computer technology and the ability to handle diurnal variations in the convection.

As grid resolutions for model simulations become more refined, the hydrostatic assumption becomes increasingly in question. Non-hydrostatic models need to be developed which do not use Boussinesq approximations and linearizations so as to handle a large baroclinic domain. This also requires re-consideration of some of the aspects of the boundary conditions and the parameterization schemes.

Another area of model development that needs continued effort is the area of scientific visualization. A numerical model outputs a large amount of data which must be interpreted by the researcher. Inadequate tools to analyze the data can be just as detrimental to the scientific research as poor data.

There currently is a substantial emphasis on four-dimensional data assimilation (4DDA) in the atmospheric science community. 4DDA may be able to assist in the problem of predictability by providing more consistent initial conditions for a numerical simulation.

9.3.2 Mesoscale convective system research suggestions

Following are some suggestions to extend this research and possibilities for additional research to enhance our understanding of mesoscale convective complexes and systems.

- The model simulations suggested that the development and subsequent propagation of the mountain/plains solenoid was crucial to the behavior of the MCC. An observational network to verify how frequently the solenoid occurs and the behavior of the solenoid in convective and non-convective situations would be helpful. The network, though, would have to be fairly large and consist of upper air observations in addition to surface stations. A domain of about 500-700 km north to south with about a 100 km resolution and 300-400 km east to west with about a 50 km resolution would be adequate to observe the solenoid. Because of the possible gravity wave responses, observations would have to be taken about every 30 minutes.

- An analysis tool needs to be developed for the model results which can identify mesoscale and gravity wave perturbations in a strongly baroclinic atmosphere. In analyzing the model simulations, it was unclear in several instances whether particular circulation features were forced by the mesoscale or the synoptic scale. This tool might be based on statistical methods, Fourier or normal mode analysis, or physical differentiations such as ageostrophic motions, etc.

- Simpler generic simulations such as the two-dimensional solenoidal simulation in Chapter 8 can be very enlightening. Further simulations of this type can be performed to examine gravity wave generation and propagation, solenoid behavior in sheared flows, or MCC development in conjunction with various synoptic regimes.

- Geostrophic adjustment in a strongly baroclinic environment where there are both vertical and horizontal wind shears is not well understood. Since all MCCs form in the presence of at least some baroclinicity, this adjustment is a necessary component to the behavior of the MCC. The adjustment process could be examined with the simpler type of simulation mentioned above.

- There are many questions on the relative importance of the large scale forcing mechanisms (low-level and upper-level jets, shortwaves, etc.) on the formation and behavior of the MCC. Sensitivity simulations could be performed which modify the strength of these features. Care must be taken in the modification so that the synoptic fields are reasonably well balanced and that only the particular feature to be modified is actually changed. It might be extremely difficult to modify some features without significantly changing the problem.

- Finally, many more simulations could be performed on the CCOPE MCC in particular. The actual MCC produced derecho winds over a large part of South Dakota which the simulated MCC did not produce. Identification of the reasons that the model did not produce the derecho event could lead to a further understanding of the environment which supports the derecho. Additionally, further sensitivity tests to various processes such as the ice phase and longwave radiation could be performed to investigate their influence on the MCC. Also, two-way interactive nesting simulations focusing, for instance, on the MCC genesis region with a 10-15 km resolution are now possible with RAMS.

Chapter 10

REFERENCES

Arakawa, A. and W.H. Schubert, 1974: Interaction of a cumulus cloud ensemble with the large-scale environment. Part I. *J. Atmos. Sci.,* **31,** 674-701.

Bader, D.C. and T.B. McKee, 1983: Dynamical model simulation of the morning boundary layer development in deep mountain valleys. *J. Appl. Meteorol.,* **22,** 341-351.

Banta, Robert Mason, 1982: An Observational and Numerical Study of Mountain Boundary-Layer Flow. Ph.D. Thesis, Colorado State University, Dept. of Atmospheric Science, Fort Collins, CO 80523, 203 pp. (Atmospheric Science Paper No. 350).

Barnes, S.L., 1973: Mesoscale objective map analysis using weighted time series observations. NOAA Tech. Memo. ERL NSSL-62, 60 pp. [NTIS COM-73-10781].

Betts, A.K. and M.F. Silva Dias, 1977: Modeling of convective downdrafts. Preprints, 11th Tech. Conf. on Hurricanes and Tropical Meteorology, Miami, Dec. 13-16, 1977, AMS, 508-511.

Blackadar, A.K., 1957: Boundary layer wind maxima and their significance for the growth of nocturnal inversions. *Bull. Am. Met. Soc.,* **38,** 283-290.

Bleck, R. and P.L. Haagensen, 1968: Objective analysis on isentropic surfaces. NCAR Tech. Note, TN-39, Dec. 1968.

Bonner, W.D., 1968: Climatology of the low level jet. *Mon. Wea. Rev.,* **96,** 833-850.

Bosart, L.F., and F. Sanders, 1981: The Johnstown Flood of July 1977: A long-lived convective system. *J. Atmos. Sci.*, **38**, 1616-1642.

Businger, J.A., J.C. Wyngaard, Y. Izumi, and E.F. Bradley, 1971: Flux-profile relationship in the atmosphere surface layer. *J. Atmos. Sci.* **28** 181-189.

Chen, C., and W.R. Cotton, 1983a: A one-dimensional simulation of the stratocumulus-capped mixed layer. *Boundary-Layer Meteorol.*, **25**, 289-321.

Chen, C., and W.R. Cotton, 1983b: Numerical experiments with a one- dimensional higher order turbulence model: Simulation of the Wangara Day 33 Case. *Boundary-Layer Meteorol.*, **25**, 375-404.

Clark, Terry L., 1977: A small-scale dynamic model using a terrain-following coordinate transformation. *J. Comput. Phys.*, **24**, 186-215.

Cotton, W.R., R.L. George, and K.R. Knupp, 1982: An intense, quasi-steady thunderstorm over mountanous terrain – Part I: Evolution of the storm-initiating mesoscale circulation. *J. Atmos. Sci.*, **39**, 328-342.

Cotton, W.R., R.L. George, P.J. Wetzel and R.L. McAnelly, 1983: A long- lived mesoscale convective complex. Part I: The mountain-generated component. *Mon. Wea. Rev.*, **111**, 1893-1918.

Cotton, W.R., R. McAnelly, J. Schmidt, and M.-S. Lin, 1984: A multi-scale observational investigation of the formation mechanisms of a mesoscale convective complex. 9th Int. Cloud Physics Conference, Tallinn, USSR, 21-28 August 1984.

Cotton, W.R., M.A. Stephens, T. Nehrkorn, and G.J. Tripoli, 1982: The Colorado State University three-dimensional cloud/mesoscale model - 1982. Part II: An ice phase parameterization. *J. de Rech. Atmos.*, **16**, 295-320.

Cotton, W.R., M.-S. Lin, C.J. Tremback, and R.L. McAnelly, 1989: A composite model of mesoscale convective complexes. *Mon. Wea. Rev.*, **117**, 765-783.

Crowley, W.P., 1968: Numerical advection experiments. *Mon. Wea. Rev.*, **96**, 1-11.

Culverwell, Arlene Holloman, 1982: An Analysis of Moisture Sources and Circulation Fields Associated with an MCC Episode. M.S. Thesis, Colorado State University, Dept. of Atmospheric Science, Fort Collins, CO, 80523, 291 pp.

Curtis, R.C., and H.A. Panofsky, 1958: The relation between large scale vertical motion and weather in summer. *Bull. Amer. Meteor. Soc.*, **39**, 521-531.

Defant, F., 1951: Local winds. *Compendium of Meteorology,* T.F. Malone, Ed., American Meteorological Society, Boston, pp. 655-672.

English, M., 1973: Alberta Hailstones. Part II. Growth of large hail in the storm. Meteorological Monographs **14,** No. 36, AMS, Boston, MA.

Flatau, P.J., G.J. Tripoli, J. Verlinde, W.R. Cotton, 1989: The CSU-RAMS cloud microphysics module: General theory and code documentation. Atmos. Sci. Paper No. 451, Colorado State University, Dept. of Atmospheric Science, Fort Collins, CO 80523.

Fortune, Michael A., 1989: The evolution of vortical patterns and vortices in mesoscale convective complexes. Ph.D. Thesis, Colorado State University, Dept. of Atmospheric Science, Fort Collins, CO 80523.

Frank, W.M., 1978: The life-cycle of GATE convective systems. *J. Atmos. Sci.,* **35,** 1256-1264.

Frank,W.M., 1984: A cumulus parameterization scheme incorporating sub-grid scale convective forcing. Postprints, 15th AMS Technical Conference on Hurricane and Tropical Meteorology, Miami, Amer. Meteor. Soc.

Frank, W.M., 1983: The cumulus parameterization problem. *Mon. Wea. Rev.*, **111**, 1859-1871.

Fritsch, J.M. and C.F. Chappell, 1980a: Numerical prediction of convectively driven mesoscale pressure systems. Part I: Convective parameterization. *J. Atmos. Sci.*, **37**, 1722-1733.

Fritsch, J.M. and C.F. Chappell, 1980b: Numerical prediction of convectively driven mesoscale pressure systems. Part II: Mesoscale model. *J. Atmos. Sci.*, **37**, 1734-1762.

Fritsch, J.M., and R.A. Maddox, 1981a: Convectively driven mesoscale weather systems aloft. Part I: Observations. *J. Appl. Meteor.*, **20**, 9-19.

Fritsch, J.M., and R.A. Maddox, 1981b: Convectively driven mesoscale weather systems aloft. Part II: Numerical simulations. *J. Appl. Meteor.*, **20**, 20-26.

Fujita, T.T., 1959: Precipitation and cold air production in mesoscale thunderstorm systems. *J. Meteor.*, **16**, 454-466.

Gadd, A.J., 1978: A split explicit integration scheme for numerical weather prediction. *Quart. J. Roy. Met. Soc.*, **104**, 569-582.

Gal-Chen, Tzvi and R.C.J. Somerville, 1975a: On the use of a coordinate transformation for the solution of the Navier-Stokes Equations. *J. Comput. Phys.*, **17**, 209-228.

Gal-Chen, Tzvi and R.C.J. Somerville, 1975b: Numerical solution of the Navier-Stokes equations with topography. *J. Comp. Phys.* **17**, 276-310.

George, R.L., 1979: Evolution of mesoscale convective systems over mountainous terrain. Atmospheric Science Paper No. 318, Colorado State University, Dept. of Atmos. Sci., Fort Collins, CO, 160 pp.

Hering, W.S., and R.T. Borden, J4., 1962: Diurnal variations in the summer wind field over the central United States. *J. Atmos. Sci.,* **19,** 81-86.

Hewson, E.W., 1937: The application of wetbulb potential temperature of air mass analysis. *Quart. J. R. Meteor. Soc.,* **63,** 9.

Hill, G.E., 1974: Factors controlling the size and spacing of cumulus clouds as revealed by numerical experiments. *J. Atmos. Sci.,* **31,** 646.

Hinrichs, G., 1888: Tornadoes and derechos. *Amer. Meteor. J.,* **5,** 306-317, 341-349.

Johns, R.H., and W.D. Hirt, 1987: Derechos: Widespread convectively induced windstorms. *Weather and Forecasting,* **2,** 32-49.

Klemp, J.B. and R.B. Wilhelmson, 1978a: The simulation of three-dimensional convective storm dynamics. *J. Atmos. Sci.,* **35,** 1070-1096.

Klemp, J.B. and R.B. Wilhelmson, 1978b: Simulations of right- and left-moving storms produced through storm splitting. *J. Atmos. Sci.,* **35,** 1097-1110.

Knupp, Kevin Robert, 1985: Precipitation convective downdraft structure: A synthesis of observations and modeling. Ph.D. dissertation, Colorado State University, Dept. of Atmospheric Science, Fort Collins, CO 80523.

Knupp, K.R., 1987: Downdrafts within High Plains Cumulonimbi. Part I: General kinematic structure. *J. Atmos. Sci.,* **44,** 987-1008.

Koch, S.E., 1985: Ability of a regional-scale model to predict the genesis of intense mesoscale convective systems. *Mon. wea. Rev.,* **113,** 1693-1713.

Kreitzberg, C.W. and D.J. Perkey, 1976: Release of potential instability: Part I. A sequential plume model within a hydrostatic primitive equation model. *J. Atmos. Sci.,* **33,** 40-63.

Krishnamurti, T.N., Y. Ramanathan, H.-L. Pan, R.J. Rasch and J. Molinari, 1980: Cumulus parameterization and rainfall rates. *Mon. Wea. Rev.*, **108**, 465-472.

Kuo, H.L., 1965: On the formation and intensification of tropical cyclones through latent heat release by cumulus convection. *J. Atmos. Sci.*, **22**, 40-63.

Kuo, H.L., 1974: Further studies of the parameterization of the influence of cumulus convection on large-scale flow. *J. Atmos. Sci.*, **31**, 1232-1240.

Leary, C.A., and E.N. Rappaport, 1983: Internal structure of a mesoscale convective complex. Preprints, 21st Conf. on Radar Meteorology, Amer. Meteor. Soc., 19-23 September, Edmonton, Alberta, 70-77.

Lee, C.-S., 1986: An observational study of tropical cloud cluster evolution and cyclogenesis in the western north pacific. Ph.D. disertation, Dept. of Atmospheric Science, CSU, Fort Collins, CO, 80523, 243 pp.

Lewis, J.M., 1975: Test of Ogura-cho model on a prefontal squall line case. *Mon. Wea. Rev.*, **103**, 764-778.

Lilly, D.K., 1962: On the numerical simulation of buoyant convection. *Tellus,* **XIV**, 2, 148-172.

Louis, J.F., 1979: A parametric model of vertical eddy fluxes in the atmosphere. *Boundary-Layer Meteorol.*, **17**, 187-202.

Lin, M.-S., 1986: The evolution and structure of composite meso-alpha-scale convective complexes. Atmos. Sci. Paper #404, Colorado State University, Dept. of Atmosheric Science, Fort Collins, CO 80523, 245 pp.

Maddox, R.A, 1980: Mesoscale convective complexes. *Bull. Amer. Meteor. Soc.*, **61**, 1374-1387.

Maddox, R.A., 1981: The structure and life-cycle of midlatitude mesoscale convective complexes. Atmospheric Science Paper No. 336, Dept. of Atmospheric Science, Colorado State University, Fort Collins, Colorado, 80523, 311 pp.

Mahrer, Y. and R.A. Pielke, 1977: A numerical study of the airflow over irregular terrain. *Beitrage zur Physik der Atmosphare,* **50,** 98-113.

Manabe, S., J. Smagorinsky, and R.F. Strickler, 1965: Simulated climatology of a general circulation model with a hydrological cyle. *Mon. Wea. Rev.,* **93,** 769-798.

McBride, J.L., and R. Zehr, 1981: Observational analysis of tropical cyclone formation. Part II: Comparison of non-developing versus developing systems. *J. Atmos. Sci.,* **38,** 1132-1151.

McCumber, M.C. and R.A. Pielke, 1981: Simulation of the effects of surface fluxes of heat and moisture in a mesoscale numerical model. Part I: Soil layer. *J. Geophys. Res.,* **86,** 9929-9938.

McNider, R.T., and R.A. Pielke, 1981: Diurnal boundary-layer development over sloping terrain. *J. Atmos. Sci.,* **38,** 2198-2212.

Means, L.L., 1944: The nocturnal maximum occurrence of thunderstorms in the midwestern States. Miscellaneous Reports., No. 16, University of Chicago Press.

Means, L.L., 1952: On thunderstorm forecasting in the central United States. *Mon. Wea. Rev.,* **80,** 165-189.

Mesinger, F. and A. Arakawa, 1976: Numerical methods used in atmospheric models. *GARP Publication Series, No. 14,* WMO/ICSU Joint Organizing Committee, 64 pp.

Molinari, J., 1985: A general form of Kuo's cumulus parameterization. *Mon. Wea. Rev.,* **113,** 1411-1416.

Molinari, J., and T. Corsetti, 1985: Incorporation of cloud-scale and mesoscale downdrafts into a cumulus parameterization: Results of one- and three-dimensional integrations. *Mon. Wea. Rev.,* **13,** 485-501.

Newton, C.W., 1950: Structure and mechanism of the prefrontal squall line. *J. Meteor.,* **8,** 210-222.

Newton, C.W., and H.R. Newton, 1959: Dynamical interactions between large convective clouds and environment with vertical shear. *J. Meteor.,* **16,** 483-496.

Ogura, Y., and M.-T. Liou, 1980: The structure of a midlatitude squall line: A case study. *J. Atmos. Sci.,* **37,** 553-567.

Perkey, D.J., and R.A. Maddox, 1985: A numerical investigation of a mesoscale convective system. *Mon. Wea. Rev.,* **113,** 553-566.

Pielke, R.A., 1984: *Mesoscale Meteorological Modeling.* Academic Press, Inc., Orlando, FL.

Pitchford, K., and J. London, 1962: The low-level jet as related to nocturnal thunderstorms over midwest United States. *J. Appl. Meteor.,* **1,** 43-47.

Raymond, D.J., 1989: A theory for long-lived mesoscale convective systems. Submitted to *Quart. J. R. Meteorol. Soc.*

Schmidt, J.M., and W.R. Cotton, 1989: A High Plains squall line associated with severe surface winds. *J. Atmos. Sci.,* **46,** 281-302.

Schubert, W.H., J.J. Hack, P.L. Silva Dias, and S.R. Fulton, 1980: Geostrophic adjustment in an axisymmetric vortex. *J. Atmos. Sci.,* **37,** 1464-1484.

Sellers, W.D., 1965: *Physical Climatology.* The University of Chicago Press, Chicago & London, 272 pp.

Smagorinsky, J., 1963: General circlation experiments with the primitive equations. Part I, The basic experiment. *Mon. Wea. Rev.*, **91**, 99-164.

Song, J.L., 1986: A numerical investigation of florida's sea breeze – cumulonimbus interactions. Ph.D. dissertation, Colorado State University, Dept. of Atmospheric Science, Fort Collins, CO 80523, 187 pp.

Tollerud, E.I., and S.K. Esbensen, 1985: A composite life cycle of nonsquall mesoscale convective systems over the tropical ocean. Part I: Kinematic fields. *J. Atmos. Sci.*, **42**, 823-837.

Tremback, C.J. and R. Kessler, 1985: A surface temperature and moisture parameterization for use in mesoscale numerical models. Preprints, 7th Conference on Numerical Weather Prediction, 17-20 June 1985, Montreal, Canada, AMS.

Tremback, C.J., J. Powell, W.R. Cotton, and R.A. Pielke, 1987: The forward in time upstream advection scheme: Extension to higher orders. *Mon. Wea. Rev.*, **115**, 540-555.

Tremback, C.J., G.J. Tripoli, and W.R. Cotton, 1985: A regional scale atmospheric numerical model including explicit moist physics and a hydrostatic time-split scheme. Preprints, 7th Conference on Numerical Weather Prediction, June 17-20, 1985, Montreal, Quebec, AMS.

Tripoli, G.J., 1986: A numerical investigation of an orogenic mesoscale convective system. Ph.D. dissertation, Colorado State University, Dept. of Atmospheric Science, Fort Collins, Colorado 80523, 290 pp. (Atmospheric Science Paper No. 401).

Tripoli, G.J., and W.R. Cotton, 1982: The Colorado State University three-dimensional cloud/mesoscale model - 1982. Part I: General theoretical framework and sensitivity experiments. *J. de Rech. Atmos.*, **16**, 185-220.

Tripoli, G., and W.R. Cotton, 1989a: A numerical study of an observed orogenic mesoscale convective system. Part 1. Simulated genesis and comparison with observations. *Mon. Wea. Rev.*, **117**, 273-304.

Tripoli, G., and W.R. Cotton, 1989b: A numerical study of an observed orogenic mesoscale convective system. Part 2. Analysis of governing dynamics. *Mon. Wea. Rev.*, **117**, 305-328.

Wallace, J.M., 1975: Diurnal variations in precipitation and thunderstorm frequency over the conterminous United States. *Mon. Wea. Rev.*, **103**, 406-419.

Wetzel, P.J., W.R. Cotton and R.L. McAnelly, 1983: A long-lived mesoscale convective complex. Part II: Evolution and structure of the mature complex *Mon. Wea. Rev.*, **111**, 1919-1937.

Williams, K.T. and W.M. Gray, 1973: Statistical analysis of satellite observed trade wind cloud clusters in the western North Pacific. *Tellus*, **25**, 313-336.

Zhang, D.-L., 1985: Meso-β scale structure and evolution of the Johnstown Flood of July 1977 using a two-way nested grid. Ph.D. dissertation, The Pennsylvania State University, Dept. of Meteorolgy, University Park, PA.

Zhang, D-L., and J.M. Fritsch, 1985: Numerical simulation of mesoscale convective systems: The Johnstown Flood of July 1977. Preprints, 7th Conference on Numerical Weather Prediction, 17-20 June 1985, Montreal, Q.P., Canada, 245-250.

Zhang,D.-L., K. Gao, and B. Parsons, 1989: Numerical simulation of an intense squall line during 10-11 June 1985 PRE-STORM. Part I: Model Verification. In preparation.